The Evolution of an Impinging Synthetic Air Jet

Rayhaan Farrelly

Department of Mechanical and Manufacturing Engineering

Parsons Building

Trinity College

Dublin 2

Ireland

April 2013

A thesis submitted to the University of Dublin in partial fulfilment of the requirements for the degree of Ph.D.

Declaration

I declare that I am the author of this thesis and that all work described herein is my own, unless otherwise referenced. Furthermore, this work has not been submitted, in whole or part, to any other university or college for any degree or qualification. I authorise the library of Trinity College, Dublin to lend or copy this thesis.

Abstract

Impinging synthetic jets are considered to offer great potential for many applications, including the thermal management of electronics. In this study, an experimental investigation into the evolution of an impinging synthetic air jet at a unique set of parameters has been undertaken. The transition from the near field, which comprises discrete vortices to a steady turbulent jet in the far field is an area where the flow mechanisms involved are dynamic and complex and, in some cases, poorly understood. Although numerous studies have been reported on in the literature for free synthetic jets, studies on the flow structures of an impinging synthetic air jet are limited. Even fewer studies have been performed with high frame rate particle image velocimetry (PIV). A comprehensive review of the existing literature is presented.

The present study utilises high speed, high resolution PIV to measure the flow field of the synthetic jet. Two dimensional high resolution PIV captures the evolution of the synthetic jet from formation to development and subsequently impingement. Simultaneous surface heat transfer measurements obtained from a hot film sensor and constant temperature anemometry, and stereoscopic PIV capture the flow structures subsequent to impingement, with the simultaneous heat transfer measurements illustrating the potential of the impinging synthetic jet for cooling applications.

For the test parameters considered, a dimensionless stroke length L_0/D=12 was identified as 'optimal' in terms of surface heat transfer and flow behaviour at impingement. It was found that this stroke length provided a greater Nusselt number than a higher stroke length; this is linked to the phase difference between the vortices subsequent to impingement. The results of this analysis provide an understanding of the impingement flow that will aid in understanding its application to convective cooling.

Acknowledgments

This work would not have been possible without the help and support of the following people I have had the pleasure and opportunity to work with. First, I would like to thank my supervisor, Professor Darina Murray, for her attention to detail, support, guidance and tolerance throughout my time at Trinity College, Dublin. Help was always at hand, while space allowed me the independence to explore. Dr. Tim Persoons for his perspicacious comments, and always being of assistance no matter his location or predicament. Dr. Anthony Robinson for his shared knowledge, dynamism, and encouragement, it has been greatly appreciated. In addition I would like to thank Professor John Fitzpatrick for his advice, enthusiasm and support.

I would like to thank the following people for their technical and administrative help, along with a positive outlook and much needed humour, Mick Reilly, Gerry Byrne, John Gaynor, Joan Gillen, Alex Kearns, and Danny Boardman.

To my fellow researchers: Karl Brown, Maurice Deasy, Brian Donnelly, Tom Lupton, Oisín Lyons, Gerard McGranaghan, Alan McGuinn and Séamus O'Shaughnessy, it was the best of times, it was the worst of times.

To my mother and father, your unwavering support and sacrifices have allowed me to get to where I am today, and for this, thank you. To my brothers, grandmother and extended family, this has been a long journey that has been enriched by your support and contribution over the years, it would not have been possible without you. Finally, an ear outside the world of Mechanical Engineering, Elizabeth Gaynor.

Contents

Nomenclature

$\bar{\omega}_{i,j}$	Average vorticity within an enclosed area $[s^{-1}]$
ϵ	Porosity [-]
Γ	Circulation $[m^2/s]$
$\hat{n}\cdot$	Unit vector [-]
μ	Dynamic viscosity $[Ns/m^2]$
ν	Kinematic viscosity $[m^2/s]$
ω	Angular frequency [Rad/s]
ϕ	Phase angle [°]
ρ	Density $[kg/m^3]$
τ	[m/s]
ε	Stokes layer thickness [-]
ζ	Peak-locking coefficient []
A_{op}	Orifice plate surface area $[m^2]$
C	Speed of sound [m/s]
C_p	Specific heat capacity [kJ/kgK]
C_{aC}	Cavity acoustic compliance=$V_c/\rho C^2$ $[s^2m^4/kg]$

C_{aD} Diaphragm compliance=$\Delta V_c/P$ $[s^2m^4/kg]$

D Diameter [m]

D_c Cavity diameter [m]

D_{op} Orifice plate diameter [m]

f Frequency [Hz]

f_H Cavity resonant frequency (Helmholtz) [Hz]

h Cavity height [m]

h Heat transfer coefficient $[W/m^2K]$

I_0 Impulse $[m^2/s]$

k Thermal conductivity [W/mK]

l Length [m]

l_o Orifice length [m]

L_0 Stroke length [m]

M_{aD} Diaphragm acoustic mass=$\frac{2\pi}{\Delta V_c{}^2}\int_0^{R^2}\rho_A[w(r)]^2rdr$ $[kg/m^4]$

M_{aN} Orifice acoustic mass=$4\rho L/3\pi r^2$ $[kg/m^2]$

M_{aRad} Orifice acoustic radiation mass=$8\pi/3\pi^2 r$ $[kg/m^4]$

Nu Nusselt number=$\frac{hL}{k}$ [-]

Pr Prandtl number=$\frac{C_p\mu}{k}$ [-]

Q Volumetric flow rate $[m^3/s]$

R Resistance $[\omega]$

r Radial ordinate [-]

Re Reynolds number=$\frac{\rho U L}{\mu}$ [-]

S Stokes number=$\frac{\tau_r U}{l}$ [-]

Sr Strouhal number=$\frac{fL}{U}$ [-]

T Temperature [K]

t Time [s]

T_{air} Ambient air temperature [K]

T_{cav} Cavity temperature [K]

T_{film} Hot film temperature [K]

T_{surf} Surface temperature [K]

T_S Sensor temperature [K]

U Mean velocity [m/s]

U Velocity $[m/s]$

U_0 Area averaged velocity [m/s]

U_m Momentum flow velocity [m/s]

U_{vortex} Vortex velocity [m/s]

V_c Cavity volume $[m^3]$

V_{avg} Average velocity [m/s]

x_{t_1} Vortex co-ordinates [mm]

x_{t_2} Vortex co-ordinates [mm]

List of Figures

List of Tables

Chapter 1

Introduction

1.1 Background

A synthetic jet is a time averaged fluid motion that is a result of the interaction of a train of vortices that form from an oscillatory flow at an orifice, it has the unique property of being formed from the working fluid of the flow system that it is deployed in. Synthetic air jets operate on a simple principle: a flexible membrane or diaphragm forms one side of a partially enclosed chamber. Opposite to the membrane is an opening, such as a jet nozzle or orifice plate. A mechanical actuator, piezoelectric diaphragm or magnetic coil causes the membrane to oscillate and periodically forces air into and out of the opening. Figure 1.1 shows a schematic diagram of the synthetic air jet setup, and the vortices that are produced from the ejection and suction of fluid across an orifice by a loudspeaker, which results in the net mass flux being zero. One of the primary advantages of the synthetic air jet is this zero-net mass flux nature, which means that it transfers linear momentum to the flow system without net mass injection across the system boundary. This eliminates the need for external ducting, thus allowing the synthetic air jet to be easily integrated into complex geometries. In recent years it has been established that synthetic air jets are extremely versatile for many applications, and offer great potential for the cooling of electronics. For example, they have been implemented in various aerodynamic flow applications, including static and dynamic stall control on airfoils [1] and jet vectoring [2]. With regard to their

cooling potential, among the first to investigate air jet impingement heat transfer with excitation of the flow structures within the jet were Nevins and Ball [3] in 1961; they concluded that there was no significant heat transfer enhancement from the pulsations present in the flow. After a period of 26 years, the work of Kataoka et al. [4] found that the presence of secondary structures in a similar type of flow aided in enhancing heat transfer; in their research it was shown that the stagnation point heat transfer is enhanced when these large-scale structures impinge on the surface.

The use of impinging synthetic jets for the cooling of electronics is a relatively new technology which has shown great promise in a number of practical applications. Research performed by Vukasinovic and Glezer [5] showed that a synthetic air jet had the potential to be utilised as an effective option for electronics cooling, particularly in environments with complex and confined geometries. Although synthetic jets have the potential for many cooling applications, this technology is a particularly attractive candidate for cooling miniature surfaces, like electronic packages, because they can effect the heat transfer on extremely small scales and enhance the transport and mixing of the heated fluid. With the introduction of multi-core processors, the amount of heat generated under heavy load has decreased. However, it has not been eliminated from the system, but has been 'relocated', with the RAM chips now producing more and more heat because they are forced to deal with all the extra traffic that a multi-core processor produces. Excessive temperatures have an adverse affect on the lifespan and performance of any system, in particular that of electronic components; in a situation where loss of cooling occurs it can lead to the sudden failure of the component. Of the numerous ways available to dissipate heat in electronic components, forced convection is utilised in most commercial applications, where the cooling system is mounted on a large heat sink. This essentially spreads the heat produced by the chip over a greater area; this solution has thus far proved adequate in satisfying the industry's cooling needs. The elaborate design of current heat sinks is an attempt to keep up with ever increasing heat flux densities; the effect of this is an increase in cost of heat sink production. In order to provide an airflow over these heat sinks, fans have increased in size, which in turn increases power consumption

and noise levels; as a result, this technology is reaching its practical, operational and economical limits. Electronics densification is the current industry objective, and it has been established that there is a need for more efficient cooling methods in these closely packed systems, with this need continuing to grow in the foreseeable future, Black et al. [6]. Synthetic air jets have a lot to offer in terms of meeting the criteria for new cooling solutions, namely their effective cooling ability, lower power consumption, small size and low cost. However, the full heat transfer capabilities of a synthetic air jet are currently unknown and it is for this reason that much more research is required to characterise and optimise the fluid flow characteristics, which will lead to an overall improvement in heat transfer performance for an impinging synthetic air jet.

It is the flow structures contained within a synthetic air jet flow that are of particular interest, as a synthetic jet is essentially a fluid motion consisting of a train of propagating vortices. To be specific, it is the vortex ring (for an axisymmetric jet) that is formed at the orifice that is the main focus, because the main variables that dictate synthetic jet formation are the dimensionless stroke length (L_0/D), the jet Reynolds number ($Re = \rho U_0 D/\mu$) and the dimensionless jet exit to impingement surface spacing (H/D). Depending on these synthetic jet formation parameters, the overall flow field can change dramatically, largely due to whether or not the vortices formed can escape from the vicinity of the orifice.

Synthetic jet heat transfer is an area that has been investigated in parallel research work carried out within the research group [7], with time-averaged heat transfer and fluctuating fluid temperature data being obtained for a synthetic air jet impinging perpendicular to a heated surface. Although considerable progress has been made in characterising the synthetic jet heat transfer, a fundamental understanding of the fluid dynamics and the relationship to the convective heat transfer mechanisms is lacking in impinging synthetic jet flows. This is the focus of the current research.

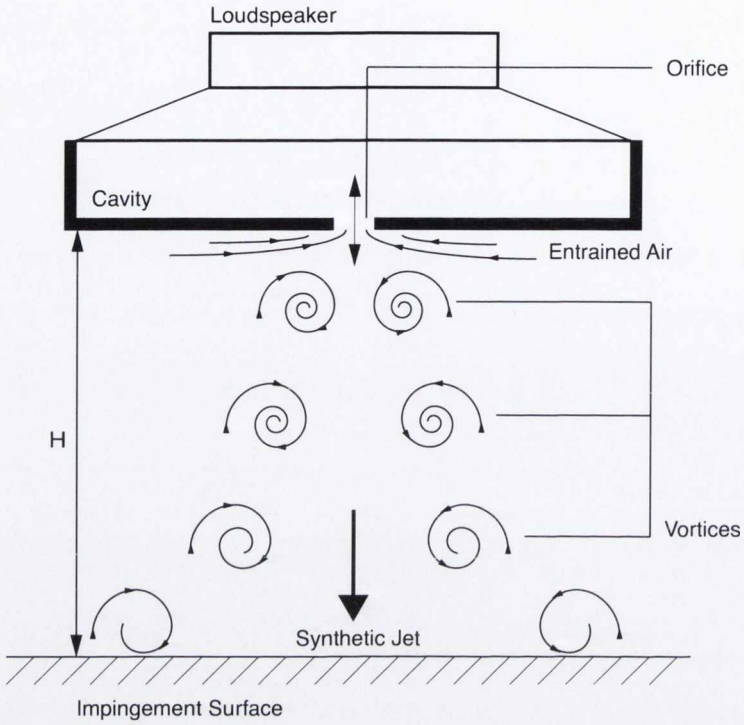

Figure 1.1 – Schematic diagram of the impinging synthetic jet facility

1.2 Research motivation and objectives

This research is concerned with a synthetic air jet impinging perpendicular to a flat surface for a unique set of parameters. There have been no previous studies reported in the literature that have characterised the fluid mechanics of an impinging synthetic air jet over the full range of parameters tested here. One of the main objectives was to characterise the main flow structures present within a synthetic jet flow. Thus, identification of the key mechanisms that encompass the evolution of a synthetic air jet prior to and following impingement is the primary motivation for this research study.

The first phase of the research involves a comparative study of steady and synthetic jets at low Reynolds numbers. The purpose of this study is to acquire an understanding of how synthetic air jets compare with and differ from steady jets at matched Reynolds numbers, and to investigate some of the dimensionless parameters of synthetic jets [8]; this is expected to yield some useful information in understanding the complex nature of a synthetic air jet.

High speed, high resolution flow visualisation is performed in order to further our understanding of the complex interactions of the synthetic air jet with the various external influences, i.e. fluid entrainment, recirculation, confinement and impingement. This fluid measurement is performed using a high frame rate particle image velocimetry (PIV) system, which allows two dimensional and stereoscopic fluid velocity in a plane, perpendicular and parallel to the impingement surface, to be calculated. This system allows a unique new insight into the synthetic jet formation. Purpose written computer code is used to analyse the recorded and processed PIV data and calculates various parameters such as vorticity, velocity and turbulence intensity.

Simultaneous synthetic jet heat transfer and fluid measurements are performed for the first time (to the author's knowledge) with a light sheet parallel to a heated impingement surface. From this study, correlation of local heat transfer values with fluid velocities is performed in order to elucidate the transfer of vorticity from the axial direction to the radial direction i.e. the nature of vortex roll-up on the impingement surface. This enhanced understanding of synthetic jet behaviour is relevant for synthetic jet cooling applications.

1.3 Dimensionless numbers

Characterisation of a jet flow requires utilisation of a broad range of fluid and jet properties. In order to provide a basis for easy comparison, results are generally presented in dimensionless form. A synthetic air jet flow is characterised by three main parameters, the dimensionless stroke length L_0/D, the Reynolds number $Re = U_0 D/v$ and the surface to orifice spacing H/D, but several other dimensionless numbers are relevant for this study and are described here.

1.3.1 Dimensionless stroke length

A synthetic air jet is formed when each vortex pair that is ejected during the blowing phase of the cycle propagates downstream, and is not re-ingested on the suction phase

of the cycle. The dimensionless stroke length (L_0/D) is used when characterising axisymmetric vortex rings based on a simple slug model [9], [10], and can be applied to a synthetic jet flow, which essentially consists of a train of propagating vortices.

$$L_0 = \int_0^{T/2} U_m(t)\, dt \tag{1.1}$$

T is the oscillation period, U_0 is the spatial and time averaged velocity, and $U_m(t)$ is the momentum velocity.

$$U_0 = \frac{L_0}{T} \tag{1.2}$$

The stroke length L_0/D is inversely proportional to a Strouhal number, since

$$\frac{L_0}{D} = \left(\frac{fD}{U_0}\right)^{-1} \tag{1.3}$$

As $L_0 = U_0/f$, dividing by the jet exit diameter D, will nondimensionalise the stroke length. Shuster and Smith [11] have confirmed (along with several other studies) that one of the proper scaling parameters for an unconfined synthetic jet flow is L_0/D, the other being the Reynolds number.

1.3.2 Reynolds number

The Reynolds number provides a measure of the ratio of inertial to viscous forces. Depending on the flow parameters, either the inertial forces dominate ($Re \gg 1$), the viscous forces dominate ($Re \ll 1$) or there is an approximate balance ($Re \approx 1$). The Reynolds number can be used to determine similarities in behaviour between different experimental (or numerical) setups, such as the onset of turbulence, or to identify certain flow regimes e.g. regular vortex shedding. It is used extensively in the present study. It is defined as

$$Re = \frac{\rho U L}{\mu} \tag{1.4}$$

where ρ and μ are the fluid density and viscosity respectively, U is the fluid velocity and L is a characteristic length; when related to jet flows it is usually selected to be the nozzle diameter. For synthetic jets, U is taken as as U_0, the time and area averaged velocity.

1.3.3 Stokes number

The Stokes number is the characteristic response time of a particle compared to the characteristic response time of the fluid flow. If the Stokes number is small, $St < 1$, this translates to the particle motion being tightly coupled to the fluid motion, i.e. the particle dispersal is the same as the fluid dispersal. If the Stokes number is large, $St > 1$ the particle will have insufficient time to respond to the varying fluid velocity; thus the particle will pass through the flow without much deflection in its initial trajectory. If the Stokes number is around 1 ($St \approx 1$) the particles migrate to the margins of the influential structures present in the flow and, in the case of PIV, the seeding or particles are 'unmixed'. The Stokes number is defined as

$$S = \frac{\tau_r U}{l} \tag{1.5}$$

where τ_r is the relaxation time of the particle, U is the mean flow velocity and l is the characteristic length of the object (jet diameter). In this study the Stokes number is utilised in selecting the correct seeding particles for PIV measurements, as particles that will follow the flow faithfully and provide homogeneous seeding are essential.

1.3.4 Strouhal number

The Strouhal number is a dimensionless parameter that provides a description of oscillating fluid flow mechanisms. It is defined as

$$Sr = \frac{fL}{U} \tag{1.6}$$

where f is the frequency of vortex shedding, L is the characteristic length and U is

the relative velocity. The Strouhal number can prove very important when analysing unsteady, oscillating fluid flow problems with periodicity. The Strouhal number represents the ratio of inertial forces due to the unsteadiness of the flow or local acceleration to the inertial forces due to changes in velocity from one point to another within a flow field.

1.3.5 Nusselt number

The Nusselt number represents the dimensionless temperature gradient at a heated surface in convective heat transfer. It is defined as

$$Nu = \frac{hL}{k} \tag{1.7}$$

where h is the heat transfer coefficient, L is the characteristic length and k is the thermal conductivity of the fluid. The characteristic length is generally taken to be the exit diameter when applied to round jets. For rectangular or slot jets the exit width is used. A good comparison of the level of heat transfer achieved across a range of scales and fluids can be achieved when using the Nusselt number to non-dimensionalise the heat transfer coefficient.

1.3.6 Prandtl number

The Prandtl number is a dimensionless number that represents the ratio of momentum diffusivity (kinematic viscosity) to thermal diffusivity in a fluid. The Prandtl number is central to the study of convective heat transfer. It is expressed as

$$Pr = \frac{\nu}{\alpha} = \frac{C_p \mu}{k} \tag{1.8}$$

where ν is the kinematic viscosity, α is the thermal diffusivity, C_p the specific heat at constant pressure, μ is the absolute or dynamic viscosity and k the thermal conductivity. The Prandtl number describes fluid properties and not flow variables as it contains no length or velocity scales.

Chapter 2

Literature Review

In this study the focus is exclusively on submerged jets, in which the jet is the same fluid as the ambient fluid i.e. an air jet emerging into air. Experimental and analytical studies of the flow field in unconfined, submerged jets have provided valuable information regarding their heat transfer and flow characteristics. In many applications, however, the jet exit is confined e.g. between parallel nozzle plates and impingement surfaces, resulting in a more complicated flow structure [12]. Also, in microelectronics cooling, air velocities are often limited by acoustic concerns, making impinging jet heat transfer in the turbulent regime impractical. Thus, from a fundamental and a practical perspective, both the laminar and turbulent flow regimes for impinging jets are relevant for further investigation. This chapter begins with a brief review of flow structure and vorticity for steady jets, before progressing to a comprehensive review of the flow characteristics of synthetic jets.

2.1 Steady Jet Flow

An impinging jet flow is commonly divided into three regions on the basis of the flow structure:

1. Free jet region
2. Stagnation region
3. Wall region

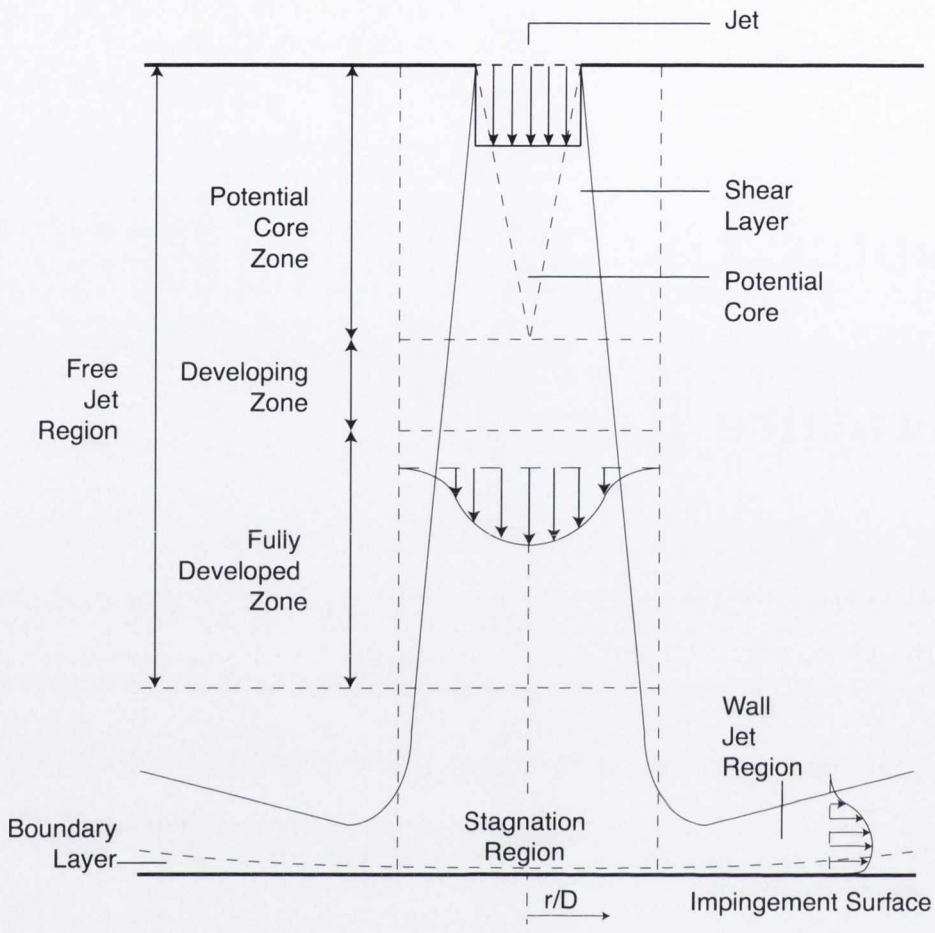

Figure 2.1 – Flow configuration of a round impinging jet.

For large jet exit to impingement surface spacings, the free jet region is further subdivided into three zones:

(i) Potential core zone

(ii) Developing zone

(iii) Fully developed zone [13]

These three zones together with the main flow regions, are shown in figure 2.1.

2.1.1 Free jet region

Within the free jet region, the shear-driven interaction of the exiting jet and the ambient fluid produces entrainment of mass, momentum and energy. The effects of this

on the flow include the development of a non-uniform radial velocity profile within the jet, spreading of the jet, and an increase of the total mass flow rate.

In the potential core the flow is characterised by a constant maximum velocity which is equal, or very close to, the jet exit velocity. Due to the growth of the shear layer surrounding the potential core, the core gradually decreases in width. The length of the potential core is dependent on the turbulence intensity at the jet exit and on the initial velocity profile [13]. According to research completed by Yule [14], the development of free jets is accompanied by the transition of an axisymmetrically coherent vortical structure to a less coherent, large scale eddy structure in the shear layer. This transition has been attributed to a natural instability of the initial shear layer; as these vortical structures move downstream they will join up with other vortical structures present in the flow. This process is known as vortex pairing, and is responsible for an increase in the scale of these vortices and in the distance between them as they move away from the jet exit. The movements and strengths of the paired vortices are random, furthermore they lose their phase agreement across the jet as they move downstream. The fluid within the potential core is subjected to an alternating acceleration and then deceleration movement due to the trains of growing vortices [4]; this results in a potential core region that contains periodic velocity fluctuations. Within the developing zone the potential core has disappeared. In this zone the axial velocity profile starts decaying and the turbulence level at the jet axis (defined as the ratio between the R.M.S. value of the axial velocity fluctuations and the initial axial velocity) begins to rise. In the fully developed zone, which starts at approximately 8 to 10 jet diameters downstream of the jet exit, the velocity profile is fully developed and both the axial velocity and the turbulence level decay.

2.1.2 Stagnation region

Fluid from a jet impinges axially on the stagnation region $r/D \lessapprox 1.0$, where there is a decrease in axial velocity and an increase in static pressure, whilst concurrently accelerating in the radial direction, which leads to the formation of a wall jet. The

nozzle geometry, and whether the jet is submerged or free, will dictate the size and axial extent of the stagnation region [15]. It has been reported for circular impinging jets of uniform velocity profile that axial deceleration begins at $x/D \approx 0.5$, and radial acceleration extends as far as $r/D \approx 0.7$, [16].

2.1.3 Wall jet region

Near the impingement surface the flow experiences a sudden deceleration in the axial direction and begins to accelerate in the radial direction; the rapid reduction in axial velocity results in a pressure increase at the stagnation point to above that of the ambient fluid. Under radial acceleration, parallel to the impingement surface, there is a reduction in the pressure difference between the jet and the ambient fluid. As fluid exits the impingement zone, turbulence increases, which in turn escalates the mixing and transition from a flow that is decelerating in the impingement region to a wall jet that is accelerating. The term 'wall jet' was first introduced by Glauert [17] to describe the flow region that develops upon impingement as the jet spreads. Glauert [17] described two subregions that exist within the wall jet region as an inner layer where the wall affects the flow and turbulence, and an outer layer where flow conditions are determined by shear interactions with the quiescent fluid. The maximum velocity in the wall jet occurs at the boundary between these two subregions.

2.2 Vorticity

Vortices are ordered structures of fluid motion, which nature prefers over chaos in many situations. The difficulty of defining a vortex is evident in the vast literature available describing what constitutes a vortex and how one is formed. Theories and laws exist that explain the properties of simple vortices, among these are the natural laws of nature that can be reduced to a few basic laws (axioms). The axioms of fluid mechanics can be categorised into two groups: the conservation laws and the constitutive equations, according to Serrin [18]. The laws of conservation state that certain physical quantities cannot be generated nor destroyed in a closed system. These con-

servation laws apply to matter, energy, momentum, and angular momentum. The constitutive equations deal with the properties of matter and indicate, for instance, whether a body is elastic, plastic, rigid, liquid, or gaseous. The law of conservation of matter states that matter can neither be created nor destroyed; an equivalent conservation law applies to energy as well. The conservation law of momentum can be expressed in such a way that the inertia (defined as mass times acceleration) of a particle is equal to the sum of all forces acting on the particle. If inertia is considered in a formal way, as a force (force of inertia), then the forces acting on a particle must be in equilibrium. For example, if a body is falling constantly under the force of gravity, flow resistance is effectively equal to the weight force, although with the opposite sign. Forces are vectors, which have a specific absolute value and a specific direction at each point in space and are added geometrically. A three dimensional vector can be decomposed into three components, x, y, and z in the cartesian co-ordinate system shown in figure 2.2a, although in describing vortical motions it is often advantageous to use cylindrical coordinates, figure 2.2b. The resultant of all forces that act on a body can be decomposed into a component parallel to the flow, called the 'drag,' and into two components normal to it, the side forces; the side force opposite to gravity is called 'lift'.

In addition to these forces, velocity and vorticity are also vectors. Vorticity may be interpreted as the angular velocity of the fluid at a point in space. Angular velocity is a vector normal to the plane of rotation (thus it coincides with the axis of rotation) and its positive direction is illustrated in figure 2.3. The same is true for the vorticity vector. In a plane flow all vorticity vectors are normal to the plane of motion. The angular momentum of a closed system is also a constant. The angular momentum of a particle is proportional to its velocity and its distance from the centre about which it is rotating. If this distance is reduced, the velocity must increase correspondingly. A commonly used example is the velocity of the earth around the sun. According to Keppler's second law (which is the conservation law of angular momentum), the earth's velocity increases whenever the earth comes closer to the sun in such a way that the areas traversed by the radius vector at equal time intervals are equal, this is

illustrated in figure 2.4 (the area law). The conservation law of angular momentum explains why the high angular velocities of vortices can occur.

To further explain the conservation law of angular momentum and its relation to vortex generation, referring to figure 2.5, a single fluid particle is considered with a small angular velocity at a distance of 30cm from a pipe outlet. As stated previously, angular momentum is proportional to its velocity and its distance from the centre of rotation, therefore as the particle is drawn towards the opening, it must increase its azimuthal velocity at a rate inversely proportional to the distance from the opening in order to maintain its angular momentum. Once the particle reaches a distance of 0.3cm from the centre of rotation, the velocity of the particle will have increased 100-fold. Angular velocity increases with the square of the distance, therefore the corresponding angular velocity of the fluid particle at 0.3cm will have increased 10000-fold. Essentially the number of rotations per second is 10000 times larger at 0.3cm than at 30cm. This relationship illustrates the fact that a small initial rotation in a fluid is sufficient to create a vortex.

In mathematical terms the vorticity ω of a fluid motion is defined as

$$\omega = curl\ u \tag{2.1}$$

It is thus a vector quantity defined at every point within the fluid. Certain flow configurations are most readily understood through a consideration of vorticity. The definition of curl by

$$\hat{n} \cdot curl\ u = \lim_{s \to 0} \frac{1}{S} \oint u\ dl \tag{2.2}$$

($\hat{n}$ is the unit vector normal to the surface S) indicates that vorticity corresponds to the rotation of the fluid; the line integral is non-zero only if fluid is travelling around the point under consideration. Buoyancy forces directly generate vorticity. Vorticity plays an important role in fluid mechanics analysis, and in several cases it has proven to be advantageous to describe physical flow phenomena in terms of the evolution of the

vorticity. Vorticity spreads through diffusion and convection [19], although they are two entirely different mechanisms. To best understand the transport of vorticity, there is a functional analogy in comparing the process of heat convection and conduction in a fluid to that of vorticity as outlined in work published by Majda and Bertozzi [20] on vorticity and incompressible flow.

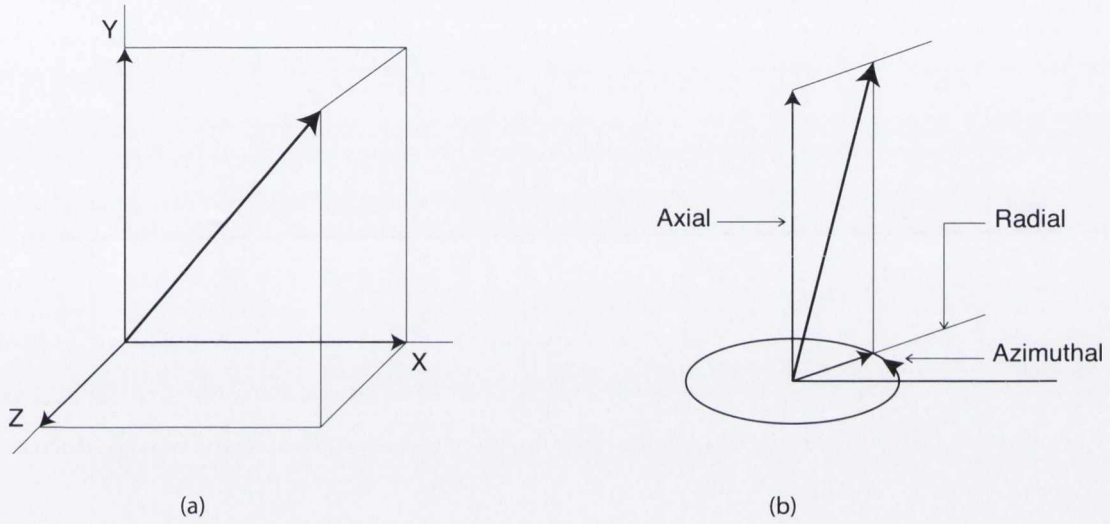

Figure 2.2 – The three components of a vector **v** (a) in Cartesian coordinates and (b) in cylindrical coordinates.

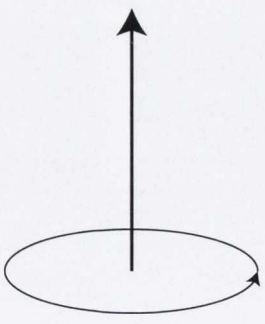

Figure 2.3 – The vector of the angular velocity is normal to the plane of rotation.

The work completed by Prandtl in 1904 [21] has become of fundamental importance in the study of fluid mechanics. He divided the flow field around a body at very high

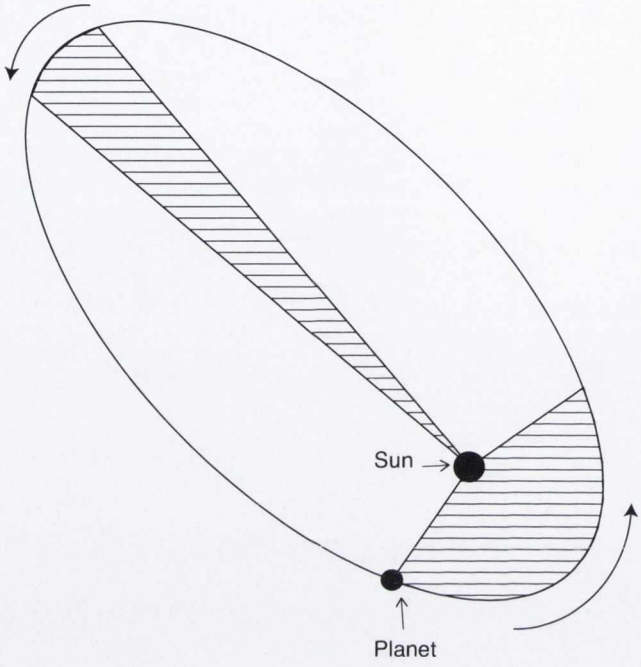

Figure 2.4 – Kepler's second law as an example of the conservation law of angular momentum. The shaded areas, which are traversed by the radius vectors at equal time intervals, are equal. Thus the planet will move faster in the vicinity of the sun than farther away.

Reynolds numbers into two regions: a thin layer near the surface in which vorticity exists, and the region outside of this, which can be considered as essentially frictionless. The thin 'friction' layer near the surface was called the boundary layer, illustrated in figure 2.6. With increasing distance from the body surface, there can also exist fluid layers in which the velocity across the layer changes rapidly and in which vorticity is quite prevalent. These regions are generated when boundary layers detach from the wall and are carried into the fluid. Such boundary layers are usually called 'shear layers' or 'shear flows'.

Figure 2.7 shows two examples of fluid motions that have the same vorticity distribution. The flow field in figure 2.7b is generated from figure 2.7a simply by superposition of a constant parallel stream, which itself has no vorticity. This type of flow behaviour highlights an important property of the vorticity field that, unlike a velocity field, the vorticity field is invariant with regard to changes of the inertial frame. In steady flow, streamlines, streaklines and pathlines are one and the same. The dependence

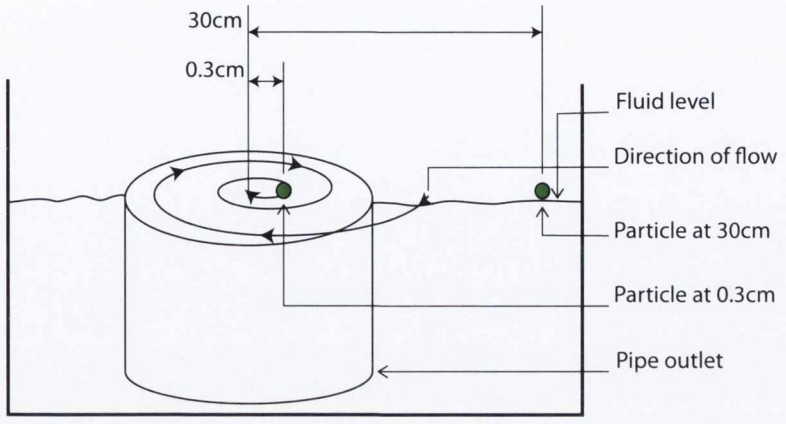

Figure 2.5 – Small initial rotation is sufficient to create a concentrated vortex.

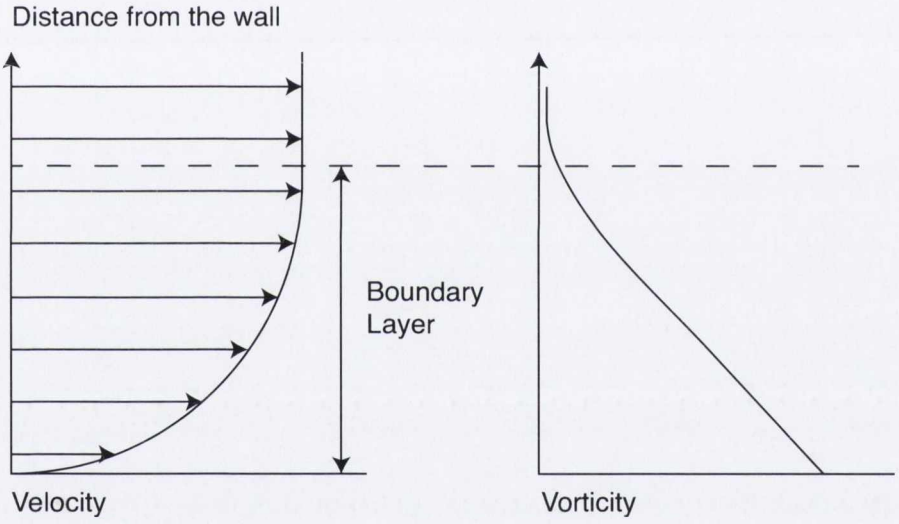

Figure 2.6 – The concept of the boundary layer.

of streamlines and pathlines on the reference frame causes considerable difficulties in the study of fluid flows, in particular defining a vortex, as vortices exist in largely unsteady fluid flows. The vorticity field is well suited to the study of time dependent flows because of its invariance property.

2.2.1 Vortex rings

Within a finite and closed stream area surrounded by a parallel flow, the vortex ring is the simplest motion, figure 2.8. These vortices are time independent and receive

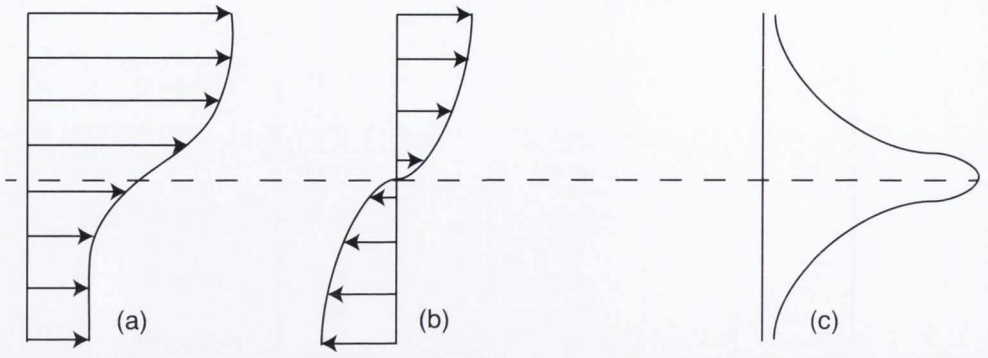

Figure 2.7 – Two shear flows (a) and (b) with an equal vorticity distribution (c).

their energy and vorticity from the boundary. Reynolds once remarked that with respect to vortex rings, nature prefers rolling over gliding. The shaded area in figure 2.8 designates the spherical vorticity field. The fluid within the sphere can not escape and is carried away with the vortex ring. It is the vortex ring that is one of the main interests of this research as it is one of the least understood aspects of a synthetic air jet. Further understanding of the vortex ring and its evolution will prove beneficial in advancing the capabilities of the synthetic air jet with regard to applications such as electronics cooling.

Free vortex rings can develop through expulsion of fluid from openings, through abrupt or oscillating motion of bodies, or through differences of temperature and density in a fluid. A simple experiment to produce vortex rings is to use a box that has a circular opening or orifice on one side and a membrane on the other. If the box is filled with smoke and then the membrane is tapped, smoke is pushed out of the opening for an instant, the smoke forms a vortex ring that moves quickly away from the opening and then decays. This is the principle of operation of a synthetic air jet.

2.2.2 Vortex ring formation

The ideal vortex ring is inviscid, for which the analysis is somewhat simplified by the neglect of viscosity. In reality, though, vortex rings are viscous in nature, with viscosity having an effect on their structure and behaviour. In general, vortex rings can go

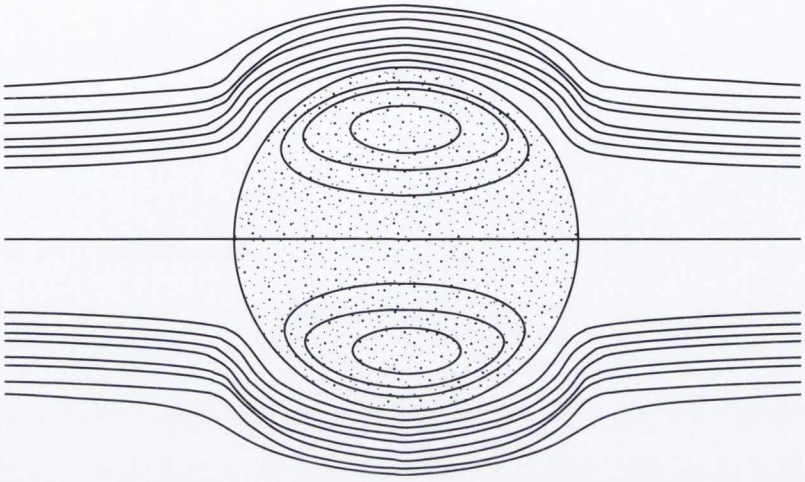

Figure 2.8 – Hill's spherical vortex (1894).

through (at least) four stages of development [22].

1. The generation or formation process
2. The stable laminar phase
3. The unstable or wavy phase
4. The turbulent phase

These stages have been evaluated experimentally in a sequence of photographs showing the formation of a laminar vortex ring by Didden [23]. There exists a formation number for a vortex ring, akin to the formation threshold for a synthetic air jet. Several researchers have reported formation numbers for vortex rings at a stroke length, $L_0/D \approx 4$, [24]. The formation threshold for a synthetic jet has been reported at being approximately the same as that for a vortex ring, [7]. There are several factors that determine whether or not a vortex ring will go through all four stages of development, however, the formation process largely depends on the initial conditions during the generation phase. For example, if the ejection velocity is low, the vortex ring may only reach stage 2 of formation and, due to viscosity, decay naturally. In contrast, if the

ejection velocity is high, the vortex ring may immediately become turbulent without passing through any of the intermediate stages.

In the formation of a vortex ring from fluid expelled through an orifice, the assumption is made that the fluid forming the core is that which has gained vorticity from the viscous diffusion processes at the orifice lip. At the beginning of the formation stages, the initially thin boundary layer separates at the orifice edge and vortical fluid rolls up into a spiral, entraining irrotational fluid in the process. According to Didden [9] this continues until $D \approx 1.08D_0$ and the vortex ring then begins to move away from the nozzle. At the end of the ejection stroke, the induced flow of the vortex ring produces a secondary vortex of opposite circulation with its axis exactly in the orifice-exit plane. The final diameter of a vortex ring produced at an orifice according to Auerbach [22], is related to the distance travelled by the piston or flexible membrane (L_0) by the following equation for $1500 \leq Re \leq 4500$.

$$D/D_0 = 1.05(L_0/D)^{1/4} \tag{2.3}$$

According to studies by Didden [9], and Saffman [25], there is a sudden decrease in vortex ring diameter at the end of the ejection phase of a vortex ring; this is attributed to the influence of the orifice wall, and the induced flow of the secondary vortex. Maxworthy [26] discovered from visualisation experiments that an intense vortex induced flow is produced at the outer edge of the orifice and that this created vorticity of opposite sign to that of the main jet flow (negative in the secondary vortex and positive in the main flow). This is illustrated in figure 2.9c, where a secondary vortex of negative sign is formed within the orifice, which then propagates backwards into the orifice; the motion created by this secondary vortex creates more positive vorticity, which is ingested into the secondary vortex ring, leading to its eventual destruction.

In figure 2.9, the development of a vortex ring is shown. The boundary layer that is formed at the orifice during the expulsion phase of the fluid is where the vorticity of the vortex ring originates, figure 2.9a. This boundary layer separates from the edge of the orifice and begins its exchange from a vorticity layer to a vortex ring. As soon

as the vortex ring that is formed detaches, it induces a flow towards the axis of the orifice, which in turn produces vorticity of opposite sign at the edge of the orifice, figure 2.9c. This vorticity forms a secondary vortex ring with rotation opposite to that of the primary vortex ring.

If, as shown in figure 2.9b, the boundary layer is sucked away during the expulsion phase of the fluid, no vortex ring can form. (In synthetic air jet terms, it would be below the forming threshold for a synthetic jet (synthetic jet forming threshold $L_0/D < 3.0$), and no synthetic air jet would be formed. The formation threshold and parameters of a synthetic air jet shall be explained in detail in section 2.4).

An inviscid vortex ring is considered to move with constant velocity without decaying but, in reality, a real vortex ring loses speed. Vortex rings decelerate not only through loss of energy due to friction but also through entrainment of surrounding fluid and the formation of a wake, as shown in figure 2.10. Fluid entrainment occurs over the whole surface of the ring, which is consequently set into rotation, and increases the overall size of the vortex ring; fluid entrainment was first described in 1939 by Krutzsch [27]. It was noted by Maxworthy [28], in the study of vortex rings, that real vortex rings eject matter and vorticity in the wake.

A vortex ring is considered as an elemental flow structure, or as a building block for more complicated flow structures, in the study of turbulent flow configurations. It is therefore of interest to understand how a vortex ring reacts with other vortex rings and impingement surfaces, particularly with regard to the 'slug' flow and vortex rings produced by a synthetic air jet. In this study there is an impingement surface (wall) present that will directly influence the flow structure of vortex rings as they impinge on the surface. It has been well documented that a vortex ring colliding with an impingement surface undergoes a rebound or experiences a reversal in axial velocity [29], [30], [31]. The most commonly accepted explanation for this effect is attributed to the influence of a secondary vortex which is generated at the surface by viscous effects. Several authors have documented this 'rebound' effect, where at a certain

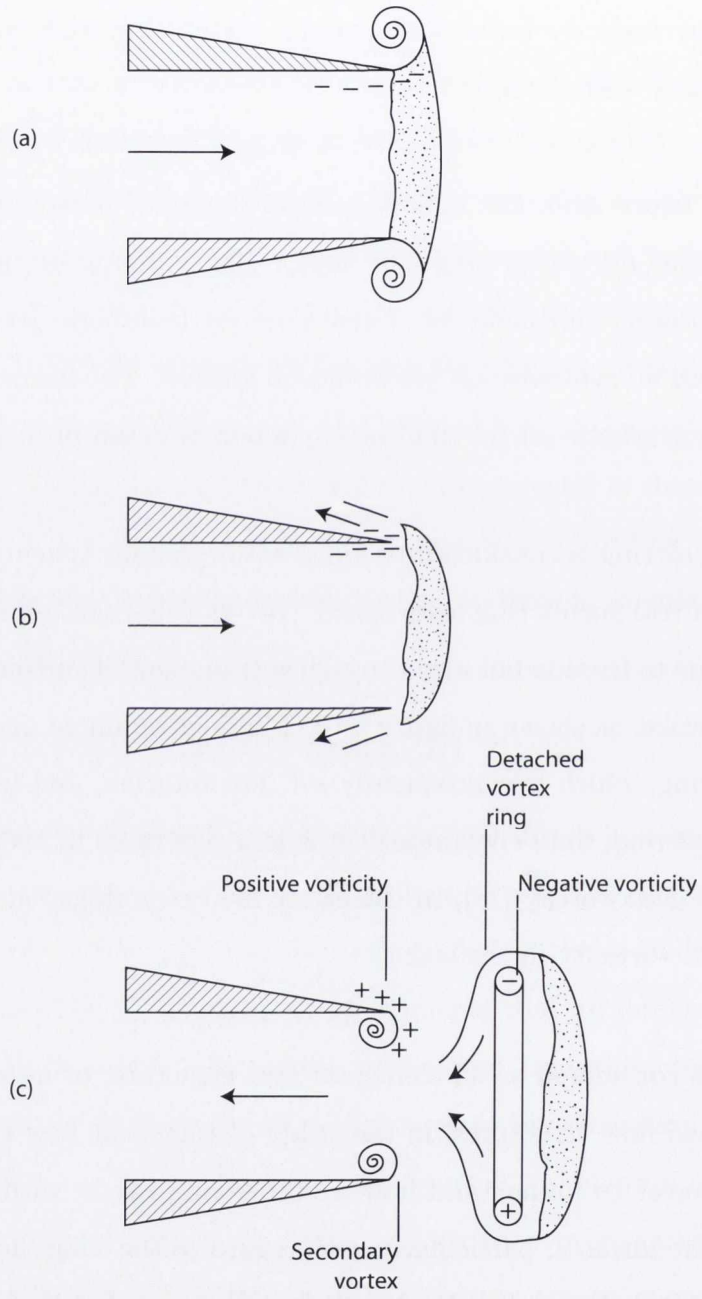

Figure 2.9 – (a) The vorticity of the boundary layer (-) generates a discontinuity surface, which rolls up to a vortex ring. (b) If the boundary layer is detached at the opening, no vortex ring can develop. (c) The detached vortex ring induces a secondary vortex with vorticity of opposite sign (+).

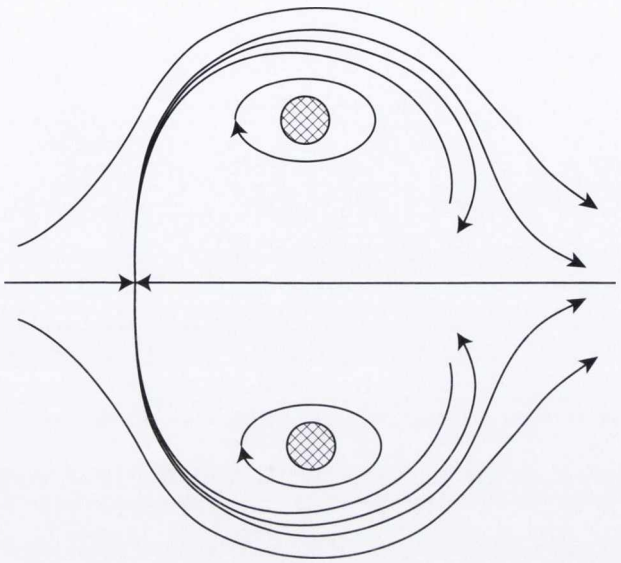

Figure 2.10 – Vortex ring, with entrainment and wake.

distance from the wall, the axial velocity changes direction and the ring moves away from the surface, [29], [31], [32], [33]. It has been suggested that the 'rebound' effect is caused by the mutual interaction of the original vortex ring and a secondary vortex generated from the boundary layer induced by the original vortex ring. The initial work that led to the interpretation of rebound was documented by Harvey and Perry in 1971 [34], who conducted experimental investigations of the behaviour of trailing wing-tip vortices approaching a ground plane. The conclusion was made that when a trailing vortex is in the vicinity of a ground plane, the local adverse pressure gradient that occurs directly below the vortex core causes the boundary layer to separate outboard of the vortex pair; the resulting separated layer eventually rolls up to form a secondary vortex with opposite vorticity to that of the trailing vortex.

The process is described as follows: As a vortex ring approaches a wall, vorticity of opposite sign is created at the wall; the two vorticity fields then cancel each other out effectively, figure 2.11. As this process occurs, secondary vortices develop at the wall where the streamlines diverge, there is an initial decrease in velocity and separation can occur. Depending on the strength of the primary vortex, the secondary vortices

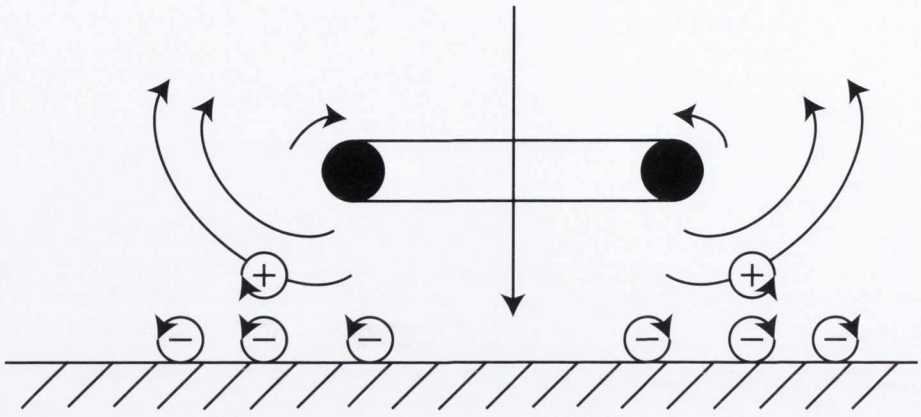

Figure 2.11 – Vortex ring 'rebound' through production of vorticity of opposite sign at a wall. In some cases, vortex rings can disappear depending on the strength of the primary vortex ring.

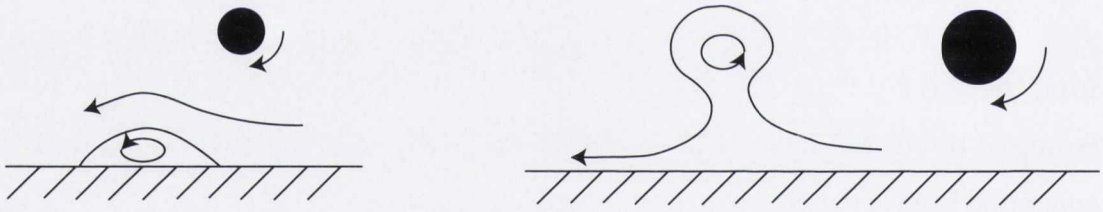

Figure 2.12 – As a primary vortex approaches an impingement surface, secondary vortices are produced.

that are developed upon impact can vary in strength and size. The initial secondary vortex produces a 'push-back' effect on the primary vortex, which in turn forces the primary vortex away from the wall ever so slightly. As the induced vortex decreases in strength it allows for the primary vortex to approach the impingement surface again and if the primary vortex is still strong enough, a second, secondary vortex is induced, and so on [33], figure 2.12. It is from this process of a vortex ring approaching an impingement surface partnered with the slug flow that is prevalent in a synthetic air jet flow at specific parameters, that the translation of axial velocity to radial velocity occurs; this shall be revisited in more depth in chapter 5.

2.3 Turbulence and Instabilities

There are several phenomena that exist in fluid mechanics that strongly influence flow characteristics, but none that have the same significance as flow instability. Towards the end of the 19th century Lord Rayleigh [35], Lord Kelvin [36] and Helmholtz [37] all recognised that this condition was present in fluid dynamics. Instability is a mechanism by which a fluid accommodates to strong forces, and new flow patterns are created. For example, in a steady flow environment in which only viscous and inertial forces are acting, diffusion cannot counteract convection above a certain Reynolds number. In most cases instability leads to turbulence and, in general, flows are largely turbulent, whether naturally occurring or created. Several types of disturbances (instabilities) can occur within fluids, with ever increasing complication. The types of instabilities that can occur are too many to list but a few examples are given below:

- Instability due to inertial forces
- Instability due to centrifugal and Coriolis forces
- Thermal instability (buoyancy effects)
- Instability due to gravitation, electromagnetic forces and surface tension

Characteristic parameters quantitatively describe the occurrence of instabilities in a fluid, e.g. the Reynolds number determines the onset of instabilities due to inertial forces in the presence of viscous forces. It has been established that for a given type of flow, a critical Reynolds number exists where below this value the flow is laminar, and above it, turbulent [38]. Above such a critical characteristic parameter the original flow can exist, provided that any disturbance is avoided that would unbalance the unstable state. For example, for a flow within a pipe of diameter D, below a Reynolds number of 2300 the flow is considered laminar; above it, turbulent. By carefully avoiding any disturbances, a flow could be kept laminar up to $Re_D = 40000$ but, in reality, disturbances are always present, and the flow would be turbulent at this Reynolds number. As stated previously, new flow patterns emerge from instabilities; the new flow pattern obtained can become steady after a sufficiently long transient time, or periodic vortex

streets can emerge from the flow being unsteady and turbulent. Of historical interest is the fact that research on vortex streets started in the field of acoustics. In 1878, Strouhal investigated sound producing vibrations in wind [39], and just over a year later Lord Rayleigh discovered that the sound generated from wires in an airstream did not require the wires to be in motion to generate sound, [35]; the existence of the vortex street was correlated to the tones generated in an airstream by Bénard in 1908 [40].

Over the last century various models for describing turbulence have been developed, although not all have shed new light on the nature of turbulence. The semi-empirical model developed by Prandtl in 1961 was one of the first models of turbulence considered to be successful [41]. This model introduced the concept of a 'mixing length' of turbulent clusters, which was analogous to the free path of gas molecules. The analogy was not exact, since turbulent clusters influence each other quite strongly and gas molecules do not, but it represented a step in the right direction as the theory of mixing length is still the basis for most turbulence calculations in engineering applications.

Although the notion of turbulence is widely used in scientific and technical literature, there is no unique, commonly accepted definition. Perhaps the best is that turbulence is 'a state of continuous instability'. Therefore, turbulent flow is usually identified by its main features. Turbulence implies fluid motion on a broad range of temporal and spatial scales, so that many degrees of freedom are excited in the system. Turbulent flow is also usually accompanied by a significant increase in momentum and mass transfer, i.e. the flow resistance and rate of mixing in a turbulent flow become much higher than they would be in an imaginary laminar flow with the same Reynolds number.

The fundamental characteristics of turbulence have been summarised in the following statements from the book on turbulence by Tennekes and Lumley [42].

1. Irregularity (randomness): a turbulent flow is unpredictable.

2. Turbulence is an exchange process, which is orders of magnitude faster than

diffusion of vorticity in the laminar region.

3. Three dimensional vorticity fluctuations: turbulence is rotational and three dimensional.

4. Energy is transported in general from large eddies to smaller eddies.

5. Turbulence is not an entirely statistical process, since coherent, long lasting vortical structures exist within it.

6. Turbulence is a feature of fluid flows and not of fluids.

In relation to the current study, the properties of turbulent vortices can be quite different from those of laminar vortices, and certain flow phenomena only exist within turbulent motion, i.e. turbulent vortices differ from their laminar counterparts in the following way: the molecular velocity in laminar motion is more or less decoupled from the macroscopic events, but in turbulent flow it is not, and interaction between the two scales of motion is strong.

At high Reynolds numbers, vortex rings that are generated by the ejection of fluid from an orifice become immediately unstable and then turbulent. In the turbulent stage, the mechanism of entrainment into the vortex ring differs conclusively from that of entrainment into a laminar vortex ring. Thus, a laminar vortex ring grows by entraining fluid over the entire surface area through molecular diffusion, figure 2.10, while the growth of a turbulent ring is governed by entrainment of turbulent fluid in the core region only.

2.4 Synthetic Air Jet

The synthetic air jet is a mean fluid motion generated by high-amplitude oscillatory flow through an orifice or nozzle. The term 'synthetic' refers to the generation or synthesis of a jet from the active medium. The characteristic features of synthetic jets are chiefly the periodically formed vortical structures at a source, and a momentum driven jet directed away from the source. The historic origins of the synthetic jet

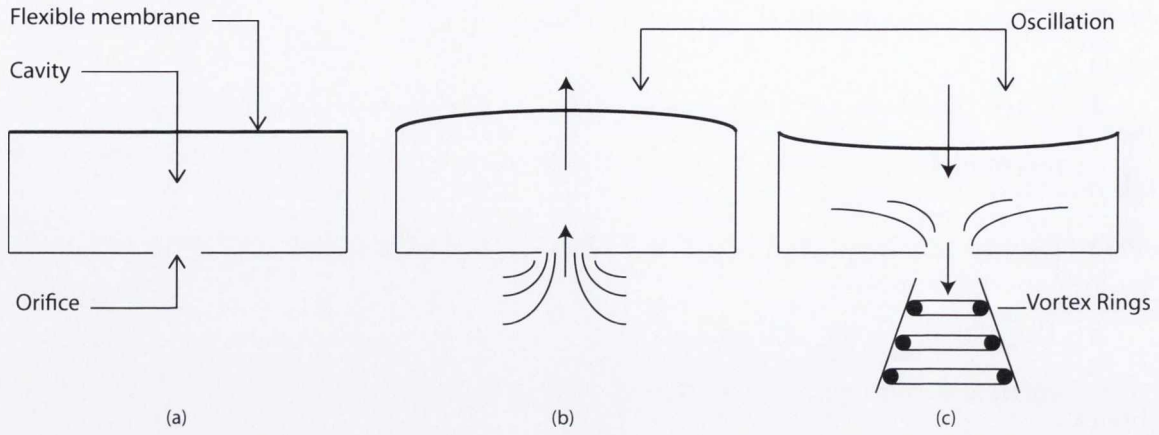

Figure 2.13 – A schematic of the operation of a membrane-cavity type synthetic jet, displaying the (a) membrane-cavity, (b) suction stroke and (c) ejection stroke.

may be found in the early 1950's [43], where jets were synthesised by acoustically driving air in a circular tube through an orifice. The formation of the characteristic periodic vortex rings and ensuing jet were linked to high intensity and frequency sound waves. A piston-cavity mechanism was employed by Mednikov and Novitskii in 1975 [44] to generate much the same effect in terms of generating a jet from the working medium itself. These types of driver-cavity setups are like those employed in present day synthetic jet actuators, that draw on the principle of acoustic energy being created and dissipated within a cavity. A common method of generating such jets is a flexible membrane on one side of a partially enclosed chamber, with an orifice opposite to the membrane, a method similar to the piston-cylinder mechanism, where the flexible membrane serves as the oscillatory driver to the flow and replaces the piston. It is this method that is utilised in the current investigation for generating a synthetic air jet. Figure 2.13 shows a schematic of the operation of a membrane-cavity synthetic jet generator. An oscillator such as a mechanical or electromagnetic actuator causes the membrane to oscillate in a sinusoidal motion. The synthesis is comprised of a cycle with two strokes: suction and ejection. During the suction stroke, figure 2.13b, the membrane moves away from the orifice, increasing the volume of the cavity and consequently decreasing the pressure within, resulting in the entrainment of low momentum fluid into the cavity. During the ejection stroke, figure 2.13c, the diaphragm moves towards the orifice, resulting in a pressure increase within the cavity and the consequent

expulsion of fluid through the orifice. On account of the differential velocity at the orifice when the fluid is expelled, a shear layer is formed. Largely depending on the dimensionless stroke length (L_0/D), the shear layer can roll up to form a vortex ring that propagates away from the orifice. A complete suction-ejection cycle is referred to as a 'period' due to the sinusoidal motion of the flexible membrane. A series of 'periods' results in the formation of a train of vortex rings that move away from the orifice. Smith and Glezer showed that these coherent structures formed at the orifice interact and break down in a transition towards either a laminar or a turbulent jet [45].

The two stroke operational principle of a synthetic air jet allows for it to be created entirely from the surrounding medium, as the same quantity that is entrained into the cavity is expelled out of the cavity over a full period. This implies a zero net mass flux across the actuator boundary, which leads to the alternative naming of a synthetic jet as a ZNMF (zero-net-mass-flux) jet. The compactness of the synthetic jet allows for it to be positioned conveniently within an enclosure, circumventing the requirement for large moving parts in the form of axial fans, that use more energy. Thus, the primary advantage of the synthetic jet is its zero-net-mass flux nature, which eliminates the need for plumbing. This property allows for the synthetic jet to be easily integrated into complex geometries and reduces the complexity involved in design and fabrication of a synthetic jet for an intended application.

Synthetic air jets are widely used as active flow control measures, effecting changes in a flow to improve the performance of a system. Applications they are most commonly used in are controlling flow separation, mixing enhancement, thrust vectoring and augmentation of lift, [46] [47], [48]. Synthetic air jets are known for having the capacity to transport momentum; in an aerodynamic application a synthetic air jet is used to energise a flow, thereby delaying the onset of separation. Seifert et al. [49], and Amitay et al. [1] are amongst many researchers investigating the application of synthetic air jets to aerodynamic control. This particular application works as follows: when a synthetic air jet is applied adjacent to a boundary layer, during the suction stroke of the actuator low momentum fluid is entrained adjacent to the orifice, which in

turn results in the movement of high momentum fluid towards the boundary. On the ejection stroke, high momentum fluid is expelled into the boundary layer; this expulsion of fluid into the boundary layer enhances the mixing process within the boundary layer and the unsteady nature of the actuator, which introduces disturbances into the flow, further augments the mixing process. Overall this results in the boundary layer becoming less susceptible to separation, as illustrated in figure 2.14.

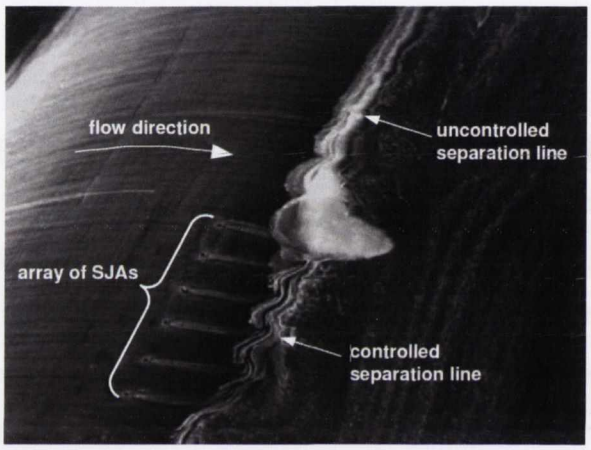

Figure 2.14 – Flow separation control on a cylinder using an array of synthetic jet actuators, [50].

Initial investigations into the interaction of synthetic jets with a cross flow over a cylinder were completed by Amitay et al. [51], with the aid of flow visualisation in a small smoke tunnel at $Re_D = 4000$, for a number of azimuthal jet positions. This is shown in figure 2.15. The apparatus consisted of a circular cylinder that had been instrumented with a pair of spanwise, adjacent rectangular synthetic jet actuators with their orifices placed flush to the cylinder surface and collinear with its axis. γ represents the azimuthal jet location; this is varied relative to the stagnation point at the front of the cylinder by rotating the cylinder about its axis. The results of this investigation provided an insight into some fundamental features of aerodynamic modification by synthetic jets. The direction of the synthetic jet flow is denoted by the white arrow. In figure 2.15a the baseline flow is shown for reference, the flow appears to separate at $\theta \approx 80°$; in figure 2.15b, $\gamma = 60°$, the effect on the cross flow is manifested by a local deformation of smoke streamlines just after the top surface

of the cylinder. This may appear to be a subtle difference in comparison to the baseline flow but it can be seen that the separation point on the top surface moves downstream. In figure 2.15c the synthetic jets are in phase and at $\gamma = 180°$, it can be seen that the flow appears to be attached to the surface of the cylinder under these test parameters. Lastly in figure 2.15d, the azimuthal angle is still $\gamma = 180°$, but the jets are operated out of phase with each other at $\phi = 120°$, the downward vectoring of the jets results in downward vectoring of the entire wake and consequently, the displacement of the front stagnation point. The spacing between the streamlines in figure 2.15d indicates a change in circulation of the flow and generation of lift. It is clear from figure 2.15c and figure 2.15d that the cross-stream symmetry of the cylinder wake is substantially altered when the azimuthal angle of the jets are adjusted to be in the region of $100° < \gamma < 180°$.

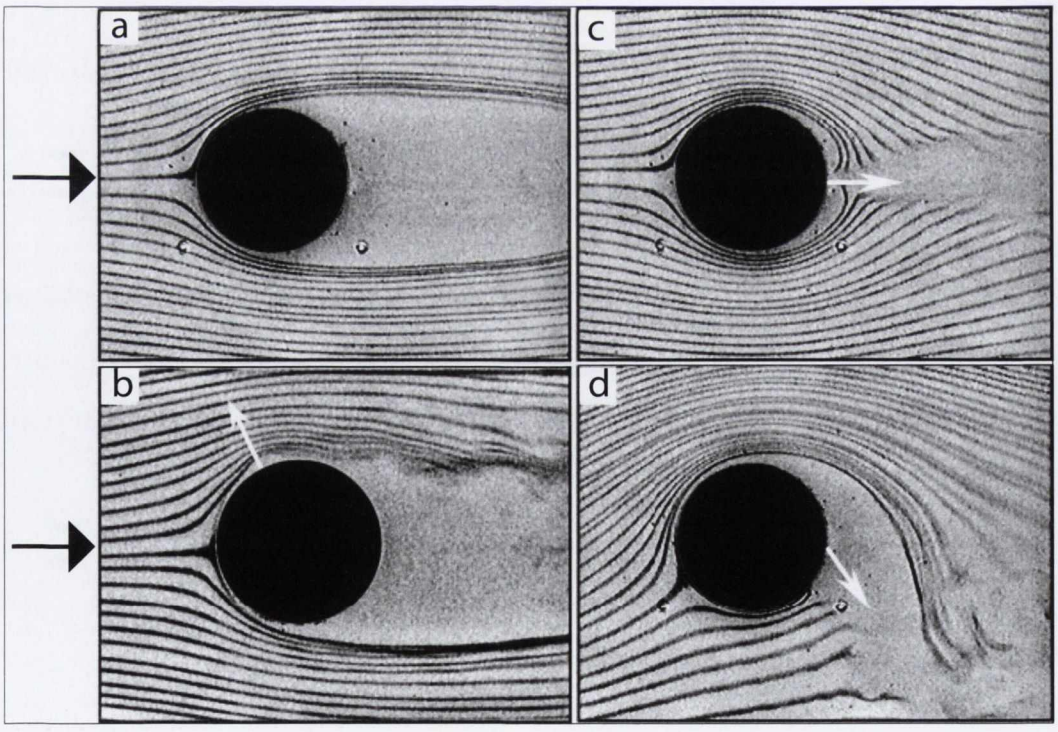

Figure 2.15 – The influence of synthetic air jets on flow separation around a cylinder (a) baseline (b) actuated: $\phi = 0, \gamma = 60°$ (c) jets located at 180° (d) $\phi = 120°, \gamma = 180°$ [51]

(θ=separation angle, γ=azimuthal jet location, ϕ=phase agreement)

Employing synthetic air jets as a mixing enhancer has shown promise in several industrial applications involving mixing of fluids. In the gas combustion industry, synthetic air jets have been utilised to improve the mixing of hot and cold fluid streams [52]. Another application in mixing is focused on improving combustion efficiencies and consequently reducing emissions; this is achieved by enhancing the quality of the fuel and air mix before the combustion process takes place [53]. The use of a synthetic jet adjacent to a steady jet has been shown to have the capability of enhancing the growth of the shear layer of the steady jet, which leads to a faster spreading and decay rate of the steady jet [54].

As mentioned before, synthetic jets have attracted a lot of attention for their potential to cool electronics [55], [56]. Electronics densification is the industry standard and with this standard comes an ever increasing thermal load that needs to be dissipated; synthetic air jets offer an alternative to traditional axial mounted fans. Vortical structures present in a synthetic jet flow facilitate the breakdown of the boundary layer thickness. In terms of heat transfer, with a breakdown of the boundary layer thickness the convective heat transfer mode is enhanced. The primary focus of the parallel research work regarding synthetic air jets that has been carried out within the research group has been on convective heat transfer for electronics. Therefore, with a view to enriching the heat transfer investigation, although the main focus of this study is on the synthetic jet evolution and flow field, a short series of tests has been carried out with simultaneous heat transfer and fluid velocity measurements of an impinging synthetic air jet.

2.4.1 Synthetic jet flow structure

The synthetic jet flow structure is influenced by several parameters that include actuator and orifice geometry, properties of the working fluid and the actuation parameters. The two properties that have been established as the key parameters governing the evolution and development of a synthetic air jet are the non-dimensional stroke length (L_0/D) and the Reynolds number (Re_{U_0}), [45], [11], as described in section 1.3. A

formation criterion for a synthetic jet was proposed and validated in research undertaken by Holman et al. [57]. A detailed schematic of synthetic jet formation, from the research of Holman et al., is presented in figure 2.16. With reference to figure 2.16, during the ejection stroke fluid exits the nozzle at a velocity V_I and a vortex ring is formed at the sides of the ejected fluid; if formation conditions have been fully satisfied, the vortex ring convects away from the orifice. Repeated oscillations result in a train of vortex rings propagating away from the orifice; downstream of the orifice a turbulent jet is synthesised as the vortex rings interact i.e. breakdown, pair, or leapfrog each other, all depending on the formation parameters.

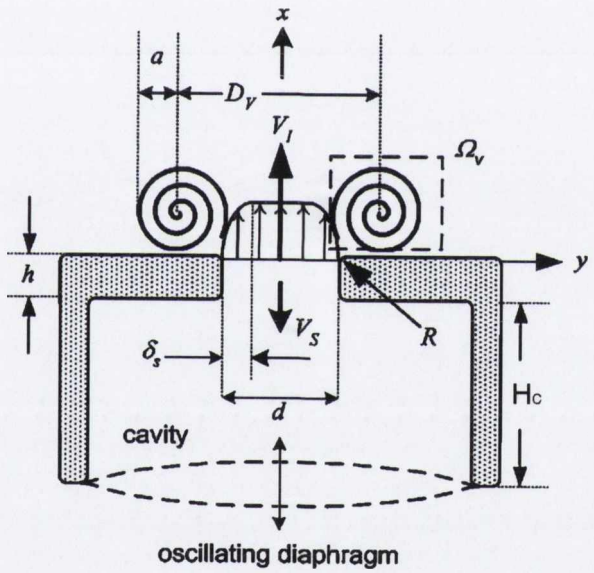

Figure 2.16 – Synthetic jet formation: boundary layer thickness δ_s, height of orifice h, depth of cavity H_c, vortex radius a, jet ejection velocity V_I, jet suction velocity V_S, distance between vortices D_V, vortex strength Ω_ν and orifice edge radius of curvature R. [57]

For convective cooling applications, the synthetic air jet is configured in such a way that it impinges normally upon a surface, this configuration has been shown to provide effective heat transfer due to the following characteristics: firstly, primary and secondary vortical structures impinge on the heated surface, which increases the wall normal velocity fluctuations through interaction with the layers closest to the wall. This results in an increase in the momentum transfer and as a consequence increases

the heat transfer rate [58]. Secondly, when compared to a steady jet, synthetic air jets entrain more fluid, which leads to a larger volume of fluid impinging on the surface resulting in a greater heat transfer capacity. The ensuing flow that is parallel to the surface, following impingement, is termed a radial wall jet, similar to that described in section 2.1.3 for steady jets.

Shown in figure 2.17 is the flow configuration of an impinging synthetic air jet. Based on the dominant flow phenomena, a synthetic jet flow is comprised of a near field and far field. The flow may be divided into four regions:

1. A region near the orifice that is typified by the presence of discrete coherent vortex rings and a fully periodic flow

2. Downstream of the orifice, vortex ring interaction and breakdown, an overall reduction in their coherence as they transition towards a turbulent free jet [45]

3. As the synthetic jet approaches the impingement surface, there is a rapid decrease in axial velocity with the static pressure increasing on account of a stagnation point at the impingement surface. The jet translates from an axial direction to a radial direction along the wall, where the flow is temporarily accelerated due to the local pressure gradient [16]

4. After impingement, the flow develops into a fully developed wall jet, where both a free and solid boundary exists

The near field of the flow structure is typified by the presence of discrete coherent vortex rings, and fully periodic flow. In the far field, the vortex rings coalesce, interact and begin to breakdown, thus reducing their coherence as they transition towards a free turbulent jet. It is worth noting that a free synthetic jet exhibits similarities to a steady free jet in that both exhibit self similar behaviour, although the synthetic jet demonstrates an enhanced spreading rate. Away from the impingement region, the flow develops into a fully developed wall jet, where both a free and solid boundary exists. Launder and Rodi [59] described a wall jet as a boundary layer flow that has had

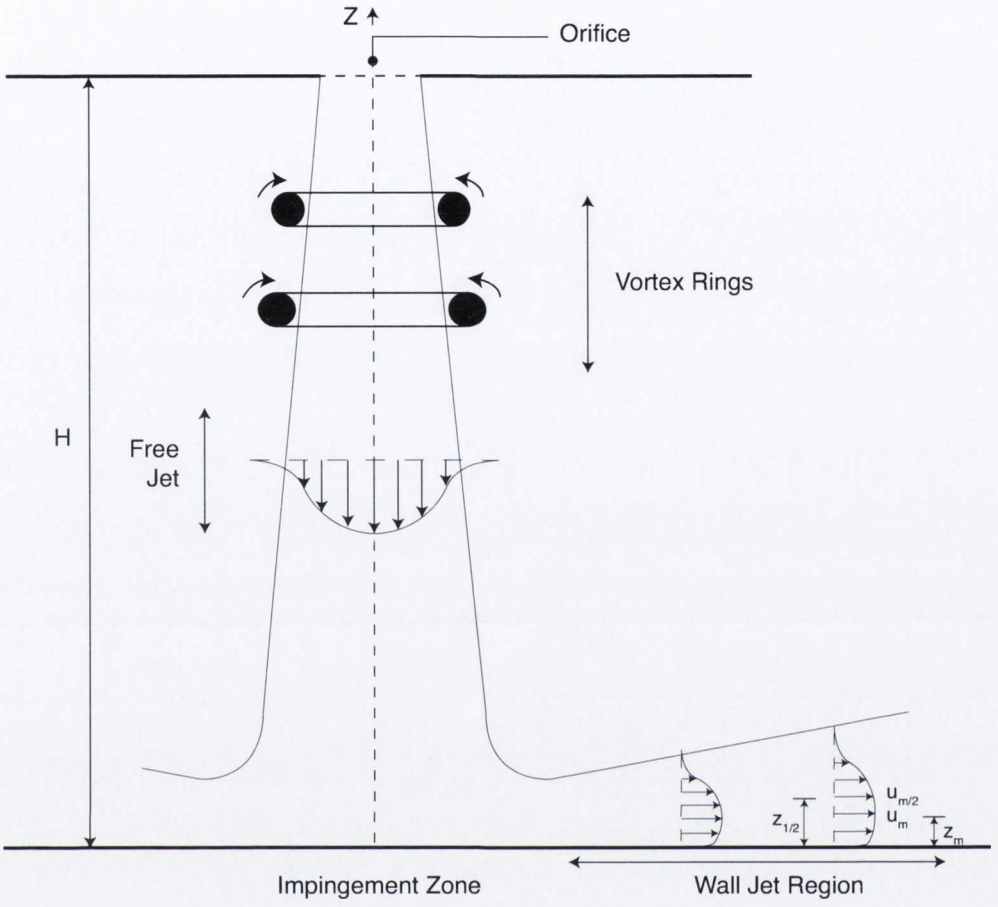

Figure 2.17 – Schematic of the evolution of a normally impinging synthetic air jet. Shown are vortex rings in the near field of the orifice, and mean velocity profiles of both free and wall jets in the far field.

momentum added upstream such that a local velocity maximum exists in the shear layer that exceeds that of the free stream. Shown in figure 2.17, the wall jet region has two distinguishable regions. There is the region closest to the wall where the velocity increases from zero at the wall to a local maximum (u_m), which is considered to be the inner layer ($0 < z < z_m$). The outer layer is the region beyond this velocity maximum where the velocity decays to the free stream velocity ($z_m < z < \infty$). The inner and outer layer as described bear some resemblance to a boundary layer and a free jet, respectively. As they are essentially shear layers, it is their interaction and dissimilar nature that give rise to the characteristics of a wall jet [59]. The outer layer spreading

rate is related to the rate of increase of the half width[1]($z_{1/2}$). Yet, the characteristic length and velocity scales describing the self-similar nature of the individual shear layers have been shown to apply to wall jets. Within each layer, there exists a dissimilar characteristic length and velocity scale, it is this particular detail that makes it nearly impossible to utilise a single scaling for the complete self similar description of the entire wall jet [60]. Wall jets subjected to periodic forcing have been shown to be additionally dependent on the excitation frequency and amplitude parameters. Research completed on a forced laminar wall jet by Quintana [61], showed that the mean velocity field is affected by even the smallest of amplitude excitations at certain frequencies. With regard to forced turbulent jets, the effect of external excitation has been shown to nominally increase the spreading rate of the jet. However, beyond a critical Reynolds number ($Re \approx 3000$), amplitude changes as large as 20% of the mean exit velocity have negligible effect on the self similar mean velocity profiles [62].

In terms of synthetic jet formation, in an impingement configuration, there are several parameters that influence the flow structure:

1. The dimensionless stroke length (L_0/D)
2. Actuator geometry
3. Actuation parameters - driving frequency, amplitude.
4. Reynolds number
5. Orifice to impingement surface spacing (H/D)

It has been reported that the dimensionless stroke length (L_0/D) distinctly identifies a synthetic jet flow [11]. If the synthetic jet flow is broken down into regions, the prevalent flow phenomena in respective flow regions differ and the frequencies and amplitudes that are used to form the synthetic jet will influence each flow region

[1] A commonly used measure to characterise the growth of the jet is to define the jet half width. It is defined as the distance measured from the centreline of the jet to where the local mean velocity is equal to half of the local centreline mean velocity, [60].

differently. As an example, the formation of vortex rings in the near field is dependent on the dimensionless stroke length (L_0/D), which is a result of the actuator driving frequency and amplitude [10]. Confinement, recirculation and entrainment are all directly affected by a change in the orifice to impingement spacing (H/D) value. Heat transfer studies by McGuinn et al. [63] and Pavlova [64], related to changing the above parameters, verify that the heat transfer rate due to synthetic air jet impingement varies appreciably. Regarding the actuator driving frequency, there has been a lot of research undertaken into how this affects not only the synthetic jet flow structure but also its heat transfer capabilities. Pavlova [64] found that if the synthetic jet actuator was driven at the natural resonant frequency, minimal modifications needed to be performed in order to gain significant performance benefits; similar results reported by McGuinn et al. [65] and Gomes et al. [66] confirmed this. In work completed by Gallas et al. [67] it has been shown that the frequency response of a synthetic jet actuator is consistent with that of a damped fourth order system governed by the cavity Helmholtz frequency (f_H) and the natural frequency of the diaphragm (f_D). Referring to figure 2.18, Gallas et al. [67] demonstrated that the synthetic jet actuator frequency response is dependent on the relative position of the Helmholtz frequency (f_H), and the diaphragm frequency (f_D). In order for the frequencies to be classified as uncoupled, the Helmholtz frequency, and the diaphragm frequency need to be sufficiently far apart, figure 2.18a. If these two frequencies are closer together, coupling will occur, which will lead to the dominance of the diaphragm frequency as it tends to be more influential than the Helmholtz frequency, figure 2.18b, and a single peak will emerge as the synthetic jet actuator response.

In relation to a synthetic air jet, the Helmholtz frequency of the cavity (f_C) and the diaphragm frequency (f_D) are defined as follows:

$$f_H = \frac{1}{2\pi}\sqrt{\frac{1}{(M_{aN}M_{aRad})C_{aC}}} \tag{2.4}$$

$$f_D = \frac{1}{2\pi}\sqrt{\frac{1}{M_{aD}C_{aD}}} \tag{2.5}$$

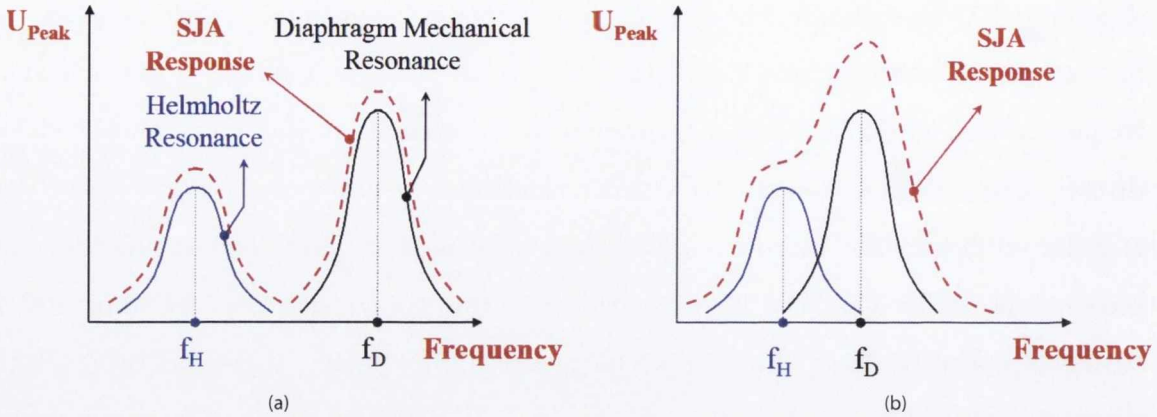

Figure 2.18 – Helmholtz and diaphragm mechanical resonance and overall synthetic jet actuator response: (a) uncoupled case (b) coupled case [66].

In equation 2.4, M_{aN} is the orifice acoustic mass, M_{aRad}, the orifice acoustic radiation mass and C_{aC}, the cavity acoustic compliance [67]. In equation 2.5, M_{aD}, C_{aD} are the diaphragm acoustic mass[2] and the diaphragm compliance respectively. Work completed by Cox and D'Antonio [68] provided a relationship for calculating the acoustic mass (M_{aN}) in relation to either a membrane or orifice as:

$$M_{aN} = \frac{\rho}{\epsilon}\left[t + 2\Delta r + \sqrt{\frac{8\nu}{\omega}\left(1 + \frac{t}{2r}\right)}\right] \tag{2.6}$$

where ρ indicates fluid density, ϵ is the material porosity, t thickness, Δ signifies end correction factor, r is the perforation radius, ν is kinematic viscosity and ω the angular frequency.

A method of calculating the Helmholtz frequency for inviscid, incompressible flow, that is not only simpler, but quite often more useful, is:

$$f_H = \frac{C}{2\pi}\sqrt{\frac{A}{V_c l_{eff}}} \tag{2.7}$$

[2] The acoustic mass refers to the effect of inertia in an acoustic system, an impeding of the transmission of sound through that system, acoustic inertance.

C is the speed of sound, A is the orifice area, V_c is the volume of the cavity (for a cylindrical geometry $V = \pi D^2/4H$) and l_{eff} the effective orifice length ($l_{eff} = l_0 + 0.85l_0$).

Gomes et al. [66] discovered through experimentally measuring cavity frequencies that the Helmholtz theory consistently over estimated the resonance frequency of the cavity by $\approx 18\%$. The roots of equation 2.7 are from the 1967 study of acoustic nonlinearity of an orifice by Ingard [69], where the relationship between pressure and velocity amplitudes was found to be almost linear at a sufficiently low pressure, and at large velocity amplitudes to approach what is known as a square law relation.

2.4.2 Velocity calculation and Reynolds number

There exist several key dimensionless parameters that define the formation of synthetic air jets. The calculation of the characteristic velocity for a synthetic air jet stems from the method (outlined in section 2.4.2.1) used for axisymmetric vortex rings [9], [10]. This method is applied to the characterisation of a synthetic air jet; this is based on the simple 'slug' model, which utilises a number of primary dimensionless numbers, defined in section 1.3 and revisited here.

2.4.2.1 Stroke length and Stokes number

Firstly, the dimensionless stroke length (L_0/D), is defined as the ratio of the fluid stroke length (L_0) to the orifice diameter (D), where the stroke length may be thought of as the length of a hypothetical 'slug' of fluid that is ejected from the orifice during the ejection stroke. The development of the term 'stroke length' comes from the inverse of the Strouhal number, as $L_0/D = (fD/U_0)^{-1}$. Holman et al. [57] and Utturkar et al. [70] reasoned that a synthetic jet formation threshold existed and it was governed by the Strouhal number; the criterion they developed was

$$\frac{1}{Sr} = \frac{Re}{S^2} > K \tag{2.8}$$

where Sr is the Strouhal number (fL_0/U_0) and is proportional to the inverse of the

dimensionless stroke length (L_0/D), Re is the Reynolds number ($U_0 D/\nu$), S is the Stokes number (defined in the next paragraph) and the constant K relies on the shape of the orifice or nozzle, and is 0.16 for axisymmetric jets, and 1 for two dimensional jets. With regard to the above criterion for the jet formation constant, once the criterion is met, the average self induced velocity of the vortex ring is seen to be greater than that induced by the suction stroke, which results in the issuing vortex ring escaping from the vicinity of the orifice and not being entrained back into the cavity. In this analysis, $Re/S^2 \approx \bar{U}/2\pi f d$, thus the formation criterion is related to the dimensionless stroke length as follows:

$$\frac{L_0}{D} = \frac{\bar{U}}{2fD} = \pi \frac{Re}{S^2} \tag{2.9}$$

This is in agreement with the work of Smith and Swift [71], which found for a two dimensional synthetic jet that there was a minimum formation stroke length of $L_0/D = 5.5$; below this no synthetic jet was formed. Once the above criterion is met, an increase in the dimensionless stroke length (L_0/D) is seen to increase the momentum; circulation and vorticity are imparted to each vortex ring [24], [72]. However, when the dimensionless stroke length is greater than 4, with respect to an axisymmetric synthetic jet, it is observed that the total circulation and vorticity imparted by the actuator to the flow is not contained entirely within the primary vortex ring formed, but is distributed between the primary vortex and the secondary trailing vortex ring. This phenomenon is attributed to the fact that, beyond a certain stroke length, the primary vortex ring cannot contain any more circulation and thus sheds the excess in the form of secondary trailing vortex rings; this feature has also been labelled as a trailing jet, [7], [11].

Another parameter that is associated with oscillatory flow is the Stokes number, S, which has been used in the synthetic jet formation criterion. A very thorough article recently published by Trávníček et al. [73] details the formation criterion for an axisymmetric synthetic jet at high Stokes numbers. Their research investigated a Stokes

number range of $S = 73 - 292$; results produced by Trávníček et al. agreed reasonably well with equation 2.8 for the range of Stokes number $S < 160$, from this, they found that the formation criterion for the synthetic jet was $(Re)_{crit} = 2.42S^{1.42}$.

Numerical simulations completed by Tang [74], demonstrated that vortex roll up related to a synthetic jet was primarily characterised by the Stokes number[3], S, which is defined as

$$S = \sqrt{\frac{2\pi f D^2}{\nu}} \tag{2.10}$$

In a fluid, the Stokes number represents the ratio of the unsteady force to the viscous force [74], [75]. The strength of a vortex sheet can be measured by the level of vorticity (Ω) it contains, where the estimation of the dimensionless form of vorticity is

$$\frac{\Omega D^2}{\nu} \sim L{\cdot}S^2{\cdot}\frac{D}{\varepsilon} \tag{2.11}$$

ε is the thickness of the Stokes layer in the orifice, which is defined as the radial distance between the position of the velocity peak and the wall at the orifice exit, figure 2.19. On the left hand side of equation 2.11 is an expression for dimensionless vorticity; this indicates that in order to obtain a similar strength vortex roll up, the vorticity (Ω) should be much higher for an actuator with a small diameter orifice. This holds true because a small scale vortex ring has a higher curvature, which in turn demands a higher vorticity in the vortex sheet. Normalising the thickness of the Stokes layer is done by dividing by the diameter (D); it is found that the normalised Stokes layer thickness (ε/D) is a function of the Stokes number, but this only holds true if the assumption is made that the oscillating flow in the orifice is a fully developed laminar flow.

[3] Section 1.3 defined Stokes number as $S = \tau_r U/l$, this is in relation to the selection of the seeding particles for use in particle image velocimetry.

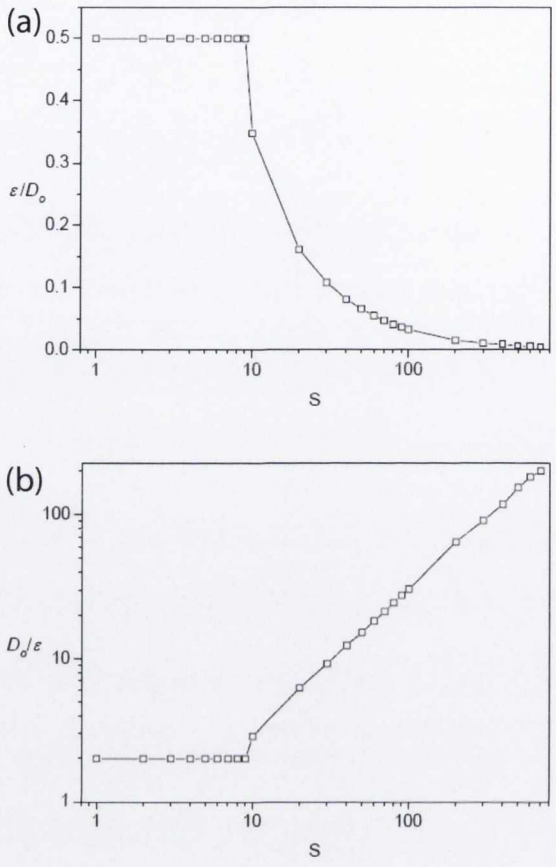

Figure 2.19 – Stokes number versus the variation in thickness of the Stokes layer in an oscillating pipe flow (a) ε/D *vs* S (b) D/ε *vs* S [74]

With reference to figure 2.19, the variation of ε/D and its inverse against Stokes number (S) is shown, respectively. Figure 2.19a indicates that the velocity peak remains at the centre of the orifice exit when $S < 10$, and as S increases beyond this, it gradually retreats towards the orifice wall. The position of the velocity peak is said to affect the roll up of the vortex sheet. Thus, when $S < 10$ there exists a 'thick' cylindrical vortex sheet with a maximum velocity at the centre that dominates the whole orifice duct; in this case, the leading edge of the vortex sheet is unable to curve and begin rollup due to the axisymmetric nature of the type of flow generated. However, when $S > 10$, there is a potential core that appears at the centre of the orifice, this in turn allows for the rollup of vortex rings to take place. For completeness, figure 2.19b shows that the inverse of Stokes layer thickness (D/ε) increases with the Stokes number, in particular for when $S > 10$, and in relation to equation 2.11, it can be seen that the dimension-

less vorticity depends more on the Stokes number, S, than on the dimensionless stroke length, L_0/D.

It is worth noting that there are three key dimensionless parameters of importance to defining a synthetic jet flow in quiescent conditions, i.e. Stokes number (S), stroke length (L_0), and Reynolds number (Re). However, only two of these parameters are independent as they are related to each other through the following relationship:

$$S = \sqrt{\frac{2\pi Re_{U_0}}{(L_0/D)}} \tag{2.12}$$

The Stokes number has an effect on the velocity profiles at the synthetic jet orifice [11], [76], as an increase in it results in the velocity profile at the orifice changing from a parabolic shape to one that resembles a top hat distribution, illustrated in figure 2.20.

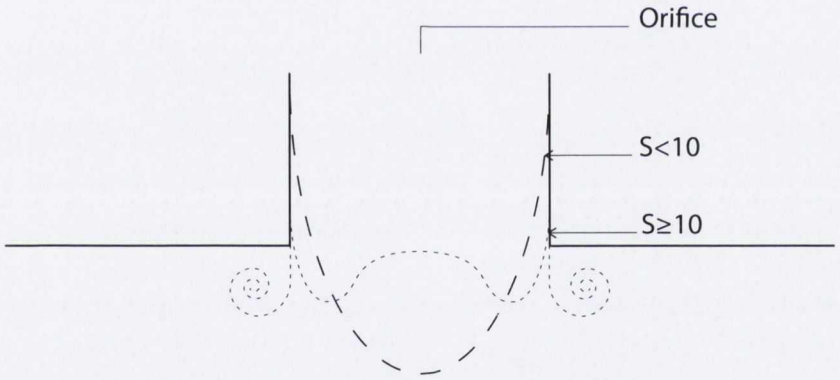

Figure 2.20 – Illustrative velocity profiles at orifice exit at low Stokes number (– –), ($S < 10$) and at high Stokes number (- - -), ($S \geq 10$), which leads to vortex roll up.

A higher Stokes number implies that a thinner boundary layer is formed on the orifice wall, as the influence of Stokes number on the jet exit velocity profile is similar to what is known for oscillating pipe flows. As stated earlier, a minimum Stokes number of about 10 ($S \approx 10$) is required for sufficient vortex rollup to occur, as documented by Zhong et al. [47] and Tang [74]; it was also noted that jet exit velocity profiles of two test cases with significantly different stroke lengths could still be similar when the Stokes numbers were identical. With stroke length being representative of the fluid

volume ejected through the orifice during the ejection stroke, the distance between successive vortex rings is dictated by the stroke length. A formation threshold exists for synthetic jets, as given by equation 2.8; if the stroke length is below the formation threshold, then the vortex rings formed cannot move far enough away from the orifice and are sucked back into the cavity on the suction portion of the cycle.

2.4.2.2 Reynolds number

As identified in section 1.3, the other primary dimensionless number used in the 'slug' velocity model that defines a synthetic air jet is the Reynolds number,

$$Re_{U_0} = \frac{U_0 D}{\nu} \tag{2.13}$$

which is based on the jet discharge velocity U_0, nozzle or orifice diameter D and the kinematic viscosity ν. Due to the nature of a synthetic air jet i.e. zero-net-mass-flux, it is difficult to define a characteristic jet velocity. Previous work on the topic by several authors, [11], [64], [77], utilised single point, centreline velocity measurements to calculate synthetic jet velocity. Smith and Glezer [45], proposed the use of a time averaged velocity

$$U_0 = fL_0 = \frac{1}{T}\int_0^{\tau} u_0(t)dt \tag{2.14}$$

where U_0 is the downstream directed velocity, which occurs during the ejection stroke, as shown in figure 2.21. f is the frequency of oscillation of the actuator, τ=1/(2f) is the blowing period of the jet, L_0 is the length of the slug of fluid pushed from the orifice during the ejection stroke, T=1/f is the oscillation period, and $u_0(t)$ is the centreline velocity as a function of time. The maximum distance over which an oscillatory flow can develop is L_0, since the flow reverses after travelling this distance. Ideally, a measurement across the profile of the jet should be taken to obtain an area averaged velocity, but this is not usually the case; the most commonly used method of measuring the velocity is at a point on the centreline of the jet or close to the jet exit.

This method of measurement comes about as a result of geometric constraints and an attempt to reduce the complexity of analysis. While it is a practical way of measuring the velocity, it is the assumption that the flow velocity $u_0(t)$ is uniform across the width of the orifice that can lead to errors in calculating the jet Reynolds number when using this model. Experimental [11], [71], [78], and numerical work [79], has shown that the spatial velocity profile can deviate significantly from the postulated 'slug' shape, thus it is preferable to replace the centreline velocity $u_0(t)$ by the spatial averaged velocity at the jet exit. Glezer and Amitay [46] outlined another method for calculating the Reynolds number based on the momentum associated with jet discharge, I_0, defined as,

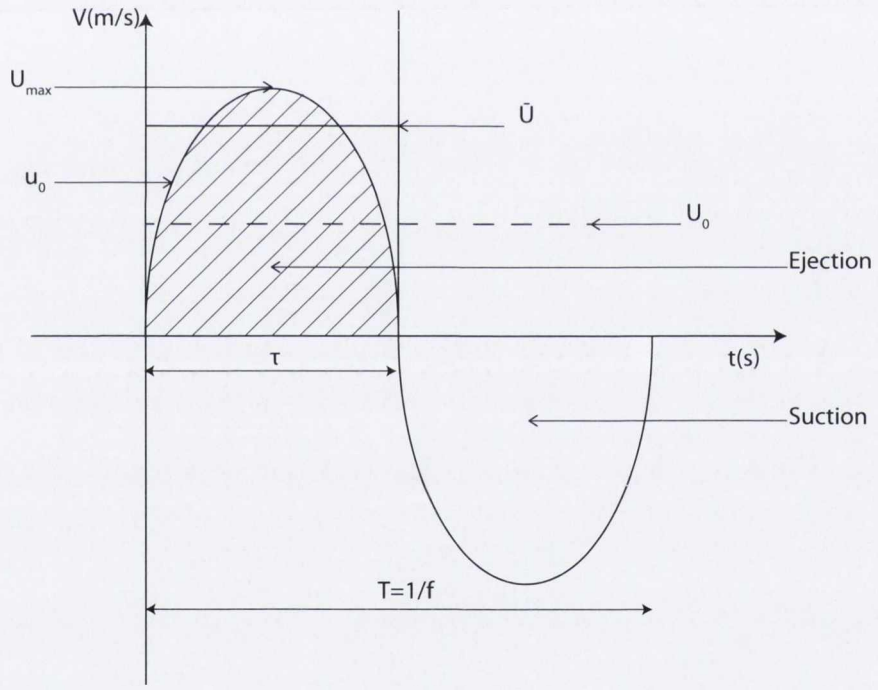

Figure 2.21 – Example of a sine wave velocity profile showing U_0.

$$Re_{I_0} = \frac{I_0}{\mu D} \tag{2.15}$$

where

$$I_0 = \rho \int_0^{\tau} \int_A u_0^2(\bar{x}, t)\, dA\, dt \tag{2.16}$$

with ρ and μ denoting fluid density and viscosity, respectively. In their analysis, the Reynolds number is seen to affect the strength of the issuing vortices but not the location of the vortex rings themselves.

Persoons and O'Donovan [80] developed a method of calculating synthetic jet velocity based on the laws of simplified gas dynamics. This method requires the measurement of the internal cavity pressure of the actuator in order to estimate the synthetic jet velocity and the deflection of the actuator. The conservation of momentum in the orifice is:

$$M_0 \frac{d\bar{U}}{dt} + F_D(\bar{U}) = pA \tag{2.17}$$

M_0 is the mass of gas in the orifice, $F_D(\bar{U})$ represents a damping force and p is the varying cavity pressure relative to the unloaded condition of the actuator; p is assumed to be small compared to the absolute pressure p_0. A centreline velocity measurement is required for this method in order to perform the calibration, but it is only required initially to characterise a pressure loss coefficient K_p, which is required to calculate the correct damping force F_D. This method leads to a velocity calculation that is very much like that defined by Utturkar et al. [70], with a Reynolds number, $Re_{\bar{U}} = \bar{U}D/\nu$, defined in terms of a spatial and time averaged exit velocity during the ejection stroke, where

$$\bar{U} = \frac{1}{\tau}\frac{1}{A}\int_A \int_0^\tau u(t,y)dtdA \tag{2.18}$$

A is the exit area and y represents the cross-stream coordinate. The blowing period or ejection duration is $\tau = 1/(2f)$. Utturkar et al. [70] showed that the two velocity scales are related by $\bar{U} = 2U_0$, referring to figure 2.21, on the ejection portion of the cycle. Thus, the dashed horizontal line represents U_0, and the solid horizontal line represents $\bar{U}$. The velocity in equation 2.14 is only calculated over the ejection stroke of the jet cycle, whereas in equation 2.18 the velocity is time averaged over the entire cycle. Thus, the jet Reynolds number calculated using equation 2.18 yields a Reynolds

number of twice the magnitude for the exact same flow parameters. Despite the differences in the Reynolds numbers calculated by equation 2.14 and equation 2.18, neither can be considered the wrong way of calculating synthetic jet Reynolds numbers. For example, equation 2.14 more accurately reflects the time averaged mass flux of fluid produced by the synthetic jet, and equation 2.18 allows for a better understanding of the state of the fluid expelled during the ejection phase by providing the peak velocities of the synthetic jet.

The velocity calculation utilised in this research is based on a Reynolds number, $Re_{\bar{U}} = \bar{U}D/\nu$, that is defined in terms of a spatial and time averaged exit velocity during the ejection stroke, with $\bar{U}$ calculated using equation 2.18, much like that defined by Utturkar et al. [70].

2.4.3 Synthetic jet flow field

The flow field of an issuing synthetic air jet is comprised of a near field and a far field based on the dominant flow phenomena, which has been previously broken down into four flow regions in section 2.4.1. A schematic of the flow field is illustrated in figure 2.17.

2.4.3.1 Vortex rings

As discussed in the section on vorticity, vortex rings are the essence of what a synthetic jet is. Initial work completed on vortex rings by researchers such as Gharib et al. [24] addressed the question *"for a given geometry, is there an upper limit to the maximum circulation that a vortex ring can acquire?"*. In their study, they utilised digital particle image velocimetry and a piston/cylinder arrangement, to complete a series of experiments for large values of non-dimensionalised piston stroke. The vortex rings produced by a synthetic jet actuator differ from those produced by a piston/cylinder arrangement in that the behaviour of the synthetic jet actuator is strongly affected by the presence of a suction flow in the vicinity of the orifice. Nonetheless, there is sufficient common ground for their research to be relevant.

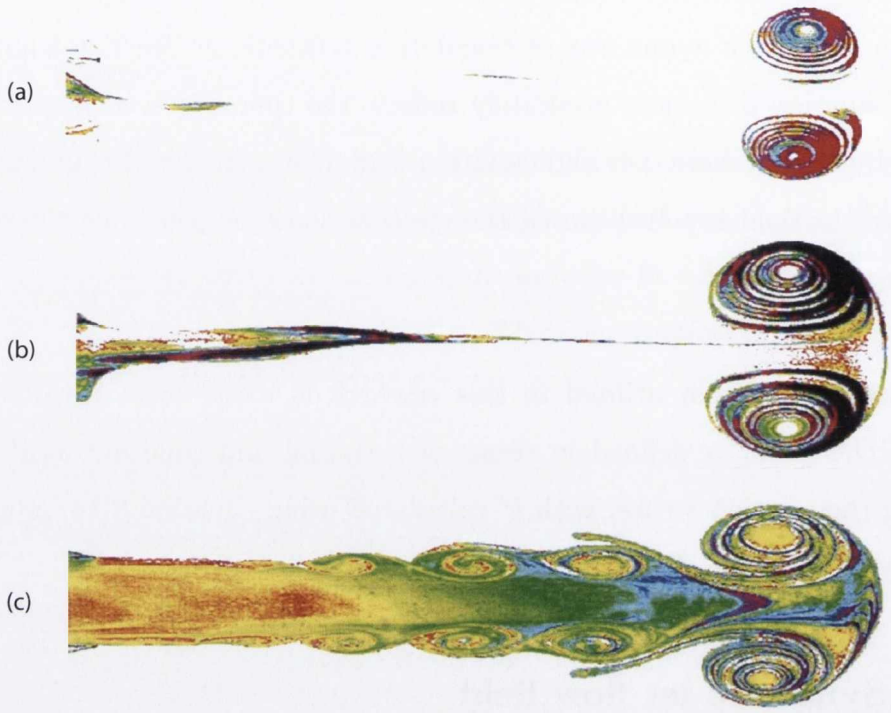

Figure 2.22 – Vortex ring visualisation (a) $L_0/D = 2$, (b) $L_0/D = 3.8$ and (c) $L_0/D = 14.5$ [24].

The research of Gharib et al. [24] identified a universal formation time scale, or formation number, which characterises the formation of vortex rings. They performed measurements of vortex ring circulation for maximum stroke displacements ($0.5 \leq L_0/D \leq 6.7$), and observed that the circulation ceased to increase beyond $L_0/D \approx 4$. The total circulation for the vortex ring produced was measured as a function of formation time $\bar{U_p}t/D = L/D$, where $\bar{U_p}$ signifies the mean velocity of the piston utilised in the experiments performed by Gharib et al. [24]. The time scale or formation time, is the time beyond which larger vortex rings are not possible; i.e. $L_0/D \approx 4$ for an impulsively started jet. With reference to figure 2.22, for $L_0/D \leq 4$, it was found that all the fluid discharged from the orifice became entrained in the vortex ring, figure 2.22a and figure 2.22b. Up to the vortex formation number, a linear relationship between the stroke length and vortex circulation was observed, shown in figure 2.23. Confirmation of the vortex formation number is reflected in figure 2.22b

and figure 2.22c, i.e. the vortex size is approximately the same in these two snapshots. For $L_0/D = 14.5$ they observed that the leading edge is 'pinched-off' from the trailing jet in terms of both velocity and vorticity fields. Vorticity in the shear layer ceases to flow into the vortex core once the pinch-off process starts, and instead proceeds to roll up into a series of vortices in a process similar to the Kelvin-Helmholtz instability[4]. The zero flux of vorticity into the primary ring also implies that there is no further increase in the vortex ring circulation.

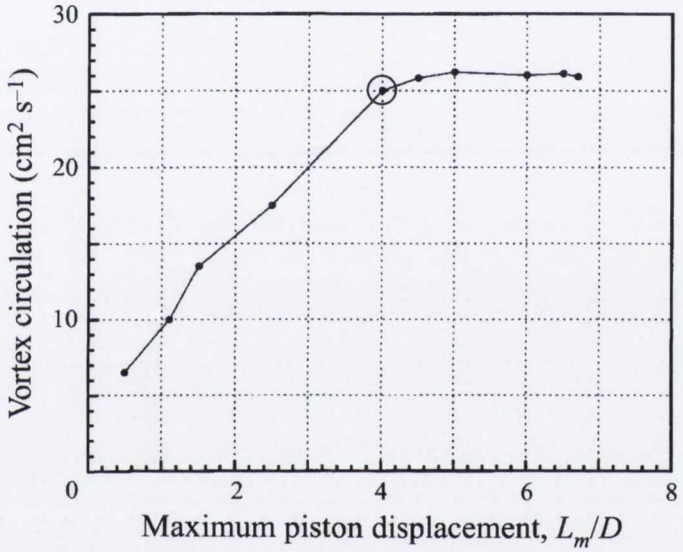

Figure 2.23 – Vortex ring circulation as a function of stroke length (L_m/D), vortex formation number (◯), [24]. (L_m/D=maximum stroke ratio)

A fast ramp test case performed by Gharib et al., that would closely resemble the ejection stroke of a synthetic air jet in terms of the speed of their piston/cylinder arrangement, resulted in a trailing jet that caught up with and interacted with the leading vortex ring. As a direct result of the interaction, merging occurred and circulation levels increased within the leading vortex ring from the vortex at the head of the trailing jet. Excess vorticity from this interaction was eventually discharged and the circulation of the leading vortex ring reduced to its initial level determined

[4] Kelvin-Helmholtz instability occurs when there is a velocity shear present in a continuous fluid flow, or when there is a sufficient velocity difference across the interface between two fluids, which leads to vortex roll-up in the shear layer

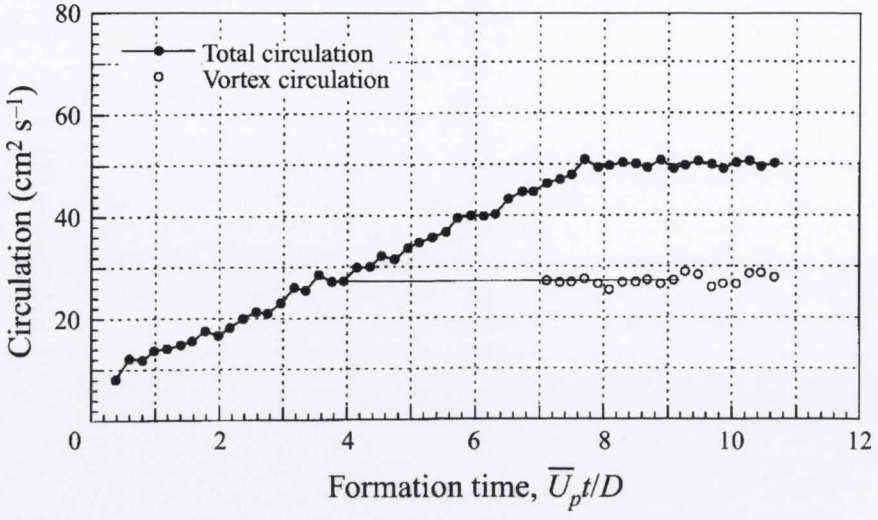

Figure 2.24 – Vortex ring circulation as a function of formation length for $L_0/D = 8$ [24].

from the formation number. Figure 2.24 is a plot of circulation versus formation time and shows that the total circulation increases as expected until the piston is stopped, while the vortex ring circulation levels out at $L_0/D \approx 4$. This shows that the maximum circulation that the vortex ring can attain is equal to the total circulation discharged from the nozzle up to $L_0/D \approx 4$. If $L_0/D \approx 4$ then the vortex ring formed would have no trailing jet, [7].

2.4.3.2 Near field

The near field is largely influenced by the periodic formation, advection and interaction of discrete vortical structures, [2], [45]. The vortex pairs or rings created ultimately become turbulent, slow down and lose their coherence. Smith and Glezer [45] noted from their flow visualisation studies of a synthetic jet that the vortex pair begins to undergo a transition to turbulence at around the start of the actuator suction stroke, which may be linked to the core instabilities associated with the reversal of the streamwise velocity at the orifice exit. Due to the suction flow, the time averaged static pressure near the orifice exit of a synthetic air jet is typically lower than the ambient pressure which results in the streamwise and cross stream velocity components reversing their direction during the actuation cycle.

The pulsatile nature of the synthetic jet flow in the near field close to the orifice leads to a stagnation point being formed during the suction stroke. Thus, if a vortex ring rolls up and moves away from the orifice, it results in part of the fluid moving away from the orifice, due to the vortex ring, while part of the fluid moves towards the orifice, due to the suction stroke. This leads to a location of zero velocity, which is known as a saddle point. It is the periodic reversal in flow direction along the jet centreline between ejection and suction strokes that results in the formation of a saddle point on the centreline downstream of the orifice; this leads to the sink like flow being confined to within a finite region near the orifice exit. The existence of a saddle point in the near field of synthetic air jets has been observed in several studies, [81], [82], [83]; the saddle point is deemed one of the more significant features of a synthetic air jet that exists in the near field. The saddle point is shown in figure 2.25 at $x/b \approx 5$; above this point it can be seen that the flow is directed away from the orifice, whilst beneath the saddle point, the flow is directed towards the orifice. The appearance of the saddle point only occurs on the suction stroke of the cycle, with its axial position being entirely dependent on when the suction phase occurs in the jet cycle. Initially the saddle point appears at the orifice exit, and as the cycle progresses the saddle point gradually moves downstream until it disappears as the cycle repeats. Research by McGuinn et al. [84] found that the saddle point location was affected by flow confinement i.e. as confinement is increased the saddle point moved ever closer to the orifice until it was undetectable; this is thought to be due to the recirculation effects between the orifice plate and impingement surface. The exact relation between the location of the saddle point and the operational parameters of a synthetic jet has not been very well documented, but it is thought to be linked to the dimensionless stroke length and the height of the orifice above the impingement surface.

The near field of a synthetic air jet flow field has an oscillatory nature that is dominated by vortex rings, which gives rise to a greater rate of entrainment of ambient fluid. As a result of this, synthetic jets have a much higher spreading rate and volume flux compared to steady jets. Research published by Cater and Soria [85] that utilised fluorescent dye visualisation, clearly illustrated that the spreading rate of a synthetic

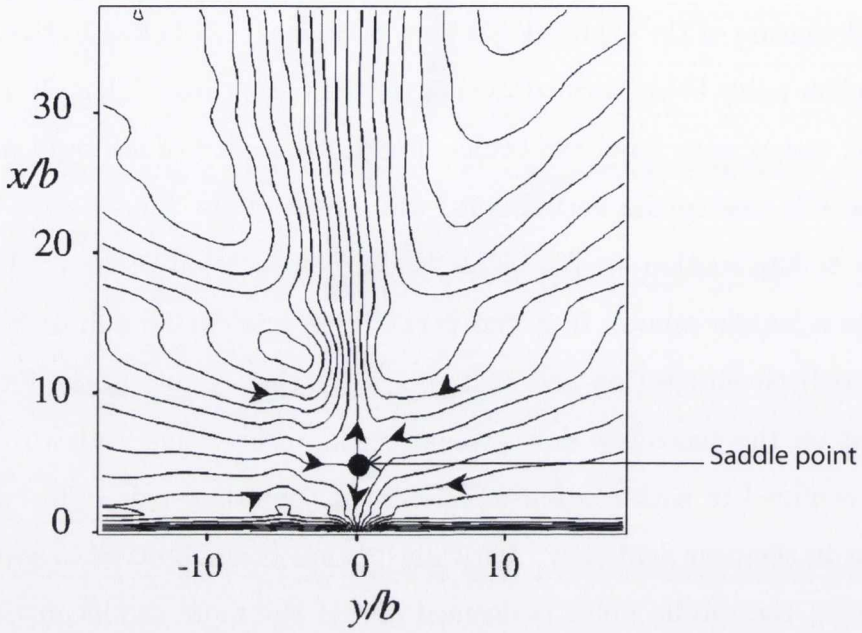

Figure 2.25 – Phase averaged streamline plots computed from PIV data; $\varphi = 270°$, $f = 300Hz$, $Re_{U_0} = 300$, $L_0/D = 29.1$, [81].

jet was higher than that of a steady jet. This is shown in figure 2.26.

2.4.3.3 Far field

In the far field of a synthetic air jet, the vortex rings eventually break down, interact and coalesce to such an extent that they become indistinguishable from the jet flow and travel with the mean jet velocity. There is a decrease in time averaged velocity in this region as a result of entrainment of the quiescent fluid with a parallel increase in the width of the jet due to a transfer of momentum. Smith and Glezer [45], and Mallinson et al. [86] found that the time averaged velocity profiles bore a resemblance to a turbulent steady jet in the form of self similarity as inferred from the collapse of the scaled mean and turbulent intensity profiles. Smith and Glezer [45] found in their research that the deceleration rate and subsequent transition to turbulence of the vortices occurred within 7 jet diameters. Thus, the behaviour of a synthetic air jet in the far field is similar to that of a turbulent steady jet. Self similarity of a steady jet implies that its characteristic width and the inverse of its centreline velocity increase linearly with distance from the orifice exit.

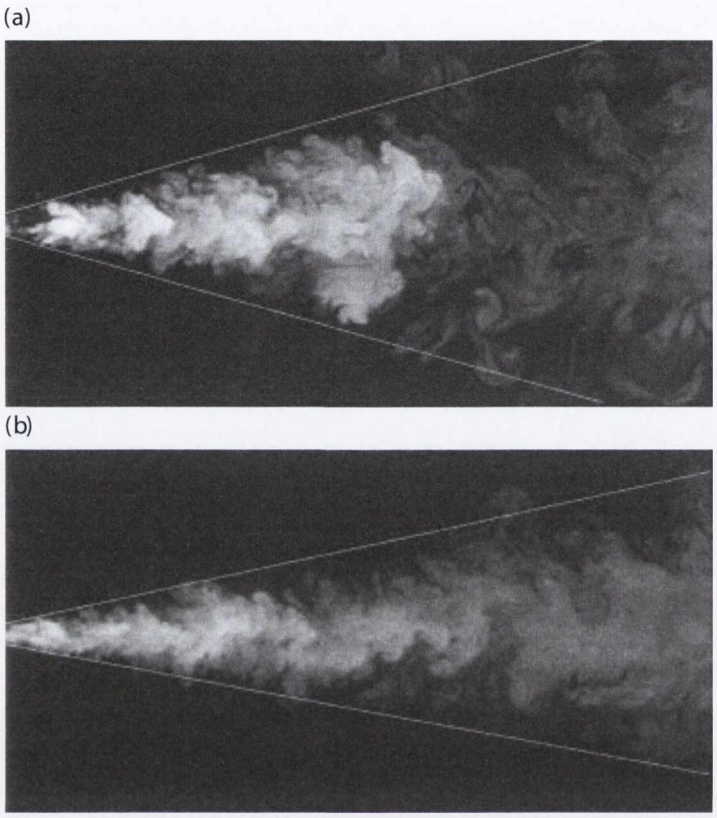

Figure 2.26 – Digitised flow visualisation of fluorescent dye marker for (a) Synthetic Jet, and (b) an equivalent Steady jet at a Reynolds number, $Re_0 = 10000$, and Strouhal number, $St_0 = 0.0015$. The light coloured lines indicate an apparent mean boundary of the dye flow, [85].

A comparison of the axial velocity profiles of a steady jet and a synthetic jet are shown in figure 2.27; this was part of a significant study completed by Cater and Soria [85] that compared the flow field properties of a steady jet and a synthetic jet. Several authors have reported that the far field of a synthetic air jet and a steady turbulent jet are quite similar [2], [85]; figure 2.27 shows the difference in the mean far field flow. Figure 2.27a and b are essentially the same data, only figure 2.27b is normalised by the centreline velocity and the radial coordinate has been non-dimensionalised by the axial location $\eta = r/(x - x_0)$; this is also known as the similarity variable. The spread rate of synthetic air jets in the far field is related to the structural differences in the near field. The significant difference in decay rate of a synthetic jet and a steady jet

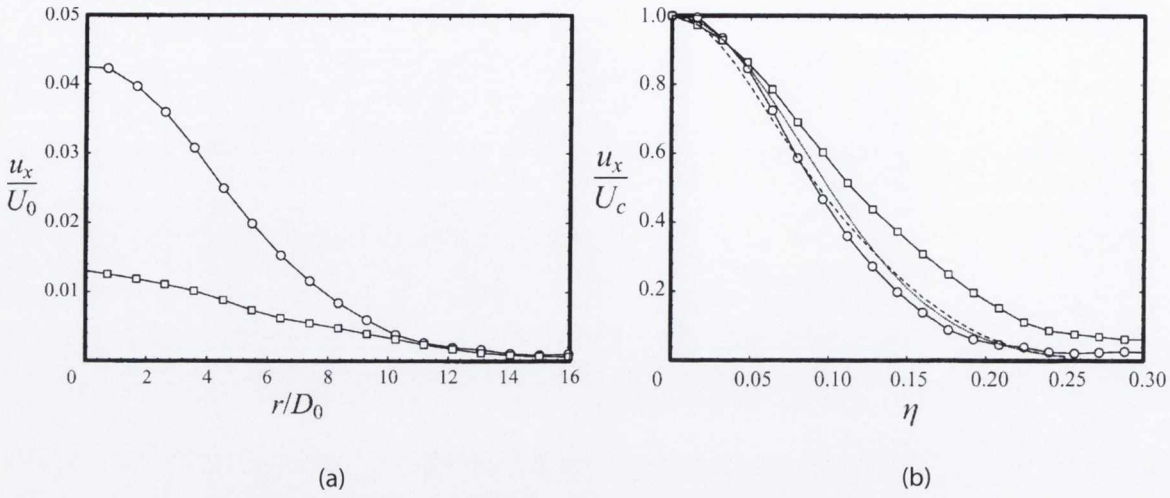

Figure 2.27 – (a) Non-dimensionalised and (b) Normalised profiles of axial velocity at $x = 60D$ for jets at $Re = 10^4$. Steady jet (○), Synthetic jet (□), Gaussian distribution (· · ·), Hussein et al. (- - -) [85].

has been attributed to the oscillatory nature of the flow, which means that it has a potential core of diminished velocity, in contrast to a steady jet.

Research completed by Smith and Swift [87] examined how a synthetic air jet resembles and differs from a steady jet whilst comparing several different parameters. They found that at matched Reynolds numbers these two different jet types have the same profile shape, but the synthetic jets were wider and slower than their steady jet counterparts. Figure 2.28a represents the mean velocity profiles in similarity coordinates. It is from this graph the jet spread rates have been calculated. A paper published by Kotsovinos [88] on the spreading rate and virtual origin of a plane turbulent jet details how the jet spread rate is calculated. A brief outline of the method utilised is described below. A cartesian coordinate system is utilised with x representing the jet axis. The lateral distribution of the mean axial velocity $\bar{u}(x, y)$ is measured at several stations at various axial distances x from the orifice of the jet, the half width $b(x)$ is calculated from the following equation.

$$\bar{u}(x, \pm b(x)) = \frac{1}{2}\bar{u}(x, 0) \tag{2.19}$$

The half widths $b(x)$ are then normalised by the orifice diameter D, and these values are then plotted versus the non-dimensional distance from the jet orifice x/D. This results in a straight line of the form,

$$b(x)/D = K_1(x/D + K_2) \tag{2.20}$$

which is fitted to the data points. The coefficient K_1 is a measure of the jet spreading rate. The virtual origin of the jet is calculated from the relation $x_0 = -K_2 D$. Figure 2.28b depicts the mean streamwise evolution of the jet velocities. The $-1/2$ power-law decay typical of plane jets is followed unlike the x^{-1} that Cater and Soria indicated in their research [85], the key difference between these two studies being that Smith and Swift used a two dimensional jet and Cater and Soria an axisymmetric jet. Thus, the difference in the jet decay can be attributed to the difference in flow produced from different orifice geometries.

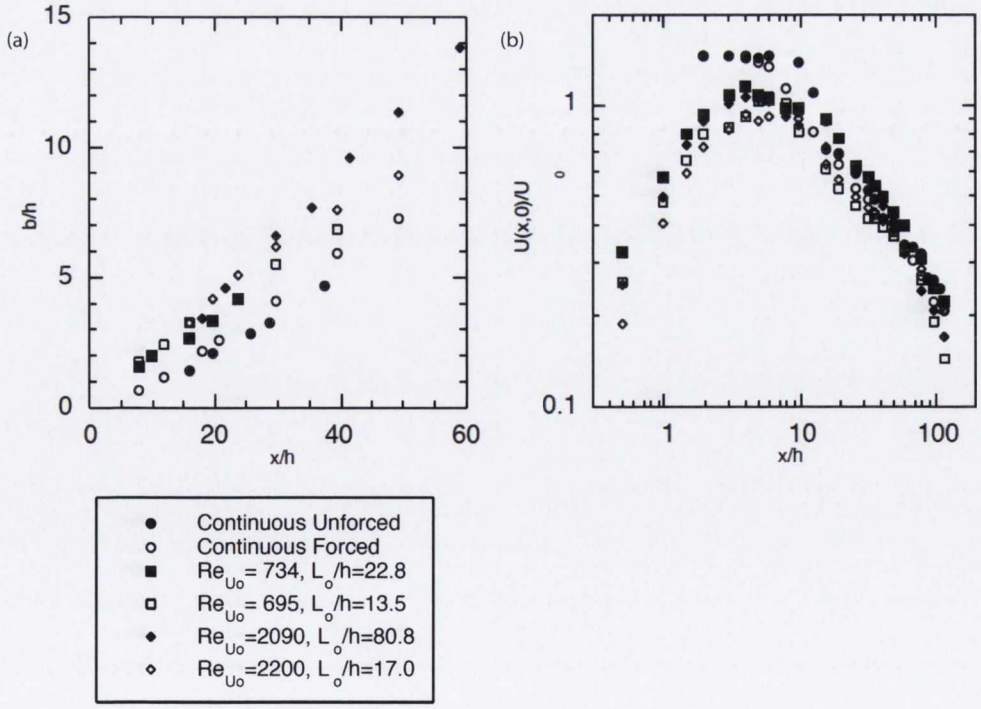

Figure 2.28 – (a) Width of jet based on half maximum velocity as a function of downstream distance (b) Time-averaged centreline velocity versus downstream distance. Symbols apply to both graphs, [87].

The spreading rates of synthetic jets and steady jets are presented in table 2.1. These spreading rates have been calculated by several researchers and have been tabulated in order to provide a direct comparison. The evolution of the jet half width as a function of axial distance, db/dx, represents the spreading rate, where b represents the cross stream half width from the centre of the jet. Cater and Soria [85] noted there was a larger spreading rate for synthetic jets when compared to a steady jet; the spread rate calculated for a synthetic jet was found to be ($db/dx \approx 0.107$) approximately 15% higher than its steady jet equivalent for the same Reynolds number. The same study indicated that the spreading rates for both the steady jet and synthetic jet increased in a linear fashion up to $x = 30D$. It was concluded that the near field structure of the synthetic jet affected the flow structure in the far field. In other words, the vortex formation, which increased the entrainment rate as the jet developed, contributes to the overall growth and spread rate of a synthetic jet. Comparison of the study completed by Di Cicca and Iuso [78] with that of Cater and Soria [85] shows a good agreement with the spreading rates calculated for steady and synthetic jets; both studies utilised the jet half width as a function of axial distance in calculating the spreading rate. Di Cicca and Iuso [78] identify two regions, each of which is characterised by an almost constant spreading rate db/dx. The spreading rate calculated by Di Cicca and Iuso [78] in the secondary region they had identified of $db/dx = 0.098$ is in reasonably good agreement with the value calculated by Cater and Soria [85] of $db/dx = 0.107$.

The study completed by Smith and Swift [87] was a direct comparison of a synthetic air jet with a steady jet. Several aspects of the jets were examined, including jet spreading rate and velocity profiles. Overall, six cases were studied, including two steady jets and four synthetic jets. As can be seen in table 2.1 a forced and unforced steady jet were tested. The forced steady jet was forced at the Kelvin-Helmholtz frequency of $600Hz$ in order to introduce some variety to the features of the steady jet. The forcing frequency for the steady jet was experimentally determined, an oscillation amplitude of 5.5% of U_{ave} initiates a rollup of the jet closer to the exit plane; this has been previously documented by Rockwell [89]. The spread rates reported by Smith and Swift [87] for a synthetic air jet are significantly different to that of Cater and Soria

Table 2.1 – Experimental spread rate comparison for synthetic and steady jets [7].

Researchers	Jet type	Geometry	Re	Spread rate (db/dx)	L_0/D
Cater [85]	Synthetic	Round	10^4	0.107	150
Cater	Steady	Round	10^4	0.092	N/A
Di Cicca & Iuso [78]	Synthetic	Round	1290-3400	0.098	23
Smith & Glezer [45]	Synthetic	2D	104-489	0.194	5.3-25
Smith & Swift[87]	Synthetic	2D	734-2200	0.174-0.213	17-22
Smith & Swift	Steady	2D	2200	0.125	N/A
Smith & Swift	Forced steady	2D	2200	0.149	N/A

[85]; this could be due to the different experimental parameters of the researchers, i.e. the stroke lengths tested by Smith and Swift are approximately six times smaller than the stroke length Cater and Soria tested at. The axial location that Smith and Swift measured each velocity profile at was where the centreline velocity U_{cl} is half that of $\bar{U}$ (steady jet velocity) or U_0 (synthetic jet velocity). From the db/dx results presented in table 2.1, the findings reported by Cater and Soria [85] that a synthetic jet has a higher spread rate than a steady jet are validated.

2.5 Synthetic jet heat transfer

Although the primary focus of this research study is on synthetic jet evolution, limited simultaneous heat transfer testing was conducted in order to complement flow measurements in the stagnation and wall jet regions and to enhance the understanding of convective heat transfer mechanisms. Thus, a brief outline of synthetic jet heat transfer is included here.

A thorough investigation into the heat transfer characteristics of a normally impinging synthetic jet has been completed within the research group, [7]. The flexibility that synthetic air jets possess in terms of implementation and system integration is what

makes them an attractive candidate for heat transfer applications. The parameters of a synthetic air jet that are of particular interest with regard to heat transfer are dimensionless stroke length, jet Reynolds number and jet exit to impingement surface spacing. The stagnation point heat transfer is of particular interest, as the most common method of application of a jet cooling solution is directing the jet towards the area that requires the highest level of cooling. Persoons et al. [90] presented a general correlation for the stagnation point Nusselt number for an axisymmetric impinging synthetic jet; they identified four heat transfer regimes that are dependent on stroke length and the axial spacing of the jet. The authors state that operating the synthetic jet at lower operational frequencies with certain larger stroke lengths proves inefficient for particular actuators that have a high resonant frequency. From the data presented it was found that a local maximum is achieved at a lower stroke length. At larger axial spacings the peak heat transfer typically occurs at the geometric centre of the jet, or stagnation point. Gillespie et al. [91] described the resulting trend as Gaussian, although with increasing radial distance from the stagnation point the trend decreases monotonically. Figure 2.29 illustrates a radial distribution in local Nusselt number for a two dimensional impinging synthetic air jet for a range of Reynolds numbers, and an axial spacing of $H/b = 3.6$, with dimensionless stroke lengths ranging from L_0=8.1b to 10.3b. Heat transfer data are commonly presented also as a mean Nusselt number, as this provides a good indication of the performance of the jet. However, the local heat transfer profiles contain detailed information as to whether or not local maxima and minima exist, and are useful for providing insight into convective heat transfer mechanisms.

From the literature it is evident that synthetic jets can provide high heat transfer rates. Kataoka et al. [4] initially explored the mechanism for the enhancement of stagnation point heat transfer utilising a pulsed jet; they found that the large scale eddies contained within the flow that were impinging on the heat transfer surfaces produced a turbulent surface renewal effect that enhanced the heat transfer from the impingement surface. Pavlova and Amitay [64] performed research that experimentally compared the performance of a synthetic jet to that of a steady jet when cooling a constant heat

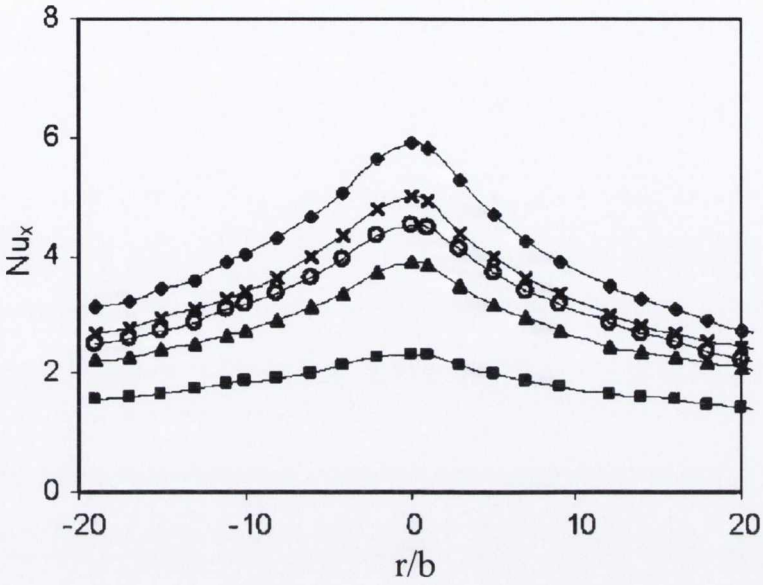

Figure 2.29 – Local Nusselt number distributions for a 2D synthetic air jet; $H/b = 3.6$, $Re =$ ■108, ○254, ▲309, ×367, ♦396, [91].

flux surface. The results of their study found that higher frequency jets ($1200Hz$) were more effective at lower H/D values and conversely, lower frequency jets ($420Hz$) were found to be more effective at higher H/D values. In addition the synthetic jets were found to cool the heated impingement surface better than the steady jets. This was all attributed to the fact that coherent vortex rings are formed by a synthetic air jet, which enhance the mixing and thus the heat transfer from the surface. Initial research performed in the course of this study provided an insight into the relative effectiveness of a synthetic air jet and a steady jet at low jet exit to impingement surface spacings. From this study it was concluded that the performance of a synthetic jet may approach that of a steady jet at the larger H/D values tested, but the synthetic air jet suffered at low H/D values, largely due to recirculation as a result of the high degree of confinement associated with the synthetic jet chamber [8]. This same effect was previously documented by McGuinn et al. [92]. The overall difference between Nusselt numbers was found to reduce as the degree of confinement was reduced; the findings from this study differ from those of Pavlova and Amitay [64]. This may be linked to the fact that the effectiveness of a synthetic air jet depends on several factors, but the study in question [8] utilised only one dimensionless stroke length for the synthetic jet.

Varying the dimensionless stroke length has a direct effect on the heat transfer rates of a synthetic jet, as reported by McGuinn, [7].

The use of synthetic jets for cooling of electronics is a relatively new technology which has shown great promise in a number of practical applications. In a review article by Glezer and Amitay [46], it was noted that impinging synthetic jets are proving to be an extremely promising technology for use in electronics cooling and also have excellent potential for cooling in manufacturing processes. Steady jets have been the industry standard for decades and it has been well established that effective rates of cooling can be achieved using conventional steady impinging air jets [93], [94]. However, it has been documented more recently that synthetic air jets can provide similar cooling effects [46], [55], [64], [8].

The design and thermal performance of a synthetic air jet cooled heat sink has been investigated by Mahalingam and Glezer [95]. Their results showed that forced convection with synthetic jets generated a flow of 4.48 CFM through the heat sink, resulting in 27.8 W/CFM and a thermal effectiveness of 0.62. They found that there was approximately a 40% increase in the heat dissipation levels with the synthetic air jet cooled heat sink compared to the standard ducted axial fan flow through the heat sink. The tests were performed at the same jet Reynolds number, and the average heat transfer coefficient in the channel flow between the fins for the synthetic air jet was 2.5 times that for steady jet flow in the same configuration. It is worth noting that the flow rates where the synthetic jets dissipated more power than an axial fan was in the 3-5 CFM range. As flow rates were increased, the steady jet flow dissipated more power, which is in line with the findings by Farrelly et al. [8].

In 2001, a study performed by Vukasinovic and Glezer [5] experimentally investigated the performance of a low-profile radial countercurrent heat sink, driven by a synthetic jet actuator at $80Hz$, normally impinging on an extended surface with a power dissipation of $50W$. Jet flow measurements were conducted using particle image velocimetry and temperature measurements utilising thermocouples embedded on a test die were

carried out at several H/D values between the synthetic jet and the impingement surface. The findings of their study showed that synthetic jets may present a viable option for the cooling of electronics where space and volume are limited. Although there have been a number of studies undertaken into heat transfer to an impinging synthetic air jet certain trends are common to these investigations. Further studies of synthetic jet heat transfer have been carried out by Chaudhari et al. [96], Gillespie et al. [91], and Travnicek et al. [77].

2.6 Summary

A comprehensive review of the literature has been presented for the flow characteristics and evolution of a synthetic jet. Several studies have been performed at specific parameters in order to characterise the synthetic jet velocity, structure, flow control capabilities and heat transfer capacity. It is evident that a synthetic air jet flow is dependent on three crucial parameters in order for a synthetic jet flow to be formed;

1. Dimensionless stroke length (L_0/D), which should be high enough so that the vortex ring that forms can escape the vicinity of the orifice so as it is not ingested back into the cavity.

2. The Stokes number, which should be high enough so that the boundary layer is thin and the shear is high enough to allow for vortex roll up.

3. Reynolds number, based on the jet discharge velocity, orifice diameter and the kinematic viscosity.

A number of these factors may have a specific influence on the flow control and heat transfer capabilities of the synthetic air jet. Although the investigations into synthetic jets have contributed to an improved understanding of the mechanisms associated with this type of flow, there still exists some issues that are unresolved. Most studies conducted have involved fixing one actuation parameter whilst varying another, e.g. fixing stroke length and varying Reynolds number. In the author's view, there exists a need to explore the vorticity and evolution of the synthetic air jet for a broader range

of operational parameters, in order to provide a better understanding of a synthetic air jet; thus this forms the basis of the research presented in this thesis. To the author's knowledge simultaneous measurements of local surface heat transfer and flow in the measurement plane parallel to the impingement surface are absent from the literature. High resolution PIV studies of the evolution of a synthetic jet also appear to be absent from the literature. Further investigation has the potential to reveal more information about the operational mechanisms of a synthetic air jet and its respective flow and heat transfer regimes. The simultaneous measurement of flow visualisation and heat transfer will provide a greater insight into the evolution of a synthetic air jet, as well as helping to elucidate convective heat transfer mechanisms.

Chapter 3

Particle image velocimetry

Early quantitative velocity measurements of fluid flows involved the use of Pitot static tubes, and at a later stage in the experimental history of fluid mechanics, the hot wire anemometer. One of the main disadvantages of these techniques is that they intrude on and in some cases influence the flow itself. The utilisation of lasers in fluid flow measurements led to the development of the laser doppler anemometry (LDA) technique. Although this technique is non-intrusive and represented a major advancement in fluid flow analysis, these techniques all have one disadvantage in common and that is that they provide point-wise measurements, rather than full flow field information. These experimental methods are still invaluable in the analysis of fluid mechanics, but the ability to record images of large parts of flow fields in a wide variety of mediums and to extract velocity information from these is a feature unique to particle image velocimetry (PIV).

Many researchers became interested in the PIV technique when it was first introduced as it offered the potential to study the structure of turbulent flow. Thus, the choices made in the development of the technique were strongly influenced by its potential to understand the phenomenon of turbulence. Due to the nature of turbulence, which extends from the largest scales of flow down to the Kolmogorov scale, a measurement technique capable of measuring over a wide dynamic range of scales in length and velocity was required. The PIV technique is based on the observation of seeding par-

ticles that are carried by the fluid during a short time interval. The seeding particles need to be sufficiently small so that they accurately follow the fluid motion and do not alter the properties of the fluid or its flow characteristics. The seeding particles are illuminated by a thin light sheet, typically generated by a pulsed laser system, thus, they need to be able to reflect enough light so that they can be recorded onto two consecutive image frames by a digital recording device, typically a CMOS camera. In order to obtain high quality PIV data, it is important that the seeding particles used are homogeneously distributed within the measurement region. This is in contrast to flow visualisation methods where fluid tracers are introduced at a specific location, as seen in figure 3.1, a dye flow visualisation of a synthetic jet by Shuster and Smith [11]. When compared to the PIV image seen in figure 3.2 for a synthetic air jet, it can be seen that the seeding is distributed throughout the measurement region in the PIV image, as opposed to being introduced at a specific point.

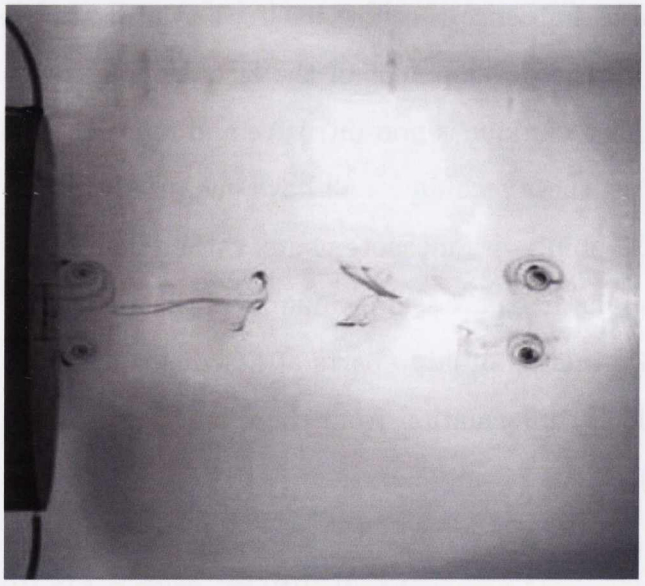

Figure 3.1 – Dye flow visualisation of a synthetic jet, L_0/D=5, Re=1500 [11]

The main advantages of PIV can be summarised as follows:

1. The technique allows for non-intrusive planar measurements of fluid flows to be performed.

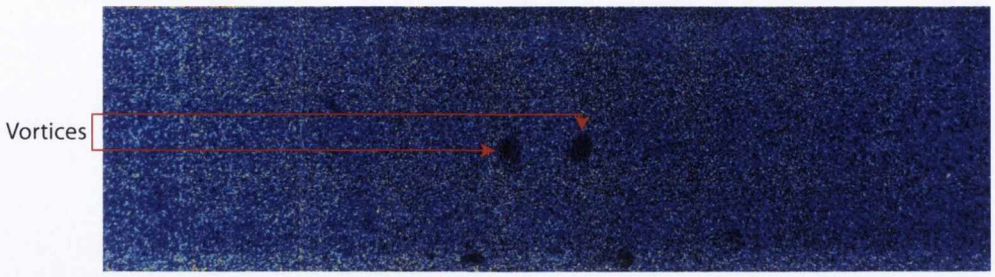

Figure 3.2 – PIV seeding example of a synthetic air jet. H/D=4, L_0/D=4, Re=1500

2. It is a whole flow field technique that has the capability of determining fluid velocity at all locations within the measurement plane simultaneously instead of having to make separate measurements at a series of different point locations.

3. In two dimensional PIV, two velocity components are measured (2D-2C[1]), but use of a stereoscopic approach permits all three velocity components to be recorded (3D-3C[2]), resulting in instantaneous 3D velocity vector maps for the whole measurement volume[3].

The application of digital image processing to flow visualisation techniques was considered a breakthrough. Quantitative and automated analysis of flow images was enabled through the application of digital image processing. Hesselink [97] provides a general review of the application of digital image processing to flow diagnostics. Work completed by Hinsch [98] proposed that a measurement system could be labelled as a (k, l, m) method, where:

1. k = 1, 2, 3 and indicates the number of velocity components measured.

2. l = 0, 1, 2, 3 and indicates the number of spatial dimensions of the measurement domain.

3. m = 0, 1 and indicates whether a measurement yields instantaneous or continuous time recording, respectively.

[1] Two dimensions and two components.

[2] Three dimensions and three components.

[3] Where the measurement volume is within the plane of the laser light sheet.

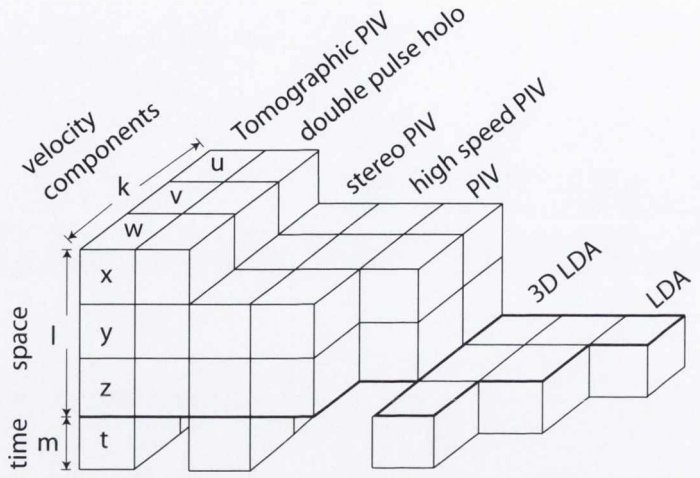

Figure 3.3 – Techniques for optical flow velocimetry and the dimensions of the data space [98]

The best single point measurement techniques are considered a $(3, 0, 1)$ method, in comparison to the simplest form of (2D-2C) PIV, which provides a $(2, 2, 0)$ method. The advancements in technology are leading to the majority of PIV systems employed in the scientific world today offering stereoscopic PIV although, for most flow applications 2D-2C PIV is sufficient. A stereoscopic PIV system is a $(3, 2, 1)$ method that is capable of providing 3D velocity data. The pinnacle in flow velocimetry would be a tomographic PIV system that belongs to the $(3, 3, 1)$ category, in which the velocity vector can be measured throughout a complete volume as a function of time. Figure 3.3 presents a three dimensional layout to better understand the (k, l, m) method as outlined by Hinsch [98].

In order to implement the PIV technique, four basic components are required. They are:

1. A test section with optical access.
2. A light source to illuminate the area of interest.
3. Recording hardware, consisting of a CMOS camera.
4. A computer with the correct software required to process the images and extract velocity information.

3.1 PIV method

The PIV system utilised in this study was supplied by LaVision [99]; it is capable of performing 2D-2C and 3D-3C PIV measurements at high frame rates. A brief discussion of the PIV technique will be outlined here, while the details of the specific system used in this investigation are explained in section 4.1.2. A more in depth synopsis on the technical details, can be found in a comprehensive book on the PIV technique by Raffel et al. [100].

3.1.1 Two dimensional PIV

A schematic of a 2D-2C PIV system is presented in figure 3.4. The digital camera is placed perpendicular to the flow field. The flow field is seeded with seeding particles. The seeding particles used in this study are $2 - 3\,\mu m$ in diameter; the method of generation and the type of seeding are covered in chapter 4. An example of a seeded flow for a synthetic air jet at an axial spacing of H/D=4, and dimensionless stroke length L_0/D=4 and Reynolds number of Re=1500 is presented in figure 3.2. The flow is illuminated in the target area with a laser light sheet. The camera lens images the area of interest onto the CMOS array of a digital camera. The CMOS is able to capture each light pulse in separate image frames. Once a sequence of two light pulses is recorded, the images are divided into small subsections called interrogation windows. A spatial cross-correlation is calculated between the interrogation windows in order to determine the statistically most probable particle displacement for each window. The spatial cross correlation is defined as:

$$R_{I1I2_i}(s) = \iint I1(x)I2(x+s)d^2x \tag{3.1}$$

where,

1. I1 and I2 represent the particle intensities measured by the camera in the first and second images respectively.

2. x is the physical spatial coordinate.

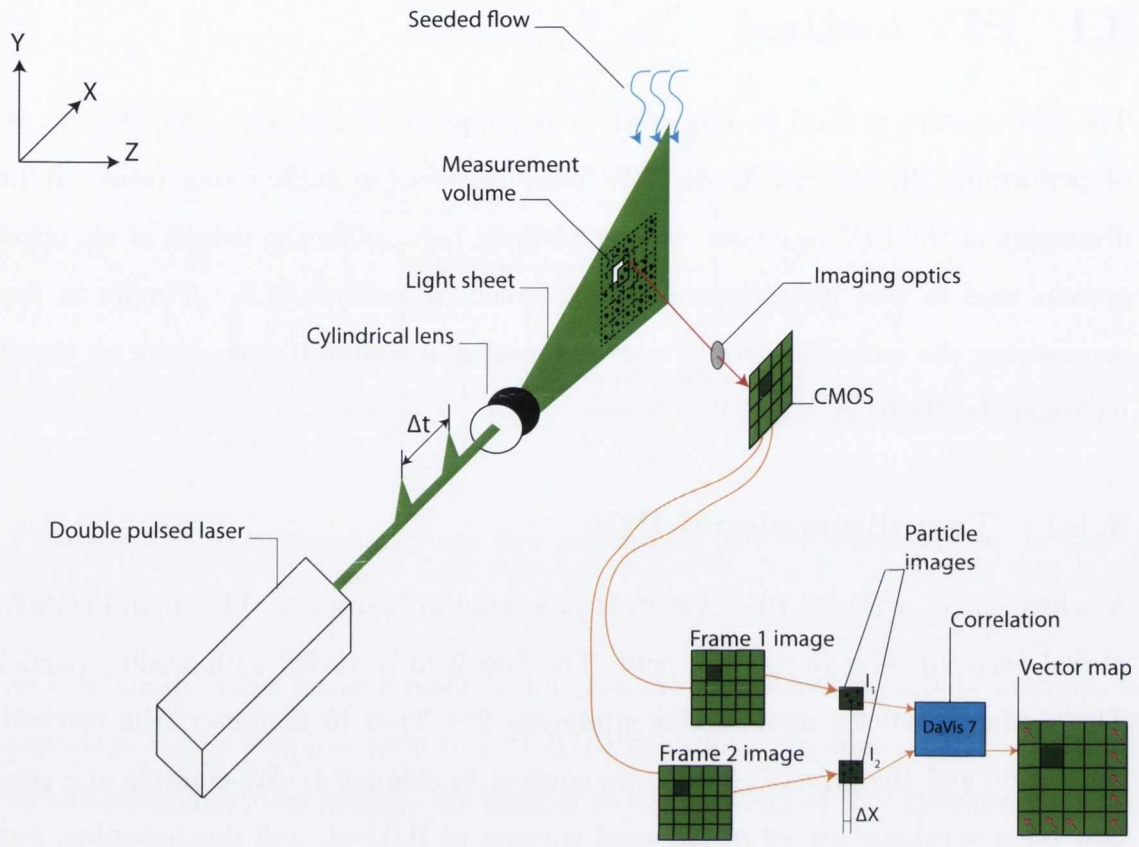

Figure 3.4 – Schematic of a digital PIV system.

3. s is the spatial coordinate in the correlation plane [101]

The interrogation windows from each image frame are cross correlated with each other, pixel by pixel. Seen in figure 3.5 is the correlation map. This consists of several peaks; the largest of these peaks is determined using a peak searching algorithm and corresponds to the most probable particle displacement. The signal to noise ratio in the correlation map of figure 3.5 is high and this is the most desirable outcome as it ensures there is a high level of confidence in the vector velocity that is calculated. A velocity vector map over the whole target area is obtained by repeating the cross correlation for each interrogation window over the two image frames captured by the CMOS digital camera. Recording both light pulses in the same image frame to follow the movements of the particles gives a clear visual sense of the flow structure. Nearly any particle that follows the flow satisfactorily and scatters enough light to be captured by the CMOS camera can be used. The number of particles in the flow is of some importance in

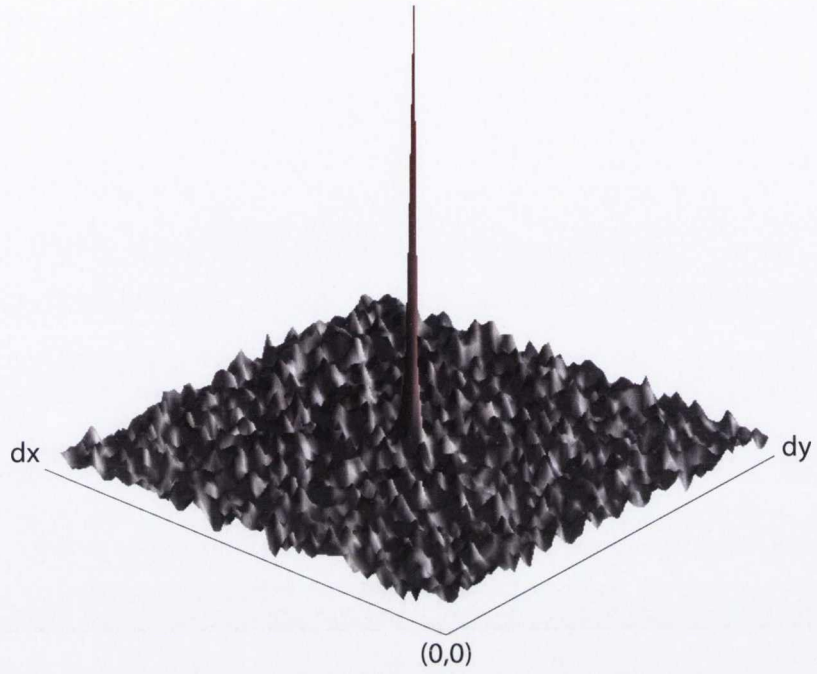

Figure 3.5 – Typical cross-correlation map between two interrogation windows of I1 and I2, the peak corresponds to the most probable particle pixel displacement

obtaining a good signal peak in the cross-correlation, along with several other factors such as the illumination, the interrogation window size, and the algorithms used to solve the cross correlation. As a rule of thumb, approximately 10 to 25 particle images should be seen in each interrogation window.

The time separation between the two images, Δt is chosen in conjunction with the size of the interrogation window. In order to obtain reliable velocity vectors, most particles captured in the first image should be in the interrogation window when the second image is captured. The cross correlation is a statistical process, and as a guide, the maximum particle displacement allowed between two pulses must not be bigger than a quarter of the interrogation window. A ratio between the distance measured in pixels on the CMOS sensor and the physical distance measured in the area of interest is required in order to translate the velocities in pixels per second on the CMOS sensor to a metres per second value in the measurement plane. The ratio, also known as the scale factor (S), is obtained from the calibration process.

The pixel displacement values of the particle corresponding to the largest correlation peak from the origin of the map seen in figure 3.5 in the x and y directions are dx and dy respectively. Combining these with dt, the time separation between the two images, the most probable components of the vector velocity in the interrogation window u and v are calculated. Thus, the velocity components for the x and y direction are expressed as $u = dx/dt$ and $v = dy/dt$ respectively. Assembling the most probable particle displacement (dx and dy) and the most probable velocity vector (u and v) from the image plane, results in the formation of a velocity vector map of the entire flow field. The magnitude of the velocity components is then expressed as follows:

$$V(x,y) = \sqrt{u(x,y)^2 + v(x,y)^2} = \frac{\sqrt{dx(x,y)^2 + dy(x,y)^2}}{dt} \tag{3.2}$$

These data can then be exported for further processing in Matlab using purpose written code to calculate values such as vorticity and streamlines. It is worth noting that the software used in this study DaVis 7.2.2 [102] can achieve a pixel displacement accuracy as high as $0.05\,px$ [103]. With the correct setup, a high spatial resolution can be achieved, making the PIV technique a valuable tool in fluid mechanics research. Calculation of vorticity can be a complicated process, but the way in which PIV data are stored in regular, uniform type grids, which are fundamentally two dimensional, facilitates the calculation of the differential field quantities such as vorticity with relative ease. Equation 2.1 shows the basic form of equation used to calculate vorticity, but for a 2D-2C PIV system, the out of plane vorticity is expressed as follows:

$$\omega = \frac{\partial v}{\partial x} - \frac{\partial u}{\partial y} \tag{3.3}$$

In the DaVis system, for example, the vorticity at any point is calculated according to the central difference scheme based on the velocity components of its four closest neighbours. A first order central difference scheme can be used to estimate the out of plane vorticity [100], [104].

$$\omega_{i,j} = \frac{v_{i+1,j} - v_{i-1,j}}{2\Delta x} - \frac{u_{i,j+1} - u_{i,j-1}}{2\Delta y} \tag{3.4}$$

where,

- i and j are the indices of the mesh points of interest in the x and y directions respectively.

Raffel et al. [100] proposed the use of an alternate algorithm to calculate vorticity based on Stokes' theorem, whereby the vorticity and circulation in a flow are related to each other through:

$$\Gamma = \oint \mathbf{U} \cdot d\mathbf{l} = \int \nabla \times \mathbf{U} \cdot d\mathbf{S} = \int \omega \cdot d\mathbf{S} \tag{3.5}$$

This expression states that the circulation around a closed contour is equal to the sum of the vorticity enclosed within that contour. Stokes theorem can also be applied to a regularly spaced PIV grid. Thus, equation 3.5 becomes:

$$\bar{\omega}_{i,j} = \frac{1}{A}\Gamma_{i,j} = \frac{1}{A} \oint_{\mathrm{l}(X,Y)} (U, V) \cdot d\mathbf{l} \tag{3.6}$$

Where $\bar{\omega}_{i,j}$ is the average vorticity within an enclosed area A. The rectangular contour of data points presented in figure 3.6 represents a mesh of velocity vectors that is used to implement equation 3.6. The circulation (Γ) around the boundaries of the square is calculated using a standard integration scheme such as the trapezoidal rule. The average vorticity is calculated by dividing the the total circulation by the enclosed area, as indicated in equation 3.7.

$$\bar{\omega}_{i,j} \approx \frac{\Gamma_{i,j}}{4\Delta X \Delta Y} \tag{3.7}$$

Where ΔX and ΔY represent the grid spacings seen in figure 3.6. Thus, $4\Delta X \Delta Y$ indicates that the contour spans the four cells seen in figure 3.6. The integration around the path of the contour is completed using the trapezoidal method [100], and

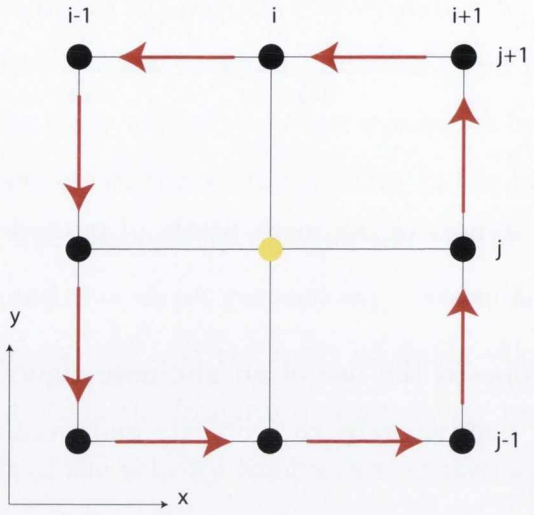

Figure 3.6 – Grid used to calculate vorticity based on the velocity components of its four closest neighbours

based on its height and width of two mesh points respectively, the estimated circulation is expressed as the circulation method:

$$\begin{aligned}\Gamma_{i,j} = &\frac{1}{2}\Delta X(U_{i-1,j-1} + 2U_{i,j-1} + U_{i+1,j-1}) \\ &+\frac{1}{2}\Delta Y(V_{i+1,j-1} + 2V_{i+1,j} + V_{i+1,j+1}) \\ &-\frac{1}{2}\Delta X(U_{i+1,j+1} + 2U_{i,j+1} + U_{i-1,j+1}) \\ &-\frac{1}{2}\Delta Y(V_{i-1,j+1} + 2V_{i-1,j} + V_{i-1,j-1})\end{aligned} \tag{3.8}$$

There are 12 separate velocities over 8 different data points used to calculate the circulation of equation 3.8. Equation 3.7 is based on the central difference method and when the circulation method result of equation 3.8 is inserted into equation 3.7, the vorticity at any point (i, j) on a velocity grid can be calculated from the velocity vector components of the flow. Vorticity calculated by equation 3.4 uses only 4 neighbouring data points, whereas equation 3.7 utilises 8 data points. As such, the uncertainty in the estimate of the vorticity using the central difference scheme is much greater [100]. It is worth noting that Westerweel [104] found the circulation method in equation 3.8 to be more accurate than the central difference scheme.

For the present study, the vorticity plots presented in chapter 5 were post processed vector maps exported from DaVis and purpose written Matlab code based on equation 3.8 was used to calculate vorticity, streamlines, and velocity.

3.1.2 Three dimensional PIV

Two dimensional PIV is only capable of recording the velocity vectors in the plane of the light sheet while the out-of-plane velocity component is lost. Stereoscopic PIV is capable of recording these three velocity components (in-plane and out-of-plane). The schematic of a stereoscopic PIV setup is presented in figure 3.7. Employing a second camera to record from a different viewing angle for setting up a 3D PIV system is considered to be the most straightforward method [105], [106], [107].

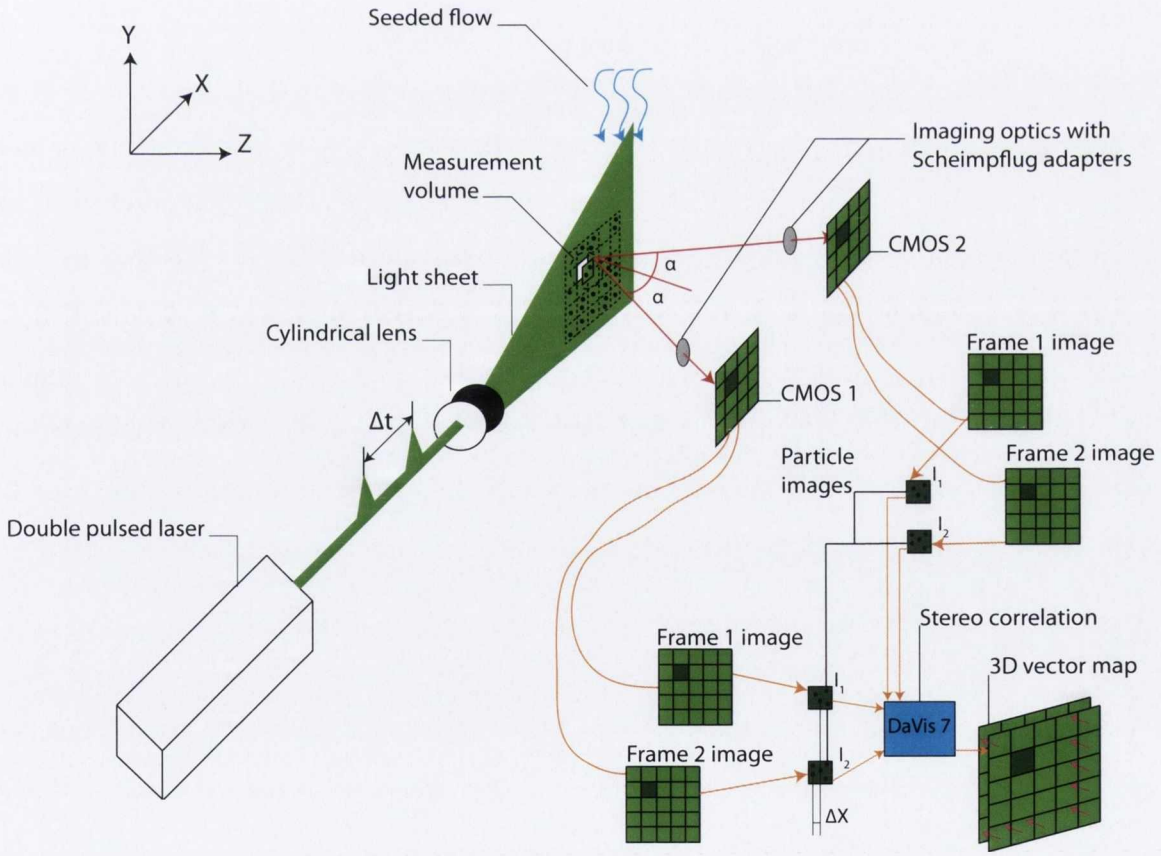

Figure 3.7 – Schematic of a stereoscopic digital PIV system

Visual access to the area of interest will govern the camera configuration. There are several different possibilities of arranging the cameras in a stereoscopic PIV system.

The method employed for the 3D PIV used in this study is known as backward forward-scattering. In this setup the cameras are mounted on the same side of the light sheet, as seen in figure 3.8.

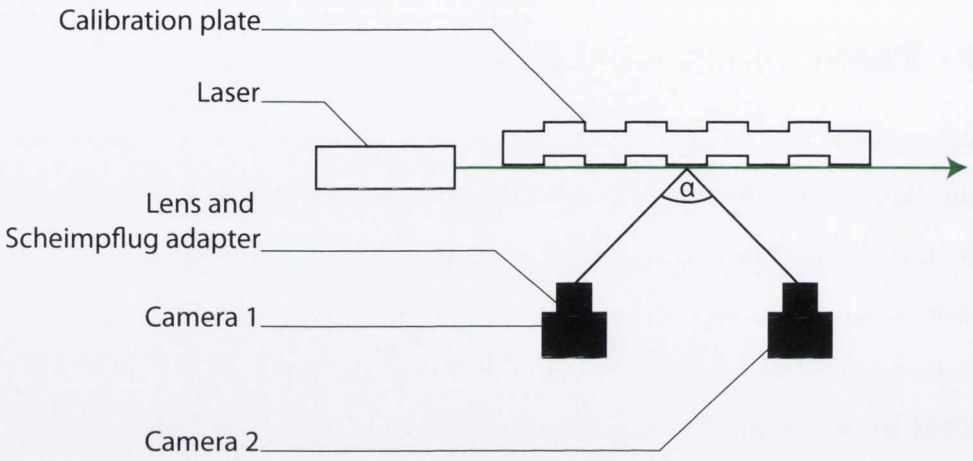

Figure 3.8 – Backward forward-scattering 3D PIV

Camera 1 typically records the light scattered in the forward direction while camera 2 will record the light scattered in the backward direction. The light intensities are slightly different for both cameras i.e. camera 2 will need a larger aperture in order to increase the light intensity it receives so that the PIV image it records will be as close as possible to that of camera 1. There are a required and recommended number of views when setting up a 3D PIV experiment. For the backward forward-scattering setup as seen in figure 3.8 the system type was classed as a camera mapped for 3D vectors, requiring 2 cameras and for the views to be coplanar and equidistant.

3.1.2.1 Scheimpflug criterion

According to research completed by Prasad [105], to obtain images in good focus over the entire image plane, the Scheimpflug criterion must be satisifed. This criterion requires the object plane, the lens plane and the image plane to be colinear, see figure 3.9. If the angle α between camera 1 and camera 2 is increased, the measurement precision of the out-of-plane component is increased. Increasing this angle (α) between the two cameras limits the depth of field, to overcome this, tilting of the image plane in respect to the orientation of the camera lens brings more of the field of view into focus

while keeping the object, lens and image planes colinear. It is worth noting that in general a tilted object or image plane will cause what is known as keystone distortion to occur, this is because of the magnification varying across the field of view. This results from the variation of object and image distances from top to bottom of the field. This distortion is often seen in over-head projectors when the top mirror is tilted to raise the image projected on the screen. This is equivalent to tilting the screen. Keystone distortion can be prevented by keeping the plane of the object effectively parallel to the plane of the image [108].

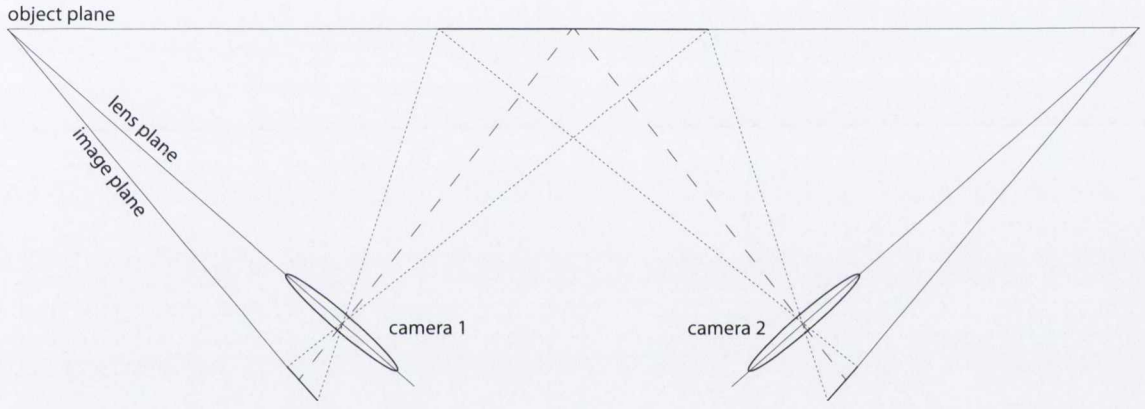

Figure 3.9 – Scheimpflug criterion

3.1.3 Vector processing

Vector field computation for 2D-2C and 3D-3C PIV in the current study was completed using a multi-pass cross-correlation technique with an interrogation window size decreasing from 64 × 64 pixels with a 50% overlap down to 32 × 32 pixels with a 75% overlap. The PIV parameters for vector field computation for 3D PIV works in exactly the same way as conventional 2D PIV except that the correlation mode needs to be set to stereo cross-correlation. The cross-correlation for 2D PIV is outlined below.

The cross-correlation calculates a vector field on two single exposed images. Figure 3.10 presents the cross-correlation technique used as one of the vector calculation parameters. Using the cross-correlation mode the original PIV image consists of two

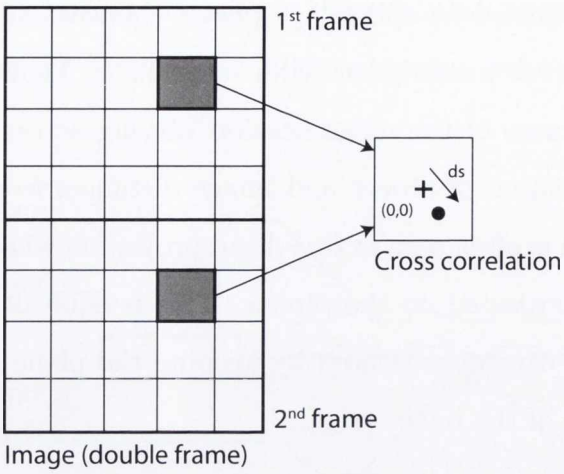

Figure 3.10 – PIV cross-correlation

frames (1^{st} frame and 2^{nd} frame). The first frame is labelled as frame 0 and contains the 1^{st} exposure, whilst the second frame labelled as frame 1 contains the 2^{nd} exposure. The algorithm used calculates the cross-correlation of all the interrogation windows between frame 0 and frame 1. The displacement vector *ds* is most likely the highest peak in the cross-correlation image. There is no peak at the zero displacement (0,0).

For the window size and weight, a rectangular size of 64 × 64 pixels was selected with a 50 % overlap decreasing to a 32 × 32 pixels with a 75 % overlap. During a multi-pass interrogation such as this, the initial interrogation window size (CMOS sensor=1024 × 1024 pixels) is divided by two in each step until the final interrogation window size is reached.

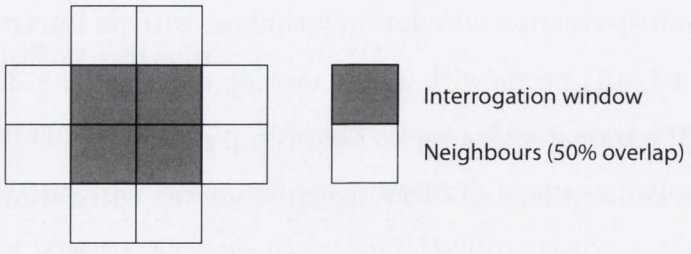

Figure 3.11 – A 50% interrogation window overlap example

Figure 3.11 presents an example of the overlap amongst neighbouring interrogation windows for a 50% overlap. The interrogation window size and the window overlap

will ultimately determine the result of the vector grid size i.e. the spacing between two neighbouring vectors in the vector field e.g. a window size of 64×64 pixels with an overlap of 50% will result in a grid size of 32 pixels.

Iterations using the multi-pass (decreasing window size) procedure calculate the vector field by an arbitrary number of iterations N_x with an interrogation window size that decreases after each consecutive pass. The first pass is selected e.g. 64×64 pixels, and a reference vector field is calculated. In the next pass the window size is halved and the vector calculated in the first pass is used as a best choice window shift. This results in a window shift that is adaptively improved to compute the vectors more reliably. This allows for a much smaller final interrogation window size than is possible without the adaptive window shifting that multi-pass decrease uses. Not only does this technique produce fewer erroneous vectors, it also improves the spatial resolution of the vectors.

3.1.3.1 Stereo cross-correlation

The stereo cross-correlation mode stores the double images of both cameras in one file in the sequence as outlined and seen in figure 3.12.

- frame 0=camera 1 (1^{st} exposure)
- frame 1=camera 1 (2^{nd} exposure)
- frame 2=camera 2 (1^{st} exposure)
- frame 3=camera 2 (2^{nd} exposure)

There are different approaches for stereo vector field computation as proposed by Prasad [105]. Calculation of a stereo vector field begins with the calculation of 2D-2C vector fields for each camera from which a stereoscopic reconstruction of a 2D-3C vector field is computed. To view a 3D-3C vector field an option has to be selected in the DaVis [102] user interface.

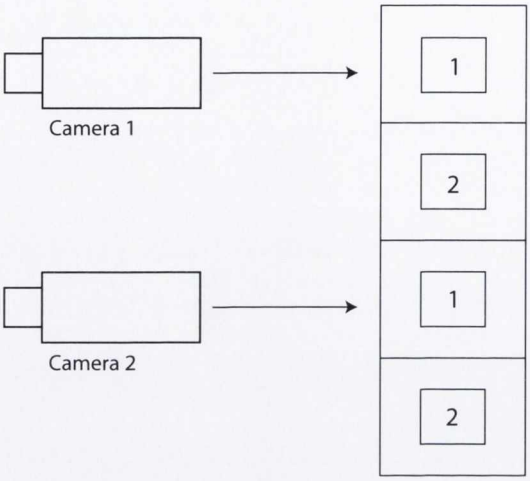

Figure 3.12 – Frame order in image buffer using stereo cross-correlation mode

3.1.3.2 PIV uncertainty

Figure 3.13 presents what is commonly referred to as a raw PIV image. The seeding in this PIV image shows good, homogeneous seeding density throughout the measurement plane; the illumination of the seeding particles is fairly homogeneous as well. There are many factors that determine the accuracy of any PIV measurement, with the distribution of the seeding and its illumination being two of the factors that can determine this accuracy.

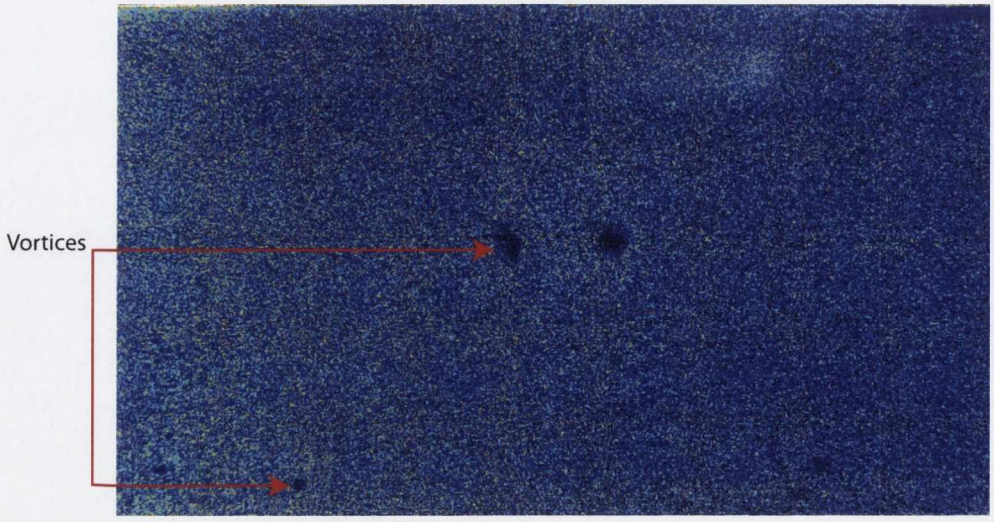

Figure 3.13 – A raw PIV image, illustrating homogeneous seeding

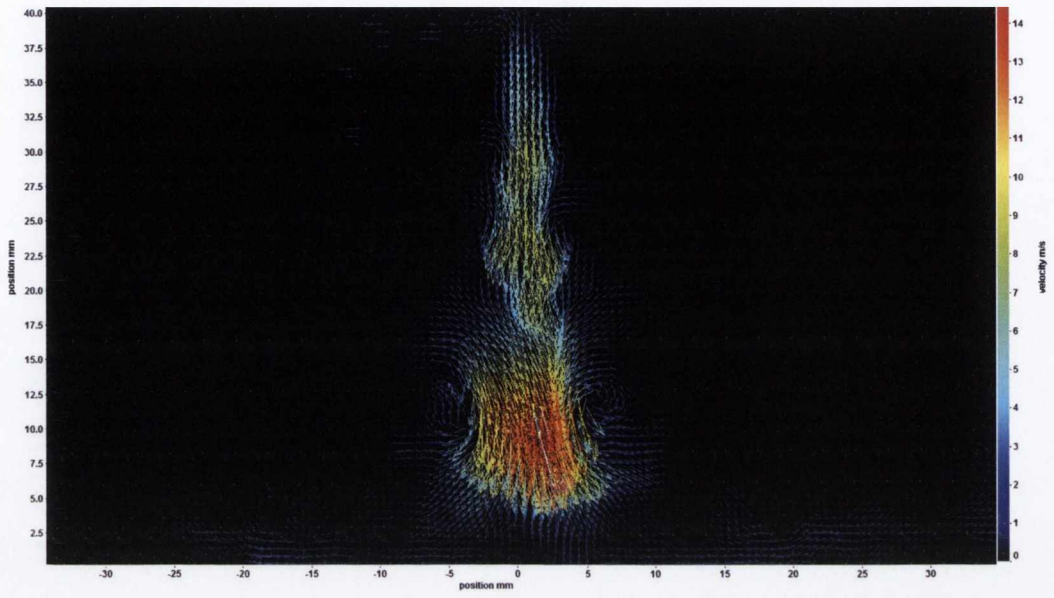

Figure 3.14 – Velocity vector plot example, H/D=8, Re=1500, L_0/D=12

The vector field presented in figure 3.14 was calculated using the multi-pass decreasing interrogation window of 64 × 64 pixels with a 50% overlap to a 32 × 32 pixels with a 75% overlap. This processing regime was found to give the highest number of accepted vectors for the experimental setup. The average number of rejected or missing vectors was less than 5% and the removed vectors were interpolated for. Raffel et al. [100] refer to a 'bias error' [109] in the calculated vectors as "peak-locking" and this term is used to describe a displacement bias error that has a periodic pattern on pixel intervals. The presence of the "peak-locking" effect can be detected in the flow field calculations by plotting a histogram of the seeding particle displacements. The source of this effect can arise from insufficient particle image size being captured on the CMOS sensor; in most cases it occurs when the particles are smaller than 3 pixels. Figures 3.15 and 3.16 present histograms of the pixel displacement in the u velocity component direction. Figure 3.15 presents a histogram that shows no sign of "peak-locking" occurring, which suggests that the random variation in the data is smaller than any systematic bias in the system. The "peak-locking" coefficient of the histogram in figure 3.15 is ζ=0.0083; this was calculated with DaVis 7.2.2. LaVision suggest that the acceptable limit for the "peak-locking" coefficient is $\zeta < 0.1$. The histogram seen in figure 3.16 is provided for a direct comparison and is the result of an experiment specifically set up to produce

a "peak-locking" effect. For the PIV data presented in this study, prior to performing each experiment a quick calculation was performed to ensure there was no occurrence of a "peak-locking" effect. The uncertainty error of the LaVision PIV algorithm can be estimated to be between 0.05 pixels and 0.06 pixels [103]. As such this is an estimate for an experimental best case scenario. The average error achieved by numerous manufacturers of PIV systems, according to experimental data in work completed by Stanislas et al. [103], is estimated to be approximately 0.1 pixels for the PIV algorithm.

To avoid loss of correlation due to excessive in-plane displacement, Keane and Adrian [110] stated that a pixel shift in the initial interrogation window should be smaller than one quarter of the interrogation window size. Using the one quarter rule, between image pairs the initial interrogation window was defined to be between 5 pixels and 7 pixels. The calibration of the cameras was always within the suggested levels by the manufacturer together with the assumption that the error estimate ≈ 0.1 pixels, suggest that the PIV calculations have an associated uncertainty of $\approx 2\%$.

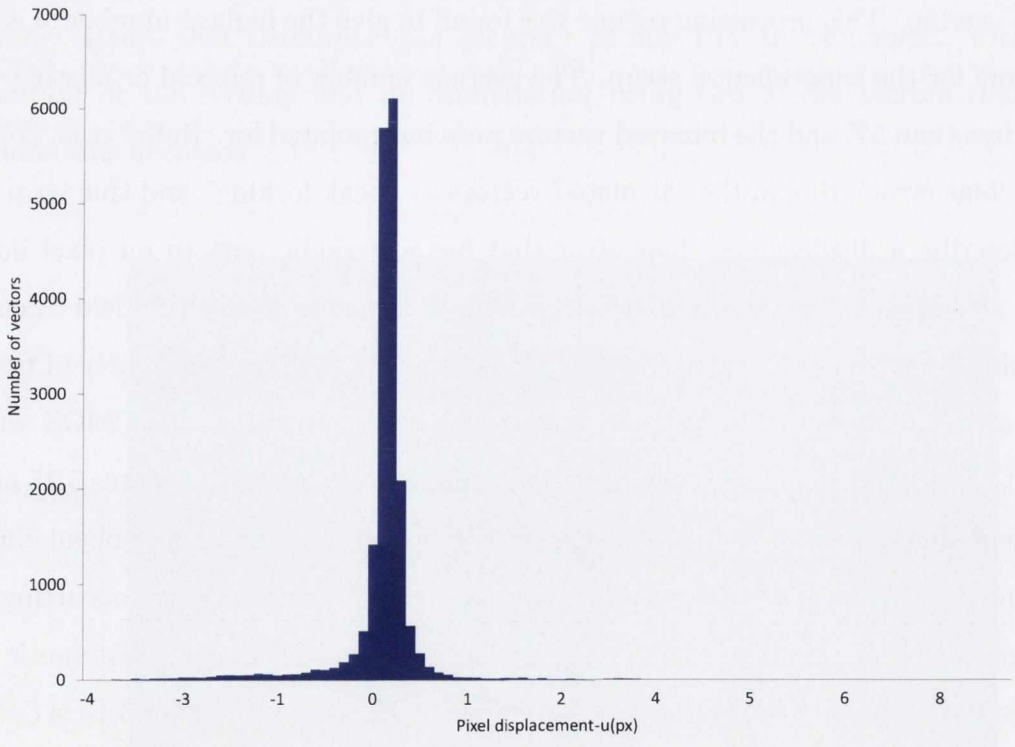

Figure 3.16 – Histogram of PIV displacement data in the u component direction. Strong "peak-locking" - $\zeta = 0.43$

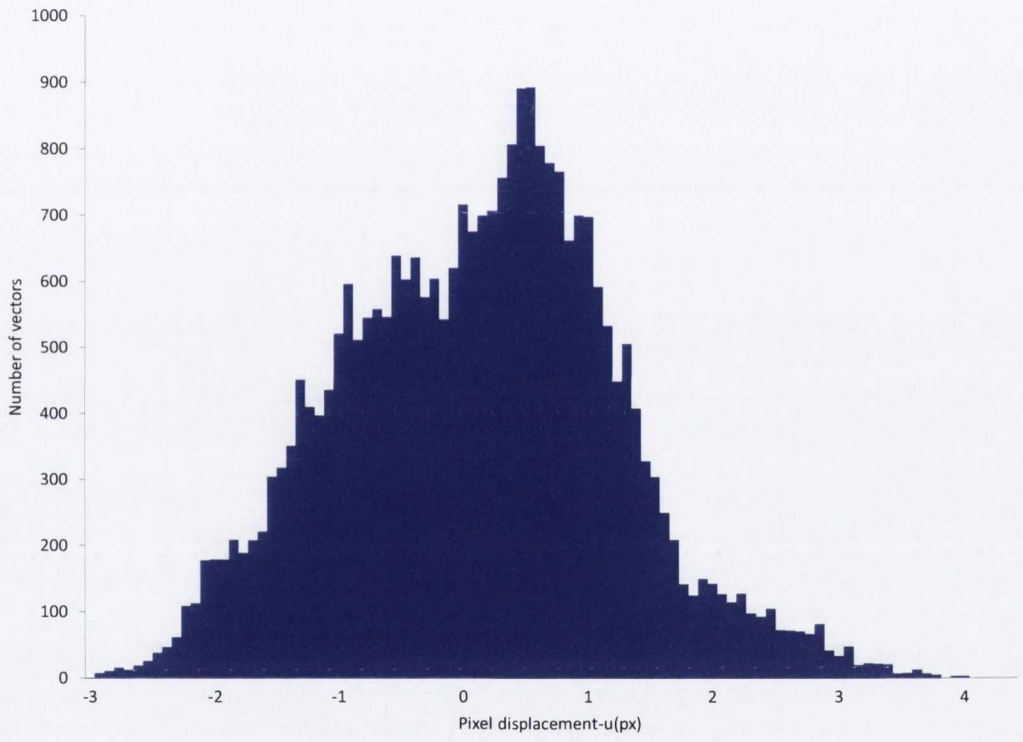

Figure 3.15 – Histogram of PIV displacement data in the u component direction. No "peak-locking" - $\zeta = 0.0083$

Chapter 4

Experimental apparatus

The experimental rig used in this study has been used in previous studies by O'Donovan [94] for steady jet impingement heat transfer research and McGuinn [7] for synthetic jet heat transfer research. The rig provides the following:

1. An impingement surface that can be heated and moved in a controlled manner that is accurate and repeatable
2. A carriage to mount and move the synthetic jet actuator in accurate steps, perpendicular to the impingement surface.
3. A computer model to input the operational parameters of the synthetic jet that was to be generated.

Changes were made to the experimental rig to advance its capabilities with regard to fluid velocity measurements with the use of particle image velocimetry (PIV). The rig had to allow for the recording of high resolution, high frame rate two dimensional particle image velocimetry of the synthetic jet, and utilise stereoscopic PIV to measure the fluid velocity in an axial plane parallel to the heated impingement surface, synchronised to the surface heat transfer.

This chapter details the equipment used to achieve these experimental goals and how the individual components are arranged in the experimental setup. The calibration process for the particle image velocimetry measurements in the two dimensional and

stereoscopic orientation is described, as are the uncertainty estimation for the measurements and the experimental procedure.

4.1 Experimental setup

The experimental rig is primarily constructed to perform heat transfer measurements from several types of impinging jets i.e. steady [58], synthetic and swirl [111] jets. The focus of this study is a synthetic jet. The carriage that the synthetic jet actuator is mounted on has a lead screw that is capable of moving the actuator perpendicularly to the impingement surface with a high degree of control and accuracy; this provides the y axis movement. Gillespie et al. [91]reported that the maximum heat transfer to an impinging synthetic jet is typically at a jet to impingement surface spacing of 8 to 12 jet diameters. The heated impingement surface is attached to a lead screw controlled by a stepper motor in order to provide accurate movements in the x axis. The main support structure of the rig is made from $45mm \times 45mm$ cross section Rexroth aluminium structural members. This main support is used to mount the heated impingement test surface, high speed cameras, the PIV laser guide arm and the synthetic jet actuator. An image of the experimental rig, without the particle image velocimetry apparatus is shown in figure 4.1.

4.1.1 Synthetic jet

The synthetic jet velocity calculation has been described in section 2.4.2 and is dependent on the jet Reynolds number and the dimensionless stroke length, L_0/D; however the components that make up the synthetic jet actuator put a constraint on the maximum average jet velocity U_0. The synthetic jet generator used in this research is a coil and magnet Visaton FR-8 loudspeaker that has a 10 W power output rating; the coil is the driving mechanism and the cone forms the oscillating diaphragm. The frequency range of the speaker extends up to $20kHz$, although synthetic jet formation does not occur much beyond a frequency of $940Hz$ due to a diminished stroke length. In this case a minimum stroke length for synthetic jet formation has been documented in the

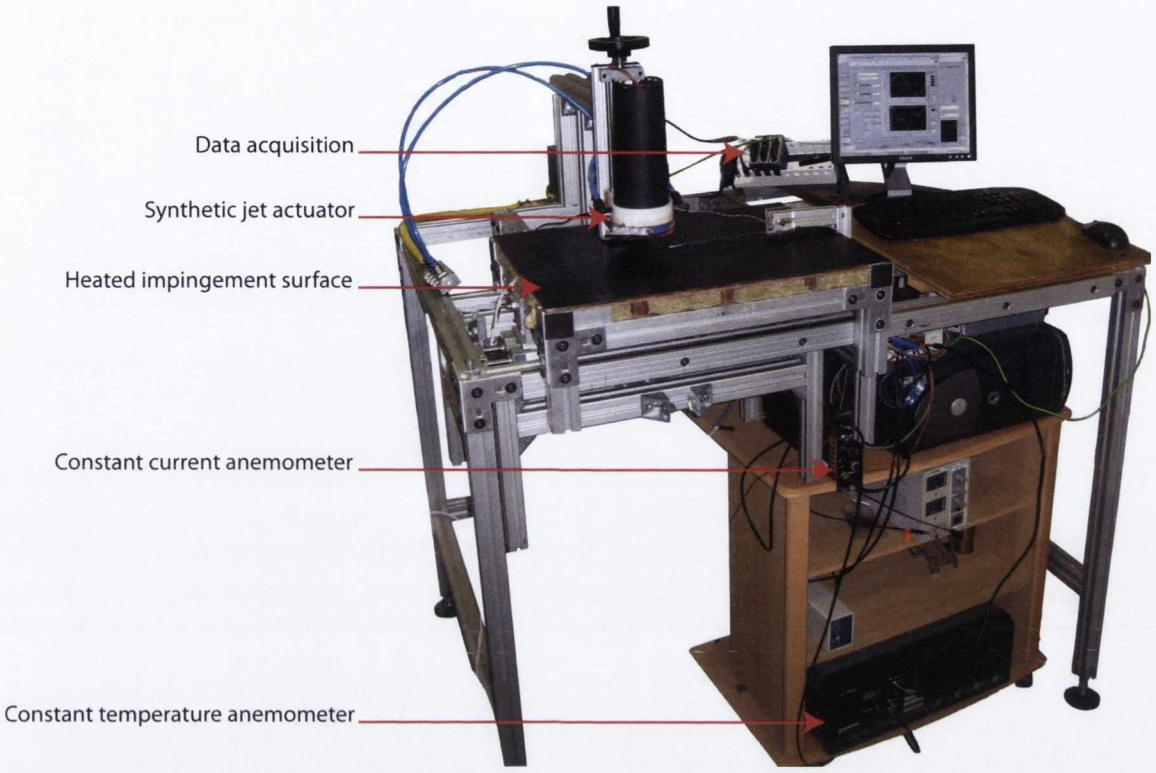

Figure 4.1 – Experimental rig without PIV apparatus

literature at $L_0/D \approx 4$ [24]. The operational limit of the loudspeaker utilised in this research is considered to be when the output signal undergoes distortion, i.e. when the observed output signal undergoes clipping [112].

There are several key factors to consider when designing a synthetic jet, these are the nozzle diameter, nozzle length and the design of the cavity. Presented in figure 4.2 is a schematic of the synthetic jet actuator and in figure 4.3 an AutoCAD rendering. The orifice has a diameter of $D = 5$ mm and a length of $l_o = 10$ mm. The loudspeaker utilised in this synthetic jet is relatively large and coupled with the simple orifice geometry, a wide range of operational parameters can be achieved. From figure 4.2 it can be seen that the cavity diameter is $D_c = 75$ mm; the cavity height inclusive of the speaker cone is $h_c = 26.4$ mm. The orifice plate has a diameter of $D_{op} = 100$ mm, which provides a large degree of flow confinement when the nozzle is placed close to the impingement surface. The cavity volume is $V_c = 101.5\ cm^3$, which results in a Helmholtz resonance of 485 Hz.

It should be noted that when performing time averaged PIV testing, which is long duration testing, there was a small but pervasive cross flow present in the testing environment as a result of the necessary health and safety ventilation ports required in any test environment. The Reynolds number of this cross flow was estimated from the PIV data to be approximately $Re \approx 80$, from this it can be concluded that at the low Reynolds number time averaged experiments, the effect of the cross flow will be relatively small in comparison to the main jet flow. Although all care was taken to minimise the effect of this cross flow, it has a small but noticeable effect on the time averaged flow fields presented in section 5.2 for high axial spacing and low stroke length, L_0/D.

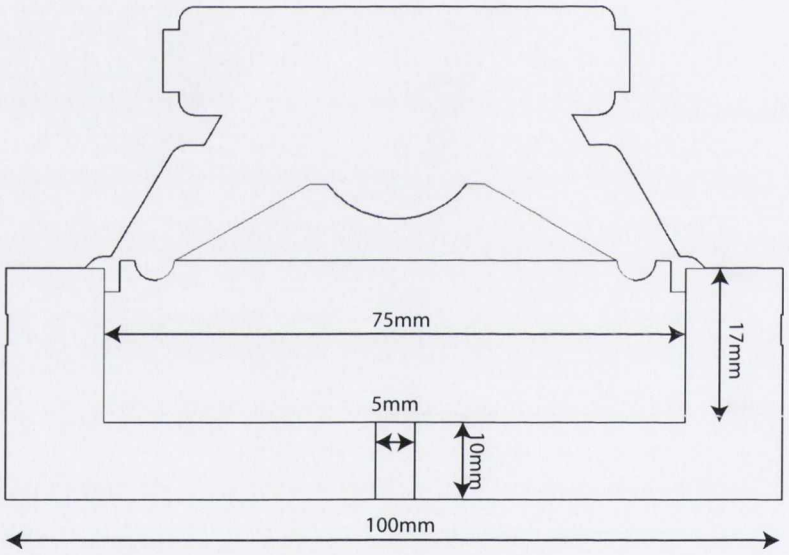

Figure 4.2 – Schematic of the synthetic jet actuator

4.1.2 Particle image velocimetry system

Particle image velocimetry (PIV) has been used extensively throughout this research, to provide flow visualisation and velocity measurements of the synthetic air jet. A complete PIV system consists of several specialised components, namely a high speed laser system, high speed cameras, data acquisition system and complex processing software. The PIV process is based on using the motion of the seeding particles which are assumed to follow the flow to calculate vectors. By measuring the displacement of par-

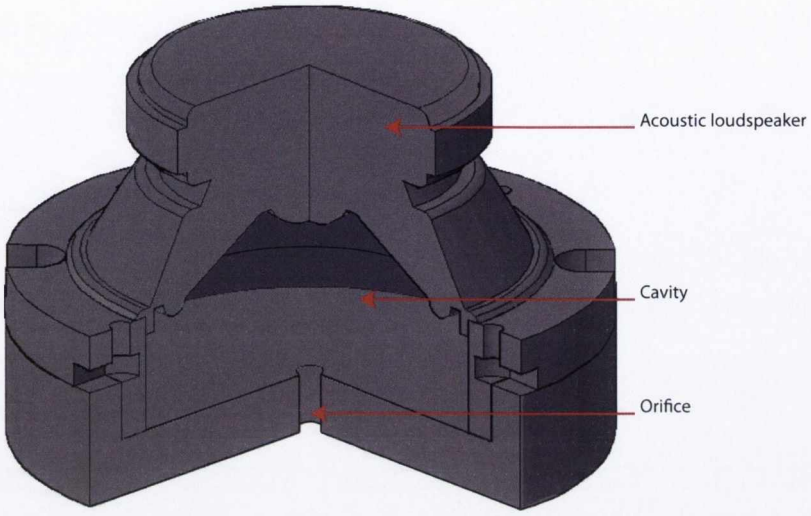

Figure 4.3 – AutoCAD rendering of the synthetic jet actuator

ticles within an interrogation window between subsequent camera frames of a known time separation, a correlation relating to the velocity of the particles is calculated, and hence the fluid velocity can be calculated. The application of these calculations across the area of interest between two subsequent frames will provide an instantaneous velocity measurement of the entire flow field; this technique can be repeated for a series of frames to provide a time series evolution of the flow velocity. A schematic of a typical digital PIV setup is shown in figure 3.4.

The manufacturer LaVision [99] supplied the overall system that is capable of two dimensional PIV, shadowgraphy and high speed stereoscopic PIV. The laser system utilised is a Quantronix Darwin-Duo [113] with two high repetition Nd:YLF laser crystals (Neodymium:yttrium lithium fluoride, $\lambda = 527\,nm$, 0.1-0.3 J/s at 1000 Hz). These crystals are installed within one laser body with a beam combining system; this allows for short duration, high frequency pulses up to 4700 Hz, with a minute time separation, $\Delta t \approx 6\,\mu s$. A laser guide arm, which is attached to the laser head, guides the light beam to the light sheet optics and to the experimental apparatus, where the beam is focused to achieve the thinnest light sheet possible, with a beam waist of approximately $1mm$ in the measurement plane. The seeding is critical to accurate PIV; the seeding particles should follow the flow faithfully. The seeding particles used can

determine the accuracy of PIV results in two ways; (i) the testing environment needs to be correctly seeded in order for the light sheet to illuminate the flow correctly, and (ii) the camera needs to be correctly focused on the particles in order to provide good images for the PIV calculation. The seeding used in this study was generated from a pea soup Colt 4 [114] portable smoke generator, which uses an oil based aerosol to produce seeding particles of $0.2 - 0.3\,\mu m$ in diameter.

The cameras used to capture the seeding produced by the Colt 4 generator are high speed CMOS (Complimentary metal-oxide-semiconductor) digital cameras manufactured by Photron [115]. The cameras are the Fastcam SA1.;, this camera provides true 12-bit performance, with a capability of over 5000 Hz at mega pixel resolution ($1K \times 1K$). Coupled with 8GB of on-board memory, up to six seconds of recording at full resolution can be accomplished. Upon capturing the images of the flow field, these data are transferred to the computer that will then process the raw images using LaVision's DaVis 7 software [99], which uses algorithms specifically designed to calculate the vectors necessary for flow field analysis. The vector calculation process is explained in chapter 3.

Figures 4.4, 4.5 and 4.6 present a 2D-2C PIV test setup. For this setup one of the Photron high speed cameras is mounted on a tripod and is oriented perpendicular to the laser light sheet. The light sheet optics are set up so that the synthetic jet flow is bisected. This is done in order to produce PIV results of the synthetic jet that are axisymmetric. Figures 4.5 and 4.6 show a test setup of 2D-2C PIV with the laser system on. The black card attached to the synthetic jet actuator body is there to mask out regions that are not required in the area of interest[1], and to divert reflections from the camera. This masking technique seen in figures 4.5 and 4.6, although crude, is very effective as it serves a double purpose here. Firstly, it prevents laser light from reflecting into the camera, which could damage the CMOS sensor, and secondly, as the laser light is very powerful, over extended test periods it tends to burn the cavity body

[1] This type of masking reduces the post processing time as the possibility of stray particles being recorded is reduced.

of the synthetic jet actuator; this black card aids in preventing this from occurring.

Through trial and error, the correct lens setup was selected to provide high quality PIV images. The optimum setup requires as much light as possible to enter the lens without damaging the CMOS sensor of the camera, whilst still retaining a good focus on the seeding particles. The lens setup selected for the range of PIV testing carried out, both 2D-2C and 3D-3C testing, was a 50mm, $f/1.4$D Nikon lens, chosen for its extremely low image distortion properties. This means that straight, parallel lines recorded remain straight and parallel in the image. Larger lens apertures allow more light to reach the sensor but smaller apertures ensure a greater depth of field[2]. The lens aperture is set to $f/4$ and this provided a suitable compromise between depth of field and lighting. The seeding particles in the field of view were observed to remain sharp and in focus at the two axial spacings of H/D=4 and H/D=8. The lens was then mounted to a $12\,mm$ extension tube, which essentially converts the lens to a macro lens. This is done to magnify and reduce the field of view that a 50 mm lens usually captures, while still retaining the aperture opening of $f/4$. This setup worked extremely well as it provided the high quality PIV data presented in chapter 5. An example of the focus on the seeding particles achieved with this lens configuration is shown in figure 4.7.

The setup used for the stereoscopic PIV testing is presented in figures 4.8, 4.9, 4.10 and 4.11. A schematic of the stereoscopic setup is presented in figure 4.8, which shows the angle of tilt of the cameras and their height above the impingement surface. Setting up the cameras prior to calibration involved tilting the cameras at the correct angle (35°)[3], so that when the Scheimpflug adapters were mounted to the cameras

[2] The depth of field refers to the range that will be in focus for a particular focus setting. The distance from the lens to the subject is known as the focus, the depth of field is plus and minus a percentage of this. A large depth of field results in objects that are closer or further away from the subject being in focus, while a small depth of field ensures only the subject will be in focus, everything further or closer away will be out of focus.

[3] The tilt angle for the cameras was decided upon from trial and error, i.e. several configurations had to be tested before the optimum setup was found.

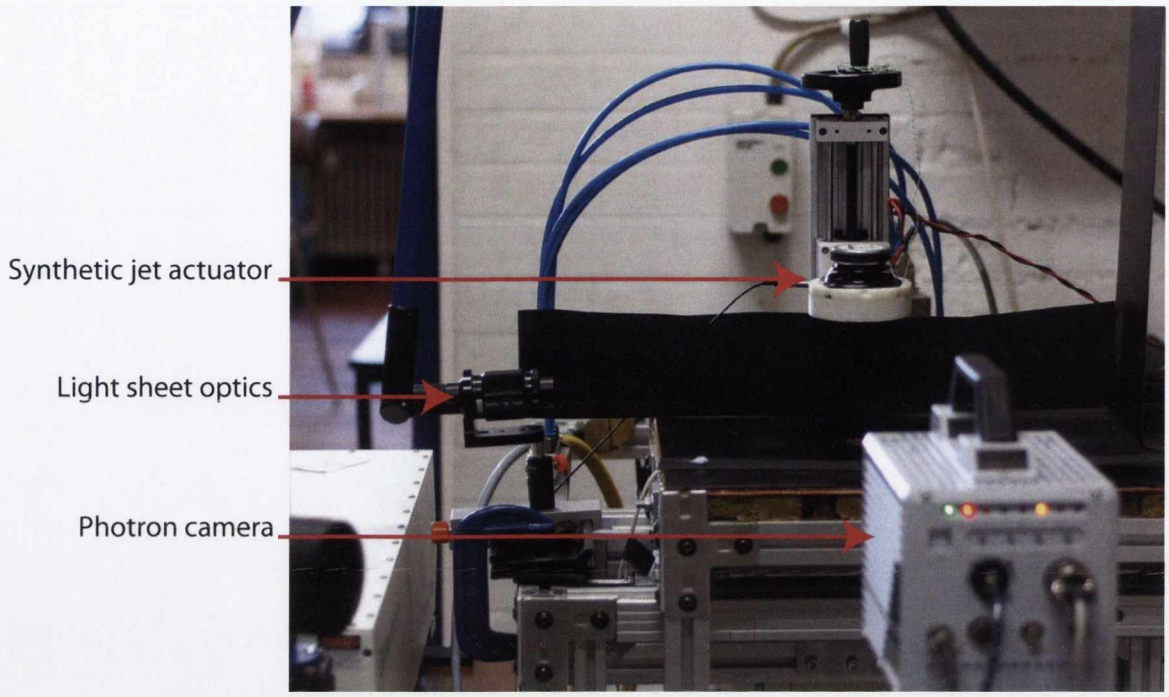

Figure 4.4 – Experimental setup for 2D-2C PIV testing

and lenses, the Scheimpflug condition[4] was satisfied whilst maintaining the correct field of view. Seen in figure 4.9 are the two Photron high speed cameras, the synthetic jet actuator, the custom calibration plate for 3D PIV, and the impingement surface moved to one side, exposing the insulation beneath the impingement surface. The objective of this test was to align the light sheet parallel to the impingement surface at approximately $2.5\,mm$, in order to capture vortex roll up on the impingement surface, whilst simultaneously recording heat transfer. A calibration plate is required to be placed in the object plane for both configurations (2D and 3D); the calibration target in this case is a type 11 calibration plate from LaVision that has a collection of equidistant dots on a cartesian grid, this target has to line up exactly with the light sheet. The calibration plate is $10\,mm$ thick, therefore prior to calibration for the stereoscopic setup, the impingement surface had to be moved so that the calibration plate could be offset $7.5\,mm$ down from the top of the impingement surface. A vernier height gauge, seen in figure 4.10, was placed on a flat metal plate next to the experimental rig and was used to accurately set the position of the calibration plate. Figure 4.11 shows

[4] The Scheimpflug condition is explained in Chapter 3

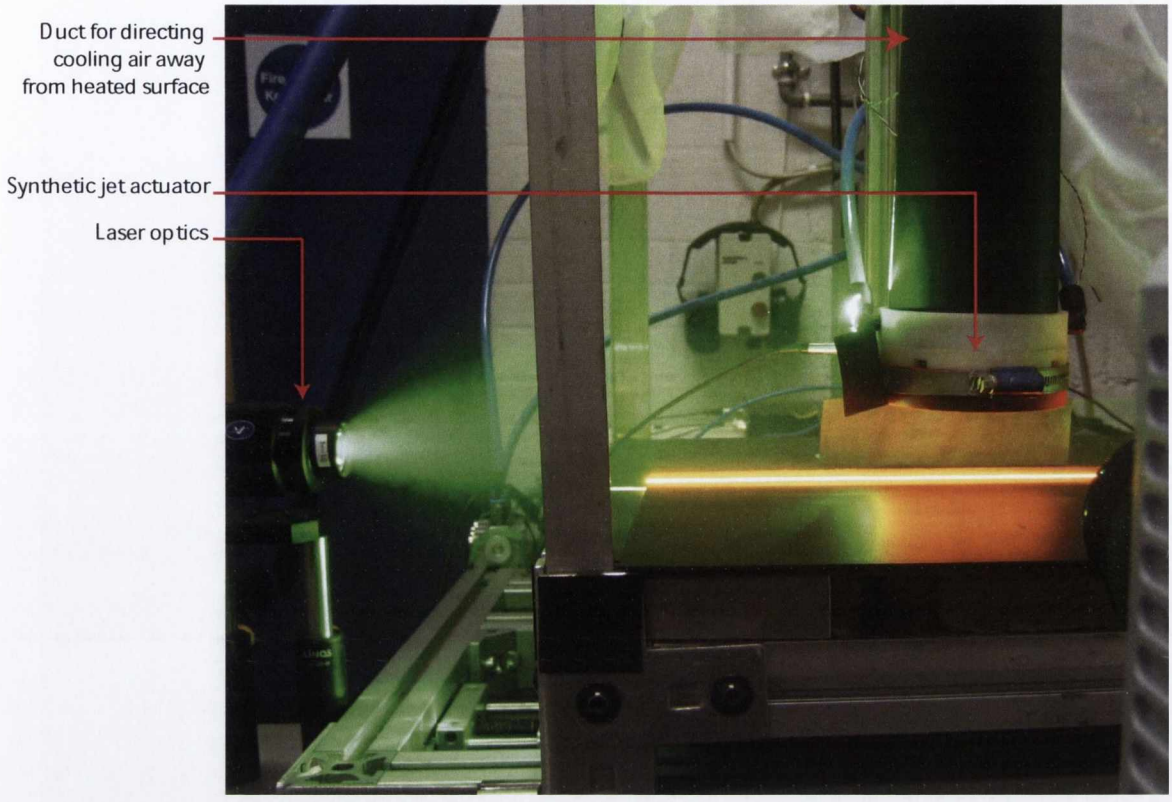

Figure 4.5 – Experimental setup for 2D-2C PIV testing, showing a test configuration with orange paint on the plate to reduce reflections

the stage of calibration setup just prior to calibrating the cameras. Upon completion of calibration, the calibration plate is removed, and the impingement surface and synthetic jet actuator are put back in their respective positions for testing to begin. Figure 4.12 presents a simultaneous surface heat transfer and stereoscopic PIV test for the parameters L_0/D=12, Re=1500. The seeded flow is correctly illuminated and the natural convection can be seen from the heated impingement surface, along with the jet region upon impingement from the synthetic air jet, indicated by the dashed red line; the hot film sensor is indicated as well.

4.1.3 Synthetic jet actuator used for stereoscopic PIV

A redesigned synthetic jet actuator had to be used for the stereoscopic PIV measurements presented in section 6.3.3 due to visual access restrictions. Seen in figure 4.12 is the stereoscopic setup with the different style actuator to allow for visual access at the

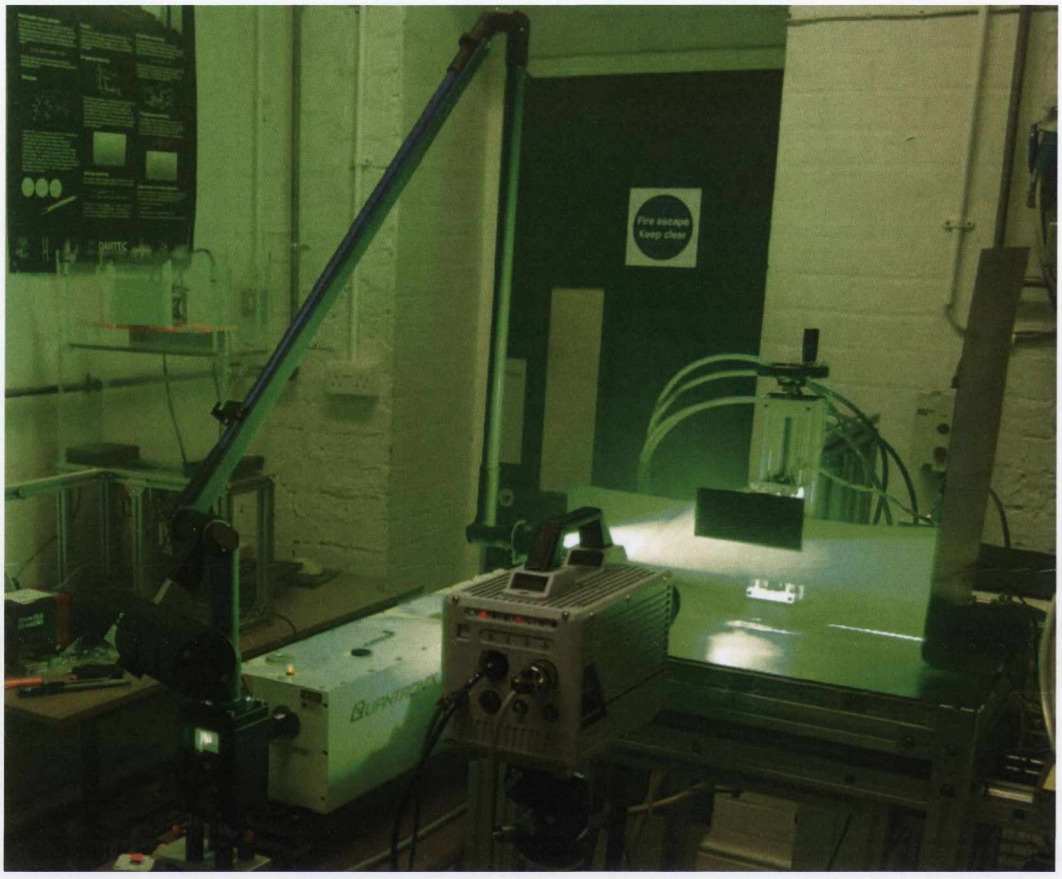

Figure 4.6 – Experimental setup for 2D-2C PIV testing, preliminary setup to configure beam stops to prevent reflections

minimum possible axial spacing of H/D=12. A schematic of the synthetic jet actuator is presented in figure 4.13. The cavity was made slimmer while still maintaining the same volume as the synthetic jet actuator described in section 4.1.1. The synthetic jet actuator described in section 4.1.1 has an orifice plate surface area of $A_{op} = 78.54\,cm^2$, where the synthetic jet actuator seen in figure 4.13 has a surface area of $A = 33.64\,cm^2$; this means that the degree of confinement is significantly reduced for the synthetic jet actuator used for the stereoscopic PIV tests compared to the synthetic jet actuator seen in figure 4.3 and used for the 2D PIV tests.

4.1.4 Impingement surface

The impingement surface used in this research was used in research by McGuinn [7] and O'Donovan [94] but slight modifications to the painted surface have been made

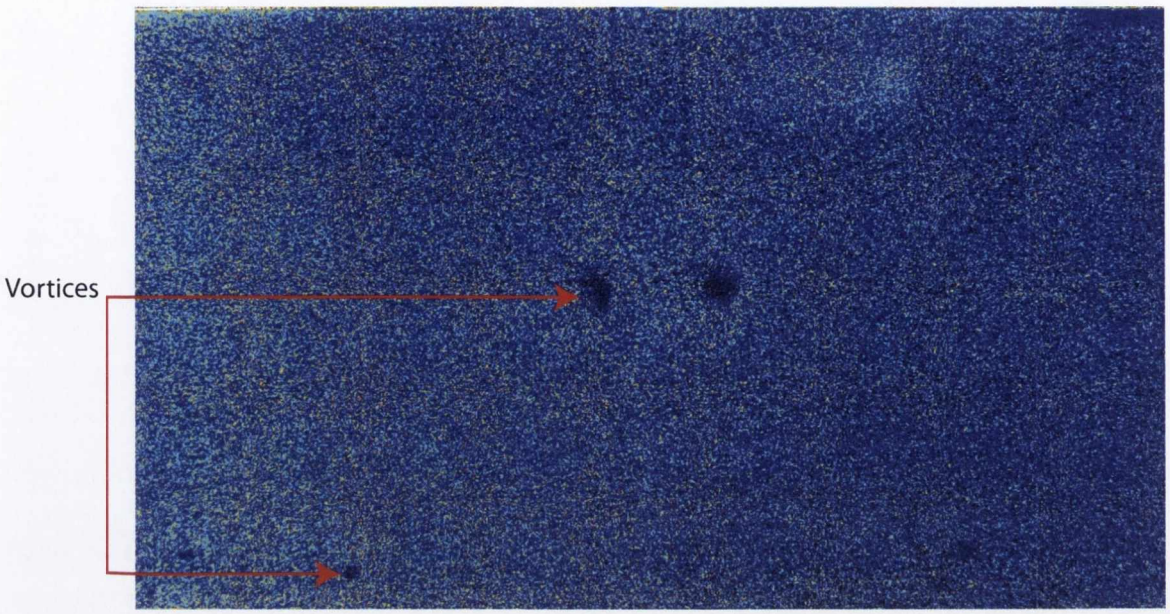

Figure 4.7 – Example of the focus achieved of the PIV seeding at an axial spacing of H/D=8

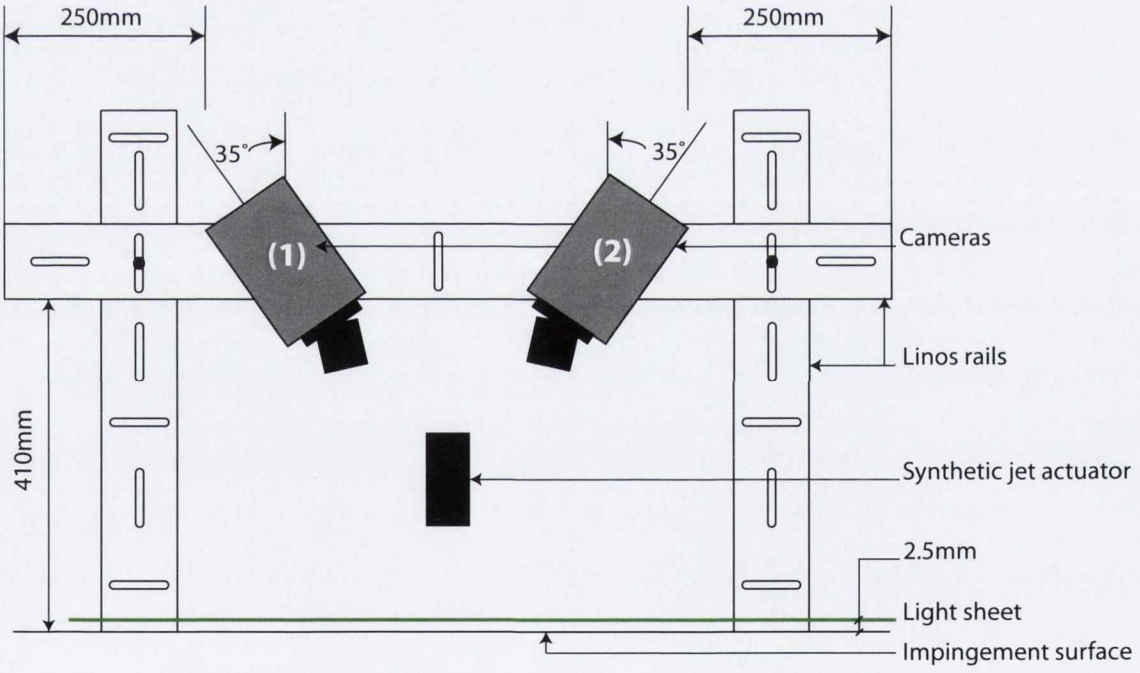

Figure 4.8 – Schematic of stereoscopic PIV test setup

in order to reduce reflections whilst performing extensive PIV testing. The impingement surface is made of a 5 mm thick copper plate; the thickness and conductivity of the copper plate is such that it approximates a uniform wall temperature boundary

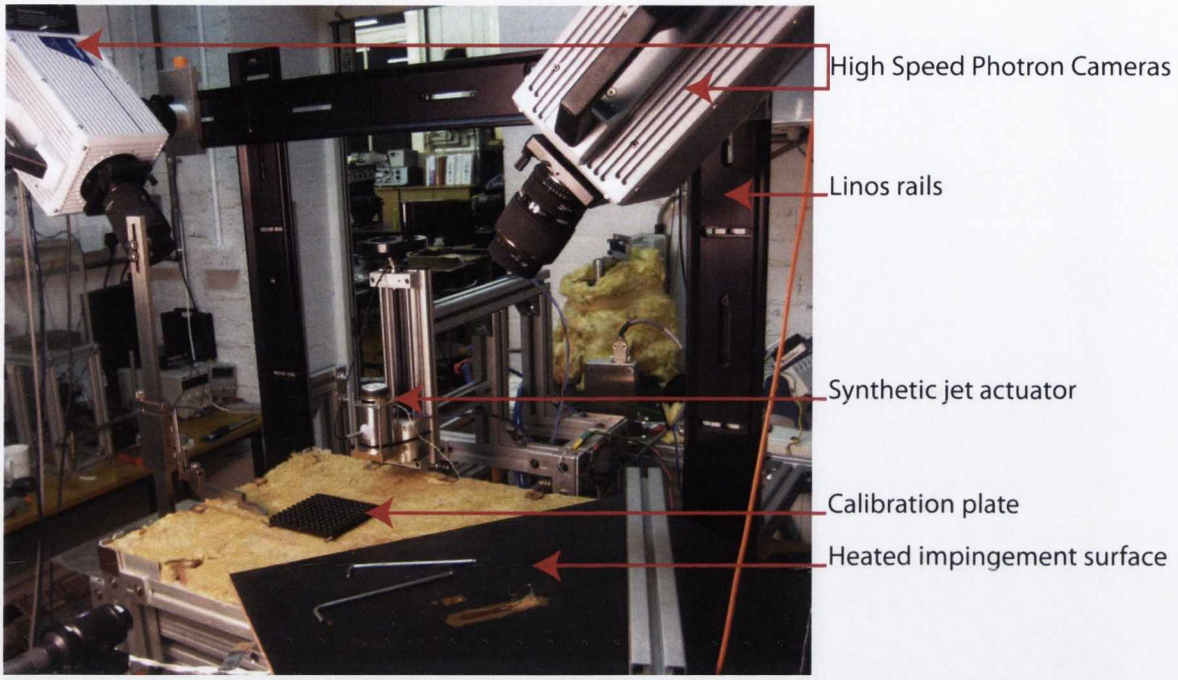

Figure 4.9 – Stereoscopic PIV camera setup for calibration procedure

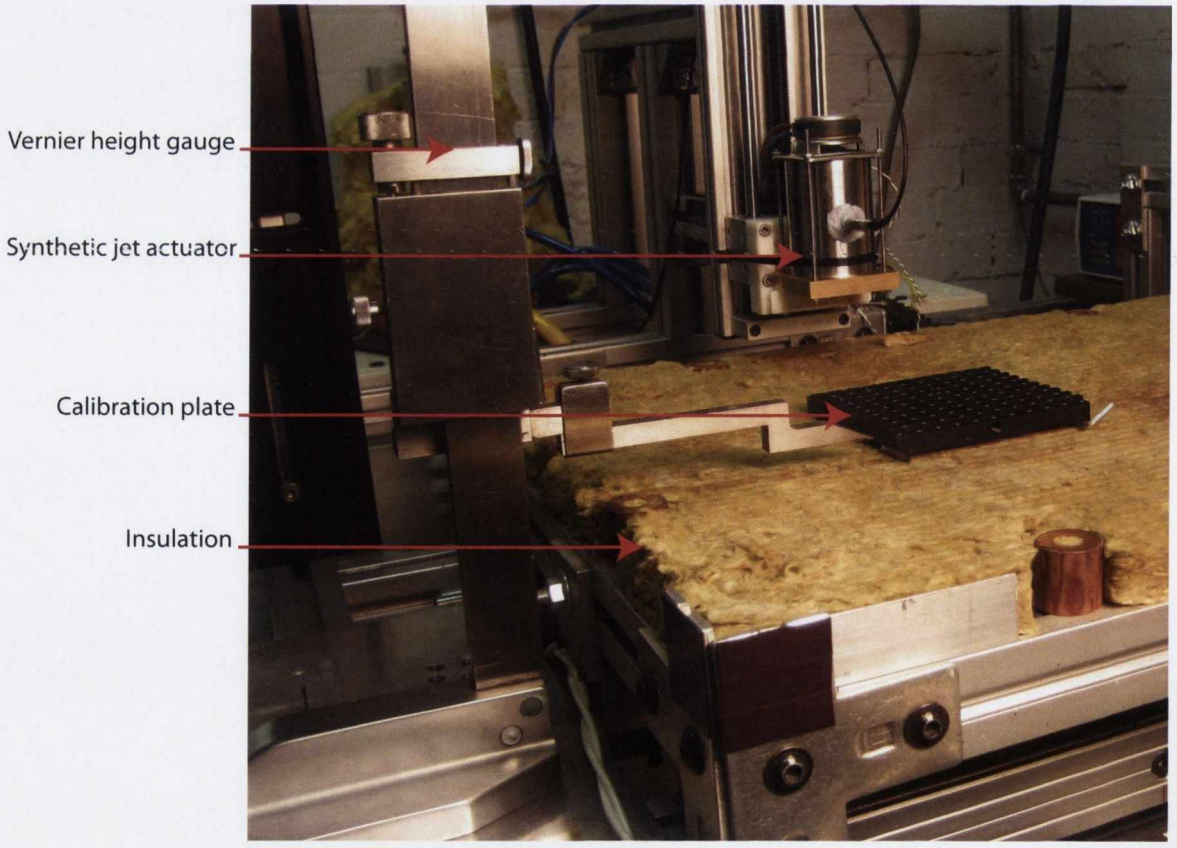

Figure 4.10 – Vernier height gauge used to set the height of the calibration plate

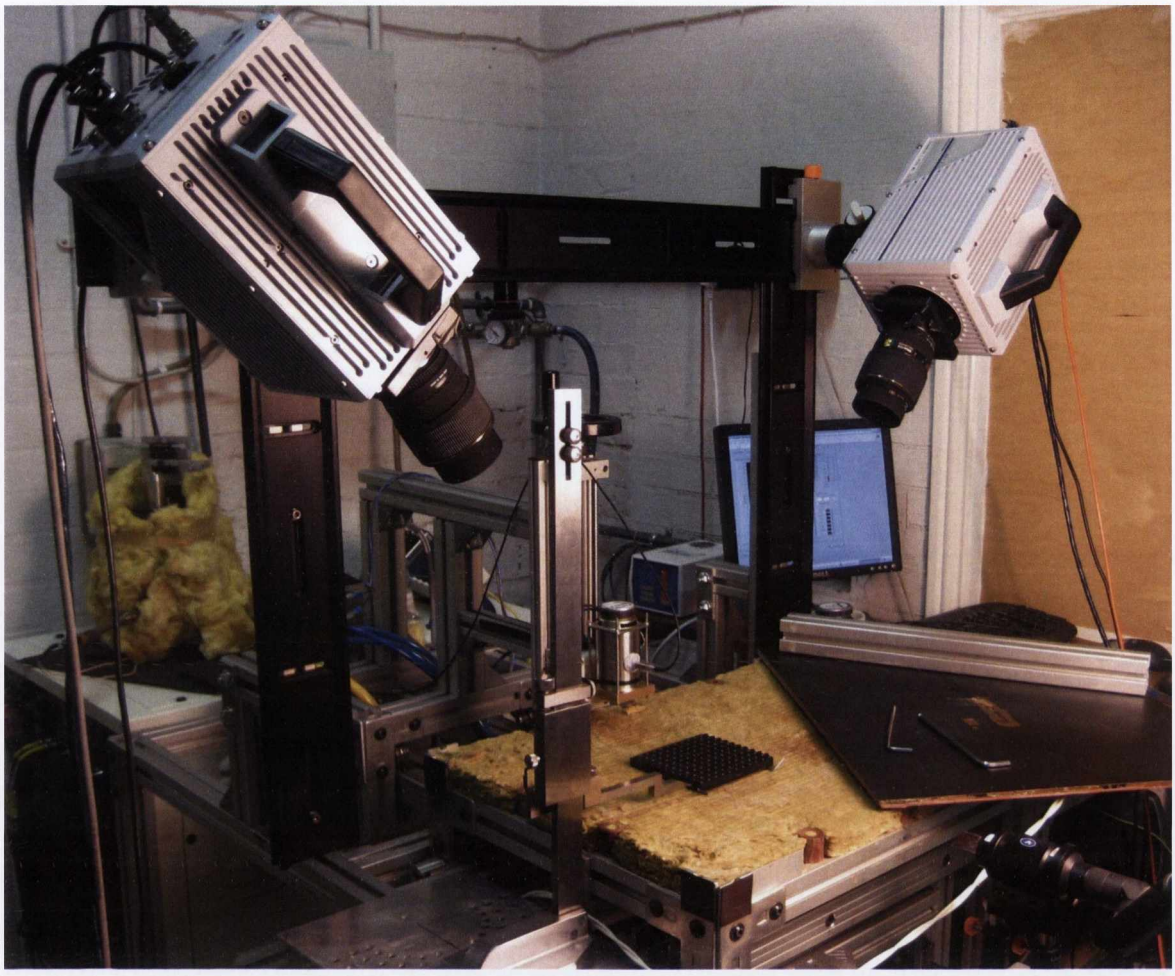

Figure 4.11 – Calibration plate in place prior to calibrating the cameras

condition. The maximum jet Reynolds number tested is Re=2000. For the limited heat transfer testing performed in this study, the heated surface was set at $60\,°C$; for a synthetic jet operating at this Reynolds number there is a maximum variation in the plate temperature of less than $1\,°C$. The temperature differential between the cooling airflow of the synthetic jet and the heated plate is, on average, over $30\,°C$, which aids in minimising errors. In an attempt to counteract the cross flows and buoyancy effects present in the lab for the simultaneous 3D PIV and heat transfer testing a fine mesh was erected surrounding the plate, seen in the background of figure 4.5. The impingement surface was heated using a silicone mat of $1.1\,mm$ thickness that was specifically designed and manufactured by Holroyd components [116]. The silicone mat was adhered to the bottom of the copper plate with a silicone glue; in order to ensure that the plate was heated uniformly the layer of glue was applied as evenly

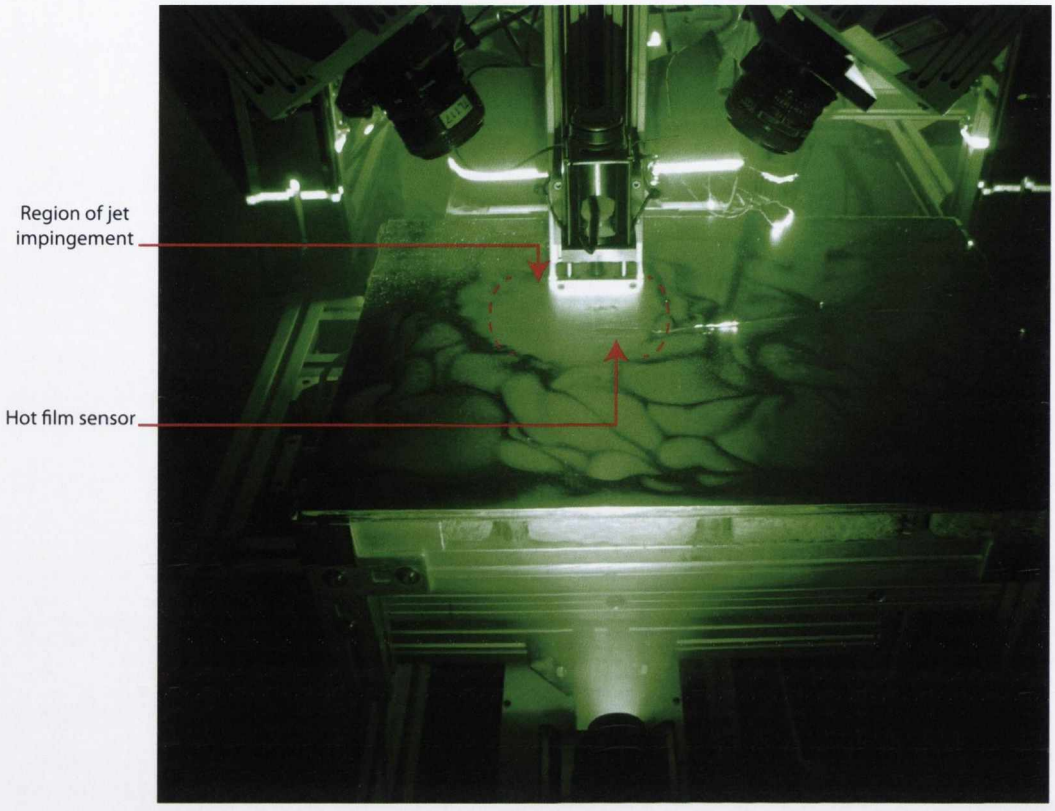

Figure 4.12 – Simultaneous surface heat transfer and stereoscopic PIV testing, H/D=12, Re=1500, L_0/D=12

as possible and the assembly was then compressed allowing the glue sufficient time to bond the two items together. The heating element embedded within the silicone mat has the same dimensional area as the copper plate of $425\,mm \times 550\,mm$ and is rated for a maximum input voltage of $240\,V$ with a power output corresponding to a heat flux of $15000\,W/m^2$. The impingement surface can be clearly seen in figures 4.10 and 4.11. The surface was painted matte black in an attempt to reduce the laser light reflections from the surface when performing 2D-2C PIV testing. By painting the surface black this also made it easier to pinpoint the hot film sensor when analysis of the simultaneous surface heat transfer and stereoscopic PIV data was performed.

4.1.5 Instrumentation

Instrumenting the synthetic air jet utilised in this research, requires an amplifier, thermocouples and a highly sensitive pressure microphone setup. The principle of

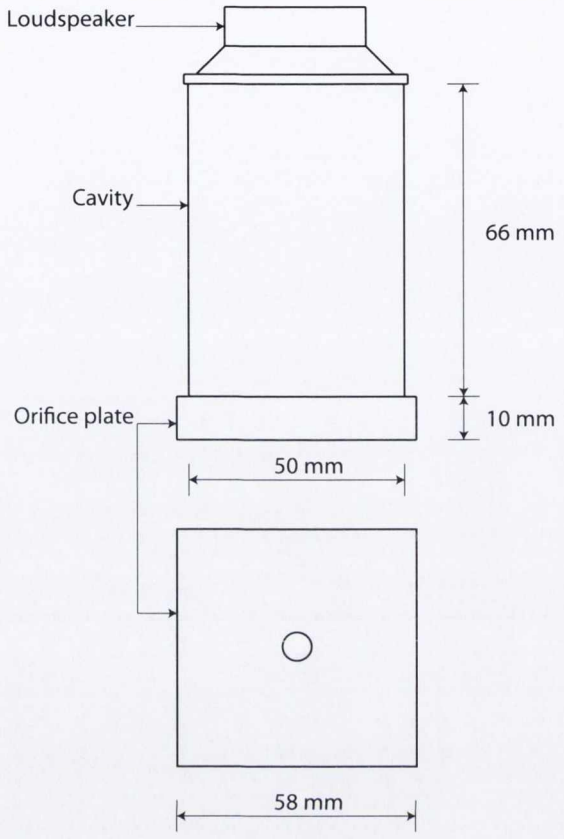

Figure 4.13 – Schematic of the synthetic jet actuator (actuator 2) used for stereoscopic PIV testing

operation of the synthetic air jet is based on entrainment of ambient air; in order to correctly measure air temperature of the air expelled from the orifice a thermocouple is placed in the cavity. As mentioned in section 4.1.1 the speaker used as the driver in this study is a Visaton FR-8; its maximum unloaded deflection is $4mm$. The speaker requires a signal of a specific power rating in order to function correctly; the signal from the data acquisition system was amplified using a 40 Watt power amplifier. Over extended testing periods and high loads, it was discovered that the magnetic coil of the speaker was overheating. This heat was conducted through the speaker cone and into the speaker cavity. This additional heat load altered the temperature within the cavity, thus affecting the efficacy of the synthetic air jet and altering the jet's working parameters, which could result in incorrect measurements. To counteract the overheating of the magnetic coil in the speaker, an additional test section with cooling

ports was produced using fused deposition modelling, and attached to the top of the synthetic jet cavity. This section that allows for steady jets to cool the magnetic coil is seen in figure 4.14. The steady jets successfully cooled the magnetic coil and the air was exhausted from the synthetic jet actuator, away from the impingement surface, through the use of a duct mounted to the top of the speaker, which is pictured in figure 4.5. The specification sheet for this speaker can be found in Appendix A.

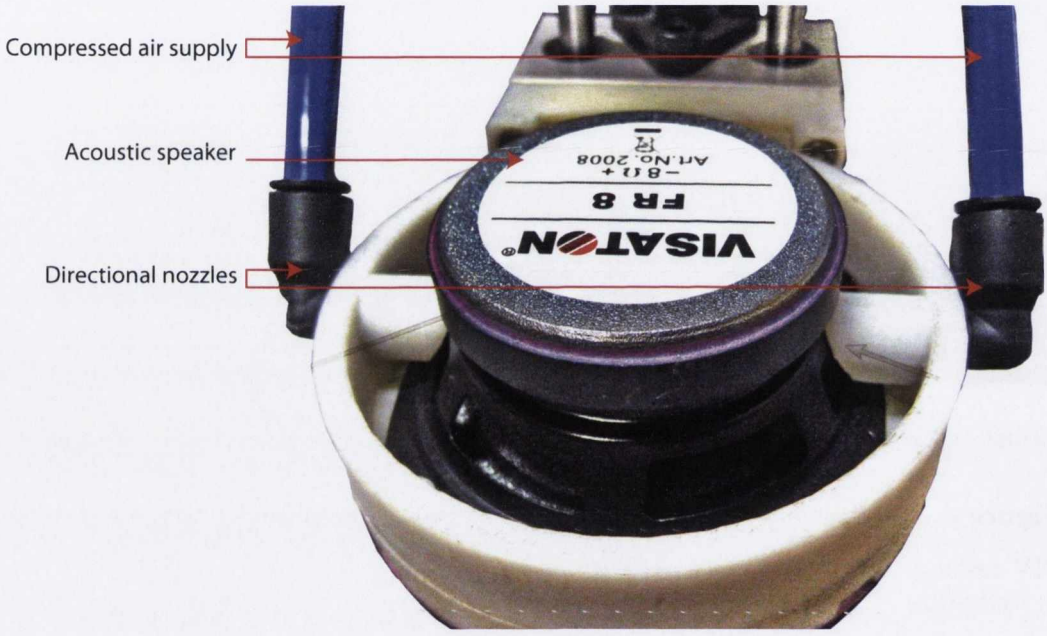

Figure 4.14 – Synthetic jet actuator with steady jets cooling the magnetic coil

4.1.5.1 Mass flow controller

The compressed air supply that cools the magnetic coil of the loudspeaker was regulated through the use of a mass flow controller. The MKS [117] 1579A is an elastomer sealed, high flow rate mass flow controller, seen in figure 4.15. This mass flow controller can provide a range of flow rates from 50 slm to 300 slm. A 1%fsd (full scale deflection) is the rated accuracy of the controller. A certificate of calibration is in Appendix A.

Figure 4.15 – MKS Instruments 1579A mass flow controller

4.1.5.2 Pressure microphone and amplifier

The calibration of the synthetic jet actuator used in this research is completed in accordance with the pressure based estimate of the synthetic jet velocity, described by Persoons [80]. This procedure was used to control the frequency and amplitude of the synthetic jet in order to set the desired jet Reynolds number and dimensionless stroke length. A 1/4inch pressure microphone, type 40BP, 1/4 inch preamplifier, type 26C and a power module, type 12AN supplied by G.R.A.S. [118] were implemented in order to measure the cavity pressure of the synthetic jet actuator. The microphone and preamplifier are seen in figure 4.16.

The power module supplies power to the preamplifier after which the signal is supplied to the data acquisition, which uses the measured pressure to estimate the jet Reynolds number, from equation 2.18, and the dimensionless stroke length. The specification sheets for these instruments are included in Appendix A. Calibration of the synthetic air jet was performed according to the method outlined by Persoons [80] and using equation 2.17. The calibration was performed within the research group [7]; the following method was used to perform the calibration. A hot wire probe operating in constant temperature anemometer mode was positioned $0.5\,mm$ in front of the orifice exit whilst the pressure microphone measured the cavity pressure. A sine wave of

Figure 4.16 – G.R.A.S. pressure microphone and preamplifier

known amplitude was supplied to the synthetic jet actuator. The data fed back from the hot wire and microphone were phase averaged over 10 periods. The centreline velocity U_{cl} is assumed to be equal to the area averaged velocity U_0 due to the orifice length being less than the minimum length required for hydraulic development ($l > 200\,mm$). A range of cavity pressures were recorded in the range of $10\,Pa$ to $1000\,Pa$, with frequencies of up to double the cavity resonance ($2f_h$). This data was then fitted to the least square linear damping model outlined by Persoons [80] using the fitting parameters of the nonlinear damping coefficient K_p and the added mass coefficient β. These fitting parameters relate the damping force F_D and the mass of the gas M_o within the orifice. Confirmation of the velocity calibrations have been completed using particle image velocimetry. An uncertainty level of under 5% on a 95% confidence interval was achieved.

4.1.5.3 Thermocouples (T-type)

T-type thermocouples are used to acquire temperature measurements from three locations. The hot film sensor has a fine gauge thermocouple embedded beneath it, located as close as possible to the hot film sensor. This thermocouple is used to monitor the impingement surface temperature. The cavity temperature of the synthetic jet actuator must be measured for the temperature difference between the cavity and the impingement surface is used for determination of local heat transfer coefficient. There is also a thermocouple measuring the ambient temperature in the testing en-

vironment; it is located away from any heat source so as to give as true a reading as possible of the ambient temperature. The T-type thermocouples are calibrated in a constant temperature water bath against a certified RTD (resistance temperature detector) master thermocouple probe (see Appendix A for calibration certificate). The results from the calibration were used to calculate a third order regression curve for each thermocouple. The third order polynomials for the calibrated thermocouples are presented in figures 4.17, 4.18 and 4.19. The third order polynomial equations for each respective calibration are presented in equations 4.1, 4.2 and 4.3.

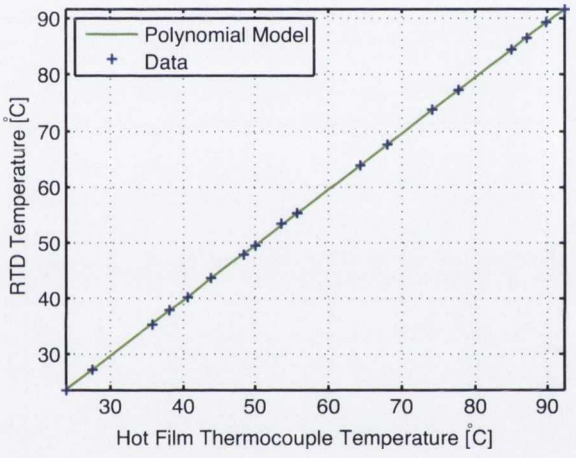

Figure 4.17 – Calibration data for thermocouple located below hot film sensor [7]

$$T_{RTD} = -2.6346e^{-6}{T_{Micro-Foil}}^3 + 0.00050327{T_{Micro-Foil}}^2 + 0.96842T_{Micro-Foil} + 0.31451 \tag{4.1}$$

$$T_{RTD} = -2.2537e^{-6}{T_{Cavity}}^3 + 0.00010438{T_{Cavity}}^2 + 1.0052T_{Cavity} - 2.2603 \tag{4.2}$$

$$T_{RTD} = 3.0267e^{-6}{T_{Ambient}}^3 - 0.00063344{T_{Ambient}}^2 + 1.0333T_{Ambient} - 2.5751 \tag{4.3}$$

A regression fit and uncertainty for each thermocouple calibration is presented in table 4.1

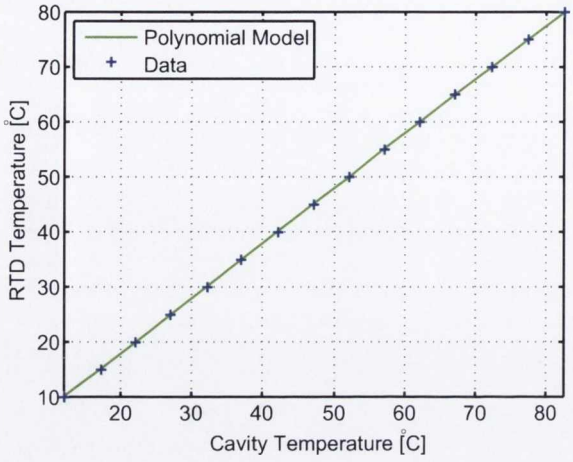

Figure 4.18 – Thermocouple calibration data for synthetic jet cavity air temperature measurement [7]

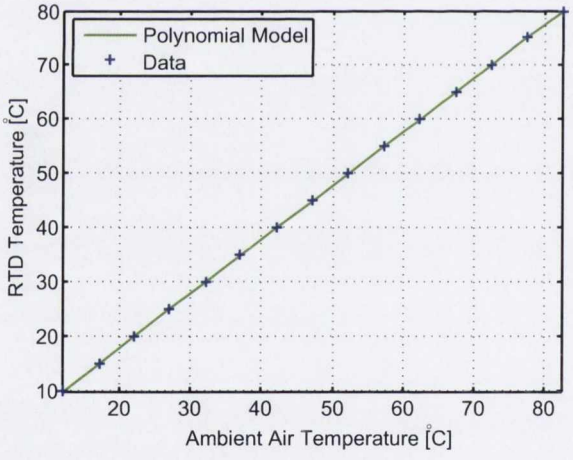

Figure 4.19 – Thermocouple calibration data for ambient air temperature measurement [7]

The uncertainty in the regression curve is considered to be small as it is less than 0.1%, which is reflected in the measurement uncertainty. Calibrations for the synthetic air jet, hot film sensor and various thermocouples were performed at the same time as work completed by joint research [7] focussing on heat transfer measurements of a synthetic air jet.

Table 4.1 – Calibrated thermocouple uncertainties at normal operating temperatures [7]

Temperature measurement	Typical operating temperature ($°C$)	Regression uncertainty (%)	Measurement uncertainty ($°C$)
Hot film	60	0.046	0.156
Cavity air	30	0.033	0.099
Ambient air	20	0.036	0.107

4.1.5.4 Senflex hot film sensor

The hot film sensor (Tao Systems Senflex SF9902) seen in figure 4.20 is used for time varying or fluctuating heat transfer measurements. The sensor is made up of copper leads on a Upilex C Polyimide film substrate that is $51 \mu m$ thick. The dimensions of the nickel sensor element are $1.2\,mm \times 0.1\,mm$ and it has been electron beam deposited onto the Polyimide substrate to a thickness of $\leq 0.2\,\mu m$.

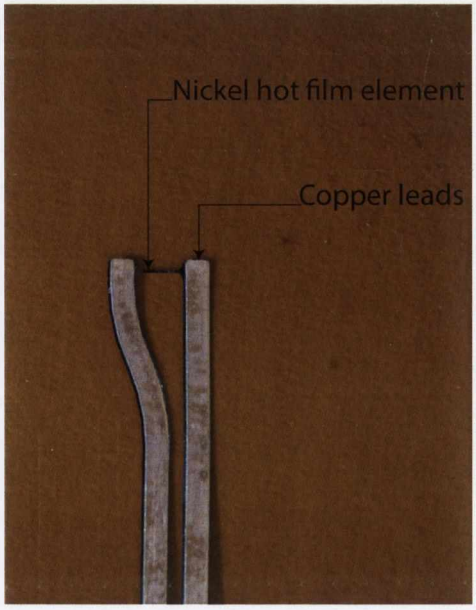

Figure 4.20 – Hot film sensor

The hot film sensor is operated by a CTA (constant temperature anemometer) from Dantec dynamics [119]; the CTA controls the film temperature. The CTA is essentially

a circuit that includes an arrangement of resistances known as a Wheatstone bridge, presented in figure 4.21 where the hot film sensor is considered to be one of the resistors (R_s) in the bridge. By varying the resistance values of the other resistors within the bridge it is possible to vary the temperature of the hot film sensor. It is necessary that the temperature of the hot film be greater than that of the impingement surface in order to achieve a high level of sensitivity, otherwise known as the "sensor overheat". This has been documented in several investigations that utilise a hot film sensor to obtain heat flux measurements, Scholten and Murray [120], McGuinn [7] and O'Donovan et al. [121].

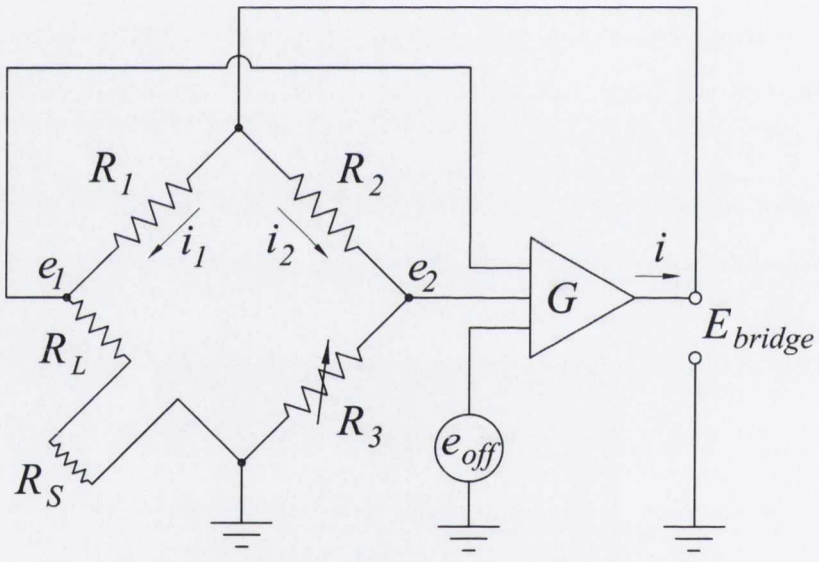

Figure 4.21 – Constant temperature anemometer Wheatstone bridge schematic [122]

To calculate the heat flux of the hot film sensor the bridge voltage, which is the voltage required to maintain the temperature overheat in the hot film sensor, is used.

$$Q_{diss} = (V_{bridge}^2 - V_0^2)\frac{R_S}{(R_p + R_2)^2} \tag{4.4}$$

$$R_p = R_S + R_L \tag{4.5}$$

Where,

1. Q_{diss} is the electrical power dissipated in the hot film sensor

2. V_{bridge} is the Wheatstone bridge voltage under test conditions
3. V_0 is the Wheatstone bridge voltage under zero flow conditions
4. R_S is the hot film element resistance
5. R_p is the probe arm resistance in the Wheatstone bridge
6. R_2 is the top resistance in the Wheatstone bridge
7. R_L is the collective resistance between the hot film and the CTA (made up of leads, connectors etc.)

In order to calibrate the hot film sensor, the effective surface area is required, and is calculated from the combination of equations 4.4, 4.6, and equation 4.7. Equation 4.6 is a correlation produced by Shadlesky [123] describing the relationship between the stagnation point heat transfer of an impinging steady jet and the axial spacing from jet to impingement surface.

$$0.585 = \frac{Nu_{stag}}{Pr^{0.4}Re^{0.5}} \tag{4.6}$$

Bearing in mind that $Nu = hD/k$, the combination of equations 4.4, 4.6, and 4.7 yields equation 4.8, used for calculation of the effective area of the hot film sensor.

$$q = hA_{eff}(T_{film} - T_{jet}) \tag{4.7}$$

$$A_{eff} = \frac{R_S(V_{bridge}^2 - V_0^2)D}{0.585(R_p + R_2)^2(T_{film} - T_{jet})kPr^{0.4}Re^{0.5}} \tag{4.8}$$

Equation 4.8 calculates the effective area of the hot film sensor, where A_{eff} is effective sensor element area when there is an overheat active; in air this is normally a number of times larger than the film's physical geometric area. $A_{eff} > A_{geom}$ due to lateral conduction within the sensor itself. Once the effective area has been correctly calculated, this information can then be used to calculate the heat flux, seen in equation 4.9.

$$q_{diss} = \frac{Q_{diss}}{A_{eff}} \tag{4.9}$$

A comprehensive study on the use of the hot film sensor for the purpose of measuring the convective heat flux from a cylinder in a cross flow was completed by Scholten [124]. The method outlined in the study by Scholten [124] has been used in this study. Different sensor overheats for the same experiments provided varying results, the reason for the difference in measurements was attributed to the shear stress of the flow over the sensor not being taken into account. Representing the heat flux from the sensor as a one-dimensional conduction at the wall is how Scholten [124] described a correction for the shear stress of the flow over the sensor.

The surface temperature of the hot film can vary during a test from the temperature recorded when V_0 was measured; a small deviation in temperature difference coupled with the thickness of the sensor being so small can lead to high heat transfer variations. Thus, additional conduction through the substrate has to be accounted for. This additional conduction term is calculated as follows:

$$q_{cond} = k_{kapton} \frac{T_{surf} - T_{surf,0}}{\delta} \tag{4.10}$$

Where,

1. k_{kapton} is the thermal conductivity of the Kapton substrate
2. T_{surf} is the surface temperature under test conditions
3. $T_{surf,0}$ is the surface temperature under zero flow conditions
4. δ is the sensor substrate thickness

The subtraction of q_{cond} from the heat flux originating from the dissipation (q_{diss}) of the electrical energy yields the convective heat transfer rate:

$$q_{conv} = q_{diss} - q_{cond} \tag{4.11}$$

The Nusselt number is calculated as follows:

$$Nu = \frac{q_{conv} D}{k(T_S - T_\infty)} \tag{4.12}$$

where T_S is the temperature of the sensor element. Equation 4.4 shows that the heat flux from the hot film sensor is dependent on both operational voltage and the sensor resistance. The value V_{bridge} in equation 4.4 is the voltage of the Wheatstone bridge under test conditions, and this value varies depending on the heat flux (Q_{diss}), the rest of the values are either fixed or known quantities or must be found through calibration. The sensor element resistance R_S must be calibrated so that the decade resistance can be set in order to achieve the desired overheat for experimental conditions. The RTD was used for the calibration of the hot film sensor element. The impingement plate was covered with insulation in order to achieve a uniform temperature for the calibration. The calibration was performed for the temperature range of 25 °C to 82 °C in increments, whilst allowing time for each increment to reach steady state. The calibration data are presented in figure 4.22.

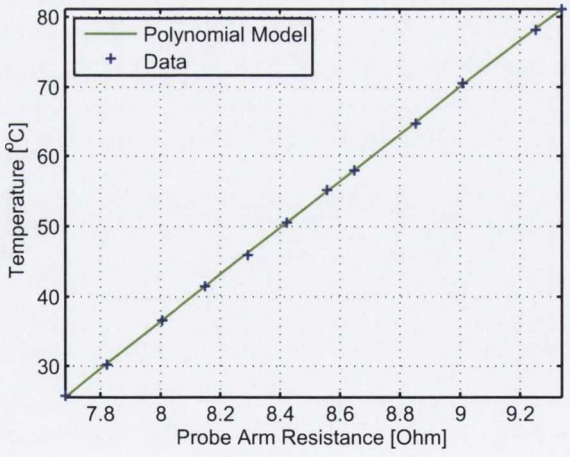

Figure 4.22 – Hot film resistance calibration [7]

From figure 4.22 it can be seen that there is a linear relationship between the probe arm resistance and the temperature. A linear fit is applied to the data, and equation 4.13 represents this:

$$R_p = 0.29843T - 6.9137 \tag{4.13}$$

The probe resistance R_p is made up of resistances seen in equation 4.5, i.e. the sensor resistance R_S and the collective resistance R_L. The collective resistance was measured to be $R_L = 0.672\Omega$. In order to correctly calculate the collective resistance, the probe arm is short circuited close to the sensor element and the bridge is balanced; from this the resistance of the connecting leads is then measured. For a hot film sensor temperature of 70 °C, the uncertainty is found to be 0.1% with a precision limit of $0.341\,°C$. The experimental uncertainty of the heat flux is calculated from the effective surface area of the hot film sensor. For the experimental setup here the uncertainty in the Nusselt number was calculated at 21% for a 95% confidence limit [7].

4.2 Data acquisition

National Instruments Corporation supplied the data acquisition boards; all the data measured from the thermocouples, microphone and the CTA were recorded on two separate National Instruments [125] data acquisition (DAQ) boards, seen in figures 4.23 and 4.24. Presented in figure 4.23 is chassis model NI cDAQ-9178, which is the data acquisition chassis that was primarily used to control the synthetic jet actuator parameters. The data acquisition card NI PCI-6036E and breakout board NI SCB-68 seen in figure 4.24 were used for all other instrumentation control such as driving the stepper motor that moves the heated impingement surface and for the remaining data acquisition.

A visual interface program designed using Labview was used to control the instrumentation and view the output signals from the DAQ boards. Calibration coefficients are integrated into the program in order to provide accurate real time data of the experimental setup. The test results are output in the form of tab delimited matrices in ASCII text files. All the data that was captured and exported from Labview was processed and plotted using purpose written code in Matlab.

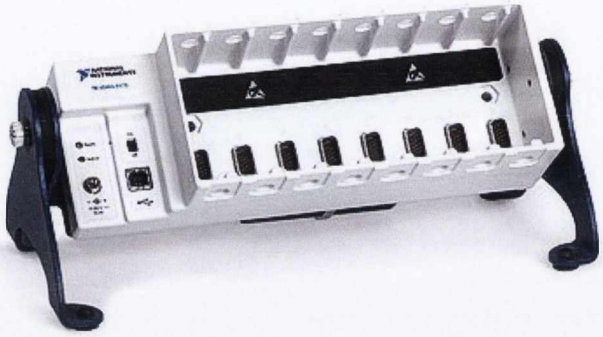

Figure 4.23 – Data acquisition module, NI cDAQ-9178

Figure 4.24 – Data acquisition module, NI PCI-6036E and NI SCB-68

Chapter 5

Results:
Synthetic jet flow regimes and time averaged PIV

Experimental results obtained for a range of parameters are presented here for a synthetic air jet impinging perpendicularly on a horizontal plate, which serves as a heated surface for heat transfer tests as well.

Three types of experiment were carried out, as outlined here:

1. Time averaged particle image velocimetry (PIV) testing: the synthetic jet impinged onto a cold plate. Volume flux data have been calculated from the time averaged PIV results.

2. Instantaneous high resolution PIV of the synthetic air jet. Results were recorded at a frame rate of $4096\,Hz$, which provides comprehensive flow field imagery of the evolution of the synthetic jet.

3. Vortex roll-up measurements were performed in a measurement plane parallel to the heated surface, i.e. simultaneous surface heat transfer and stereoscopic PIV measurements were conducted with the laser light sheet parallel to and axially located approximately $2.5\,mm$ above the impingement surface. The location of

the light sheet was chosen from the estimated vortex diameter obtained from 2D PIV measurements of the synthetic jet.

The synthetic jet actuator and experimental setup was described in chapter 4. All testing was performed on a semi-confined synthetic air jet issuing through an orifice of diameter $5\,mm$ and length $10\,mm$. The range of operational parameters that have been investigated is shown in table 5.1. The main parameters are the jet Reynolds number, dimensionless stroke length (L_0/D) and nozzle to plate impingement distance (H/D). The synthetic jet flow regimes covered with this combination of test parameters encompasses the full range of synthetic jet flow fields encountered, which are discussed in section 5.1 and identified as (a) below jet formation threshold, (b) the threshold of jet formation, (c) slug flow regime, and (d) fully developed flow.

Table 5.1 – Synthetic jet test frequencies for 2D and 3D PIV experimental setups.

			L_0/D							
H/D	Re		2	3	4	8	12	16	28	32
4, 8, 12	500	$f(Hz)$	N/A	N/A	80	40	28	20	N/A	10
4, 8, 12	1000	$f(Hz)$	N/A	N/A	160	80	50	40	N/A	20
4, 8, 12	1500	$f(Hz)$	470	310	240	118	80	58	35	28
4, 8, 12	2000	$f(Hz)$	N/A	N/A	310	155	103	76	N/A	39

This chapter is outlined as follows; section 5.1 details the overall synthetic jet flow field from (high frame rate instantaneous) PIV measurements, providing a comprehensive flow field analysis. High frame rate instantaneous PIV data is used to identify flow field structures such as the vortex ring and trailing jet. Section 5.2 presents time averaged PIV data in the form of vorticity plots overlaid with streamlines. These plots also display the bulk fluid motion on the periphery of the synthetic jet. Once the main features of the synthetic air jet flow have been established, chapter 6 details the characteristics of a singular vortex ring from formation to impingement for the set of parameters found in table 5.1.

5.1 Synthetic jet flow regimes

A synthetic air jet produces a flow field by a periodic oscillation of a membrane over a cavity, which generates alternating phases of ejection and suction across an orifice [45]. As a consequence, momentum can be injected into the surrounding ambient fluid even though the mass flux in a period of oscillation remains equal to zero. The resulting periodic in and out flow at the orifice leads to a near field that is characterised by what are considered to be dominant vortical structures. The far field is characterised by a downstream directed motion similar to that of a steady jet. Lying in between the near field and far field is a saddle point that divides streamlines directed toward the orifice and in the downstream direction. These flow characteristics have been experimentally investigated by means of particle image velocimetry.

Gharib et al. [24] presented a study focussed on impulsively started jets and a limited number of velocity programs. Although relevant, none of the velocity programs tested in their research are directly comparable to the velocity program produced by a synthetic air jet, such as the one that has been used in this study. The application of a sinusoidal wave voltage of a specific frequency and amplitude to a loudspeaker results in the periodic synthetic jet flow produced at an orifice, therefore, the velocity program across the jet orifice of the synthetic jet can be regarded as a sine wave, see figure 5.1.

Contours of the streamwise vorticity, ω_z, with an overlay of velocity vectors are presented in figure 5.2 at twelve incremental phase angles of $\phi \approx 30°$, for one complete synthetic jet cycle at H/D=8, Re=1500 and L_0/D=12. Referring to the sine wave shown in figure 5.1, a complete synthetic jet cycle is 360°. The beginning of the cycle starts at $\phi = 0°$, which represents the start of the ejection stroke, where the velocity is equal to zero, this is the point where the membrane is at the top of its stroke, and the cavity volume is at its maximum. In terms of the synthetic jet period this is the point where the suction stroke has just ended and is just before the ejection stroke begins, the phase is $\phi \approx 360°$, and as the ejection stroke begins, changes to $\phi \approx 0$.

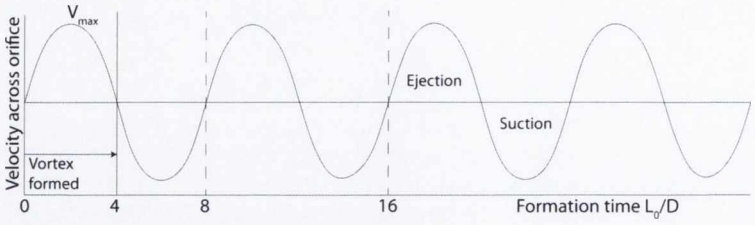

(a) Instantaneous velocity for formation time $L_0/D \leq 4$

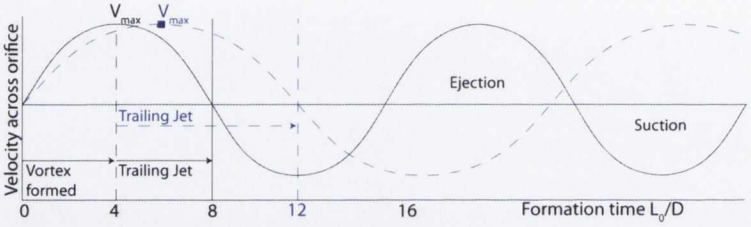

(b) Instantaneous velocity for formation time $4 < L_0/D \leq 8$, (- - -)L_0/D=12

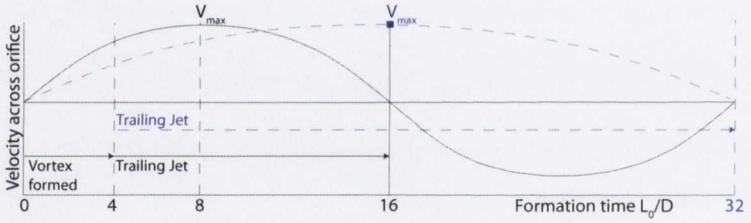

(c) Instantaneous velocity for formation time $L_0/D > 8$, (- - -)L_0/D=32

Figure 5.1 – Jet formation with increasing dimensionless stroke length.

The ejection and suction phase of the synthetic jet cycle comprise 180° respectively of this cycle. The phase angles chosen for representation of a complete synthetic jet cycle shown in figure 5.2 are 30° per phase, there is no significance to this particular phase angle selection other than that it allows for a complete depiction of the important stages of the jet evolution at these parameters. The colour bar applies to all images in figure 5.2, with red signifying negative vorticity and blue positive. Figures 5.2a to c show the flow just before the expulsion portion of the actuator cycle and up to where the vortex ring forms just in front of the orifice. There is evidence of vortices on the impingement plate at $r/D \approx 2.5$ in figure 5.2a; these are from a previous synthetic jet cycle. As the expulsion portion of the cycle is beginning these vortices will dissipate,

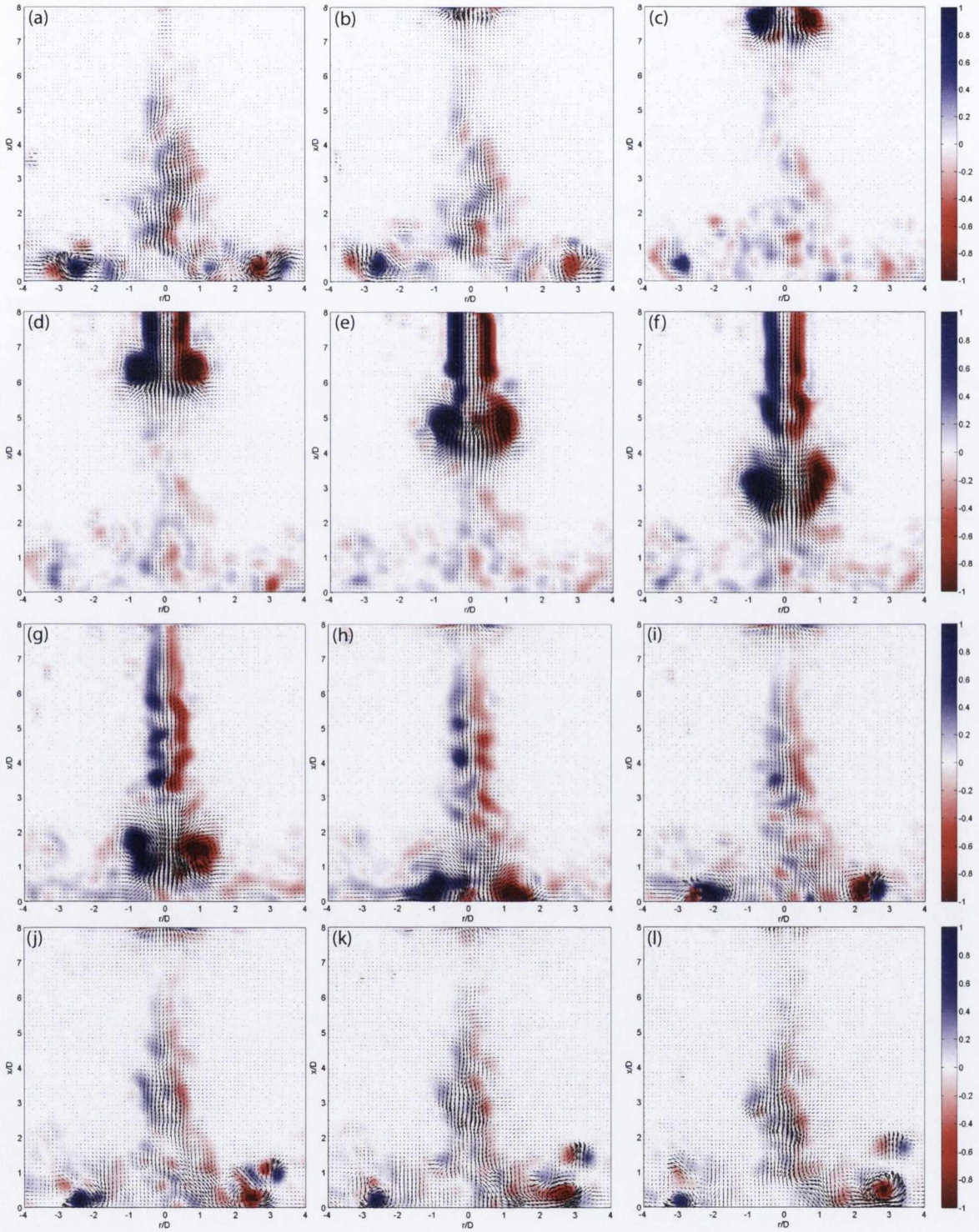

Figure 5.2 – A complete cycle of a synthetic air jet from instantaneous high frame rate PIV. Contours of the streamwise vorticity, ω_z with an overlay of velocity vectors at phase increments $\phi \approx 30°$, starting from $\phi = 0°$. H/D=8, Re=1500, L_0/D=12.

as can be seen from figure 5.2c. Figure 5.2d, ($\phi = 90°$) shows what is considered as the formation location ($x/D = 6.5$) of the vortex ring in this test. The formation location of a vortex ring above the formation number ($L_0/D \approx 4$) is considered as the point just before vortex ring pinch off from the fluid behind it as it leaves the orifice [126], [127], [128] i.e. just before the end of vorticity entrainment into the vortex ring. The physics of vortex formation for a synthetic jet is akin to that of an impulsively started jet. Several authors have noted and shown that there exists a universal stroke length for vortex formation [24], [11], and beyond this stroke length ($L_0/D \geq 4$) additional fluid that is ejected from the orifice does not roll up into the formed vortex and instead begins the process of forming a trailing jet. Shuster and Smith [11] documented the presence of a trailing jet at L_0/D=5, however their study did not investigate the effect of the trailing jet on the vortex ring.

Figure 5.2d-h show the presence of a trailing jet. Once the primary vortex ring has been formed the excess fluid forms a trailing jet, which is evident from figure 5.2d through to figure 5.2h when the vortex ring impinges.

Figure 5.1 presents the instantaneous velocity as a function of increasing dimensionless stroke length. Figure 5.1a illustrates the universal jet formation time as documented by Gharib et al. [24]; it can be seen that V_{max} occurs halfway through the vortex formation. An increase in stroke length from $L_0/D \approx 4$ results in the formation of a trailing jet behind the vortex, shown in figure 5.1b;[1], in this case it is thought that the peak velocity occurs at the end of the vortex formation. Even though the vortex is fully formed, there is still fluid being ejected and this is what forms the trailing jet, as once the vortex is formed there is no further roll up of fluid into the vortex. Figure 5.1b suggests that V_{max} should occur at approximately the interface between the formed vortex ring and the trailing jet. However, it can be seen from figure 5.3, that the maximum velocity occurs at the point indicated by the arrow; this is because the fluid contained in the trailing jet is at a higher velocity than that of the vortex ring, leading

[1] Which can be seen from the PIV measurements taken in figure 5.2f

to V_{max} being in the centre of the vortex ring in this case. Figure 5.4, for L_0/D=12, shows V_{max} occurring approximately in the centre of the vortex ring. In figure 5.1b the dotted sine wave represents L_0/D=12 and it shows that for this stroke length V_{max} should occur just beyond the stage of vortex formation. For H/D=8, Re=1500, and L_0/D=12, vortex formation occurs at $x/D \approx 6.5$, and from the location of the vortex ring shown in figure 5.4 ($x/D \approx 5$), the vortex ring is at the point in the synthetic jet cycle phase that is approximately 30° beyond vortex formation, meaning that V_{max} should have already occurred prior to this phase of $\phi = 150°$.

Increasing the stroke length beyond L_0/D=12, results in a large ejection of fluid and it can be seen from figure 5.1c that the vortex formation constitutes only a fraction of the overall ejection time; a large majority of the ejected fluid forms a trailing jet. Figures 5.2f and 5.2g show the trailing jet appearing slightly less coherent and there appears to be a degree of detachment from the vortex ring. As the flow progresses through the cycle, there is vortex impingement shown in figure 5.2h. The vortex impinges axially on the stagnation region, where there is a decrease of axial velocity and an increase in static pressure, whilst concurrently accelerating in the radial direction. This results in the vortex rollup experienced at the periphery of the impact zone, resulting in the observable vortices on the impingement plate at $r/D \approx 2.5$, figure 5.2i-l. The cycle then repeats itself. It is worth noting that few authors, with the exception of Cater and Soria [85] and Crittenden and Glezer [129] have documented synthetic jet formation or the evolution of an ejection much further than L_0/D=10.

Figure 5.1b shows that at L_0/D=8 once V_{max} is reached at the end of vortex formation a trailing jet follows until the end of the ejection stroke. Even though the PIV measurements taken show that there is a weak trailing jet at this stroke length, it has not been found to have a huge impact on the vortical structures present in the flow, as shown in figure 5.5. The effects of the trailing jet will be explained in detail in section 6.2.

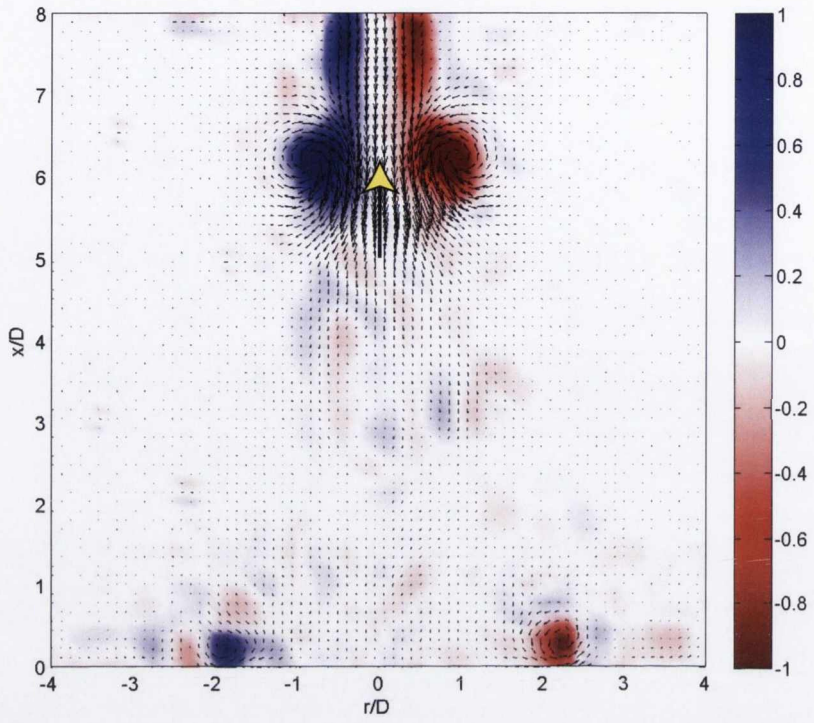

Figure 5.3 – H/D=8, Re=1500, L_0/D=8, $\phi \approx 150°$. Yellow arrows indicate points of interest.

5.1.0.5 Findings

This section on synthetic jet flow regimes outlined and confirmed the basis of a formation number for synthetic jet formation (L_0/D=4), as documented in the literature. The maximum circulation for a vortex ring was shown to occur at a dimensionless stroke of L_0/D=4, and beyond this formation number, a trailing jet was formed behind the leading vortex. Despite the existence of a trailing jet at stroke lengths higher than L_0/D=4, the trailing jet is seen to only effect the vortex ring at stroke length values higher than L_0/D=8.

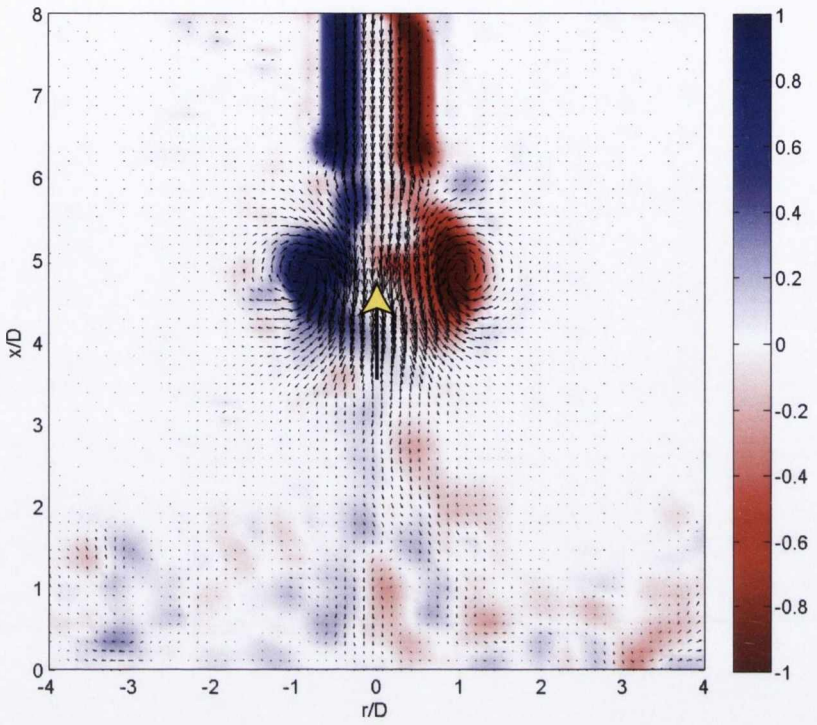

Figure 5.4 – H/D=8, Re=1500, L_0/D=12, ϕ≈150°. Yellow arrows indicate points of interest.

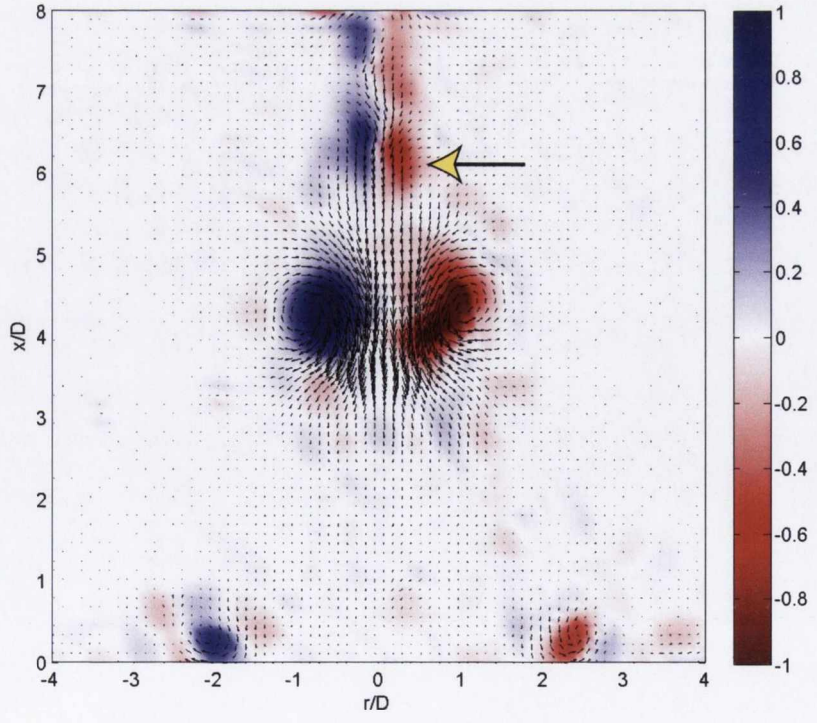

Figure 5.5 – Weak trailing jet, H/D=8, Re=1500, L_0/D=8, ϕ≈210°. Yellow arrows indicate points of interest.

5.2 Time averaged particle image velocimetry

Time averaged PIV measurements were obtained at low frame rates in order to provide a longer recording duration of the synthetic jet flow; this provides mean flow fields that illustrate how changes in the stroke length and Reynolds number can affect the flow in the mean. One of the main interests of a time averaged flow as presented in figure 5.6 is the streamlines that represent the recirculation, entrainment and flow structures in the field of view. The average vector field that is used to produce figure 5.6 is calculated initially with LaVision's DaVis program from the long exposure data of the synthetic jet flow according to the equation in the DaVis software [102].

$$V_{avg} = \frac{1}{n}\sum_{i=1}^{n}(V_i) \tag{5.1}$$

Upon completion of the statistical analysis to provide the average velocity field data, it is then further processed with purpose written Matlab code in order to generate a vorticity overlaid with streamlines plot as shown in figure 5.6. From these mean flow fields, the mean streamline patterns are derived from the streamslice function in Matlab which consist of streamlines derived from slice planes of the vector field data (U, V). Mean jet width, recirculation zones and vorticity concentration are presented in these plots. The flow is considered axisymmetric, therefore if necessary only one half of the flow domain needs to be shown, but for clarity the full flow domain is presented here; when referring to radial locations only the positive r/D locations will be noted, in order to reduce clutter. Where applicable, the time averaged synthetic jet flow is compared to instantaneous PIV data in order to highlight noteworthy flow field characteristics. For the entire range of time averaged data presented here, the effect of the synthetic jet stroke length for varying Reynolds number is presented.

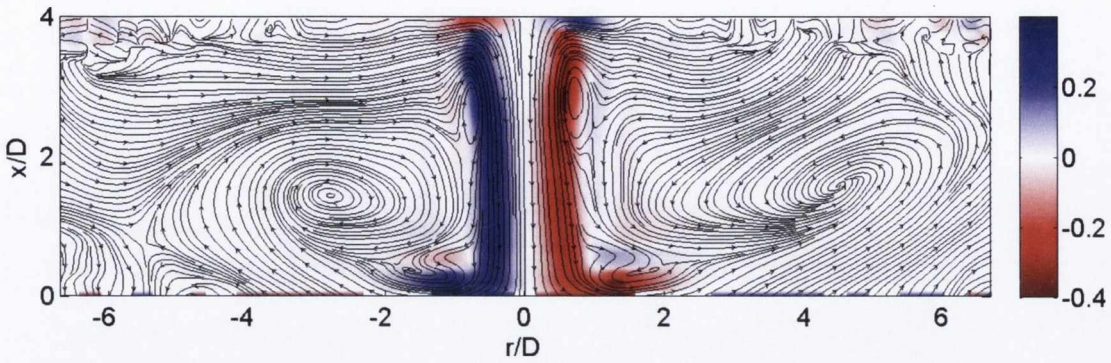

Figure 5.6 – Time averaged streamwise vorticity with streamlines overlaid for H/D=4, Re=500, L_0/D=4

5.2.1 Axial spacing of 4 jet diameters (H/D=4)

5.2.1.1 $L_0/D = 4$

Figure 5.6 shows the mean streamline pattern for a synthetic jet formed at H/D=4, Re=500 and L_0/D=4. The closed streamlines present either side of the jet centreline at $x/D \approx 3$ suggest small recirculation regions, or a stationary vortex, arising from the formation and passage of the vortex rings that are generated at L_0/D=4; a similar stationary vortex ring was observed by Mallinson et al.[130] and Cater and Soria [85]. The formation location of the vortex for these parameters is $x/D \approx 3.5$, the occurrence of the closed streamlines in figure 5.6 is thought to be due to the frequent passage of a fully formed vortex ring that feels no effect from the suction portion of the cycle at this stroke length. Referring to figure 5.1a, it can be seen that at this stroke length ($L_0/D \approx 4$), there is no trailing jet present. Once the vortex has formed and the ejection stroke begins again, another vortex is formed at a very short time interval after the previous vortex, leading to the frequent passage of vortex rings at the x/D location indicated. The streamlines reveal a low pressure prevailing near the orifice that draws fluid from the ambient fluid and along the face of the orifice plate. The sink like flow that arises from this low pressure can be seen to affect the ambient fluid up to $x/D \approx 2$, just beneath the closed recirculation regions that are present. There is a noticeable narrowing of the jet as the flow develops before impingement in figure 5.6.

At Re=500 and L_0/D=4, the jet velocity is relatively low, and without the presence of a trailing jet, the vortex seems to lose its celerity, and with a loss of momentum its core diameter appears to shrink. An instantaneous velocity plot in figure 5.7 at $\phi = 287°$ for the same test parameters of H/D=4, Re=500 and L_0/D=4 shows a reduction in vortex diameter prior to impingement, (the dashed lines indicate the formed vortex centre at $x/D \approx 3$) which is visible in the time averaged plot of figure 5.6.

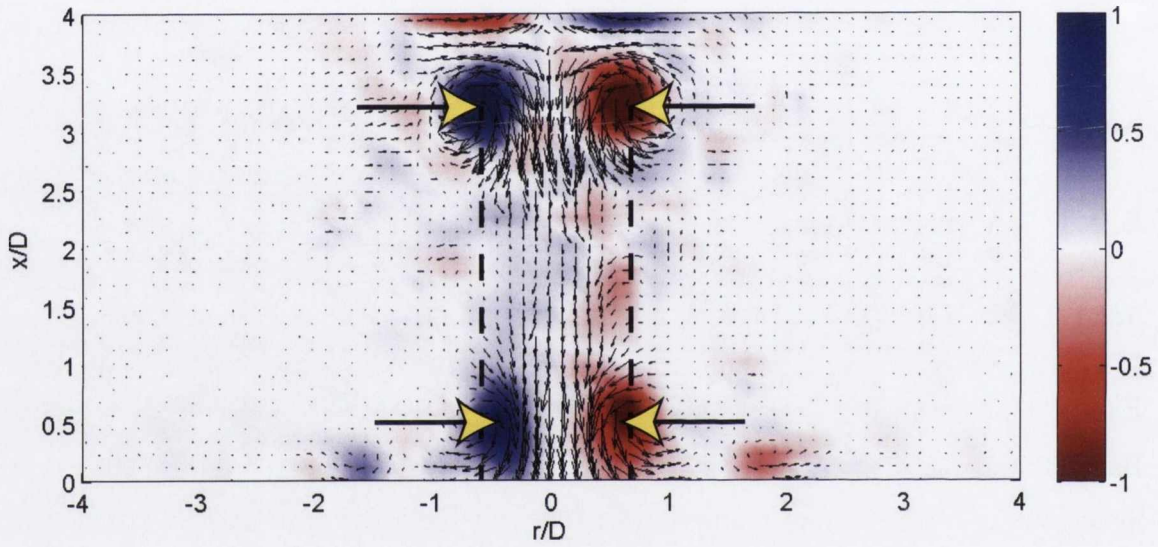

Figure 5.7 – H/D=4, Re=500, L_0/D=4. Instantaneous velocity plot at ϕ=287°, illustrating vortex diameter reduction, yellow arrows indicate the vortex centres.

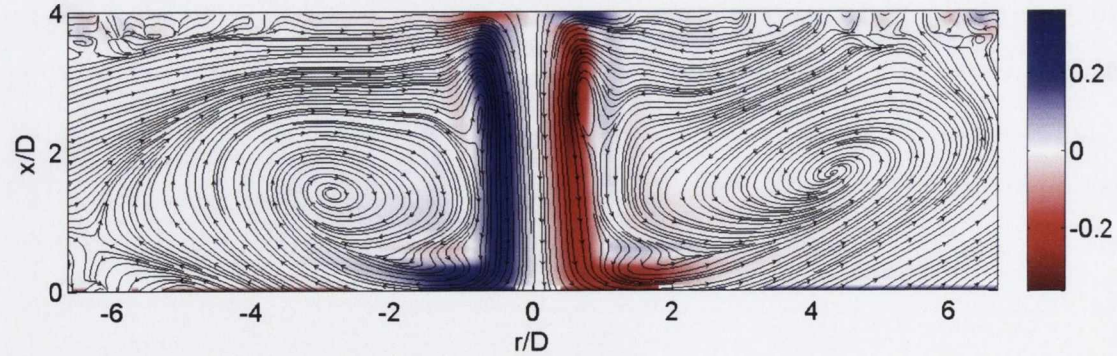

Figure 5.8 – Time averaged streamwise vorticity with streamlines overlaid for H/D=4, Re=1000, L_0/D=4

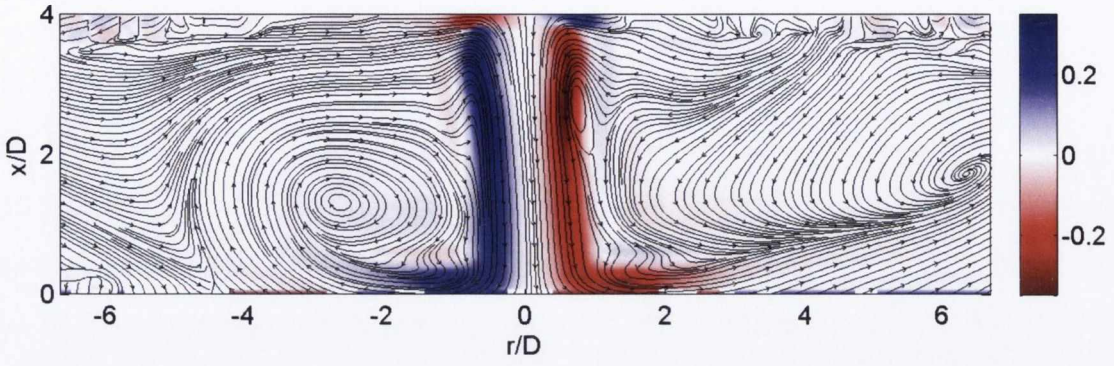

Figure 5.9 – Time averaged streamwise vorticity with streamlines overlaid for H/D=4, Re=1500, L_0/D=4

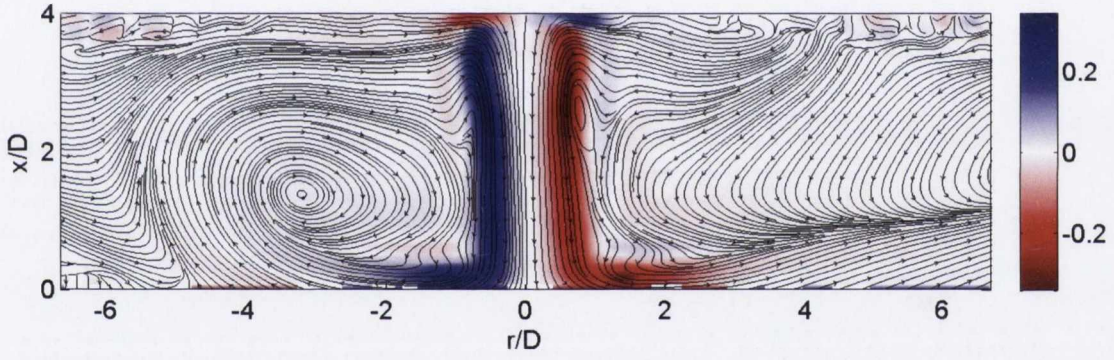

Figure 5.10 – Time averaged streamwise vorticity with streamlines overlaid for H/D=4, Re=2000, L_0/D=4

Figure 5.8 to figure 5.10 show the effect of increasing Reynolds number for the same dimensionless stroke length and jet to plate spacing. All three of these time averaged plots exhibit a similar feature to that of figure 5.6, which is the apparent narrowing of the synthetic jet as it evolves over the axial spacing of H/D=4. The time averaged plots presented here indicate a Reynolds number independence i.e. the plots for different Reynolds number but with a stroke length held constant exhibit similar overall flow features. Thus, one of the main parameters that dictates a synthetic jet flow has been changed, with a marginal effect on the overall flow structure. The streamlines in these time averaged plots clearly show the entrainment pattern of the synthetic air jet. For L_0/D=4, the streamlines exhibit a slight asymmetry in the flow; this is

due to the type of flow created at this stroke length. Thus, where there is a train of vortices (with no trailing jet), the small but pervasive cross flow that was present in the testing environment[2] had a slight effect on the flow and was observed at this stroke length for all Reynolds numbers. This cross flow does not significantly influence the performance of the synthetic air jet, as heat transfer data presented from within the research group has shown [7]. The streamlines plotted for all the time averaged data exhibit several interesting features of the synthetic jet flow. In figures 5.6 to 5.10, it can be seen that at high x/D the streamlines approach the jet centre normal to it and deflect upstream at the shear layer and turn downstream as they enter the higher velocity region near the jet axis. With a progression downstream ($x/D \approx 2$), it can be seen that the streamlines do not deflect upstream. The upstream streamlines deflect in this manner due to the influence of the suction stroke of the synthetic jet cycle. At this stroke length, the closed recirculation region at $x/D \approx 3$ results in a variation in the spacing of the streamlines near the orifice, which is indicative of a flow that is accelerating, decelerating and then accelerating in sequence, due to this mean recirculation region. From visual inspection of the flow at this stroke length, this sequence is clearly discernible.

5.2.1.2 $L_0/D = 8$

Figures 5.11 to 5.14 present time averaged streamline plots for H/D=4 and L_0/D=8, at four different Reynolds numbers of 500, 1000, 1500 and 2000. Overall the data indicate a Reynolds number independence, which is due to the presence of very similar flow structures in each figure for different formation parameters. As the dimensionless stroke length is increased, referring to figure 5.1b, at L_0/D=8 a trailing jet is now present. At this stroke length it is relatively weak in comparison to the trailing jet formed at higher stroke lengths, shown in figure 5.5, thus it does not influence the vortical structures present in the flow as much as it does at higher stroke lengths. Figure 5.11 shows the presence of strong vortices residing at r/D=2 on the impingement surface, indicated by the closed streamlines and dense colouring of the vorticity.

[2] The cause of this cross flow is explained in section 4.1.1.

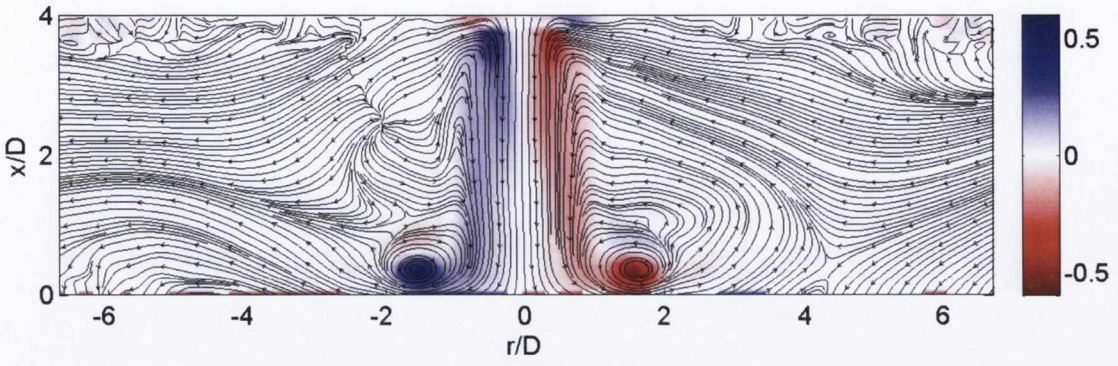

Figure 5.11 – Time averaged streamwise vorticity with streamlines overlaid for H/D=4, Re=500, L_0/D=8

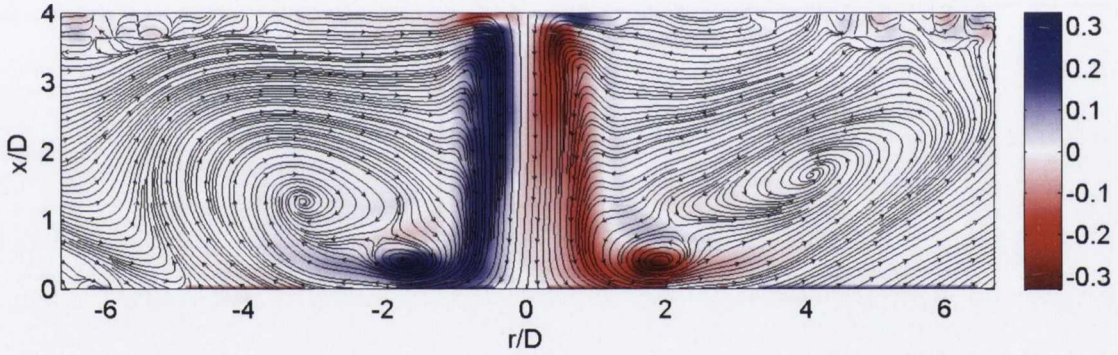

Figure 5.12 – Time averaged streamwise vorticity with streamlines overlaid for H/D=4, Re=1000, L_0/D=8

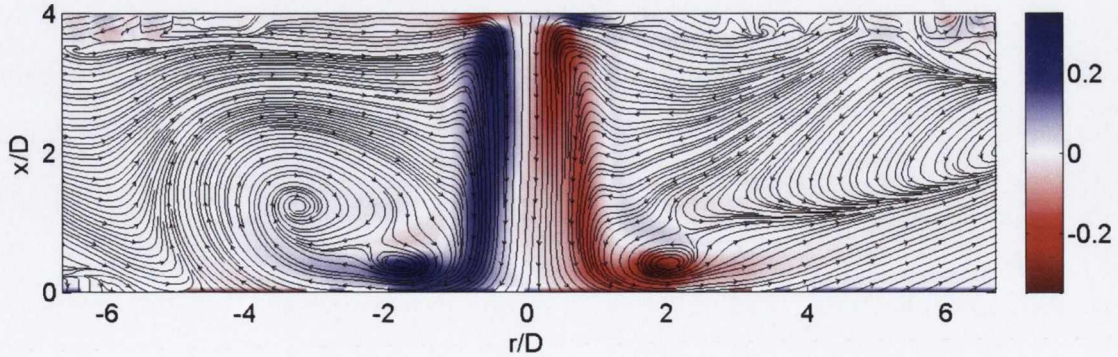

Figure 5.13 – Time averaged streamwise vorticity with streamlines overlaid for H/D=4, Re=1500, L_0/D=8

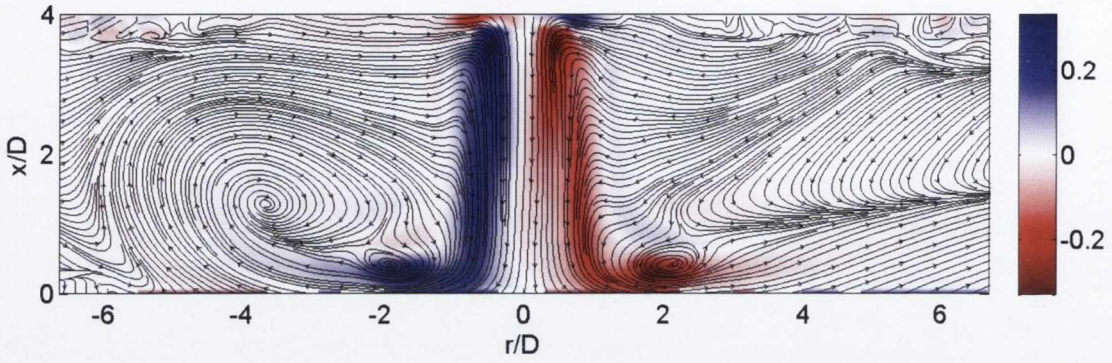

Figure 5.14 – Time averaged streamwise vorticity with streamlines overlaid for H/D=4, Re=2000, L_0/D=8

There is a distinct difference between the time averaged data for L_0/D=4 in section 5.2.1.1 and that of L_0/D=8 in section 5.2.1.2, that is the presence of vortices on the impingement surface at r/D=2. Closed streamlines along with regions of dense colour, signifying a stationary vortex at r/D=2, are present in figures 5.11 through to figure 5.14. Contours of the streamwise vorticity, ω_z, with an overlay of velocity vectors from instantaneous PIV data are presented in figure 5.15 at twelve incremental phase angles of $\phi \approx 30°$, for one complete synthetic jet cycle at H/D=4, Re=500 and L_0/D=8. Figure 5.15 provides a visual aid to explain the presence of the residing vortices on the impingement surface; the colour bar applies to all images in figure 5.15, with red signifying negative vorticity and blue positive. Figure 5.15a at $\phi = 0°$ indicates, with the aid of arrows, the residing vortices from the previous synthetic jet cycle. Figure 5.15b shows the emergence of a vortex ring and the presence of vortices that have impinged from the previous cycle and deconstructed into smaller scale vortices residing at r/D=2. Figure 5.15c indicates that these vortices are still present at $\phi \approx 60°$. Figures 5.15d-g show the developing flow, the vortex forming and the emergence of a weak trailing jet[3]. Upon impingement in figure 5.15h, the vortex ring breaks down and interacts with the residing vortices that are present at r/D=2 on the impingement plate. As the flow accelerates radially and begins the process of vortex roll up, there is an interaction between these vortices, seen and indicated by

[3] The trailing jet at L_0/D=8 is weak, shown in figure 5.15h.

the arrows in figure 5.15i and figure 5.15j. Vorticity of opposite sign can be seen at r/D=2 in figure 5.15j where the vortex has rolled up subsequent to impingement and interacted with the vortex that was already present on the impingement plate. This leads to the vortex that had been present on the impingement plate being absorbed, resulting in an increase of the vorticity present within the vortex that will now be the new residing vortex on the impingement surface, seen in figure 5.15k and indicated in figure 5.15l. This is the process that leads to the closed recirculation regions and stationary vortex seen in the time averaged plots of figures 5.11 to 5.14 at their respective radial locations of r/D=2.

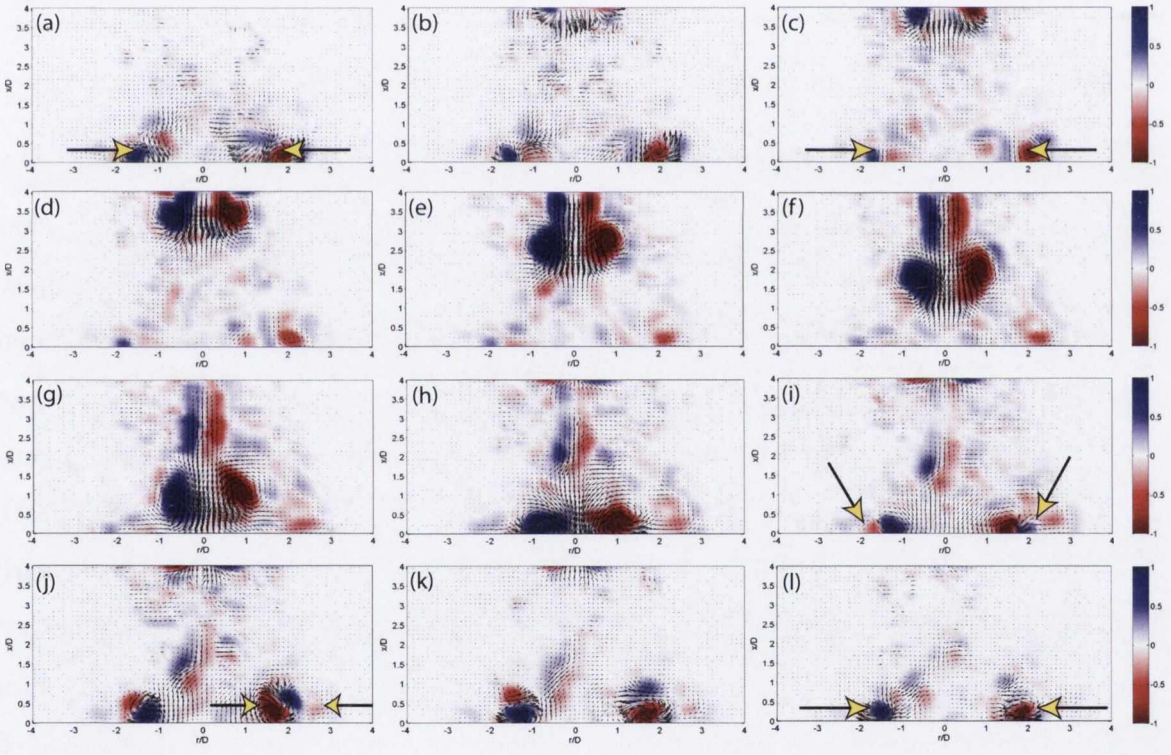

Figure 5.15 – A complete cycle of a synthetic air jet from instantaneous high frame rate PIV. Contours of the streamwise vorticity, ω_z with an overlay of velocity vectors at phase increments $\phi \approx 30°$, starting from ϕ=0°. H/D=4, Re=500, L_0/D=8. Yellow arrows indicate points of interest.

There is an increase in the power of the suction stroke portion of the synthetic jet cycle as the jet Reynolds number is increased, seen in the streamlines of figures 5.11

to 5.14. The approach of the streamlines near to the orifice ($r/D \approx 1$) is normal to the y-axis with a strong deflection upstream indicating that the suction stroke portion of the cycle is quite influential as the ambient fluid experiences the sink like flow from as far as $r/D \approx 4$. The streamlines deflect upstream at the shear layer and turn downstream once they enter the jet centre. The closed streamlines present at $r/D = 2$ are the stationary vortices previously discussed. There are large recirculation regions also present in the surrounding bulk fluid at $r/D \approx 4$, which are present partly due to the influence of these strong residing vortices on the impingement plate at $r/D = 2$. These recirculation regions can be seen in figure 5.13 and figure 5.14. Confinement and recirculation affects a synthetic air jet flow at lower axial spacings i.e. when comparing these effects at H/D=4 to H/D=8, it can be seen that these effects are more pronounced at the lower axial spacing.

5.2.1.3 $L_0/D = 12$

The time averaged plots presented for H/D=4, L_0/D=12, display similar flow characteristics to those of the time averaged plots for H/D=4, L_0/D=8 presented in section 5.2.1.2, the main similarity being the strong vortices present on the impingement surface at a radial spacing of $r/D \approx 2$. The increase in stroke length leads to a larger volume of fluid being ejected, thus more fluid impinging on the plate. This, in turn, leads to larger recirculation regions present in the ambient fluid, as can be clearly seen in figures 5.16 to 5.19. The entrainment pattern of the synthetic air jet is clearly illustrated by the streamlines in these figures for H/D=4, L_0/D=12. The strength of the stationary vortex on the impingement plate at the four different Reynolds numbers presented for L_0/D=12 appears to be reduced in comparison to that of L_0/D=8. One hypothesis for this apparent reduction in vortex strength can be drawn from the instantaneous PIV data presented in figure 5.20, in which the data are presented in the same manner as for figure 5.15.

At $r/D \approx 3$ the presence of vortices from the previous synthetic jet cycle can be seen in figure 5.20a. These vortices appear to dissipate by the time the vortex emerges in figure 5.20c, unlike those in figure 5.15b that remain in the field of view. Figure 5.20c

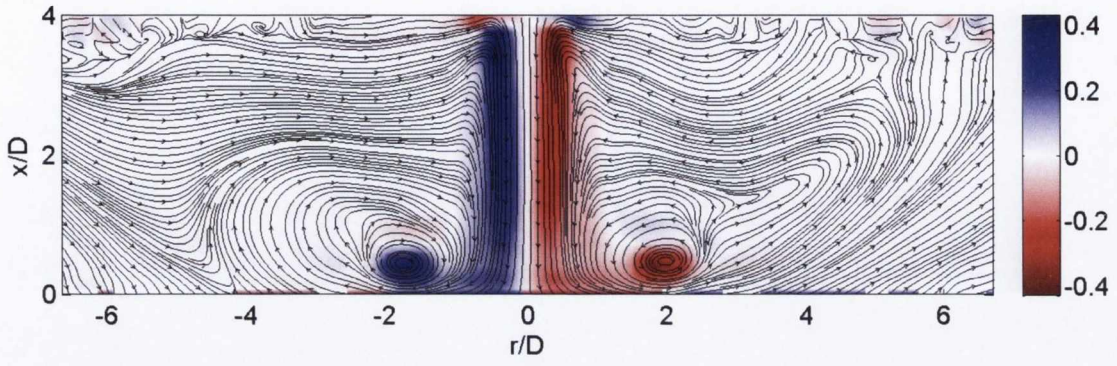

Figure 5.16 – Time averaged streamwise vorticity with streamlines overlaid for H/D=4, Re=500, L_0/D=12

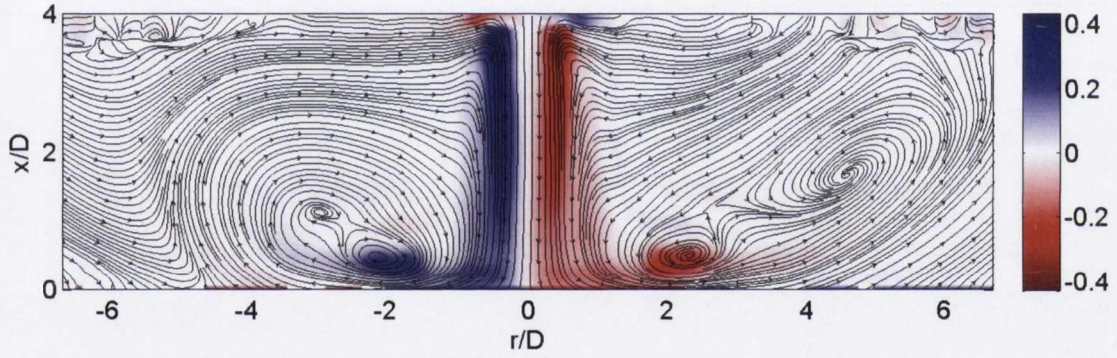

Figure 5.17 – Time averaged streamwise vorticity with streamlines overlaid for H/D=4, Re=1000, L_0/D=12

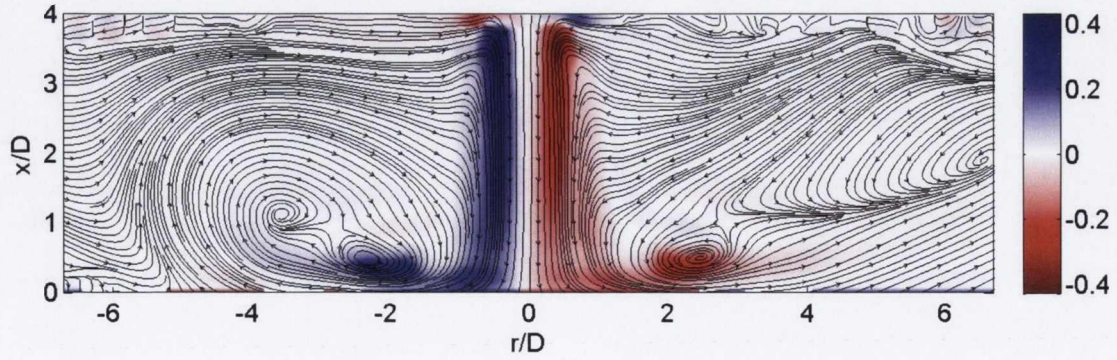

Figure 5.18 – Time averaged streamwise vorticity with streamlines overlaid for H/D=4, Re=1500, L_0/D=12

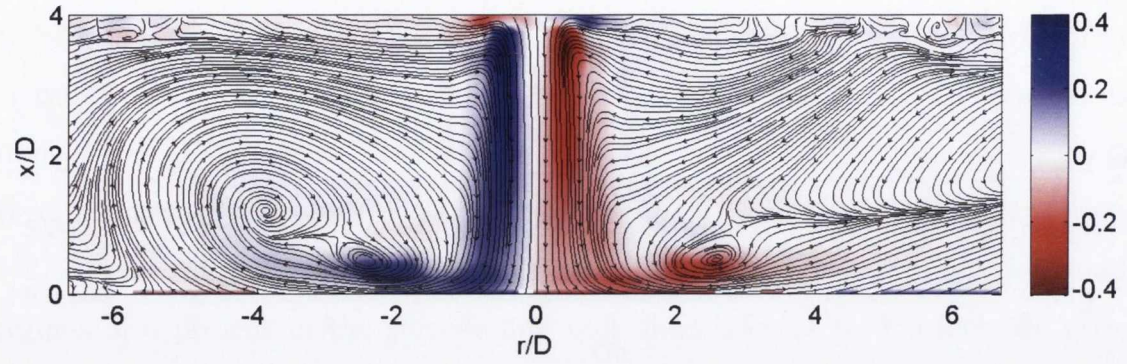

Figure 5.19 – Time averaged streamwise vorticity with streamlines overlaid for H/D=4, Re=2000, L_0/D=12

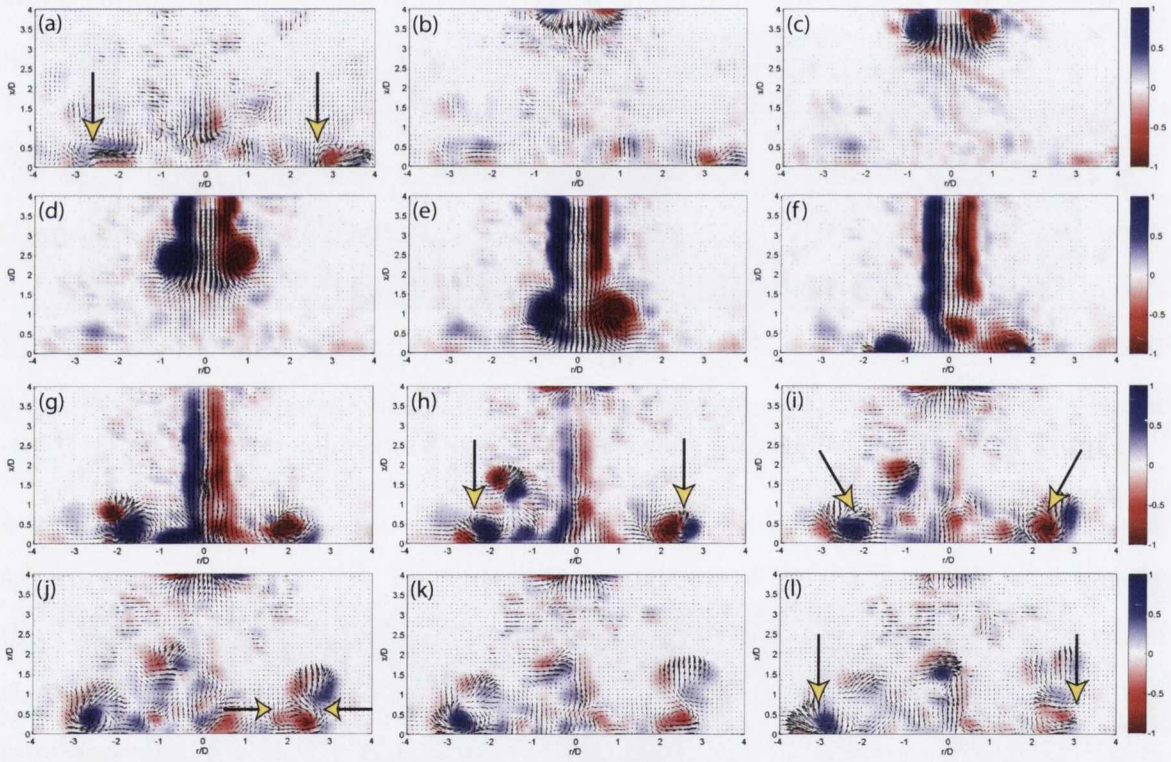

Figure 5.20 – A complete cycle of a synthetic air jet from instantaneous high frame rate PIV. Contours of the streamwise vorticity, ω_z with an overlay of velocity vectors at phase increments $\phi \approx 30°$, starting from $\phi = 0°$. H/D=4, Re=1000, L_0/D=12. Yellow arrows indicate points of interest.

shows that there is evidence of vorticity still on the impingement surface at $r/D = 3$ but there is no coherency to the structures present, which indicates the vortices have

nearly dissipated. The increase in strength of the trailing jet can be seen in figure 5.20g. The vortices that roll up on the impingement surface reach a greater radial distance in figure 5.20l than those at L_0/D=8, seen in figure 5.15l. The small but pervasive cross flow that was present in the testing environment had a slight effect on the flow and was observed at this stroke length for all Reynolds numbers, which can be seen in figures 5.16 to 5.19. It is worth noting that the recirculation regions for the time averaged plots presented for L_0/D=12 are all similar in magnitude and radial spreading despite the slight effect of the cross flow.

5.2.1.4 $L_0/D = 16$

Time averaged plots for H/D=4, L_0/D=16 are presented in figures 5.21 to 5.24. The flow structures present at this stroke length are more uniform, thus verifying the axisymmetric nature of the synthetic jet. The higher stroke length means a larger ejection of fluid, therefore more fluid contributes to the recirculation regions, and a stronger suction stroke as indicated by the streamlines that deflect strongly upstream. The uniformity of the flow that is seen in these plots is quite remarkable, even with the developing flow having to overcome the effects of recirculation and confinement. As the Reynolds number is increased, the radial distance that the vortices roll up and travel to, on the impingement surface increases. A stationary vortex is present at $r/D \approx 2$ for all the Reynolds numbers presented here for L_0/D=16. However, as the jet Reynolds number is increased, there is an apparent widening of the jet, indicated by the r/D locations that the vorticity of the shear layer of the jet spreads to. The vortex ring detaches from the trailing jet at this stroke length and impinges before the trailing jet, which then impinges and forces the vortices that had subsequently rolled up from the impinging vortex ring to spread further; this is shown in the instantaneous PIV data presented in figure 5.25. The data presented in figure 5.25 is displayed in the same manner as that in figure 5.20. The instantaneous PIV data shown in figure 5.25 reveals how the vortex ring is destroyed upon impingement by the trailing jet, which is indicated by arrows in figure 5.25e.

As the stroke length is increased there is an increase in the magnitude of the trailing

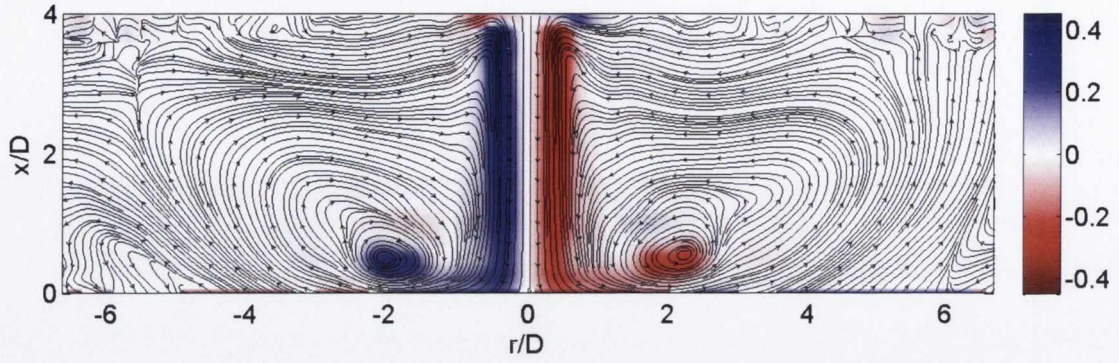

Figure 5.21 – Time averaged streamwise vorticity with streamlines overlaid for H/D=4, Re=500, L_0/D=16

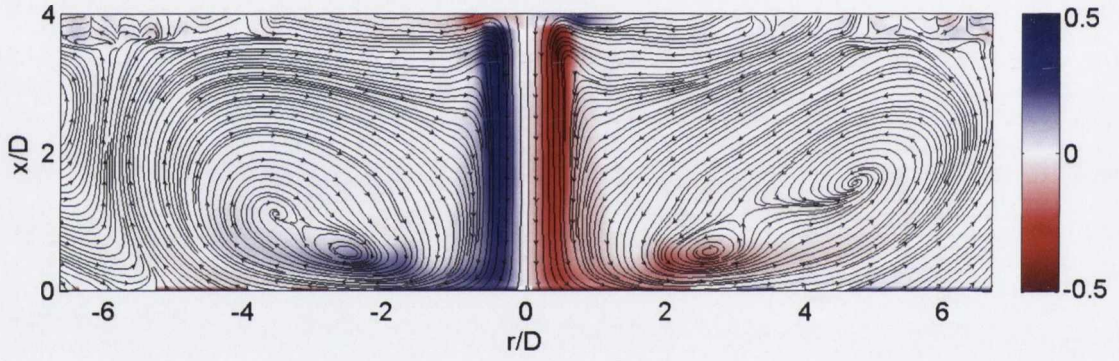

Figure 5.22 – Time averaged streamwise vorticity with streamlines overlaid for H/D=4, Re=1000, L_0/D=16

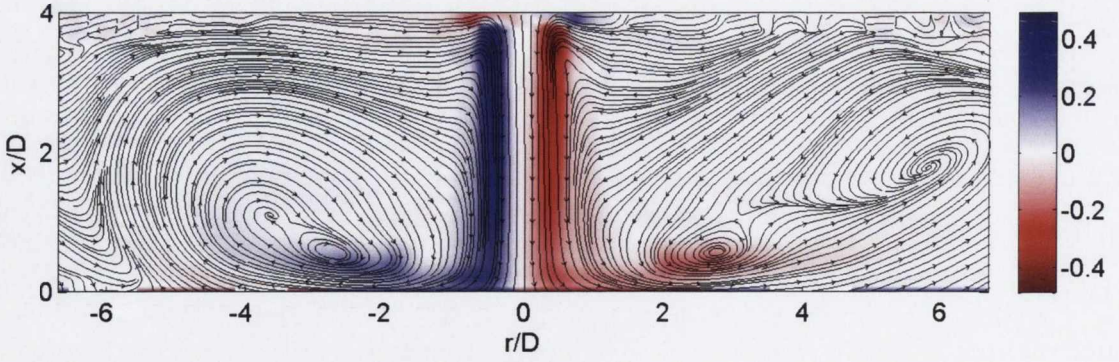

Figure 5.23 – Time averaged streamwise vorticity with streamlines overlaid for H/D=4, Re=1500, L_0/D=16

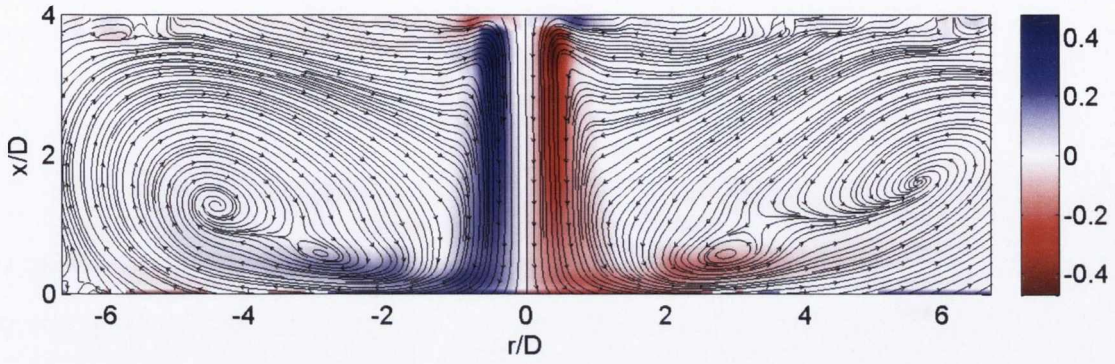

Figure 5.24 – Time averaged streamwise vorticity with streamlines overlaid for H/D=4, Re=2000, L_0/D=16

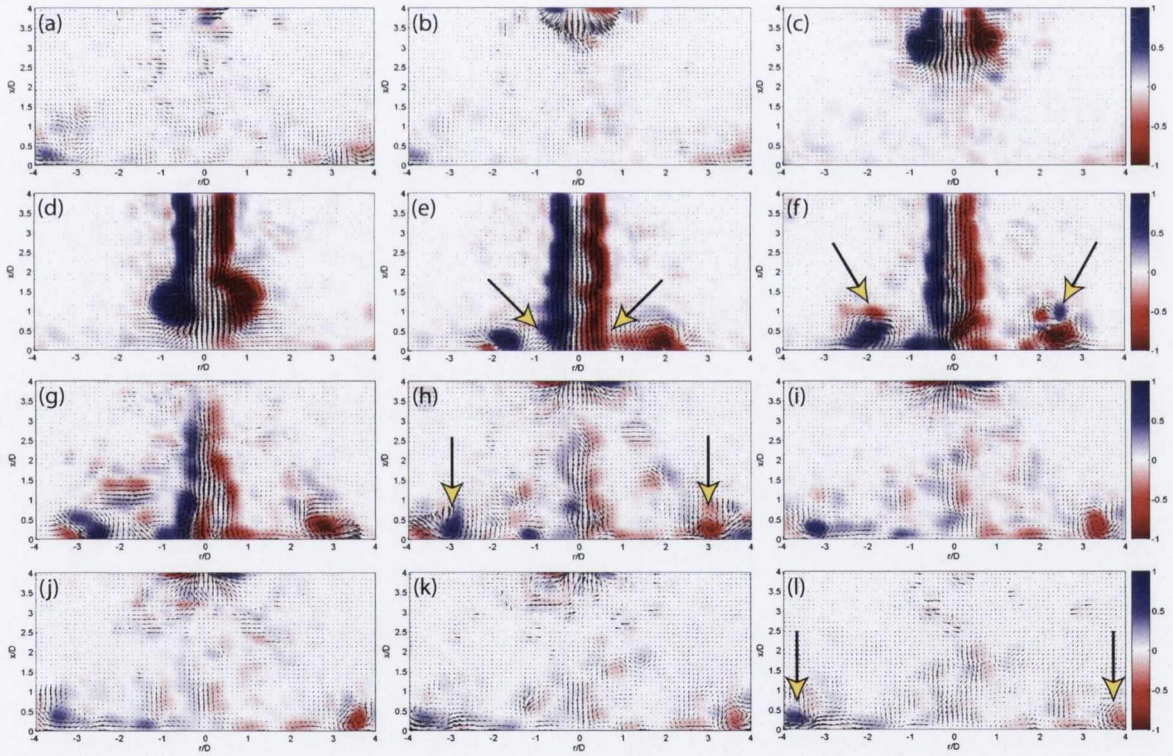

Figure 5.25 – A complete cycle of a synthetic air jet from instantaneous high frame rate PIV. Contours of the streamwise vorticity, ω_z with an overlay of velocity vectors at phase increments $\phi \approx 30°$, starting from $\phi = 0°$. H/D=4, Re=2000, L_0/D=16.

jet that is present once the vortex has been formed; this is evident from the data shown in figure 5.25. Referring to figure 5.1c for L_0/D=16, the trailing jet encompasses approximately 75% of the ejection stroke, if the time for vortex formation is

$L_0/D \approx 4$. If a comparison of the flow structures present in figure 5.25 to those of figure 5.20 is performed, it can be seen that they are two very different flows indeed. The most obvious difference is the strength of the trailing jet that is generated. Thus, for L_0/D=12 in figure 5.20 the trailing jet is present and influential on the vortex ring, but not to the extent that it dictates the evolution of the flow, as is the case in figure 5.25 at L_0/D=16. It is evident that once the vortex impinges, figure 5.25e, the trailing jet impinges shortly after. The vortex path appears to be somewhat discontinuous upon impingement, seen in figure 5.24 at $r/D \approx 1.8$ and seen in figure 5.25e at approximately the same radial location. The vortex ring moves from impingement to commencing vortex roll up and before it has a chance to complete vortex roll up, the high velocity trailing jet forces the vortices along the impingement surface creating the neighbouring areas of strong vorticity seen in figure 5.25f. The two areas of closed streamlines present in figures 5.22 to 5.24 at $r/D \approx 3$ and $r/D \approx 4$ are a direct result of the vortices travelling in the radial direction. Figure 5.25i-l show the radial distance that the vortices reach along the impingement surface, $r/D = 4$.

5.2.1.5 $L_0/D = 32$

The time averaged plots presented for H/D=4, L_0/D=32 show the strength of the trailing jet generated at a large stroke length. Figure 5.1c illustrates the ejection stroke of a synthetic jet cycle at L_0/D=32.

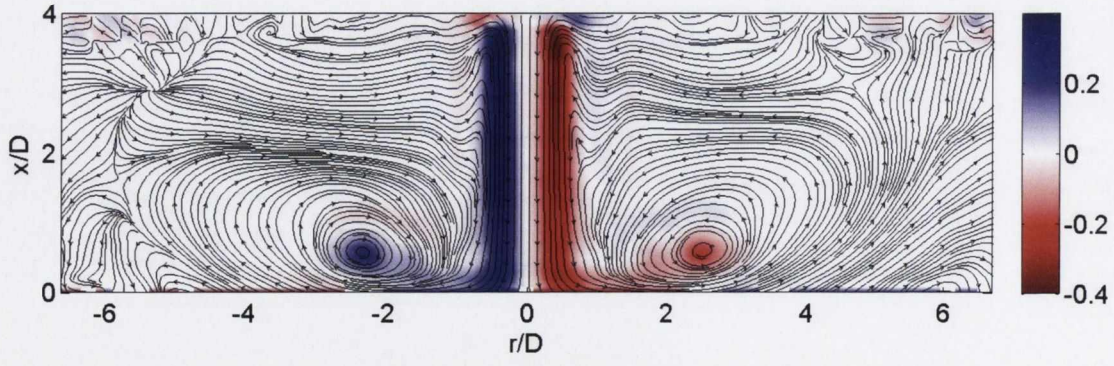

Figure 5.26 – Time averaged streamwise vorticity with streamlines overlaid for H/D=4, Re=500, L_0/D=32

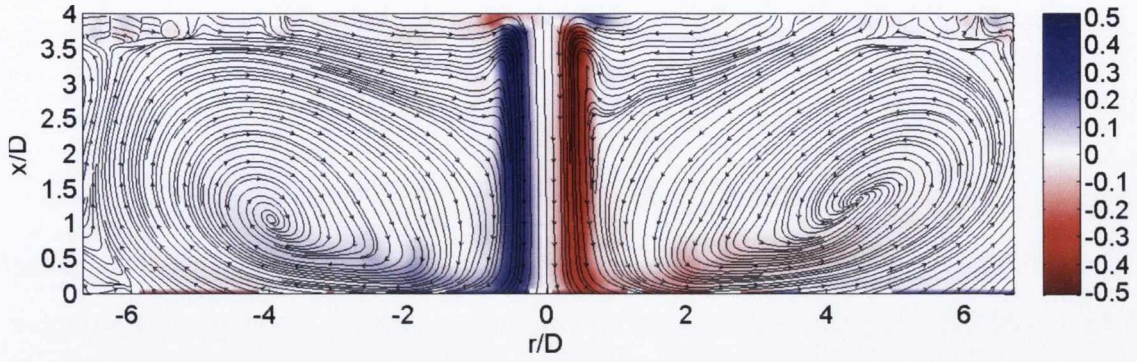

Figure 5.27 – Time averaged streamwise vorticity with streamlines overlaid for H/D=4, Re=1000, L_0/D=32

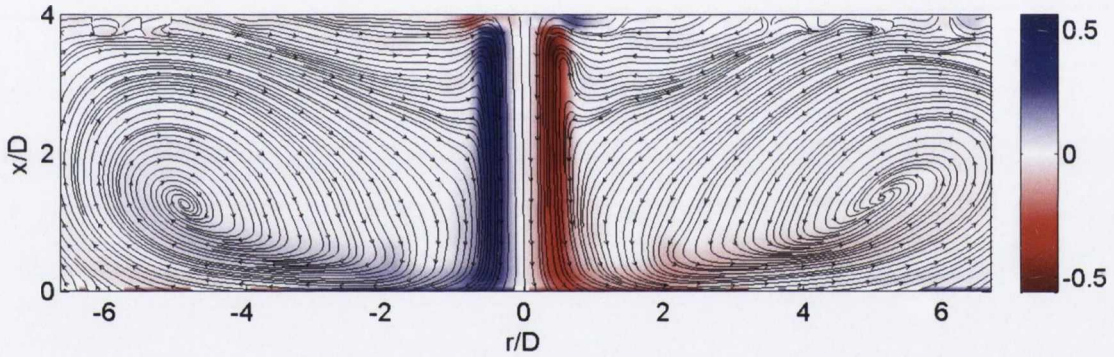

Figure 5.28 – Time averaged streamwise vorticity with streamlines overlaid for H/D=4, Re=1500, L_0/D=32

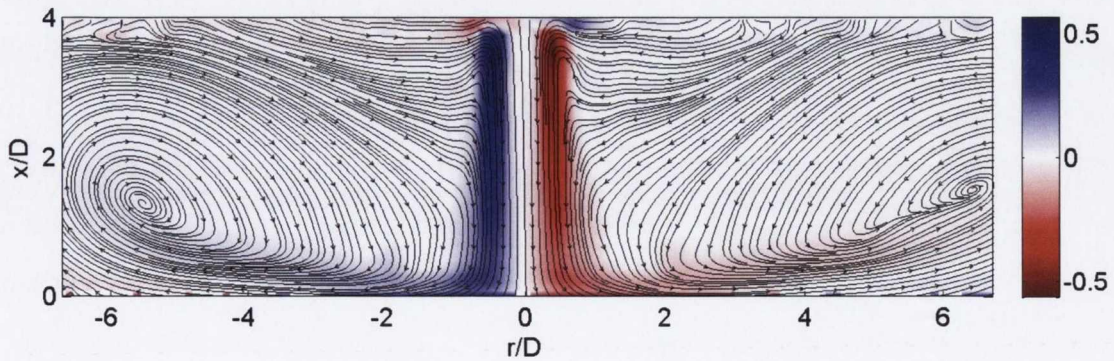

Figure 5.29 – Time averaged streamwise vorticity with streamlines overlaid for H/D=4, Re=2000, L_0/D=32

With reference to figure 5.1c, the formation time taken to produce the trailing jet for the ejection portion of the synthetic jet cycle is quite large when compared to the rest of the stroke lengths tested here. Inspection of the time averaged plots of figures 5.26 to 5.29, shows the symmetric nature of the synthetic jet flow at this stroke length, with large recirculation zones occurring in the surrounding fluid, extending as far as $r/D = 6$. Figure 5.30 shows instantaneous PIV data that helps to explain the reason for the occurrence of the large recirculation zones seen in the time averaged plots. The r/D values shown in figure 5.30 extend to r/D of ± 6 because of the distance that the vortices travel along the impingement surface. The recirculation regions in three of the time averaged plots extend to nearly the full distance of the axial spacing of H/D=4, as indicated by the streamlines in figure 5.27, figure 5.28 and figure 5.29. There is evidence of a stationary vortex in figure 5.26 at $r/D \approx 2.5$, which is indicated by the closed streamlines. It can be seen in figures 5.26 to 5.29 that the streamlines deflect upstream at the shear layer and deflect downstream rather abruptly as they enter the jet centre, this is due to the increased entrainment rates at L_0/D=32. The data presented in figure 5.30 are presented in the same style as that of figure 5.25.

The trailing jet produced at L_0/D=32 requires the majority of fluid ejected at this stroke length; it is also considered to be responsible for the radial distance that the vortices travel along the plate subsequent to impingement. Figure 5.30a-c shows how rapidly the vortex reaches the impingement surface, in going from $\phi = 0°$ to $\phi = 60°$. When compared to figure 5.25a-c, it can be seen that there is a significant difference in the early stages of a synthetic jet at the higher stroke length of L_0/D=32. In figure 5.30d impingement has occurred and vortex roll up has already begun; the trailing jet is still being ejected in figure 5.30e, and imparting vorticity to the vortices that are travelling along the plate. Figure 5.30f shows several small scale vortical structures on the impingement surface that are travelling radially to $r/D = 4$. The remnants of the ejected trailing jet can be seen in figure 5.30h where the vorticity on the plate is present at the radial distance of $r/D \approx 5$. The remaining vorticity continues to travel to the indicated distance of $r/D = 6$ which account for the significant recirculation zones seen in the time averaged plots of figures 5.26 to 5.29. Figure 5.29 presents the

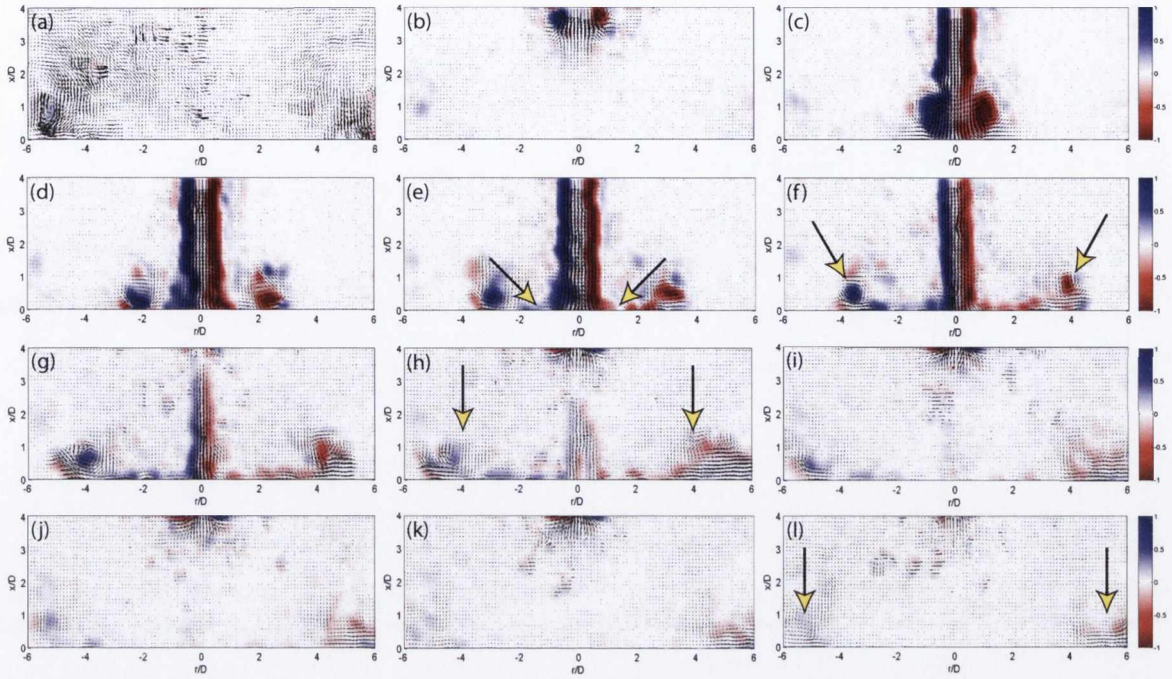

Figure 5.30 – A complete cycle of a synthetic air jet from instantaneous high frame rate PIV. Contours of the streamwise vorticity, ω_z with an overlay of velocity vectors at phase increments $\phi \approx 30°$, starting from $\phi = 0°$. H/D=4, Re=1500, L_0/D=32.

test setup with the highest velocity flow; a widening of the vorticity in the shear layer of the jet at the impingement surface occurs only at this Reynolds number. The other Reynolds number data presented in figure 5.26, figure 5.27 and figure 5.28 shows what is considered a uniform shear layer thickness right up to impingement.

It is worth noting that at this low axial spacing of H/D=4, it is difficult to pinpoint the axial location of the saddle point. For all the time averaged plots presented here for H/D=4, the approximate location of the saddle point can be seen at $x/D \approx 3$, as indicated by the streamlines.

5.2.1.6 Findings

The results for the axial spacing H/D=4 confirm the effects that recirculation and confinement have on the flow structures of a synthetic air jet. It can be seen from the flow fields presented for the range of time averaged PIV results with respect to dimensionless stroke length (L_0/D) for this axial spacing that the synthetic jet exhibits a

Reynolds number independence. However, an increase in jet Reynolds number leads to an increase in the strength of the suction stroke of the synthetic jet. The effects of the trailing jet as a result of increasing the dimensionless stroke length were confirmed with the comparison of instantaneous PIV data to the time averaged PIV data. The lower dimensionless stroke length values were seen to have closed recirculation regions due to stationary vortices on the impingement surface; as the stroke length was increased these closed recirculation regions moved further away from the shear layer of the jet.

5.2.2 Axial spacing of 8 jet diameters (H/D=8)

This section presents time averaged flow data at the higher axial spacing of H/D=8. The higher axial spacing provides time for the flow to develop, and for the trailing jet that is formed at the higher stroke lengths to further interact with the vortex ring formed prior to impingement. The overall flow characteristics seen in the time averaged plots at H/D=8 are broadly similar to those presented in section 5.2.1, but for completeness these data have been included.

5.2.2.1 $L_0/D = 2$

Figure 5.31 is included to illustrate the effect that a low stroke length of L_0/D=2 has on the synthetic jet flow. The regions of vorticity present at the orifice ($r/D = 0$) are due to the beginning of vortex formation in front of the orifice. The partially formed vortex is unable to escape the orifice due to insufficient momentum being imparted to it, thus it is ingested on the suction stroke before it has a chance to escape the vicinity of the orifice. The streamlines seen in figure 5.31 show that there is no influence on the ambient fluid seen in the field of view.

5.2.2.2 $L_0/D = 3$

Figure 5.32 presents a synthetic jet flow field for a stroke length of L_0/D=3 and Reynolds number of Re=1500 at the jet to plate spacing of 8 diameters. There is vorticity evident at the orifice exit but the vortex ring formed at this stroke length

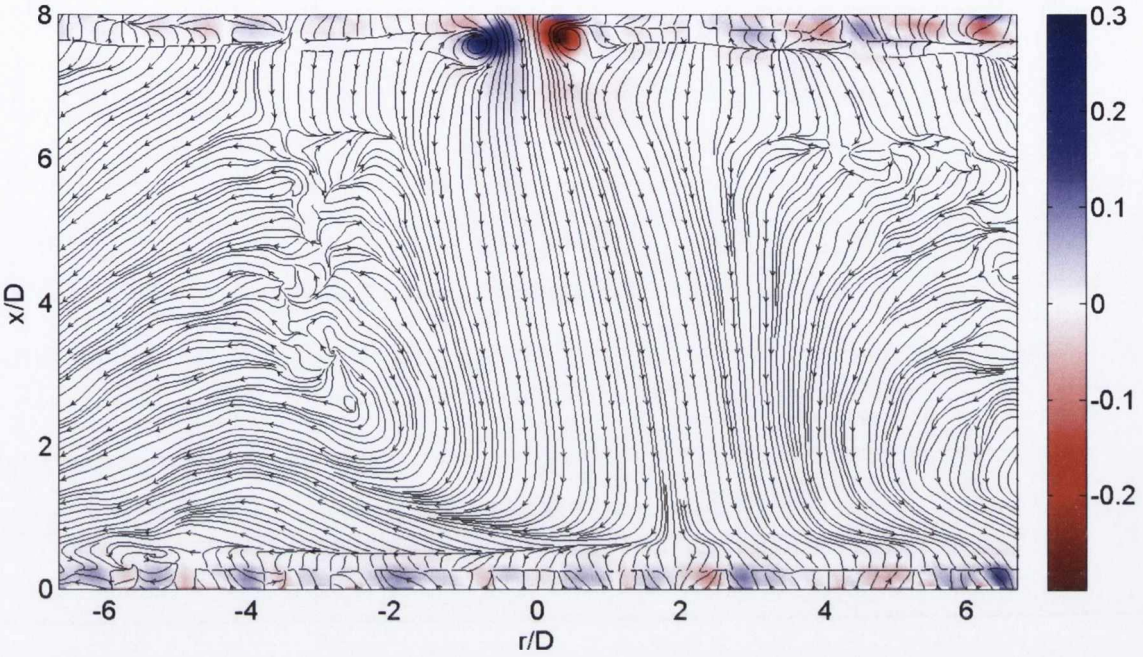

Figure 5.31 – Time averaged streamwise vorticity with streamlines overlaid for H/D=8, Re=1500, L_0/D=2

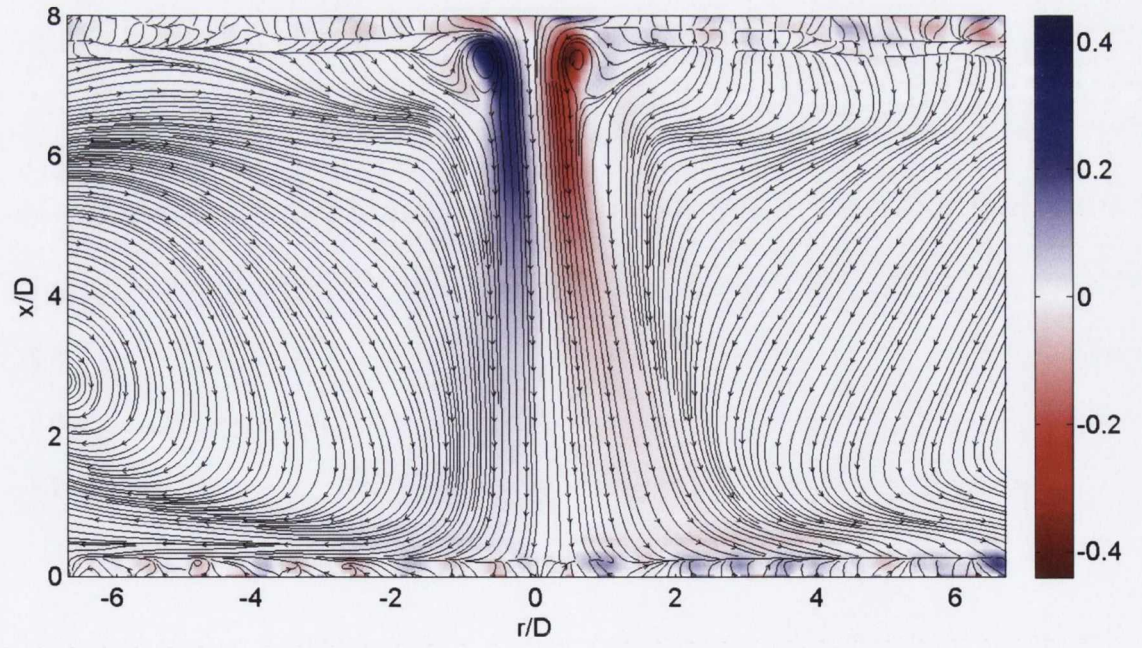

Figure 5.32 – Time averaged streamwise vorticity with streamlines overlaid for H/D=8, Re=1500, L_0/D=3

is very weak and would not be considered as an operational parameter for use in a heat transfer application, for example. From the streamlines shown in figure 5.32 it is evident that the suction stroke has little or no influence on the ambient fluid. There are recirculation regions occurring either side of the jet centre despite the reduced momentum at this stroke length. Although there is little vorticity present in the far field, there is a diminished, turbulent net flow established as is evident from the streamlines directed downstream and from the level of vorticity present. This flow is a result of a small amount of high velocity fluid at the front of the partially formed vortex. This flow has diminished momentum and at this axial spacing of H/D=8 the fluid impinging on the plate is of significantly reduced velocity (seen to begin at $x/D \approx 5$) and appears to lack periodicity.

5.2.2.3 $L_0/D = 4$

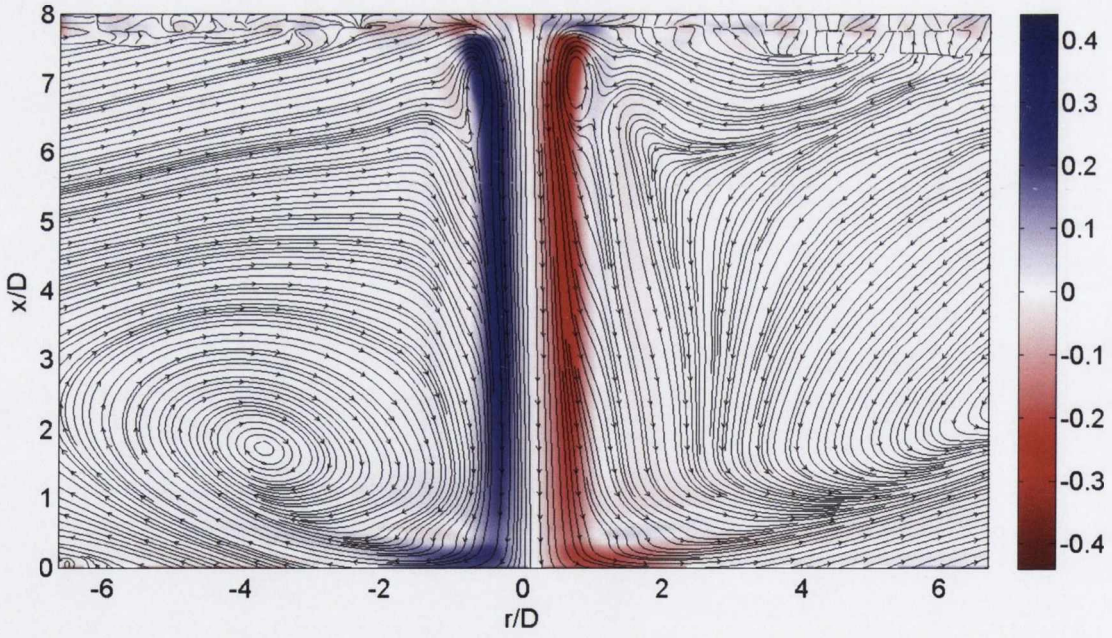

Figure 5.33 – Time averaged streamwise vorticity with streamlines overlaid for H/D=8, Re=500, L_0/D=4

The time averaged plots presented for H/D=8, L_0/D=4 show that there is an immediate difference in terms of the vorticity reaching the impingement surface when

compared to the two previous examples in figure 5.31 and figure 5.32. The closed streamlines that were present at the lower axial spacing of H/D=4 in figure 5.6 are seen here in figure 5.33 at $x/D \approx 7$; these streamlines signify the presence of a stationary vortex. This axial location compares to the location noted from figure 5.6 of $x/D \approx 3.5$ at H/D=4. The stationary vortex location is broadly similar for the cases if the distance from the orifice plate down to the axial location is considered[4], rather than the distance from the impingement plate up to the x/D location. Confinement effects are significantly reduced as the orifice to impingement spacing is increased thus, at H/D=8, the closed streamlines indicating the presence of a stationary vortex occur slightly further from the orifice plate, due to the flow being allowed to develop further.

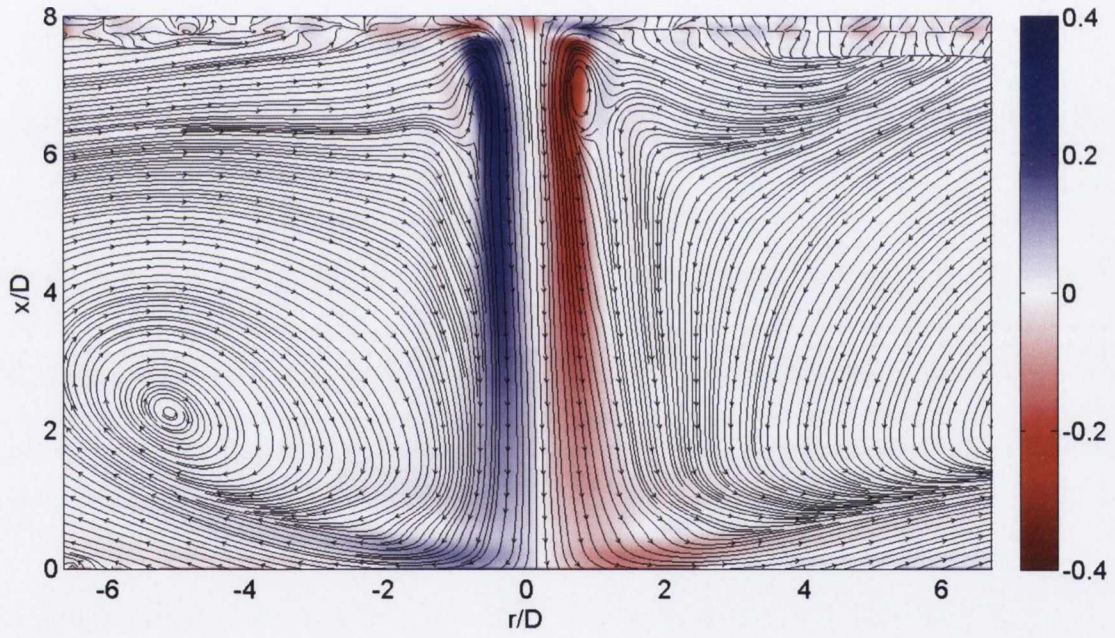

Figure 5.34 – Time averaged streamwise vorticity with streamlines overlaid for H/D=8, Re=1000, L_0/D=4

The apparent narrowing of the synthetic jet that was seen in section 5.2.1.1 is seen in figures 5.33 to 5.36. The narrowing extends to $x/D = 4$ in this case, which corresponds to the H/D=4 value for the time averaged plots in section 5.2.1.1. The increased axial spacing here allows for the flow to develop, thus the jet begins to widen as it approaches

[4] H/D=4, $x/D \approx 0.5$, and H/D=8, $x/D \approx 1$

the impingement surface. This same trend can be seen in all the time averaged plots presented in figures 5.33 to 5.36.

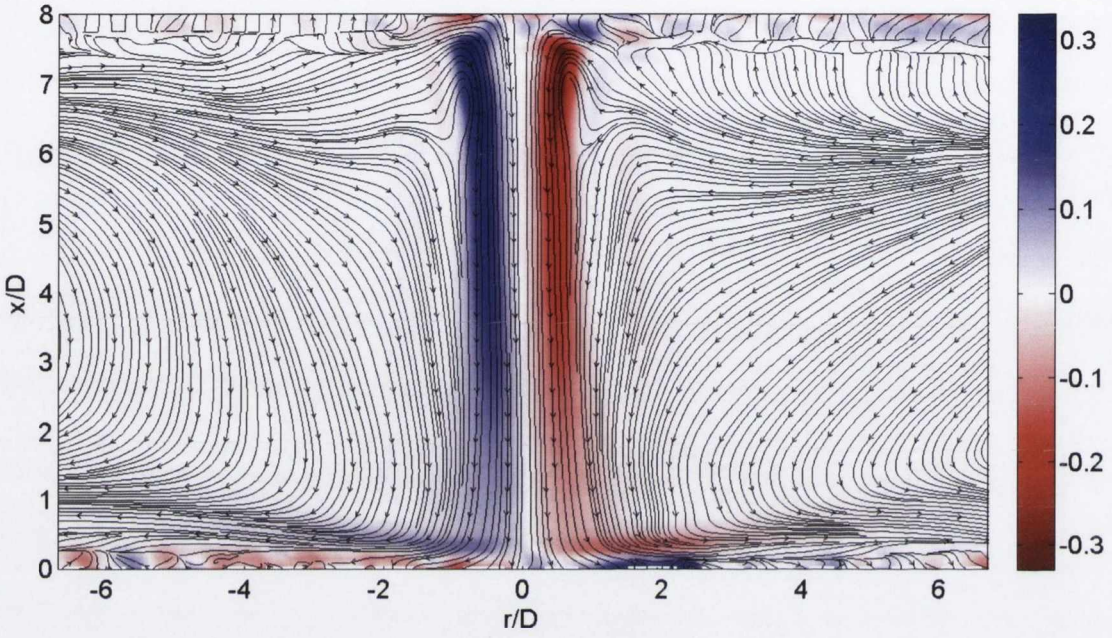

Figure 5.35 – Time averaged streamwise vorticity with streamlines overlaid for H/D=8, Re=1500, L_0/D=4

As the Reynolds numbers is increased the recirculation regions present either side of the jet become more symmetric. There is no evidence of a stationary vortex on the impingement surface in figures 5.33 to 5.36. The increased axial spacing means that the vortex rings produced at this stroke length impinge separately on the plate, but they are of low momentum and velocity as the radial location that they travel to is indicative of vortices dwelling on the plate.

5.2.2.4 $L_0/D = 8$

Time averaged plots for H/D=8, L_0/D=8 exhibit similar trends to those of H/D=4, L_0/D=8 that were seen in section 5.2.1.2. The vorticity plot in figure 5.11 shows similar colour intensities to that in figure 5.37. Due to the higher axial spacing there is a slight skewing of the jet prior to impingement because of the reduced momentum

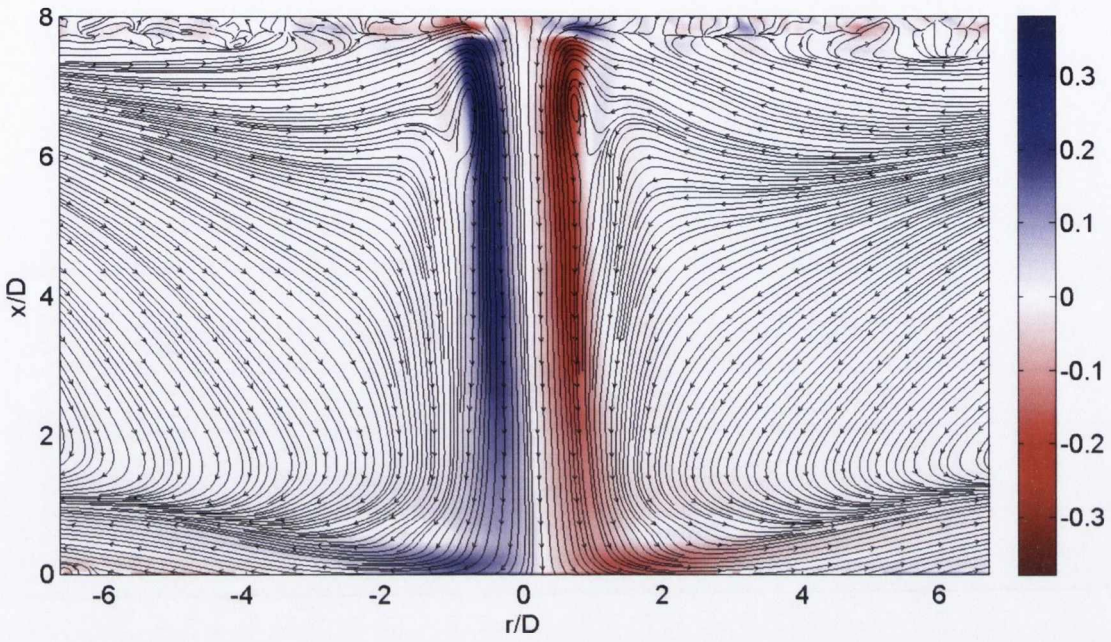

Figure 5.36 – Time averaged streamwise vorticity with streamlines overlaid for H/D=8, Re=2000, L_0/D=4

associated with a Reynolds number of Re=500. The radial distance between the stationary vortices seen on the impingement surface is approximately the same in both figure 5.11 and figure 5.37.

As the streamlines deflect downstream in figure 5.38 they display signs of being affected by what appears to be the regular passage of a strong vortex, seen in the irregular path they take as they travel toward the jet centre. An increase in the Reynolds number results in a jet with higher momentum, thus there is less skewing of the jet prior to impingement. Stationary vortices are present on the impingement surface at the same radial location of $r/D = 2$ in both figure 5.12 and figure 5.38. The overall symmetry of the recirculation zones is seen to increase as Reynolds number increases, due to the increase in momentum and mass flux of the jet. The streamlines seen at $r/D \approx 2$ at the impingement surface in figure 5.39 suggest a mean recirculation region, or stationary vortex. This mean recirculation region in figure 5.39 is seen to dissipate at a slightly higher rate than the stationary vortices seen in figure 5.38 at $r/D \approx 2$; this is attributable to the increased velocity at the higher jet Reynolds number in

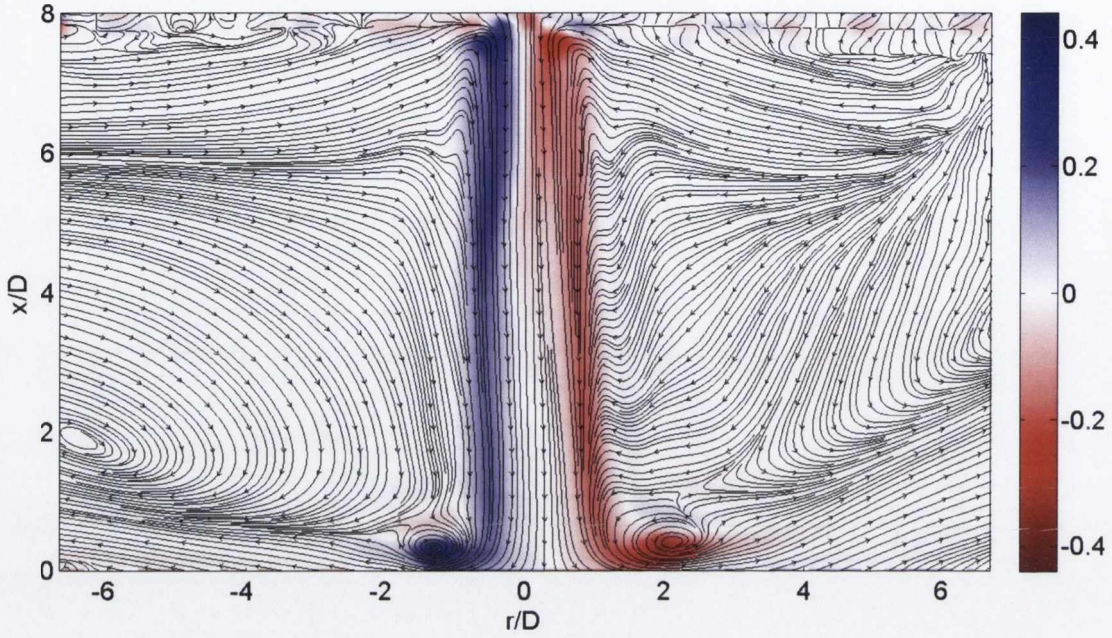

Figure 5.37 – Time averaged streamwise vorticity with streamlines overlaid for H/D=8, Re=500, L_0/D=8

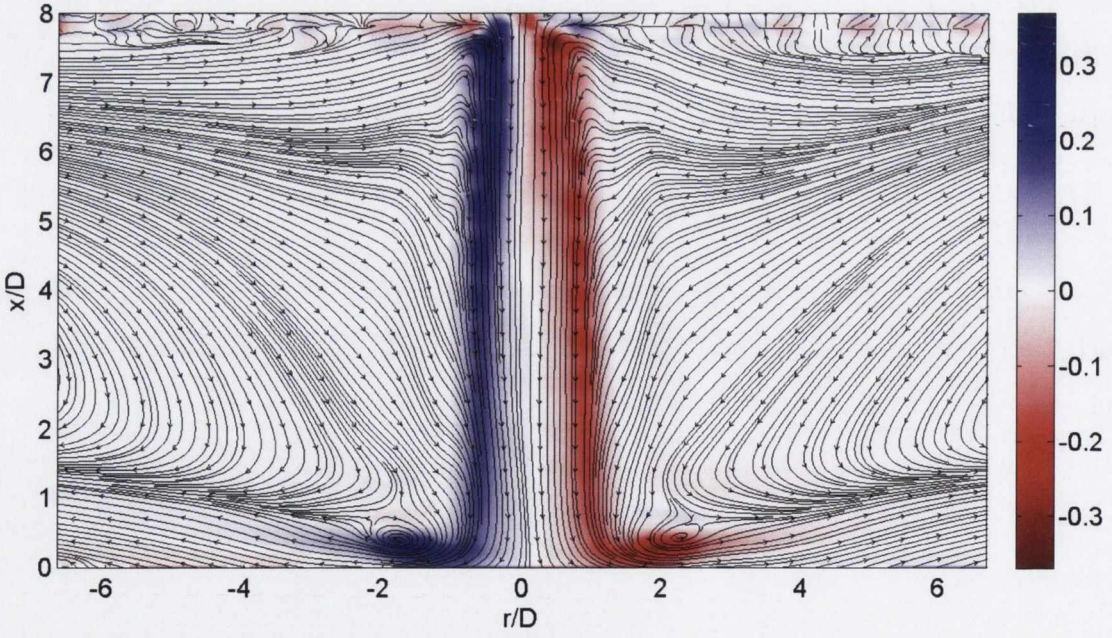

Figure 5.38 – Time averaged streamwise vorticity with streamlines overlaid for H/D=8, Re=1000, L_0/D=8

figure 5.39.

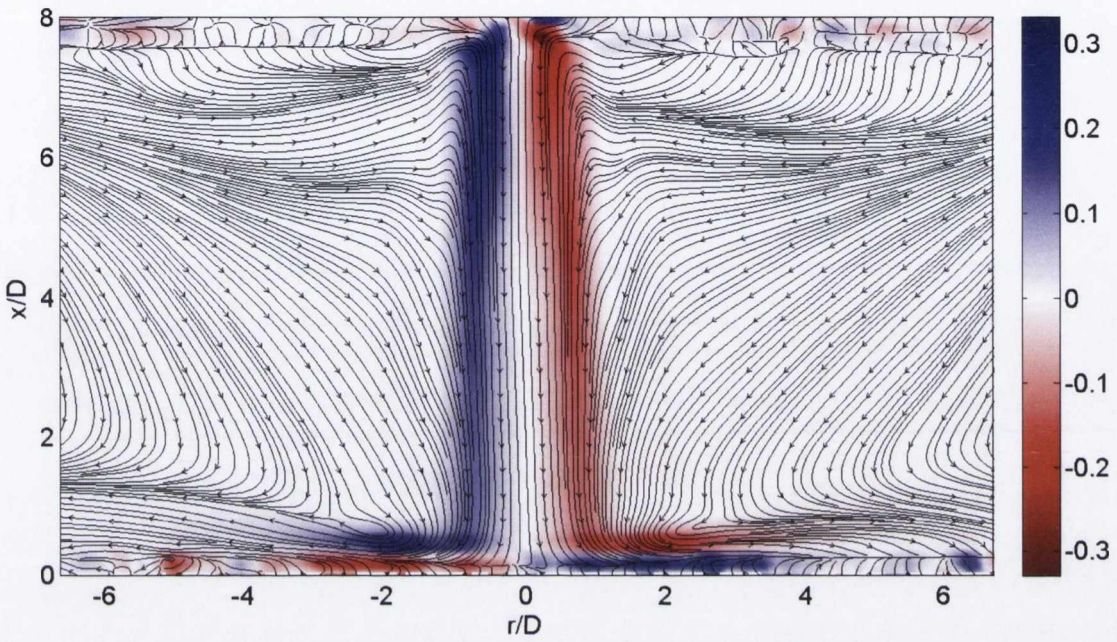

Figure 5.39 – Time averaged streamwise vorticity with streamlines overlaid for H/D=8, Re=1500, L_0/D=8

As the jet develops and spreads, the negative vorticity plots (red) presented in figures 5.37 to 5.40, show signs of an irregular decrease in thickness of the shear layer from the jet centre outwards. The irregularity extends to an axial distance of $x/D \approx 2$ measured from the orifice plate downstream. The positive vorticity plots in figures 5.37 to 5.40 show signs of a smooth transition as the jet evolves. This irregularity in the shear layer is seen also at the lower axial spacing of H/D=4, and extends to approximately the same axial location $x/D \approx 2$ measured from the orifice plate downstream in figures 5.12, 5.13 and 5.14. At the lower axial spacing the jet would have less time to develop than it would at the higher axial spacing, thus it is difficult to understand exactly why it occurs at both axial spacings. This irregular spreading may be due to orifice effects, although it appears to only occur for the stroke length of L_0/D=8 at both axial spacings of H/D=4 and H/D=8.

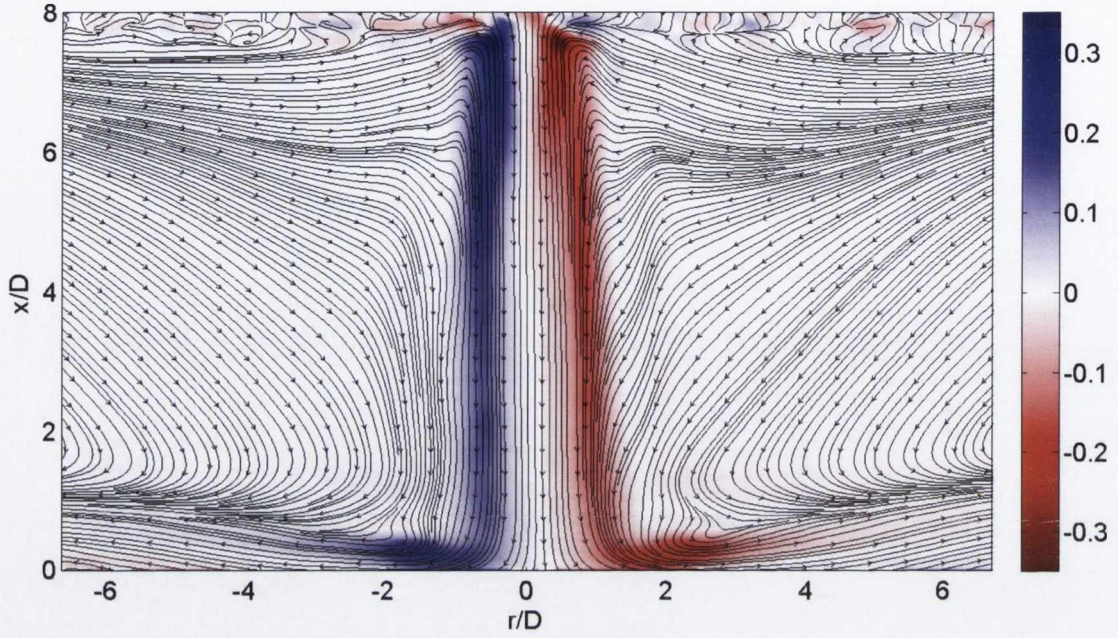

Figure 5.40 – Time averaged streamwise vorticity with streamlines overlaid for H/D=8, Re=2000, L_0/D=8

5.2.2.5 $L_0/D = 12$

The time averaged plot presented for H/D=8, L_0/D=12, Re=500 in figure 5.41 shows what appears to be a slight skewing of the core of the jet. With reference to figure 5.42 and as indicated by the upper arrows there appears to be another vortex at $x/D \approx 4$, just in front of the trailing jet and immediately after the leading vortex has detached from the trailing jet at $\phi \approx 190°$. Progressing to $\phi \approx 212°$ in figure 5.43 it can be seen that the vortex that was created in front of the trailing jet at $x/D \approx 4$ in figure 5.42 has broken down and coalesced with the trailing jet. Prior to impingement in figure 5.43 the leading vortex has widened and skewed, creating regions of opposite vorticity at the impingement surface.

The dashed yellow lines shown in figure 5.42 show the difference in paths that the vortices take as the jet develops. Comparing the instantaneous PIV data presented in figures 5.42 and 5.43 with the time averaged plot in figure 5.41, the reason for the apparent skewing of the core of the jet becomes clear, i.e. the path that the right hand side vortex takes leads to the skewing present in the time averaged plot. The skewing

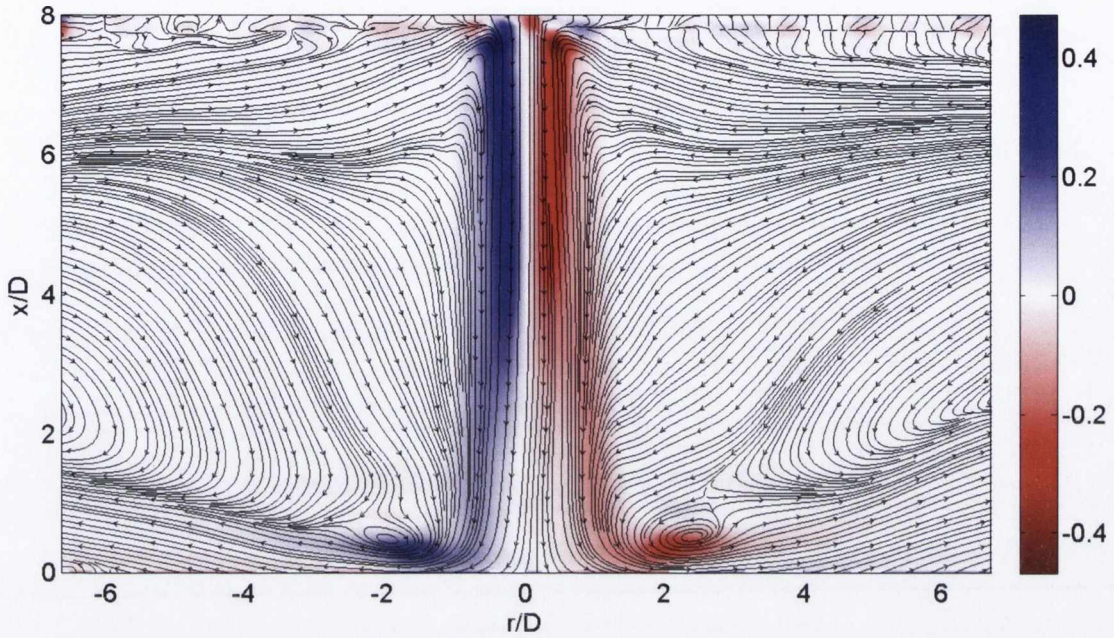

Figure 5.41 – Time averaged streamwise vorticity with streamlines overlaid for H/D=8, Re=500, L_0/D=12

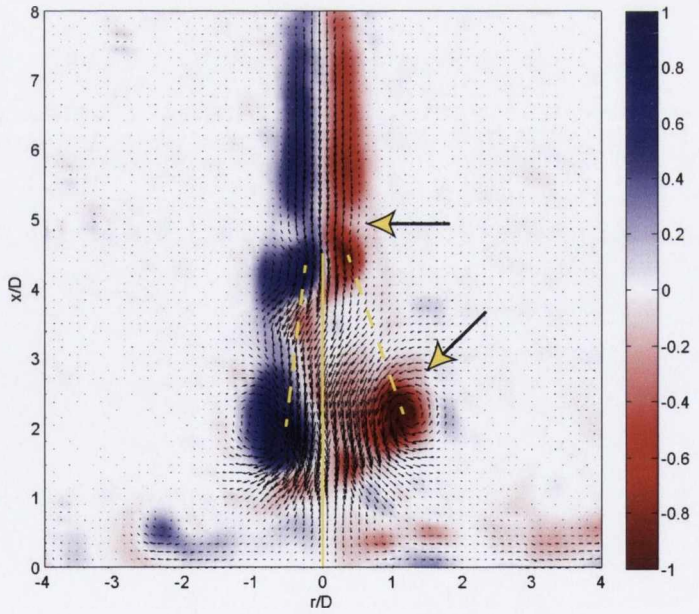

Figure 5.42 – Instantaneous PIV data illustrating vortex and trailing jet breakdown, H/D=8, Re=500, L_0/D=12, ϕ≈190°. Yellow arrows indicate points of interest.

of the core of the jet seen in figure 5.41 is not as prevalent in figures 5.44 and 5.45. However, similar skewing of the core seems to occur in figure 5.46 at an axial location

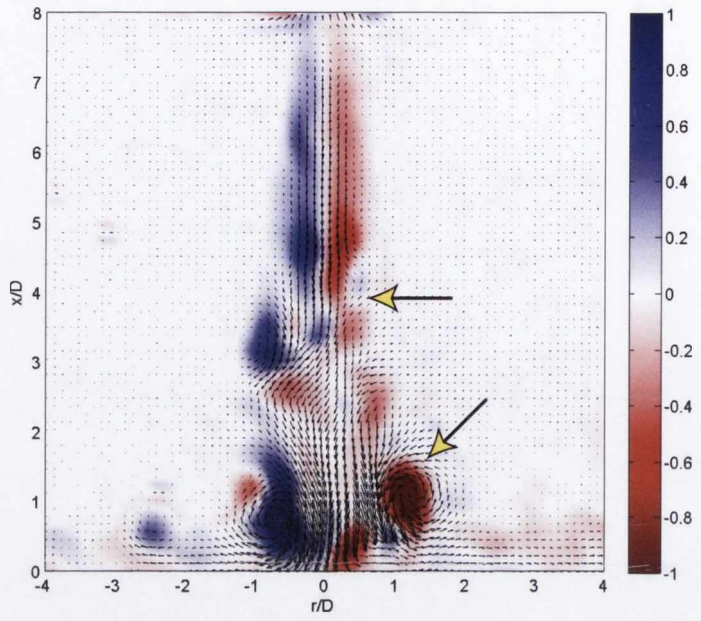

Figure 5.43 – Instantaneous PIV data illustrating vortex and trailing jet breakdown, H/D=8, Re=500, L_0/D=12, ϕ≈212°. Yellow arrows indicate points of interest.

of $x/D \approx 4$, which can be seen in the negative vorticity plot. Instantaneous PIV data for the time averaged plot of figure 5.46 is shown in figure 5.47 and figure 5.48.

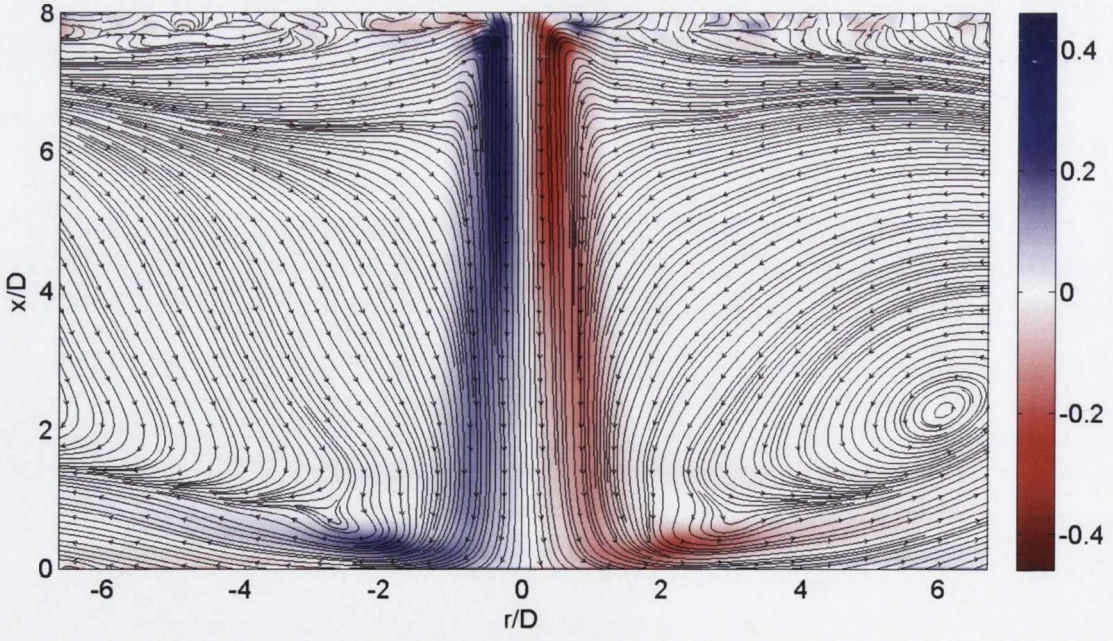

Figure 5.44 – Time averaged streamwise vorticity with streamlines overlaid for H/D=8, Re=1000, L_0/D=12

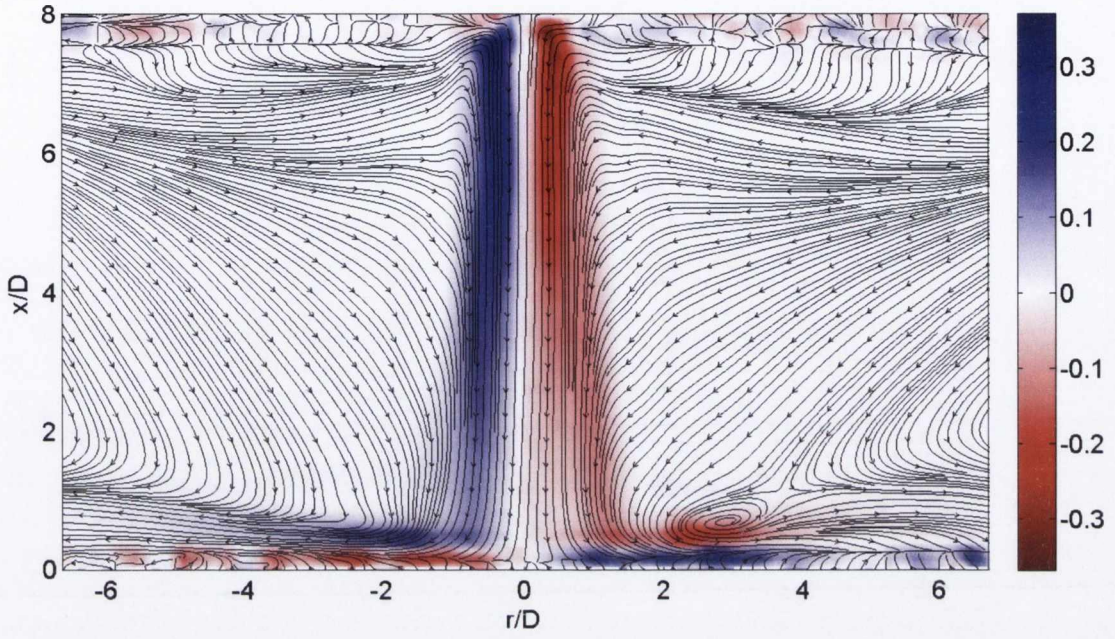

Figure 5.45 – Time averaged streamwise vorticity with streamlines overlaid for H/D=8, Re=1500, L_0/D=12

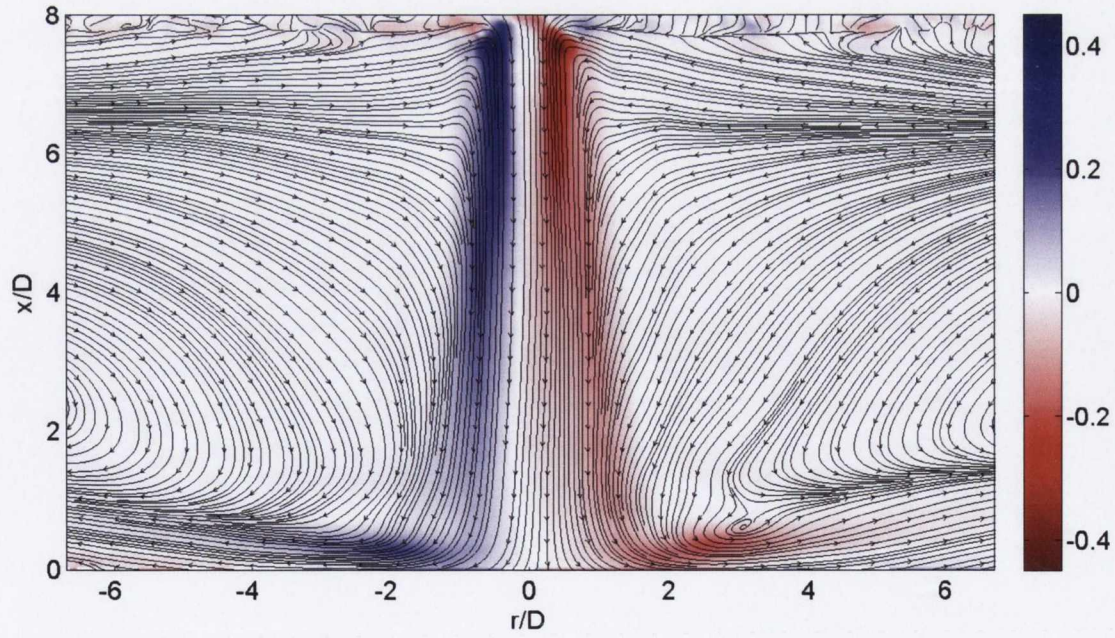

Figure 5.46 – Time averaged streamwise vorticity with streamlines overlaid for H/D=8, Re=2000, L_0/D=12

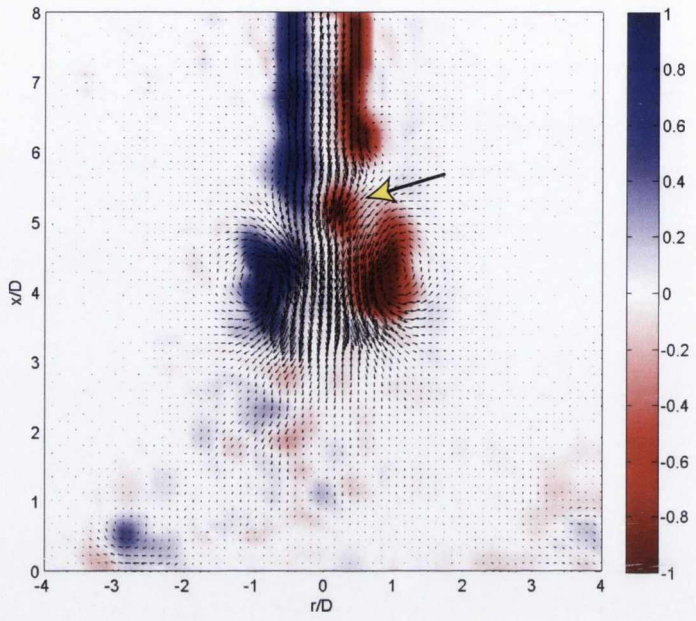

Figure 5.47 – Instantaneous PIV data illustrating vortex and trailing jet breakdown, H/D=8, Re=2000, L_0/D=12, ϕ≈150°. Yellow arrows indicate points of interest.

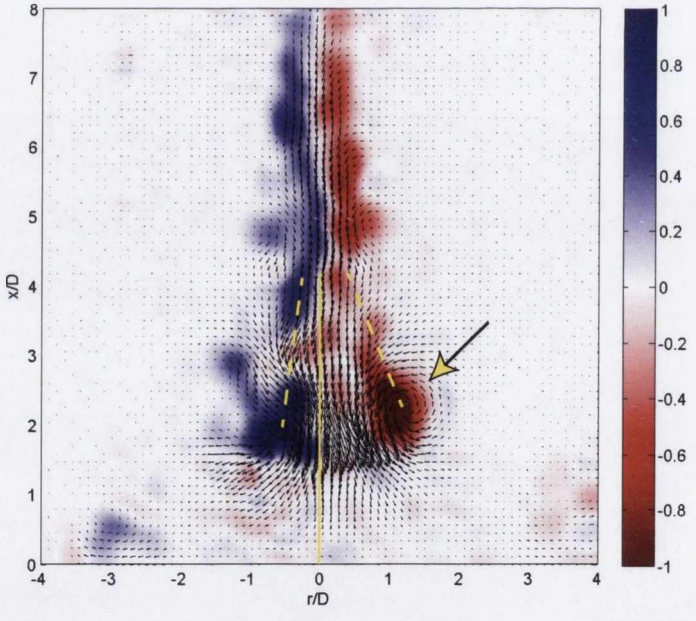

Figure 5.48 – Instantaneous PIV data illustrating vortex and trailing jet breakdown, H/D=8, Re=2000, L_0/D=12, ϕ≈190°. Yellow arrows indicate points of interest.

The PIV data presented in figure 5.47 show a similar breakdown of the trailing jet to that seen in figure 5.42 once the leading vortex has detached. At $\phi \approx 190°$ in figure 5.48, the vortex has widened and spread in the same manner as that seen in

figure 5.43. The estimated vortex path in both figures 5.43 and 5.48 is indicated by the yellow dashed lines, with a solid line indicating $r/D = 0$. It is apparent from figures 5.43 and 5.48 that there is a deviation from the imagined path that the vortex should travel without disturbances. The right hand portion of the vortex ring is seen to travel at a larger angle than that of the left hand portion from the jet centre, which leads to the creation of the trend seen in the vorticity plots of the time averaged data of figures 5.41 and 5.46.

5.2.2.6 $L_0/D = 16$

The time averaged plots presented for H/D=8, L_0/D=16 are seen in figure 5.49, figure 5.52, figure 5.53 and figure 5.54. From these plots it can be seen that there is a widening of the jet when compared to the previous time averaged data that have been presented, indicated by the radial location of the mean recirculation regions at $r/D \approx 2$ to 3.

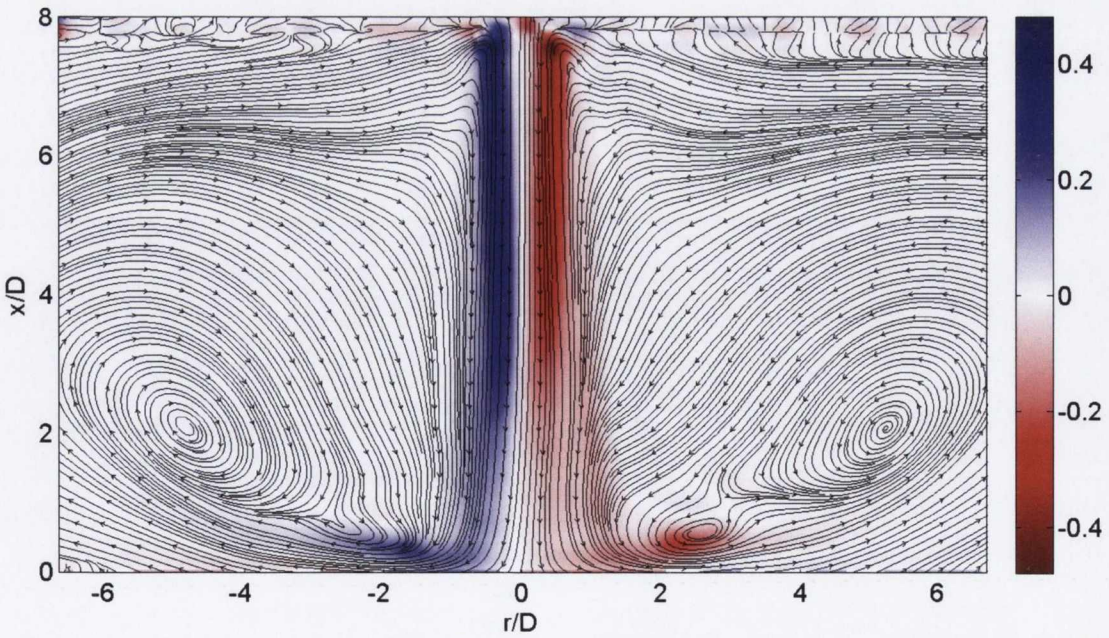

Figure 5.49 – Time averaged streamwise vorticity with streamlines overlaid for H/D=8, Re=500, L_0/D=16

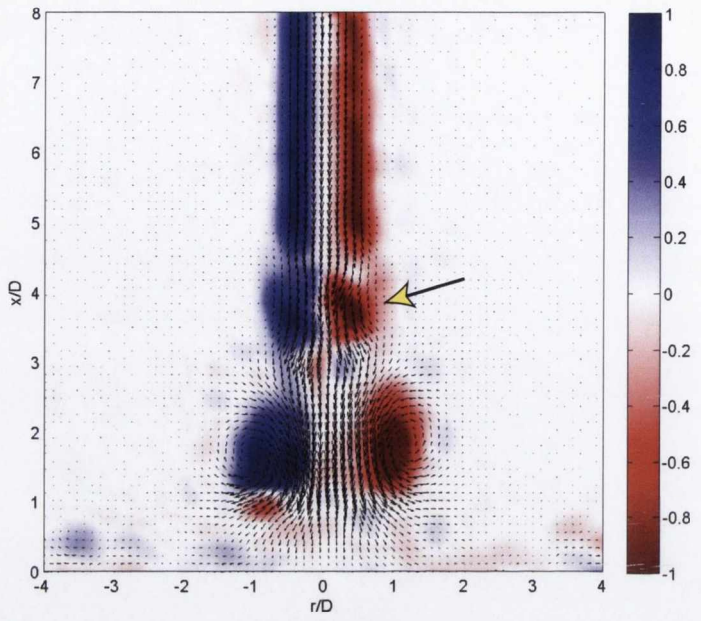

Figure 5.50 – Instantaneous PIV data illustrating vortex and trailing jet breakdown, H/D=8, Re=500, L_0/D=16, ϕ≈150°. Yellow arrows indicate points of interest.

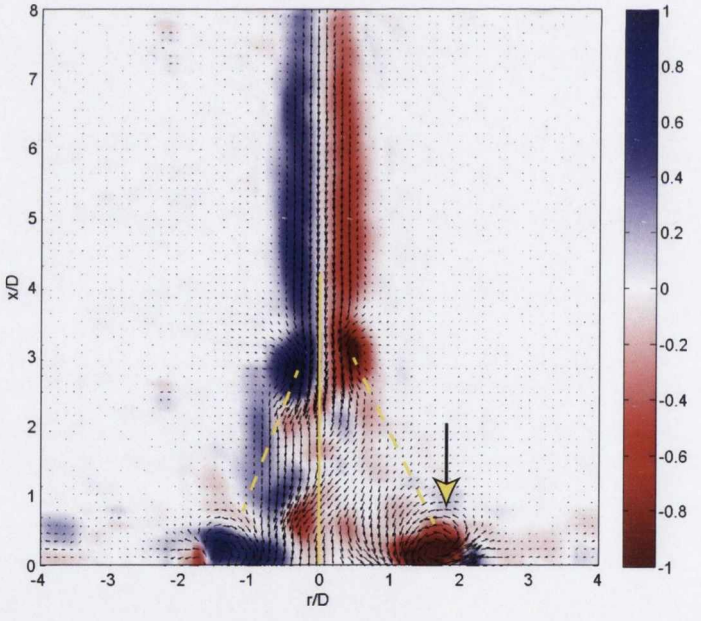

Figure 5.51 – Instantaneous PIV data illustrating vortex and trailing jet breakdown, H/D=8, Re=500, L_0/D=16, ϕ≈190°. Yellow arrows indicate points of interest.

The instantaneous PIV data presented in figure 5.50 and figure 5.51 highlight flow features that are present at this stroke length of L_0/D=16. Instantaneous PIV data for Re=500 in figure 5.42 and figure 5.50 exhibit similar flow features, in that another

vortex forms in front of the trailing jet after the primary vortex has detached. The vorticity plot of figure 5.49 shows a similar breakdown in the shear layer to what was seen in figure 5.41. The core of the jet in figure 5.49 extends to a greater axial location than that of figure 5.41, which is consistent with an increase in the stroke length here. Shown in figure 5.51 is the spreading of the primary vortex subsequent to impingement. Thus, the arrow at $r/D \approx 2$ marks the right hand side portion of the vortex ring. Referring to figure 5.49 there is a mean recirculation region present at $r/D \approx 2$ on the right hand side of the plot, which corresponds to the location of the impinging vortex in figure 5.51.

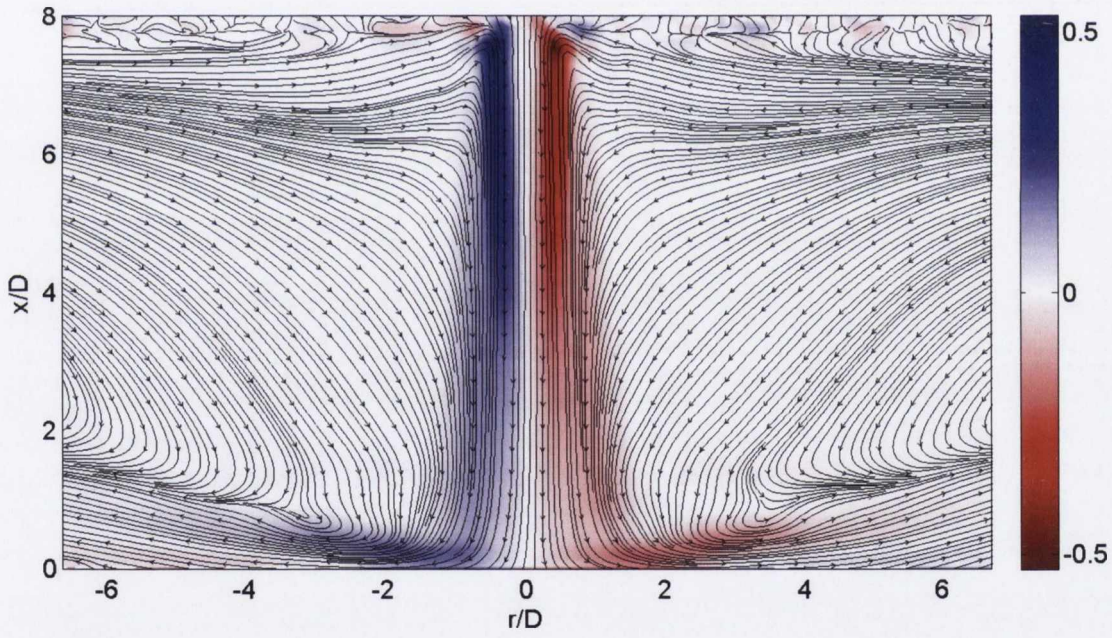

Figure 5.52 – Time averaged streamwise vorticity with streamlines overlaid for H/D=8, Re=1000, L_0/D=16

Figures 5.52, 5.53 and 5.54 show the existence of large symmetric entrainment regions either side of the core of the jet. The presence of the saddle point in the synthetic jet flow is clearly seen at an axial location of $x/D \approx 6$ and $r/D \approx \pm 1$ in figures 5.49, 5.52, 5.53 and figure 5.54, as indicated by the streamlines. The recirculation regions present in the time averaged plots for L_0/D=16 bear some resemblance, in terms of the radial location of the mean recirculation regions present on the impinge-

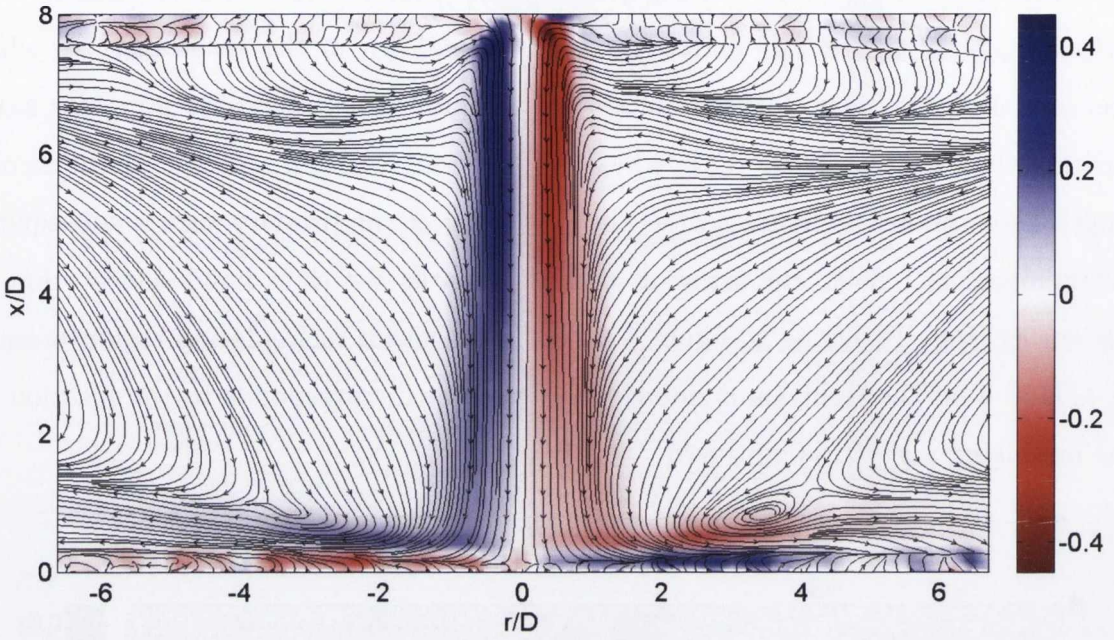

Figure 5.53 – Time averaged streamwise vorticity with streamlines overlaid for H/D=8, Re=1500, L_0/D=16

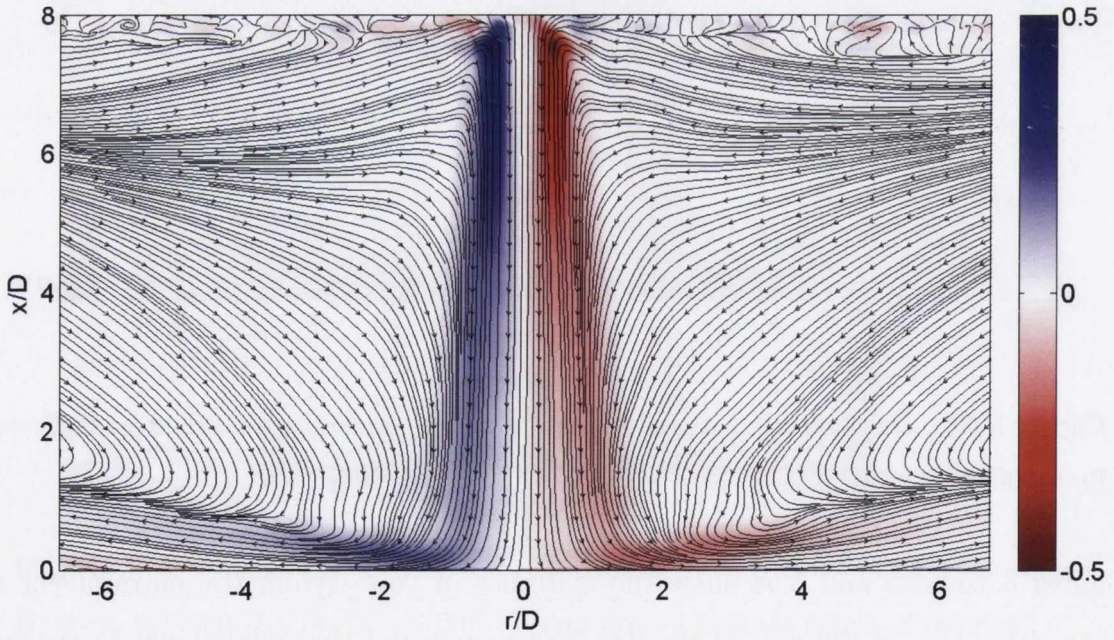

Figure 5.54 – Time averaged streamwise vorticity with streamlines overlaid for H/D=8, Re=2000, L_0/D=16

ment surface, to the time averaged plots presented in section 5.2.1.4 for $H/D = 4$. Confinement affects jets at low axial spacings, and affects synthetic jet flow more than a steady jet, as shown by the author, [8]. This is seen in the comparison between the time averaged plots for L_0/D=16 at the two different axial spacings presented; similarities exist in the flows, but due to the low axial spacing the flow is unable to develop fully for the H/D=4 case. This explains the differences existing in the large recirculation regions extending to a larger radial location either side of the core of the jet at H/D=8.

5.2.2.7 $L_0/D = 32$

Time averaged plots for H/D=8 and L_0/D=32, the largest stroke length examined, are presented here. The large stroke length equates to large ejections of fluid, which results in large recirculation regions, as seen in figures 5.55, 5.57, 5.58 and 5.59.

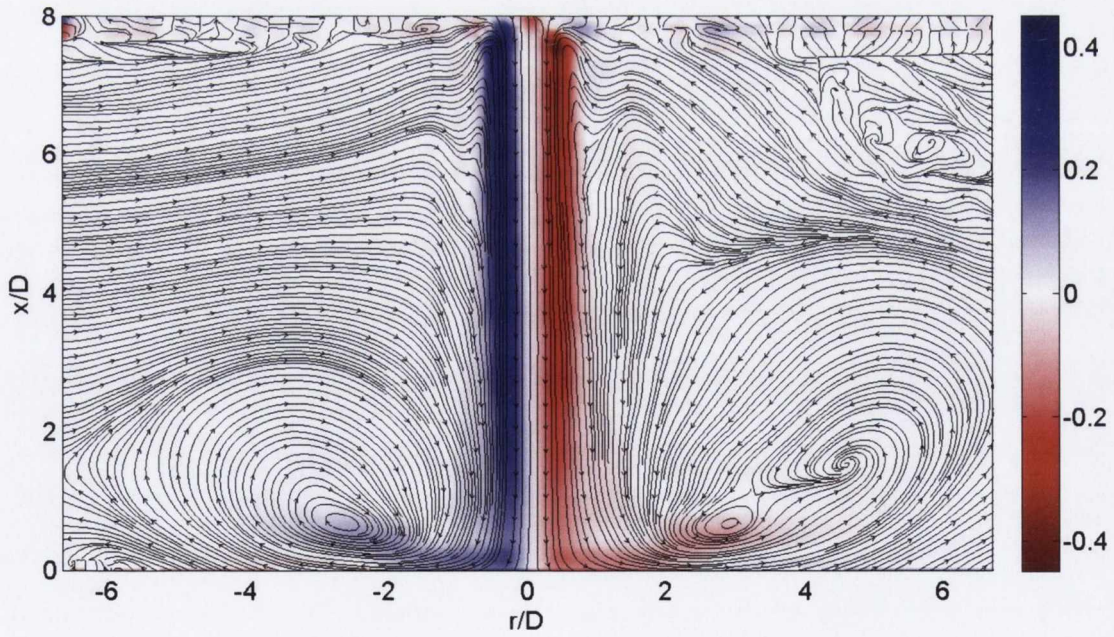

Figure 5.55 – Time averaged streamwise vorticity with streamlines overlaid for H/D=8, Re=500, L_0/D=32

The trailing jet produced at this stroke length encompasses approximately 87.5% of the fluid ejected from the orifice at L_0/D=32. Instantaneous PIV data at $\phi \approx 180°$

is presented in figure 5.56. Strong vortex roll up is experienced on the impingement surface at L_0/D=32. Seen in figure 5.56, as indicated by the arrows, are forceful vortices subsequent to impingement; there exists also strong areas of neighbouring vorticity, even at the low Reynolds number of Re=500. The trailing jet impinges with force and the impinging fluid transitions from an axially impinging jet, to vortex roll up, resulting in the mean recirculation regions seen in figure 5.55.

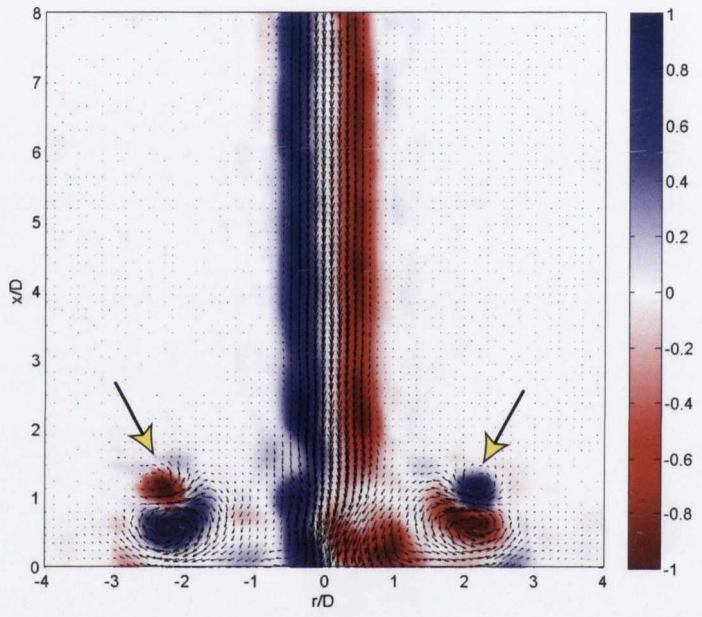

Figure 5.56 – Instantaneous PIV data illustrating vortex and trailing jet breakdown, H/D=8, Re=500, L_0/D=32, $\phi \approx 180°$. Yellow arrows indicate points of interest.

The suction stroke that the ambient fluid experiences at this large stroke length of L_0/D=32 is quite powerful, as indicated by the streamlines in figures 5.55, 5.57, 5.58 and 5.59. The streamlines approach the jet centre approximately normal to the y-axis, experience a sharp deflection upstream at the shear layer, and turn downstream as they enter the high speed region near the jet centre. The symmetry of the flow in figures 5.58 and 5.59 is quite remarkable. The high volume of fluid ejected at L_0/D=32, combined with the higher velocity flows associated with the respective Reynolds numbers of figures 5.58 and 5.59, result in the flows produced. Figure 5.60 shows vortex detachment prior to impingement at $x/D \approx 2.5$; the leading vortex and trailing jet are entirely destabilised. The vortex present in figure 5.60 is close to

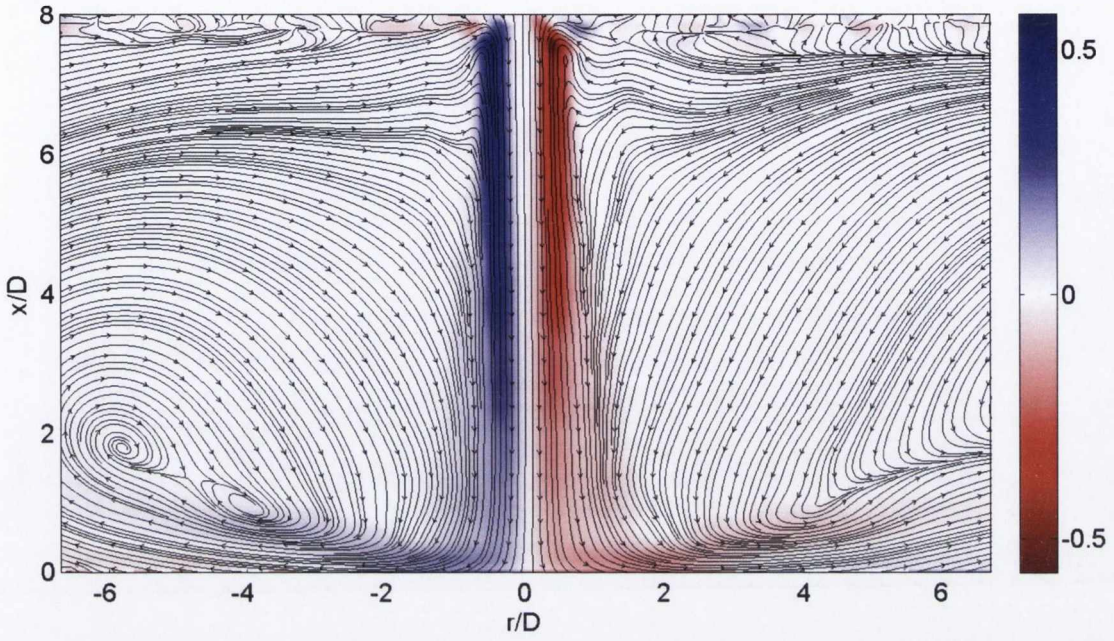

Figure 5.57 – Time averaged streamwise vorticity with streamlines overlaid for H/D=8, Re=1000, L_0/D=32

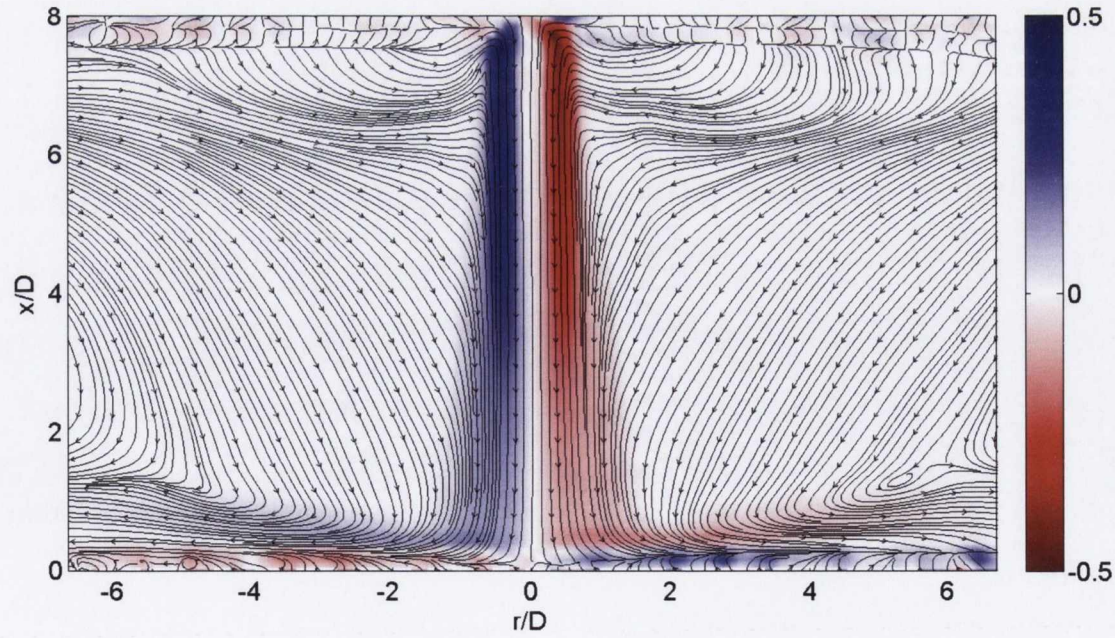

Figure 5.58 – Time averaged streamwise vorticity with streamlines overlaid for H/D=8, Re=1500, L_0/D=32

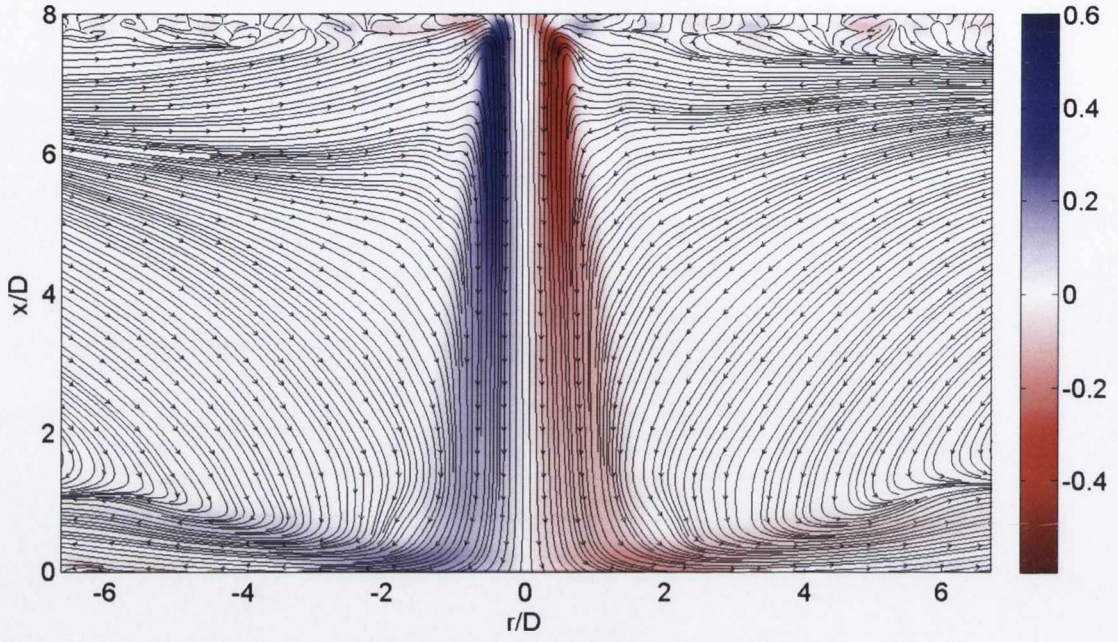

Figure 5.59 – Time averaged streamwise vorticity with streamlines overlaid for H/D=8, Re=2000, L_0/D=32

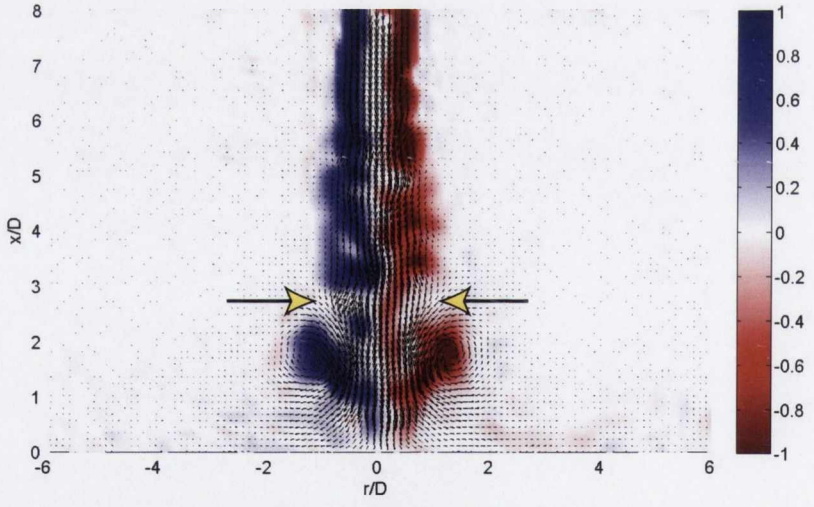

Figure 5.60 – Instantaneous PIV data illustrating vortex and trailing jet breakdown, H/D=8, Re=2000, L_0/D=32, ϕ≈90°. Yellow arrows indicate points of interest.

complete destruction, while the trailing jet is essentially a high velocity fluid ejection that will impinge on the surface and begin vortex roll up subsequent to impingement, as seen in figure 5.61. It is worth noting that at H/D=8, the approximate axial location of the saddle point for all the time averaged plots presented here is $x/D \approx 6$,

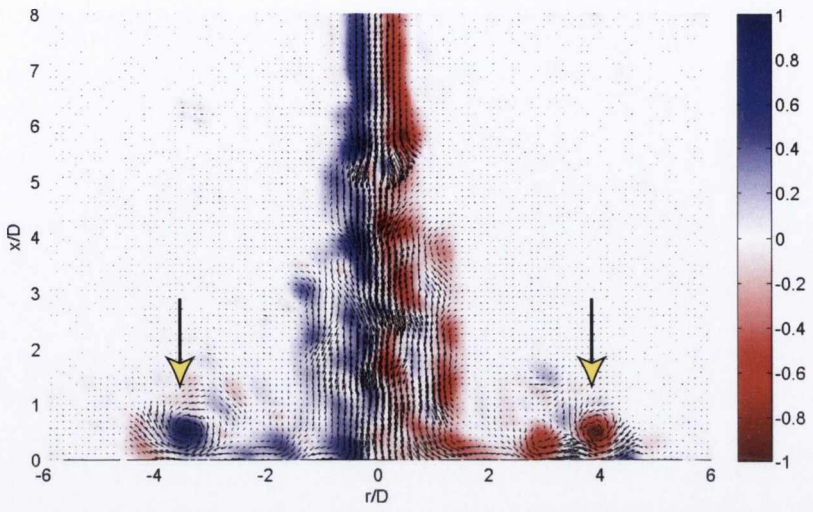

Figure 5.61 – Instantaneous PIV data illustrating vortex and trailing jet breakdown, H/D=8, Re=2000, L_0/D=32, $\phi \approx 170°$. Yellow arrows indicate points of interest.

as indicated by the streamlines.

5.2.2.8 Findings

The results for the axial spacing H/D=8 confirm that the effects of recirculation and confinement are reduced as the axial spacing is increased. However at high stroke lengths the recirculation patterns are quite large, indicating that the trailing jet that is produced affects the higher axial spacing by boosting recirculation. It can be seen from the flow fields presented for this axial spacing that the synthetic jet exhibits a general Reynolds number independence as well. As the flow has more time to develop at this higher axial spacing the destabilisation of the vortex ring at high stroke length values prior to impingement can be seen. The lower dimensionless stroke length values were seen to have closed recirculation regions due to stationary vortices just downstream from the orifice and on the impingement surface.

The data presented in the figures referenced here, to the author's knowledge show flow structures that have not been documented in the literature for an impinging synthetic jet flow. There are unique flow structures contained within this flow that are presented in these figures.

- Vortex pinch off is responsible for the occurrence of a smaller vortex ring being created after the main vortex detaches from the trailing jet at the stroke length of L_0/D=8 and Reynolds number of Re = 1500, seen in figure 5.5.

- Narrowing of the synthetic jet is seen to occur from formation to just prior to impingement for the stroke length L_0/D=4. Seen in figure 5.7 the core of the synthetic jet appears to narrow up to an axial location of $x/D \approx 4$. For the axial spacing H/D=8 after $x/D \approx 4$ the jet stays at this width up to impingement, seen in the results presented in section 5.2.2.3.

- The regions of opposite vorticity appearing on the left hand side of the jet flow is seen to occur in figure 5.43 along with a similar occurrence of vortex pinch off that was seen previously in figure 5.5. The regions of opposite vorticity appearing on the left hand side of the jet flow leads to the right hand vortex being skewed and impinging at a different radial location to the left hand vortex.

- Vortex and trailing jet breakdown is seen to occur as a result of vortex pinch off where regions of opposite vorticity have crossed over within the core of the jet before impingement, seen in figure 5.47.

- Skewing of the vortex ring prior to impingement from a destabilisation of the vortex ring is seen in figure 5.48. It can be seen in this figure that the right hand side vortex has moved away from the left hand vortex, leading to the impingement of the vortices at different radial locations, which will have an effect on the overall efficacy of the synthetic jet.

- The appearance of two vortex rings in front of the trailing jet is presented in figure 5.50. The vortex separation from the trailing jet has caused another leading vortex to appear in front of the trailing jet.

- A synthetic jet flow at a phase angle of $\phi \approx 190°$ is presented in figure 5.51, which is a phase difference of 40° on from figure 5.50 and shows the leading vortex subsequent to impingement and the appearance of the other vortex ring in front of the trailing jet.

- The vorticity plot of figure 5.56 appears to be uniform, it shows the vortex ring subsequent to impingement at a large dimensionless stroke length L_0/D=32, even though the vortices seen at $r/D \approx 2$ either side of the jet core appear to be uniform, there is a gap in the vorticity plot at an axial location of $x/D \approx 1$ on the right hand side of the jet flow, this is thought to occur when the flow transitions from the axial direction to the radial direction.

- The widening of the vortex ring prior to impingement seen in figure 5.60 at the point indicated shows the effect the trailing jet has on the leading vortex. This is considered a high velocity synthetic jet flow at a stroke length L_0/D=32 with a jet Reynolds number of Re=2000.

- Subsequent to impingement, just after vortex roll up has taken place, seen in figure 5.61 is the interaction of the trailing jet with these vortices on the impingement surface. The trailing jet interacts with these vortices by forcing them along the impingement surface, as indicated by the radial distance they travel to.

Chapter 6

Results:

Volume flux, vortex evolution and roll-up

Volume flux and the location of vortex formation are presented in section 6.1 and section 6.2.1 respectively. Simultaneous stereoscopic high speed PIV and heat transfer data are presented in section 6.3 as vortex roll up, to correctly identify the features of the flow from this experiment the data has been phase averaged. Phase averaging has been adopted in order to achieve high accuracy and decrease the turbulent characteristics of the signal. The relationship between vortex roll up and the heat transfer is explored in this section.

6.1 Volume flux

The time averaged flow field data presented in section 5.2 have been used to calculate the volume flux data presented here where volume flux is in units of cm^3/s. The volume flux is calculated using the following equation.

$$Q(x) = \sum U_x(r, x) 2\pi r dr \tag{6.1}$$

where r extends outwards to a radial distance of two diameters from the jet centre, and x is the axial coordinate. Due to the effects that the suction phase of the synthetic jet cycle near the orifice can have on the net volume flux, the streamwise positive velocities from the ejection phase were used to calculate the volume flux.

The data for the average volume flux are presented in such a manner that $x/D = 0$ indicates the orifice plate, with x/D increasing to the axial distance of the impingement surface in jet diameters for both spacings of H/D=4 and H/D=8. Table 6.1 presents the calculated peak flux for each stroke length at specific Reynolds number and axial spacings.

6.1.1 H/D=4

The volume flux data presented for H/D=4 in figures 6.1 to figure 6.5 show an overall increase in both axial flux and radial flux as Reynolds number is increased. This is as expected, because entrainment rates increase with an increase in Reynolds number. The streamlines representing the recirculation and entrainment of the synthetic jet have been presented in section 5.2, and are seen to follow a similar trend. Thus, as Reynolds number increases the streamlines are seen to become more symmetric, meaning the entrainment rates are increasing.

The dip seen in figure 6.1a for L_0/D=4 corresponds to the approximate axial location ($x/D \approx 1$) of the stationary vortex seen in the time averaged data in figure 5.6. It is interesting to note from figure 6.1 and table 6.1 that the lowest stroke length value of L_0/D=4 has a higher volume flux than the highest stroke length of L_0/D=32. This is thought to occur because at the stroke length L_0/D=4 each vortex that impinges is allowed to do so unhindered by a trailing jet, where the stroke length of L_0/D=32 is largely influenced by a trailing jet, seen in figure 6.2. The vorticity plot seen in figure 6.2 shows that subsequent to impingement the trailing jet forces the vortex to roll up and re-ingestion of the vorticity to the trailing jet is seen to occur, thus reducing the overall volume flux of the synthetic jet at L_0/D=32, Re=500. There is

what appears to be a nearly linear relationship between the volume flux and the axial location for H/D=4, Re=500 in figure 6.1, up to the axial location of $x/D \approx 3$. The peak that occurs at the axial location $x/D \approx 3.5$ is a result of the flow approaching the impingement surface, as this occurs there is an increase in radial velocity that is shown in figure 6.1b. Figure 6.1a shows that the stroke lengths of L_0/D=8, L_0/D=12, and L_0/D=16 are very close in magnitude, with L_0/D=16 showing a slight deviation in comparison to the other stroke lengths as the flow approaches the impingement surface.

Table 6.1 – Average volume flux of synthetic jet in the axial direction, (cm^3/s).

L_0/D	Re	$H/D = 4$	$H/D = 8$
4	500	129.4	113.9
8	500	159.7	138.6
12	500	160.1	162.9
16	500	138.5	157.1
32	500	92.88	127.2
4	1000	269.3	259.5
8	1000	345	312.9
12	1000	301.2	383.9
16	1000	314.1	424.6
32	1000	260.5	357.7
4	1500	434.5	428.8
8	1500	507.4	530.3
12	1500	471.8	587.1
16	1500	448	616.1
32	1500	394.6	564.7
4	2000	563.7	573.3
8	2000	660.9	707.2
12	2000	660.8	835
16	2000	631.3	815.8
32	2000	631.8	852.7

The step seen in the trendline for the stroke length L_0/D=4, seen and indicated in figure 6.1b at $x/D \approx 3.5$, corresponds to the recirculation region presented in sec-

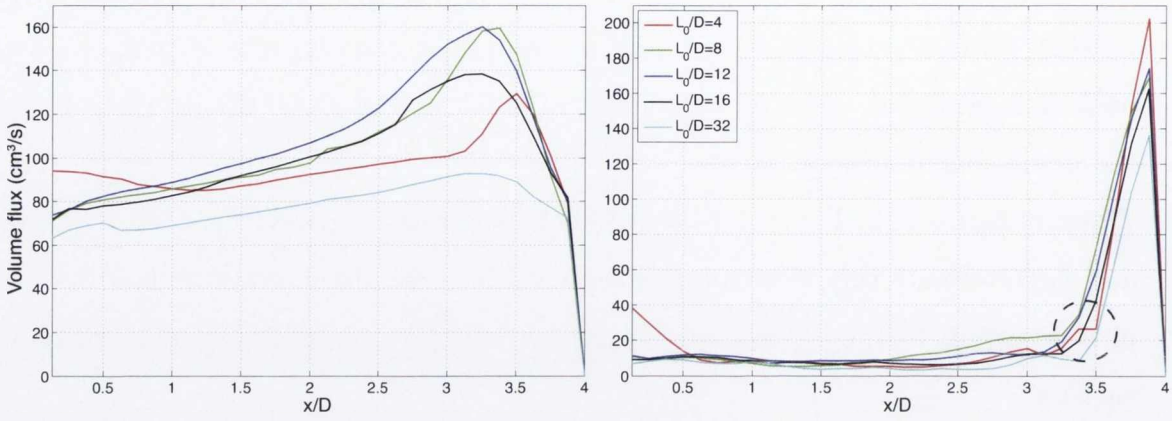

(a) axial flux

(b) radial flux

Figure 6.1 – Average volume flux in the axial and radial directions from $r = \pm 2D$ at H/D=4, Re=500.

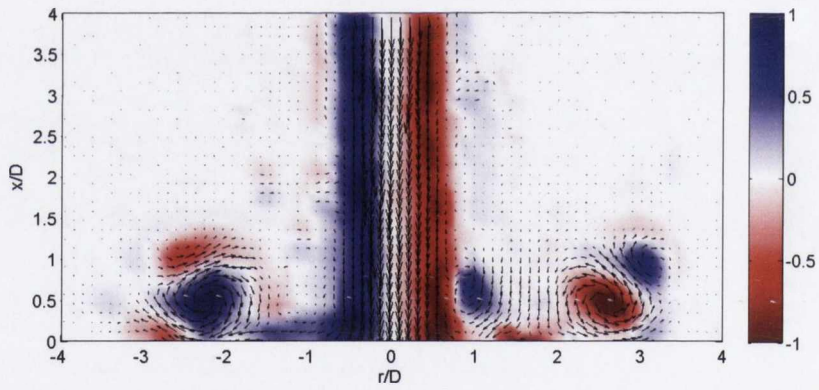

Figure 6.2 – Instantaneous PIV illustrating the effect of the trailing jet, H/D=4, Re=500, L_0/D=32, $\phi \approx 135°$.

tion 5.2.1.1, figure 5.6 at $x/D \approx 0.5$[1] where there are closed streamlines present. Increasing the dimensionless stroke length of a synthetic jet usually results in an increase in the maximum radial flux experienced subsequent to impingement [45]. This is usually attributed to the greater momentum in the flow due to the larger stroke length, however this is not the case for the data seen in figures 6.1b, 6.3b and 6.4b. It is suggested that the lower Reynolds number data presented result in an opposite

[1] The time averaged data are measured from the impingement surface up, where the volume flux data presented here are measured from the orifice plate down.

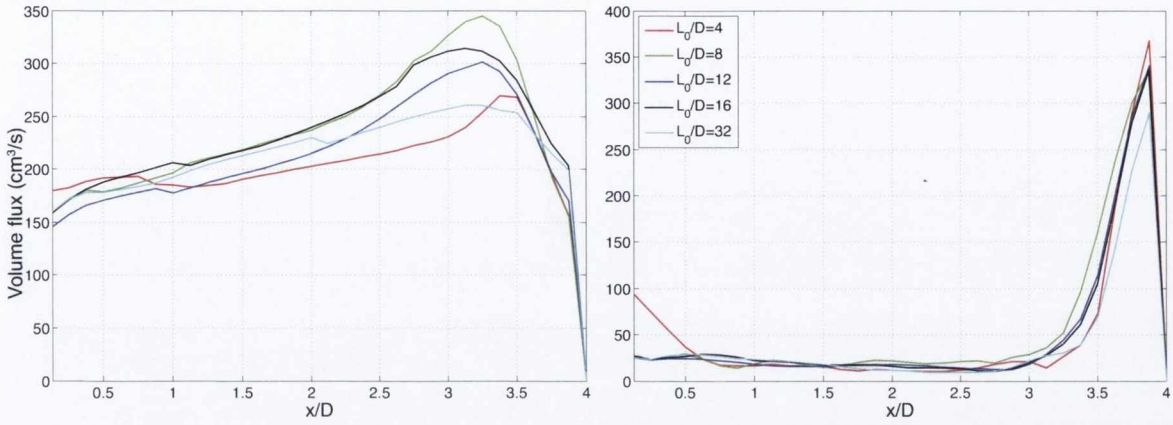

(a) axial flux (b) radial flux

Figure 6.3 – Average volume flux in the axial and radial directions from $r = \pm 2D$ at H/D=4, Re=1000.

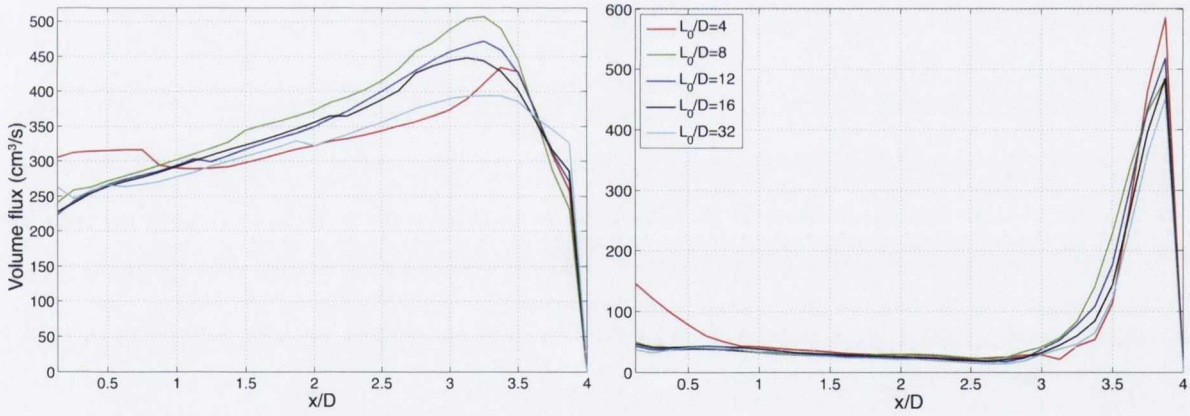

(a) axial flux (b) radial flux

Figure 6.4 – Average volume flux in the axial and radial directions from $r = \pm 2D$ at H/D=4, Re=1500.

trend as the higher stroke lengths are affected by the trailing jet, as seen in figure 6.2. At the jet Reynolds number of Re=2000 increasing the stroke length results in an increase in the maximum radial flux; this is thought to occur because this flow is considered to be a high velocity synthetic jet flow. The rate at which a jet spreads has a direct impact on the volume flux of the jet. Interestingly, the maximum radial flux achieved is achieved at L_0/D=4 for the synthetic jet for Re=500, Re=1000 and

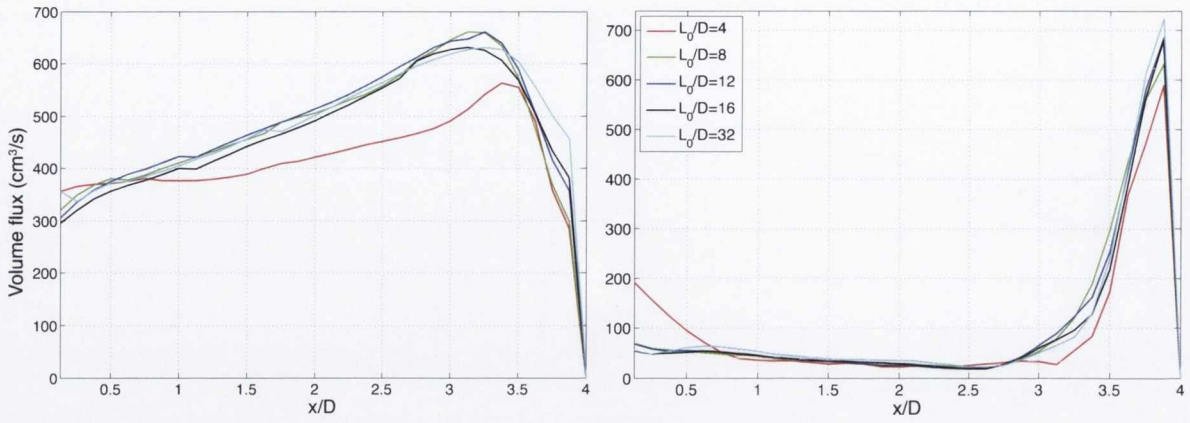

(a) axial flux

(b) radial flux

Figure 6.5 – Average volume flux in the axial and radial directions from $r = \pm 2D$ at H/D=4, Re=2000.

Re=1500. This is attributed to the capability of the vortices to travel further along the impingement surface for a stroke length of L_0/D=4, as the vortices impinge separately and are allowed to travel along the surface unhindered. Visual inspection of the flow at Re=2000 shows that the vortices impinge with a lot more force and they recirculate back into the main jet flow, thus not travelling as far on the impingement surface. The volume flux data presented for H/D=4 in figures 6.1 to figure 6.5 shows that at approximately one diameter from the impingement surface the direction of the volume flux appears to be influenced by the plate.

6.1.2 H/D=8

The average volume flux for the axial spacing of H/D=8 is presented here. The general trend of the volume flux having a near linear relationship up to an axial location of $x/D \approx 3$ followed by a peak at $x/D \approx 3.5$, seen in the axial flux data for H/D=4 in section 6.1.1, is not seen in the axial flux data for H/D=8.

Comparing the data for H/D=4 in section 6.1.1 to results for H/D=8 in figures 6.6 to figure 6.9, it can be seen that once the jet approaches the impingement surface at $x/D \approx 6$ the trendlines for H/D=8 follow a much smoother transition prior to

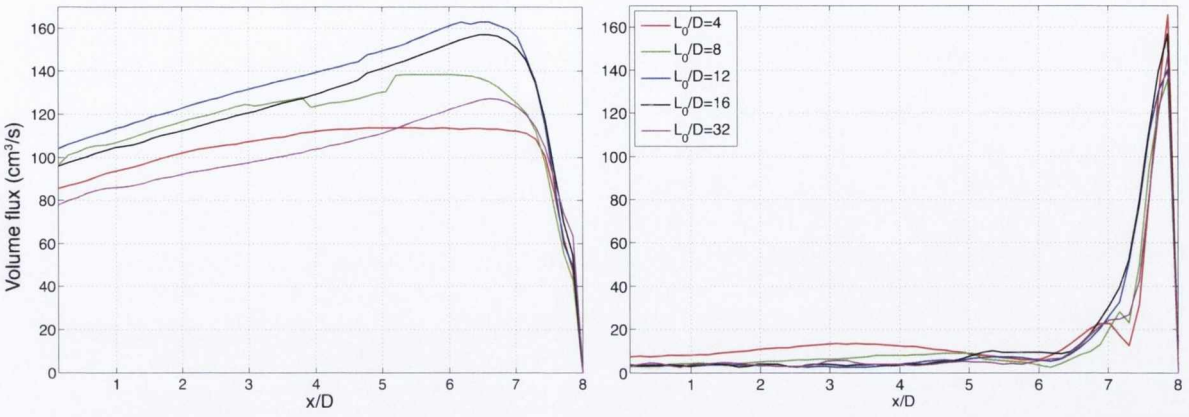

(a) axial flux

(b) radial flux

Figure 6.6 – Average volume flux in the axial and radial directions from $r = \pm 2D$ at H/D=8, Re=500.

impingement. The peak axial flux at dimensionless stroke length of L_0/D=32 for the axial spacing of H/D=4 is always significantly lower than the axial flux recorded for H/D=8, indicating that the flow is not granted sufficient time to develop and entrain ambient fluid. Referring to table 6.1 the peak volume flux data reported for H/D=8 for the larger stroke length values i.e. L_0/D=12, L_0/D=16, and L_0/D=32 have a much higher volume flux than their counterparts at the lower H/D=4. It is suggested that this is due to the higher axial spacing, which results in reduced confinement effects, and increased entrainment rates, as the flow is able to develop further.

It is worth noting that the peak flux for the synthetic jet in figure 6.8 is recorded for a stroke length of L_0/D=16; a similar finding for the comparable test parameters was observed by McGuinn [7].

Figures 6.6b, 6.7b, and 6.8b for L_0/D=4 and L_0/D=8 show signs of the existence of a stationary vortex at $x/D \approx 7$; this is indicated by the sharp dip in radial volume at this location. Comparing the volume flux data to the time averaged data presented in section 5.2.2 for the corresponding stroke lengths and Reynolds numbers, this station-

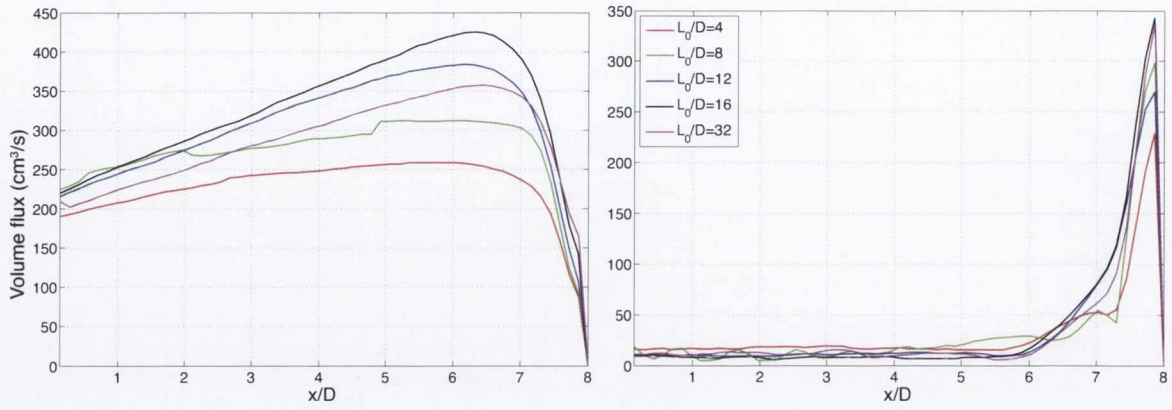

(a) axial flux (b) radial flux

Figure 6.7 – Average volume flux in the axial and radial directions from $r = \pm 2D$ at H/D=8, Re=1000.

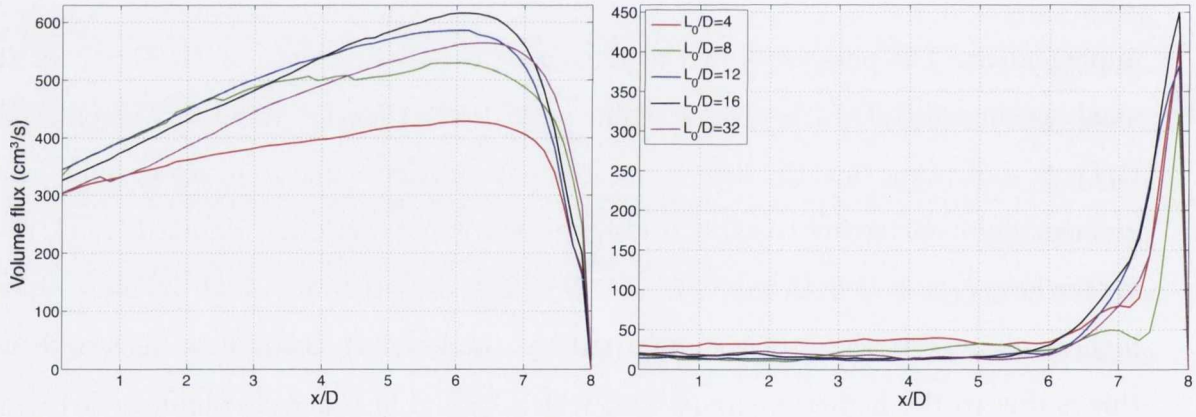

(a) axial flux (b) radial flux

Figure 6.8 – Average volume flux in the axial and radial directions from $r = \pm 2D$ at H/D=8, Re=1500.

ary vortex can be seen at a radial location of $r/D \approx 2$ and axial location of $x/D \approx 1$[2], seen in figures 5.33 to 5.35 for L_0/D=4 and figures 5.37 to 5.39 for L_0/D=8. There are irregularities in the streamlines for L_0/D=4 as the flow approaches the impingement surface. For the stroke length of L_0/D=8 there are closed streamlines on the

[2] The method of measuring the axial locations for volume flux and time averaged data is the same as explained previously in footnote 1

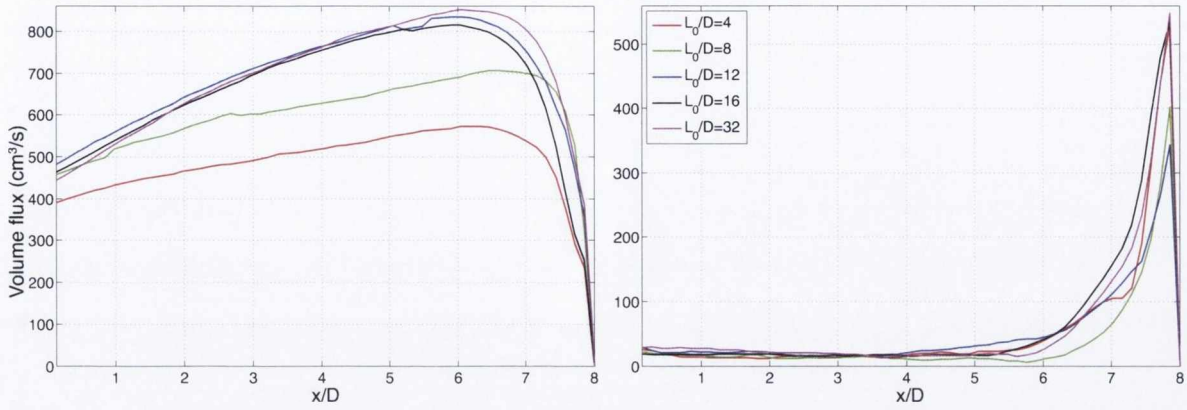

(a) axial flux

(b) radial flux

Figure 6.9 – Average volume flux in the axial and radial directions from $r = \pm 2D$ at H/D=8, Re=2000.

impingement surface, indicative of a stationary vortex. Comparing the radial flux of the synthetic jet at H/D=4 to that of H/D=8 it is interesting to note that the radial flux of the higher axial spacing shows an overall decrease in magnitude. This is attributed to the loss of momentum associated with the higher axial spacing of H/D=8. Peak axial flux is experienced for both axial spacings at Re=2000 and a stroke length L_0/D=32.

6.1.2.1 Findings

The results for volume flux have shown that at the axial spacing of H/D=4 and Re=500, the stroke length of L_0/D=4 produced a higher volume flux than the largest stroke length L_0/D=32, due in part to the effects of the trailing jet and how it affects the synthetic jet flow at low axial spacings. When compared to the higher axial spacing of H/D=8 and Re=500, the volume flux of the highest stroke length L_0/D=32 produces the highest volume flux, as the flow is allowed time to develop.

At the lower axial spacing of H/D=4, the highest radial flux was attained by the lowest stroke length value of L_0/D=4 for all but the highest Reynolds number of Re=2000. All Reynolds numbers presented for H/D=4 for the dimensionless stroke

length L_0/D=4 show signs of a stationary vortex from $x/D = 0$ to $x/D = 0.5$. At the higher axial spacing, due to reduced confinement effects, the stationary vortex is not present. Increasing the Reynolds number increases the overall radial flux of the synthetic jet. An increase in the axial spacing to H/D=8 produced an overall increase in the axial flux prior to impingement, due to the increased time available for entrainment. The rate at which a jet spreads has a direct impact on the volume flux of the jet. The volume flux data for the stroke lengths L_0/D=4 and L_0/D=8 and H/D=8 shows signs of a stationary vortex, which compares well with the time averaged data PIV data presented for the same test parameters.

6.2 Vortex evolution

A comprehensive study of the evolution of the synthetic jet vortex from formation to impingement has been carried out and is reported on in this section. Attention is focussed on vortex formation times, vortex velocities and impingement velocities, knowledge of which aid in the explanation of entrainment rates, and the effects of confinement and the orifice geometry. Vorticity, vortex co-ordinates (based on a Cartesian co-ordinate system) and vortex centre velocities were recorded at the formation and impingement times to provide a basis for calculation of vortex flight times. The mean jet width 'b' was determined to be the distance between the points on either side of the jet centreline where the mean streamwise velocity is approximately equal to $0.5U_{cl}$, [87]. Visual inspection from LaVision's PIV software DaVis [102] was used to determine several of the characteristics explained here. To ensure that the centre of the vortex was used for the co-ordinates, from the vorticity plots the densest parts of the core structure were examined for the x-y co-ordinates. These numerous characteristics were analysed from the passage of a singular vortex ring from formation to its degradation prior to impingement.

Figure 6.10 is a plot of extrapolated time of flight of a single vortex ring versus times of flight calculated from the PIV data. The process of obtaining the extrapolated vortex flight times is based on a simple method of obtaining vortex centre co-ordinates

and calculating the distance travelled between frames i and $i + 8$ based on the time taken to travel this distance[3]. Referring to figure 6.11, x is the cartesian coordinates corresponding to the vortex location, U is vortex velocity, b is the jet width, H the axial spacing and the subscripts f and i correspond to formation and impingement respectively. An instantaneous PIV data plot of the vortex formation location for H/D=8, Re=1500, L_0/D=8 is shown in figure 6.12. The raw image of the seeded flow in figure 6.12 is overlaid with vectors that have been coloured to represent vorticity. Figure 6.12 is included to provide a visual reference of the vortex location when compared to the sketch seen in figure 6.11.

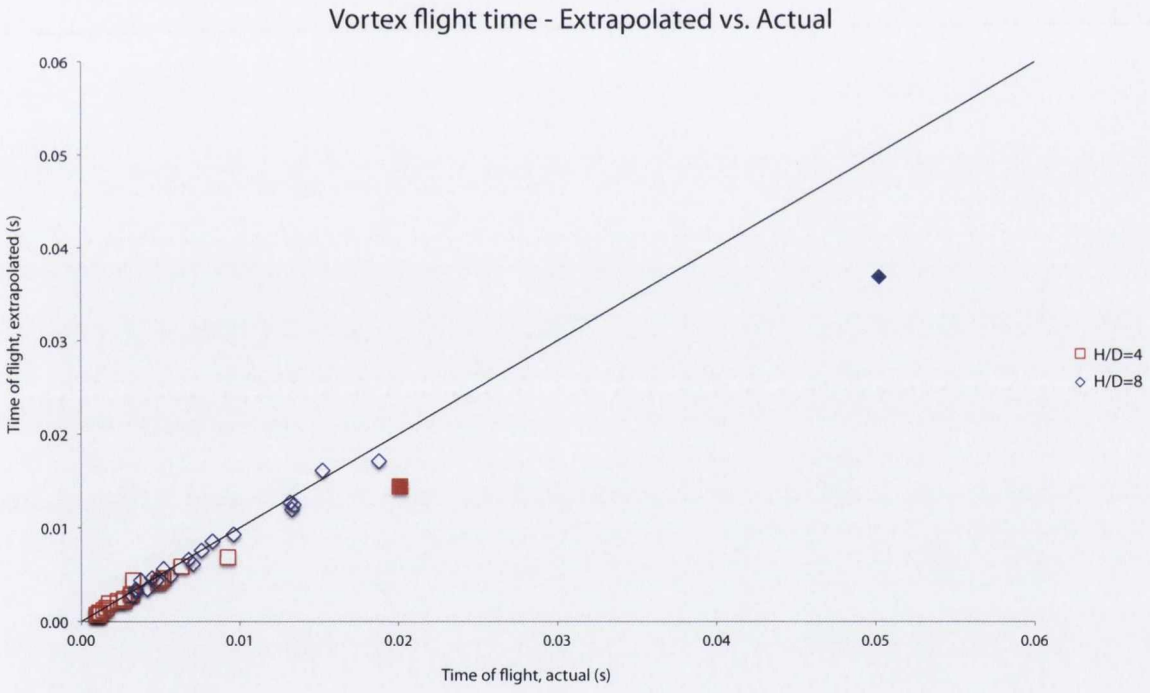

Figure 6.10 – Vortex flight times in seconds, □ H/D=4, ◇ H/D=8. Re=500, 1000, 1500, 2000. L_0/D=4, 8, 12, 16, 32

The actual vortex time of flight is obtained from the PIV software DaVis. Each PIV experiment is completed over a specific time period, i.e. one second for the high frame rate tests. 4096 frames are recorded in one second, which is considered one test. The frame where vortex formation occurs is noted and the acquisition time in the time

[3] The acquisition frequency was 4096Hz for all test cases examined here.

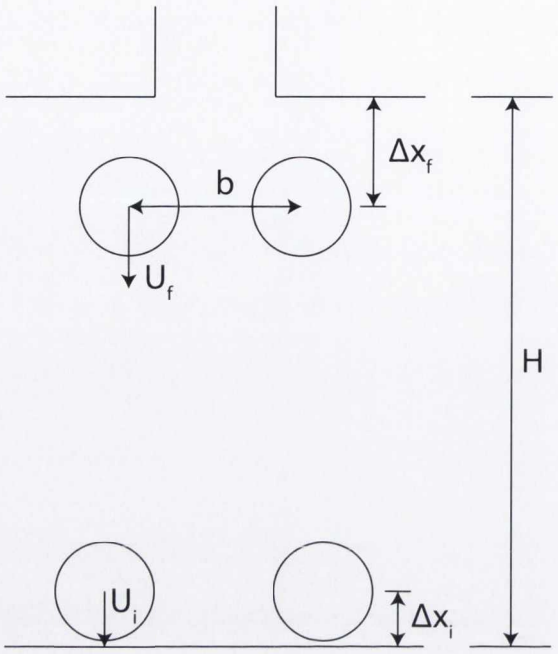

Figure 6.11 – Vortex flight time sketch. U-velocity, x-coordinates, f-formation, i-impingement, b-jet width

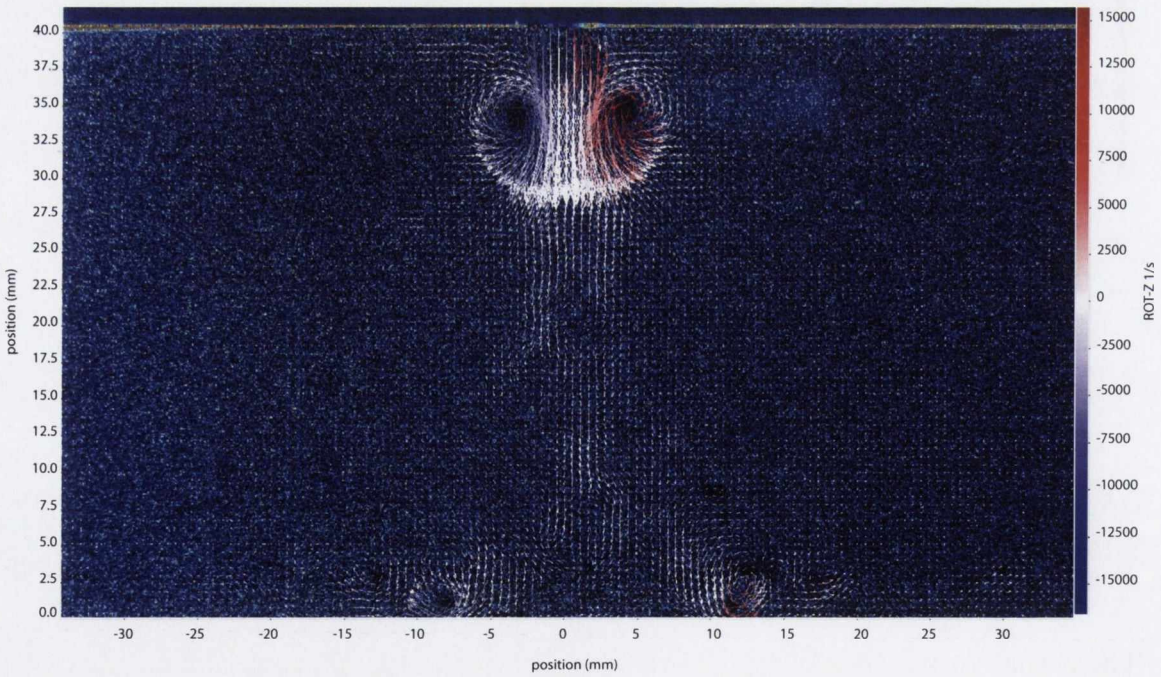

Figure 6.12 – Instantaneous PIV raw image showing location of vortex formation, overlaid with vectors representing vorticity. H/D=8, Re=1500, L_0/D=8

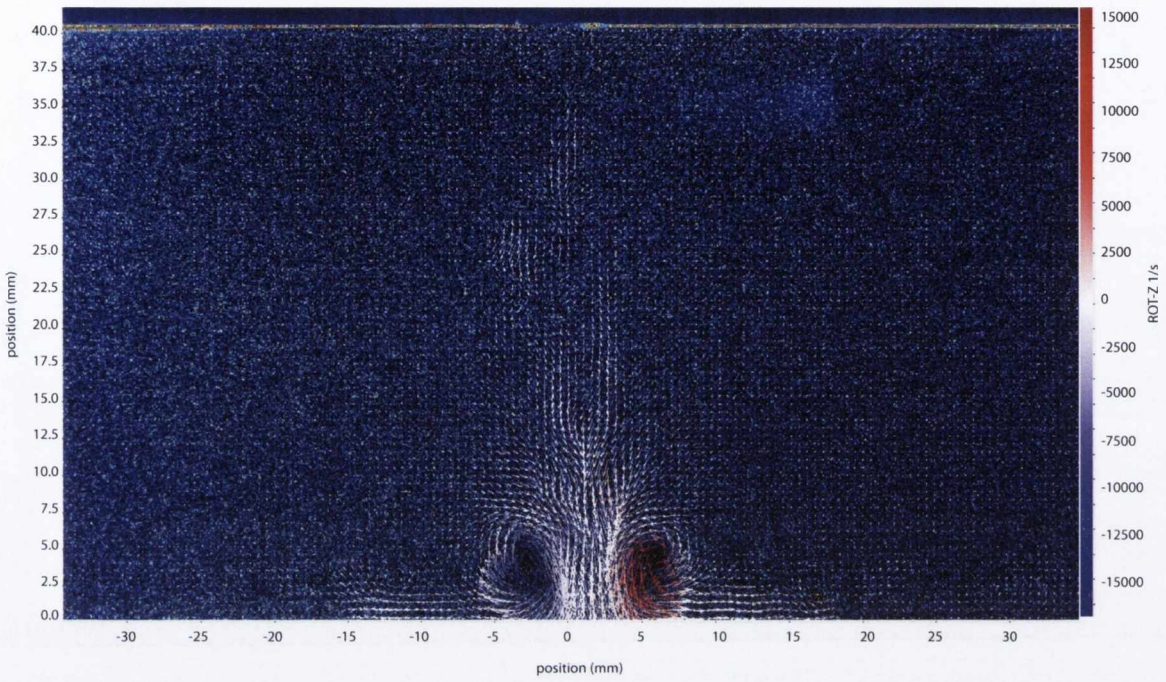

Figure 6.13 – Instantaneous PIV raw image showing location of vortex impingement, overlaid with vectors representing vorticity. H/D=8, Re=1500, L_0/D=8

series of the test is presented in μs; this is repeated for the impingement vortex. The time at vortex impingement is then subtracted from the time at vortex formation, thus yielding the actual vortex time of flight.

An example calculation for the extrapolated vortex time of flight is shown.

$$U_{vortex} = \frac{(x_{t_2} - x_{t_1})/1000}{t_2 - t_1} \tag{6.2}$$

$$Dt_{flight} = \frac{(H - (x_i + x_f))/1000}{U_{vortex}} \tag{6.3}$$

where,

1. U_{vortex}=Velocity of vortex over distance travelled from frame i to frame $i + 8$.

2. x_{t_1}=co-ordinates of vortex centre in frame i.

3. x_{t_2}=co-ordinates of vortex centre in frame $i + 8$.

4. t_1=corresponding time in frame i i.e. 0ms.

5. t_2=corresponding time in frame $i + 8$ i.e. 2ms.

6. Dt_{flight}=the predicted vortex time of flight in s.

7. H=height of orifice plate above impingement surface in mm.

8. x_f=co-ordinates of vortex centre at formation.

9. x_i=co-ordinates of vortex centre at impingement.

The vortex characteristics explained above are taken from a test, e.g. vortex characteristics and coordinates for $Re = 500$, $L_0/D = 8$ yield,

$$U_{vortex} = \frac{(8.4876 - 4.895)/1000}{0.002 - 0} \tag{6.4}$$

$U_{vortex} = 1.7963\, m/s$.
and,

$$Dt_{flight} = \frac{(20 - (4.8 + 3.86))/1000}{1.7963} \tag{6.5}$$

$Dt_{flight} = 0.006314\, s$

In order to correctly calculate the extrapolated time of flight of the vortex from formation to impingement, the vortex centre at formation and impingement had to be subtracted from the overall distance travelled. The co-ordinates of the vortex centre at formation and impingement were obtained through visual inspection of a vector map of the flow, seen in figure 6.12 and figure 6.13.

The time of flight data reported here provides a basis in the steps towards understanding the effect of the 'trailing jet', confinement, recirculation and entrainment on

the vortex ring that is associated with a synthetic air jet.

Figure 6.10 represents the vortex times of flight for the entire range of parameters tested here, four Reynolds numbers, (Re=500, 1000, 1500, 2000) five stroke lengths (L_0/D=4, 8, 12, 16, 32), and two heights above the impingement surface ($4D, 8D$). For a clearer understanding of figure 6.10, a summary of the values graphed is shown in table 6.2. From table 6.2, it can be seen that the Reynolds number and stroke length of the synthetic jet appear to be linked with respect to the decrease in vortex flight time, i.e. as these linked parameters are increased, the vortex flight times generally decrease for both H/D values.

The extrapolated values for vortex times of flight represent when the vortex is anticipated to impinge[4], and the actual values represent the exact length of time taken from formation to impingement. There is an obvious decrease in the length of time taken for the vortex to travel from its formation to impingement as the Reynolds number and stroke length are increased. This is largely due to the increase in velocity as the Reynolds number and stroke length of the jet are increased, resulting in a decrease in time taken to travel distance 'x'. The time decrease is not entirely linear though, as can be seen in table 6.2. Thus, at an axial distance of H/D=4 above the impingement surface there is a decrease in vortex flight time from L_0/D=4 to L_0/D=12 but at L_0/D=16 the vortex flight time, for both extrapolated and actual values increases and then decreases again for L_0/D=32. This pattern exists for all four Reynolds numbers tested here. It would appear that, due to the low axial spacing, recirculation and confinement affects the vortex flight time for L_0/D=16 because, when compared to the axial spacing of H/D=8, the vortex flight times for the extrapolated values at this stroke length follow the same trend. Comparing the actual vortex times of flight for H/D=4 to those of H/D=8, the flight times at the lower axial spacing follow the trend of the extrapolated values described above, whereas the actual vortex flight times at the higher axial spacing are in line with an overall linear decrease in time,

[4] This is based on the values calculated from equation 6.5

Table 6.2 – Vortex times of flight in seconds.

L_0/D	Re	$H/D = 4$		$H/D = 8$	
		Extrapolated	Actual	Extrapolated	Actual
4	500	0.02010	0.01440	0.05021	0.03687
8	500	0.00631	0.00586	0.01521	0.01611
12	500	0.00500	0.00439	0.01316	0.01270
16	500	0.00519	0.00464	0.01340	0.01245
32	500	0.00326	0.00439	0.01327	0.01196
4	1000	0.00924	0.00684	0.01877	0.01709
8	1000	0.00316	0.00293	0.00828	0.00854
12	1000	0.00230	0.00220	0.00677	0.00659
16	1000	0.00268	0.00244	0.00706	0.00610
32	1000	0.00173	0.00195	0.00567	0.00488
4	1500	0.00484	0.00415	0.00961	0.00928
8	1500	0.00272	0.00220	0.00519	0.00562
12	1500	0.00138	0.00122	0.00470	0.00464
16	1500	0.00158	0.00146	0.00474	0.00439
32	1500	0.00112	0.00098	0.00416	0.00342
4	2000	0.00311	0.00293	0.00761	0.00757
8	2000	0.00116	0.00094	0.00375	0.00439
12	2000	0.00095	0.00073	0.00343	0.00342
16	2000	0.00108	0.00073	0.00346	0.00317
32	2000	0.00098	0.00073	0.00321	0.00269

indicating that confinement and recirculation have less of an effect on the synthetic jet at H/D=8. Referring to figure 6.10, it is evident that there is a large cluster of data points near the origin, indicating very short lengths of time for the vortex to travel to the impingement surface. The effect of the low axial spacing on vortex flight time is evident here, as the majority of data points clustered near the origin relate to the lower spacing of H/D=4. The synthetic jet parameters L_0/D=4, Re=500, for H/D=4 and H/D=8 are the two solid data points[5] for each series that are not clustered near

[5] ■ H/D=4, ♦ H/D=8

the origin; these are the slowest vortex flight times in this test setup, due to the low velocity corresponding to these synthetic jet parameters.

Figures 6.14 and 6.15 provide an insight as to why the extrapolated vortex flight times increase at L_0/D=16, as is evident from table 6.2. These graphs represent vortex velocity (U_{vortex}) normalised[6] by U_0. Of the four profiles shown for each H/D value, the velocity profiles collapse quite well.

It can be seen in these two figures that there is an obvious peak in the trendlines for all four Reynolds numbers at L_0/D=12, followed by a slight dip at L_0/D=16. The velocities plotted in figures 6.14 and 6.15 were utilised in equation 6.3 to calculate the predicted vortex times of flight, so it follows that they are related.

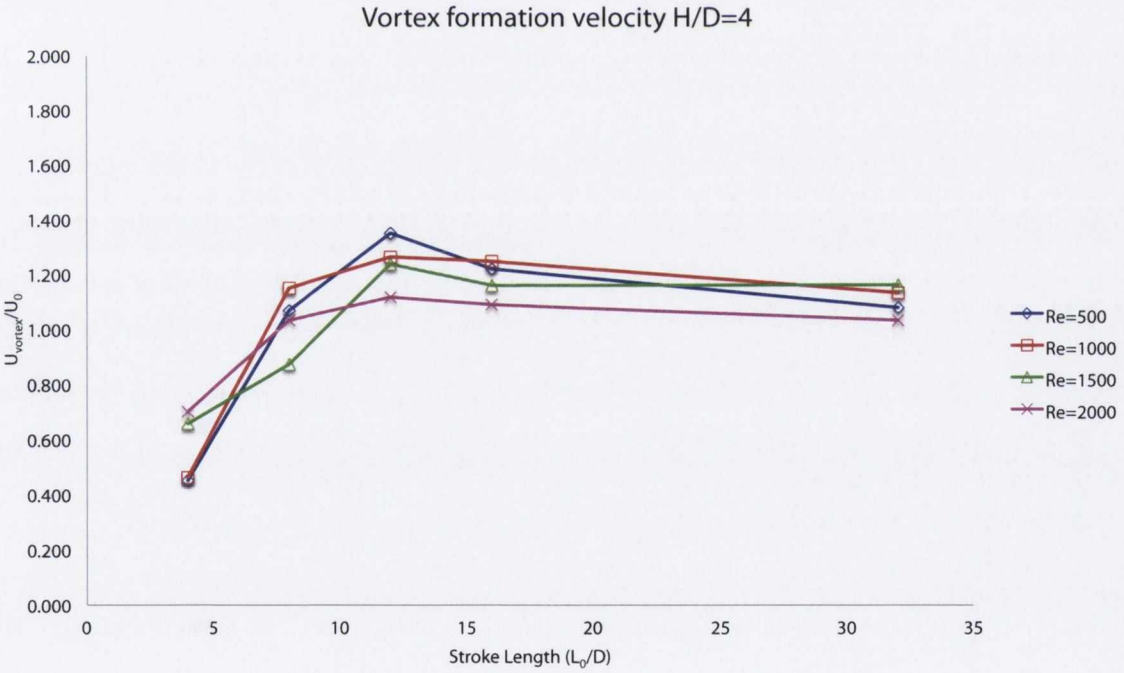

Figure 6.14 – Vortex velocities normalised by U_0, H/D=4, ◇Re=500, □Re=1000, △Re=1500, ×Re=2000.

Figure 6.16 is a result of a fitting procedure performed to collapse the data from fig-

[6] This was done to evaluate U_0 as a scaling velocity

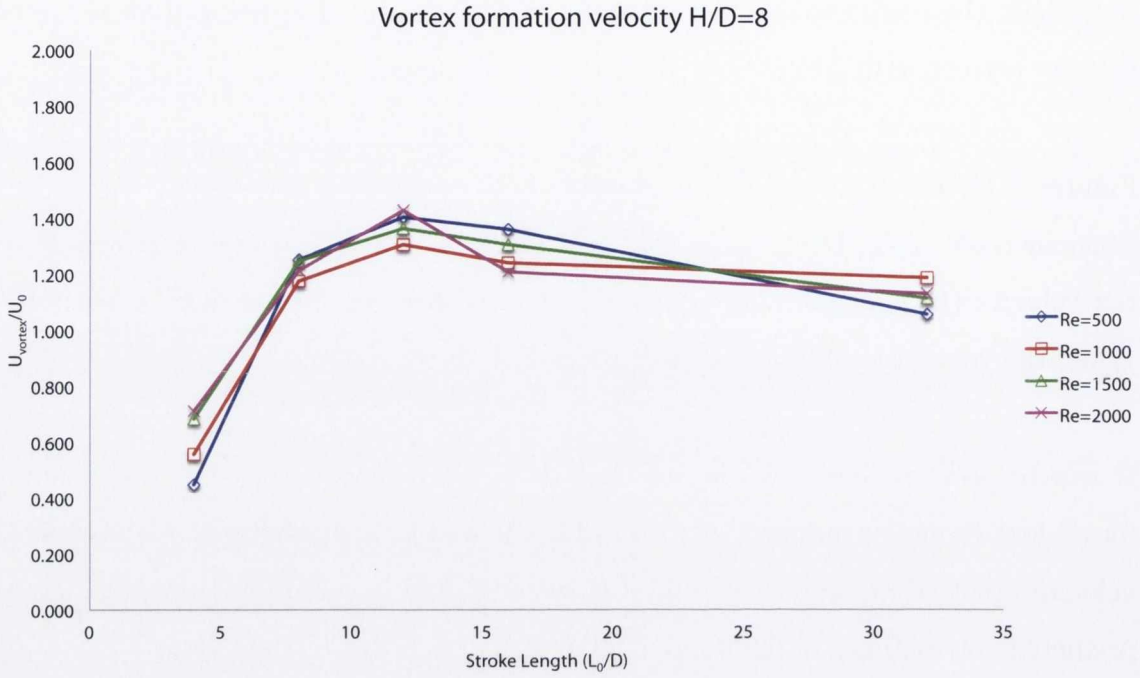

Figure 6.15 – Vortex velocities normalised by U_0, H/D=8, ◇Re=500, □Re=1000, △Re=1500, ×Re=2000.

ures 6.14 and 6.15 to a correlation of the form $(L_0/D)^a Re^b$. The values selected for the exponents were a=0.9 and b=0.4. These values were selected as a result of a fitting procedure that involved quantifying the degree of collapse of the graphs according to a standard deviation of the values of the correlation $(L_0/D)^a Re^b$. The fact that the exponent values selected for the correlation are both less than or equal to one, this means that the Reynolds number has little or no effect in this range and the trends seen in figure 6.16 are all due to the stroke length.

There are a number of reasons suggested in the literature as to why vortex rings might slow down [131], [132], [133]. One common suggestion is that the core grows by diffusion thereby reducing the velocity [9]; another hypothesis is that decay occurs due to mutual friction with the normal fluid component, or a further possibility cited is that the vortex ring may become turbulent in some sense and start to break up [26]. These interpretations all relate to a single vortex ring, rather than a synthetic jet. While the fundamental structure of a synthetic jet is a vortex ring, the stroke length

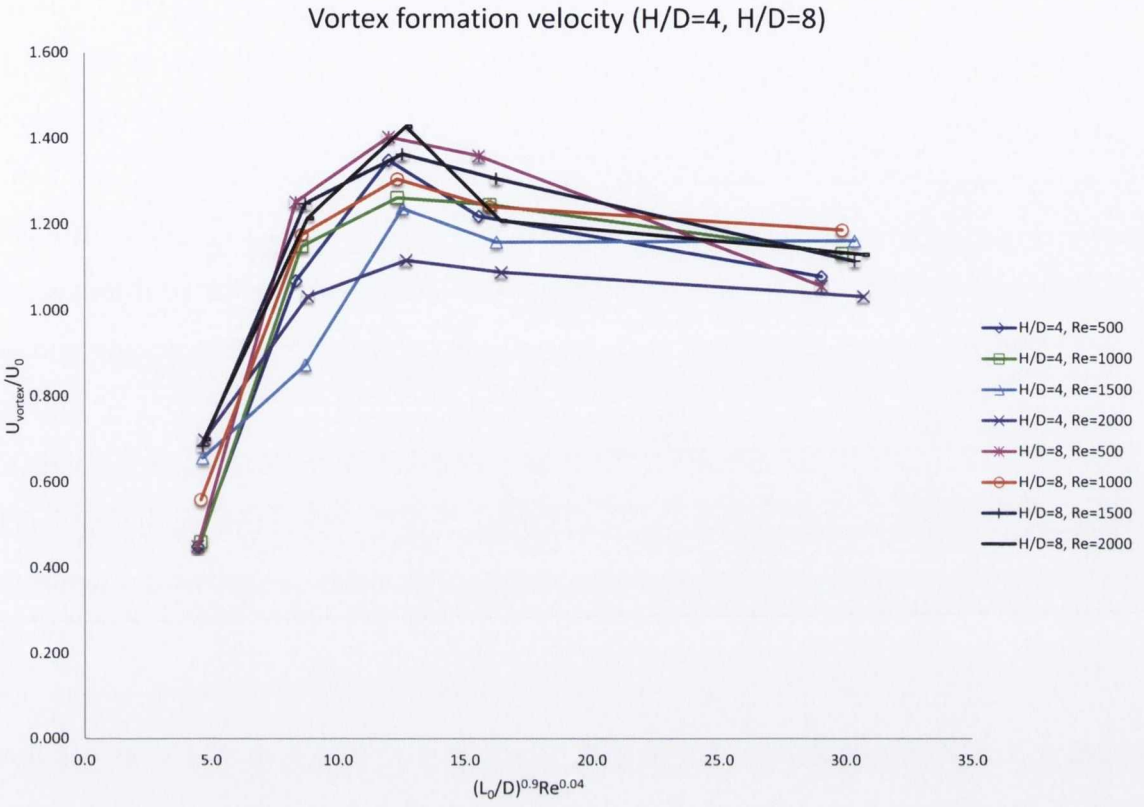

Figure 6.16 – Vortex velocities normalised by U_0, H/D=4 and H/D=8 versus $(L_0/D)^{0.9}Re^{0.4}$.

of the jet will dictate the frequency of the vortex ring formation, and the occurrence of a trailing jet; this, of course, interacts not only with the vortex ring but also with its surroundings. In some cases this trailing jet can cause the vortex ring to speed up, decay and skew before impingement. Instantaneous PIV data taken at a high frame rate of $4096Hz$ provide a better picture of the vortex ring and trailing jet. Thus, the effects of the trailing jet can be inferred from figures 6.17 and 6.18. Figure 6.17 represents the formation and impingement vortex velocities for the entire range of tests carried out at both H/D=4 and H/D=8. The velocities plotted have all been normalised by U_0. It can be seen that the profiles collapse quite well for formation and impingement at both axial spacings. The effect of the trailing jet can be identified at L_0/D=32 for the impingement velocities, which are represented by the dotted lines. Thus, the increase in impingement velocity to higher than the formation velocity at this stroke length is attributed to the trailing jet that is formed behind the vortex ring at high

stroke lengths. This trailing jet essentially pushes the vortex ring along, leading to an increased velocity vortex ring impinging on the plate. Figure 6.18 represents the difference between the formation velocity ($U_{formation}$) and the impingement velocity ($U_{impingement}$).This reveals that the trailing jet not only affects L_0/D=32, but can be seen to increase the velocity of the vortex ring for L_0/D=16 at the highest Reynolds number tested here. Figure 6.18 shows that the trailing jet begins to dominate the flow from the vortex ring for the stroke length of L_0/D=32 at all Reynolds numbers and both axial spacings i.e. the trailing jet is now leading the flow prior to impingement. For both axial spacings and a Reynolds number of 2000, which corresponds to a relatively high velocity for a synthetic jet flow, at L_0/D=16 also the trailing jet has led to an increased velocity of the impinging vortex. It can also be seen from figure 6.18 at H/D=4, Re=2000 that L_0/D=12 is affected slightly by the presence of a trailing jet, as its momentum and velocity have not diminished nearly as much as the other data points below the x-axis. This could also be due to the effects of recirculation and entrainment rates increasing at H/D=4, as this stroke length does not show signs of being influenced by a trailing jet, for the larger axial spacing.

Instantaneous high frame rate PIV data for H/D=4 and H/D=8 respectively are presented in figures 6.19 and 6.20 to provide a visual appreciation of the trailing jet. The colour bar applies to both figures 6.19 and 6.20, with red signifying negative vorticity and blue positive. These figures are presented in ascending order i.e. from the lowest Reynolds number to the highest. The stroke lengths selected correspond to the positive data points in figure 6.18, at which the effect of the trailing jet starts to dominate the flow field. In effect, the trailing jet takes precedence over the vortex ring at these stroke lengths. Thus, instead of being allowed to convect on its own to the impingement surface, the vortex ring coalesces with the trailing jet, and in some cases with high stroke lengths and Reynolds number the trailing jet will impinge before the vortex ring. With an increase in the Reynolds number the vortex ring is forced to widen beyond its original diameter at formation, along with a coalescence of the trailing jet and vortex ring, prior to impingement. Shuster and Smith [11] documented the presence of a trailing jet at L_0/D=5, however their study did not investigate the

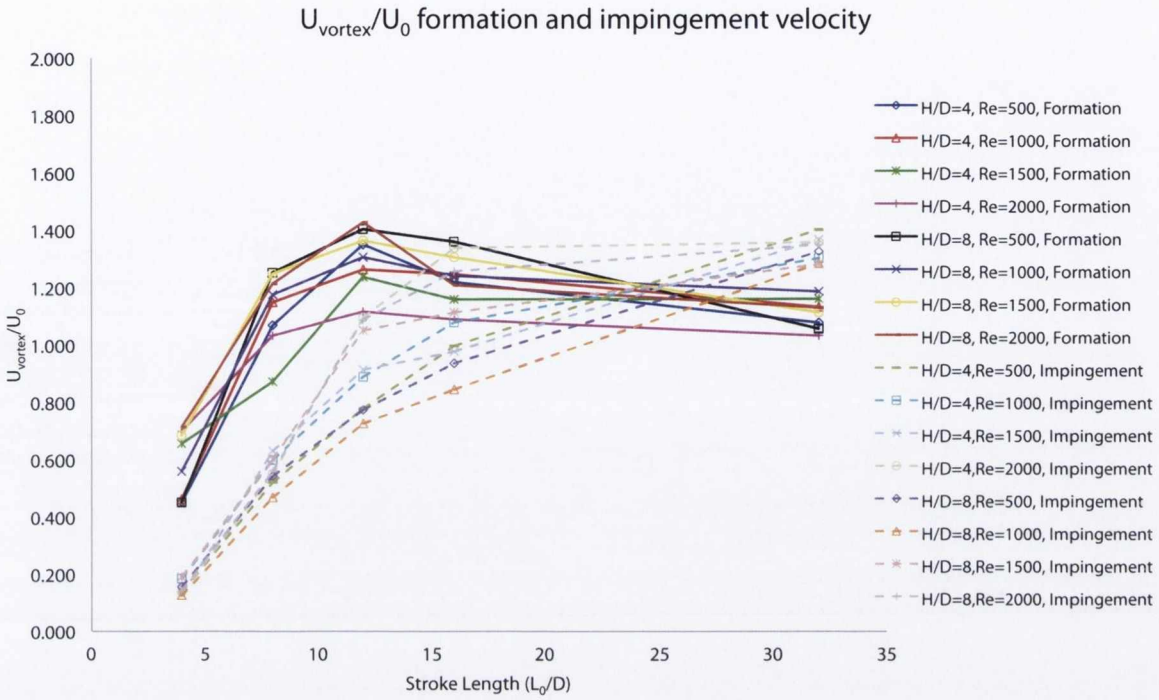

Figure 6.17 – Formation and impingement vortex velocities normalised by U_0.

effect of the trailing jet on the vortex ring.

In figure 6.19 it is evident that at H/D=4 the trailing jet dominates the entire field of view, primarily because of the low axial spacing. For the same synthetic jet operational parameters but at a higher axial spacing of H/D=8 it can be seen from figure 6.20 that, due to the increase in height, the trailing jet has sufficient time to develop and interact with the leading vortex ring. Thus, in figure 6.20b, c, d and e the trailing jet has coalesced, destabilised and caused vortex breakdown prior to impingement at these operational parameters. At high stroke lengths ($8<L_0/D<32$) the trailing jet catches up with the vortex and causes an increase in velocity, along with a destabilisation of the vortex ring, as shown in figure 6.20. From a heat transfer perspective, this is detrimental to the efficacy of the synthetic jet (as a potential cooling source), as the vortex strength is decreased and heat transfer rates can decrease [134]. Even though the PIV measurements taken show that there is a weak trailing jet at L_0/D=8, it has not been found to have a huge impact on the vortical structures present in the flow as mentioned previously. With reference to figure 6.18 it can be seen that the trail-

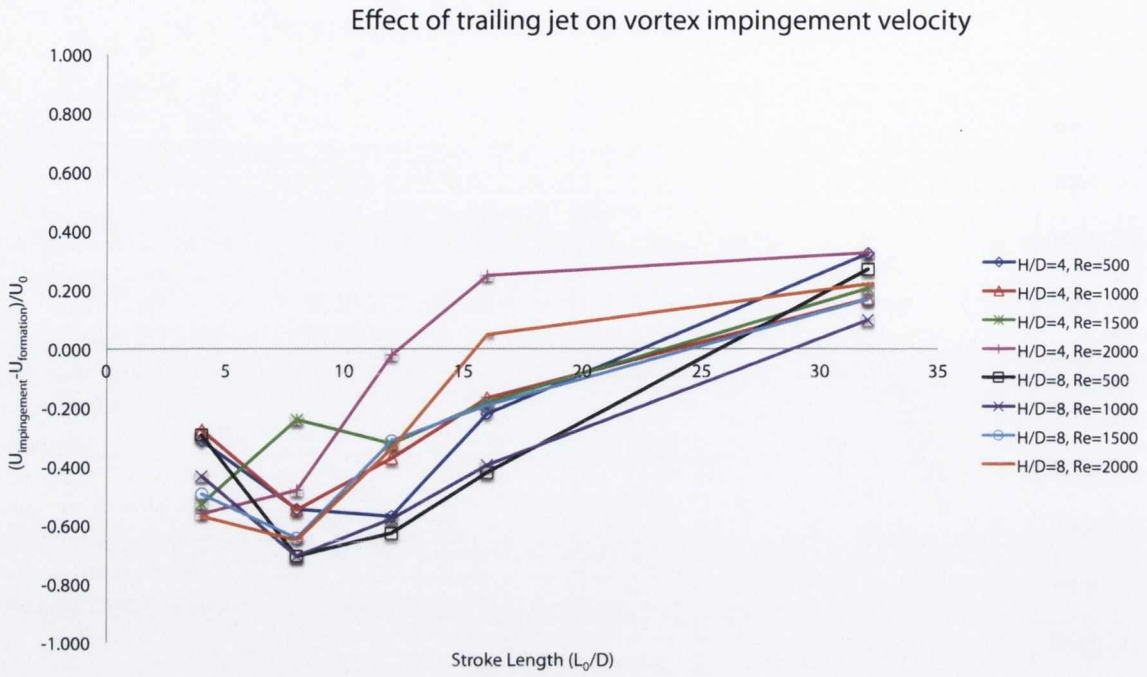

Figure 6.18 – Effect of trailing jet on vortex impingement velocity, normalised by U_0.

ing jet primarily has an effect, in terms of increasing vortex velocity from formation to impingement, on the stroke lengths and Reynolds numbers specified and shown in figures 6.19 and 6.20.

6.2.0.2 Findings

The results presented for vortex evolution have shown that at high dimensionless stroke lengths the trailing jet has quite a large effect on not only the vortex ring, but also the flow structure of the synthetic jet, as seen in the instantaneous PIV data presented. This is also seen in the vortex time of flight results, in which there is a linear decrease in the vortex time of flight until the stroke length L_0/D=16, at the point there is an increase, although marginal. The same trend exists for all Reynolds numbers at H/D=4, and for the extrapolated values of H/D=8. Comparing large dimensionless stroke length values ($L_0/D \geq 12$) with the lower stroke length values, the impinging vortex velocity is seen to be higher due to the interaction of the trailing jet with the leading vortex.

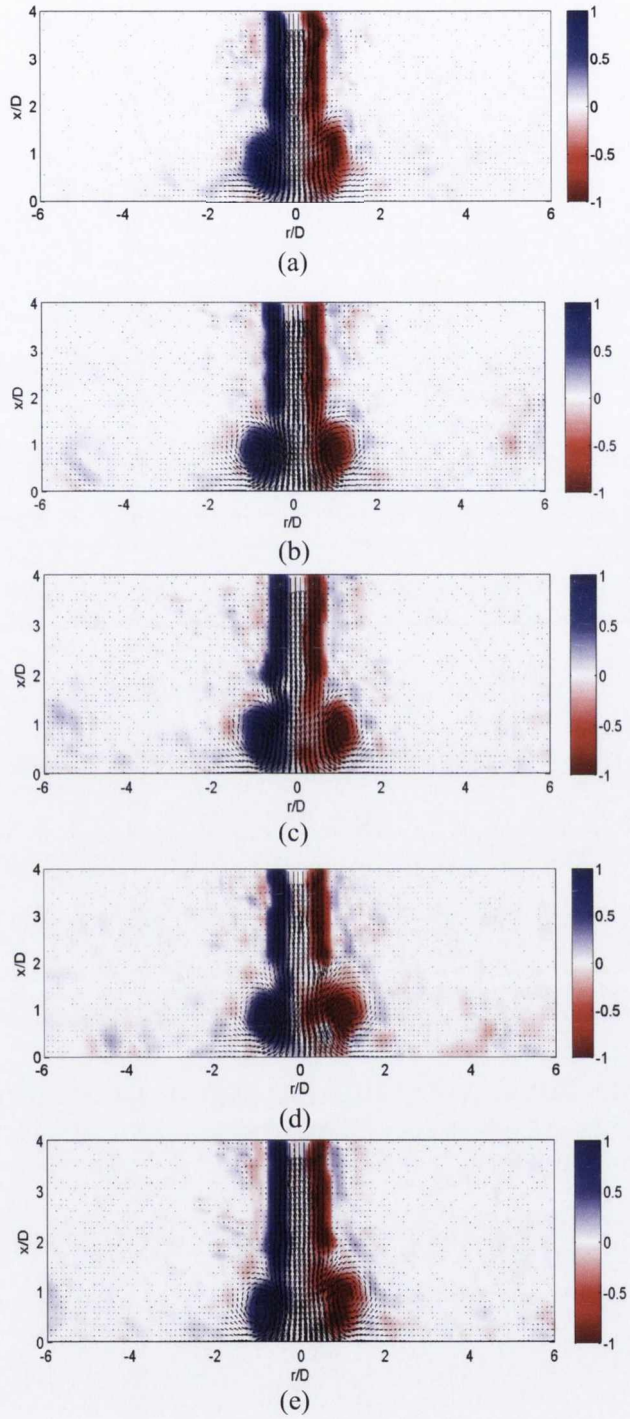

Figure 6.19 – Effect of trailing jet on vortex at H/D=4, (a) ϕ=70°, Re=500, L_0/D=32 (b) ϕ=60°, Re=1000, L_0/D=32 (c) ϕ=65°, Re=1500, L_0/D=32 (d) ϕ=107°, Re=2000, L_0/D=16 (e) ϕ=64°, Re=2000, L_0/D=32.

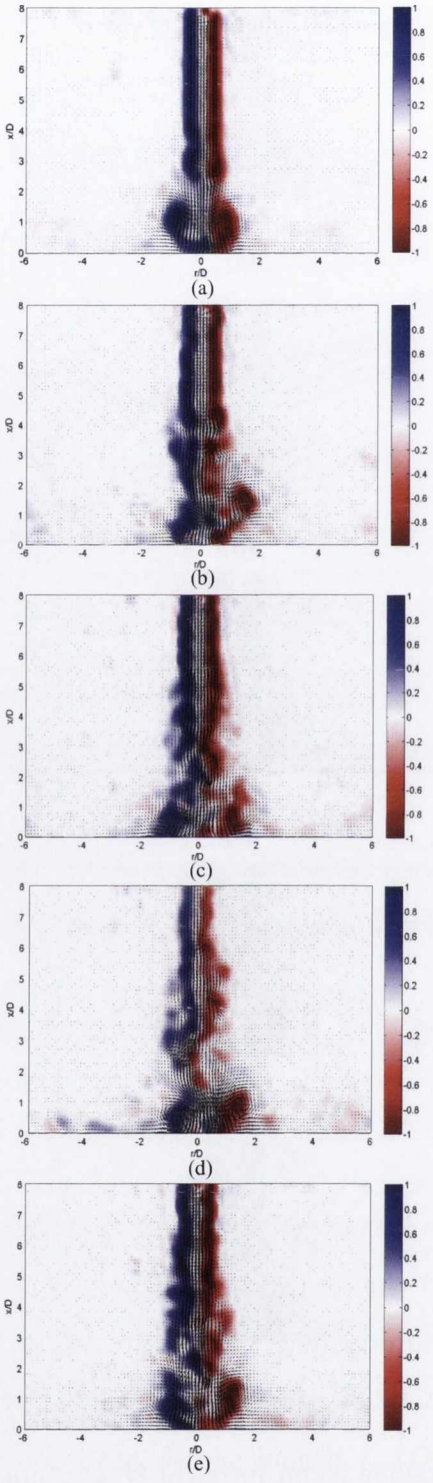

Figure 6.20 – Effect of trailing jet on vortex at H/D=8, (a) ϕ=108°, Re=500, L_0/D=32 (b) ϕ=93°, Re=1000, L_0/D=32 (c) ϕ=98°, Re=1500, L_0/D=32 (d) ϕ=174°, Re=2000, L_0/D=16 (e) ϕ=97°, Re=2000, L_0/D=32.

6.2.1 Location of vortex formation

The cross stream location at which the streamwise velocity is half of the centreline velocity is a commonly used quantitative measurement of the width of a jet [11], [87]. Thus, in this study, the mean jet width was determined as the distance between the points on either side of the jet centreline where the mean streamwise velocity is approximately equal to $0.5U_{cl}$. Figures 6.21 and 6.22 compare the variations in the formation location of the vortex ring for synthetic jets formed at the two axial spacings for the five stroke lengths and four Reynolds numbers tested. The streamwise distance (x) has been scaled on the actuator stroke (L_0) in an attempt to see if the data plotted would collapse. When scaled in this manner it is evident that there is a common cluster point for the data points seen in figure 6.21 (for H/D=4) at approximately $x/L_0 \approx 0.12$; this value corresponds to the point at which the vortex has just detached from the orifice plate. For the axial spacing of H/D=8, $x/L_0 \approx 0.12$ is also the approximate point of vortex detachment from the orifice plate, which indicates that vortex formation is not hindered by the effects of recirculation or entrainment at the lower H/D value. With regard to the effect of Reynolds number on the streamwise variation and vortex detachment, from figure 6.21 at H/D=4, the indications are that vortex detachment is largely independent of Reynolds number. For H/D=8, shown in figure 6.22, the x/L_0 values seem to be slightly more variable, however it is worth noting that the difference between these points is small. The spread in b/D_0 values as Reynolds number and stroke length increases indicates that the jet width at the vortex formation location is growing as these parameters are increased; this is expected. However, there appears to be a decrease in the jet width at the location of vortex detachment for a stroke length of L_0/D=32 at a Reynolds number of Re=2000 for both axial spacings. This can be seen for H/D=4 in figure 6.21d, and similarly for H/D=8 in figure 6.22d. The data for figure 6.21 and figure 6.22 are presented in table 6.3.

The stroke length of L_0/D=4 is almost unaffected by the increase in Reynolds number in terms of x/L_0, and there is almost no change in jet width (b/D_0) for H/D=4. Interestingly, the jet width for L_0/D=4 is slightly lower for the H/D=8 case for the

Table 6.3 – x/L_0 represents the axial location of the formed vortex and b/D_0 represents the jet width, both are non-dimensional.

		$H/D = 4$		$H/D = 8$	
		Location of vortex formation	Jet width	Location of vortex formation	Jet width
L_0/D	Re	x/L_0	b/D_0	x/L_0	b/D_0
4	500	0.13	1.52	0.15	1.41
8	500	0.12	1.52	0.17	1.52
12	500	0.09	1.52	0.11	1.63
16	500	0.08	1.52	0.10	1.52
32	500	0.06	1.62	0.08	1.63
4	1000	0.14	1.52	0.19	1.52
8	1000	0.13	1.52	0.13	1.52
12	1000	0.10	1.63	0.13	1.73
16	1000	0.08	1.52	0.14	1.95
32	1000	0.04	1.52	0.09	1.95
4	1500	0.15	1.52	0.25	1.41
8	1500	0.14	1.62	0.16	1.63
12	1500	0.13	1.63	0.12	1.73
16	1500	0.09	1.63	0.09	1.73
32	1500	0.07	1.84	0.10	2.06
4	2000	0.16	1.52	0.18	1.41
8	2000	0.23	1.52	0.19	1.73
12	2000	0.16	1.84	0.14	1.63
16	2000	0.13	1.73	0.14	1.84
32	2000	0.07	1.63	0.07	1.84

majority of Reynolds numbers, and the formation location is slightly further away from the orifice plate than for H/D=4.

The lower axial spacing of H/D=4 of figure 6.21 shows that there is not as much variability in the jet width (b/D_0) when compared to the higher axial spacing of H/D=8 in figure 6.22. It is suggested that confinement has an effect on the jet width at vortex for-

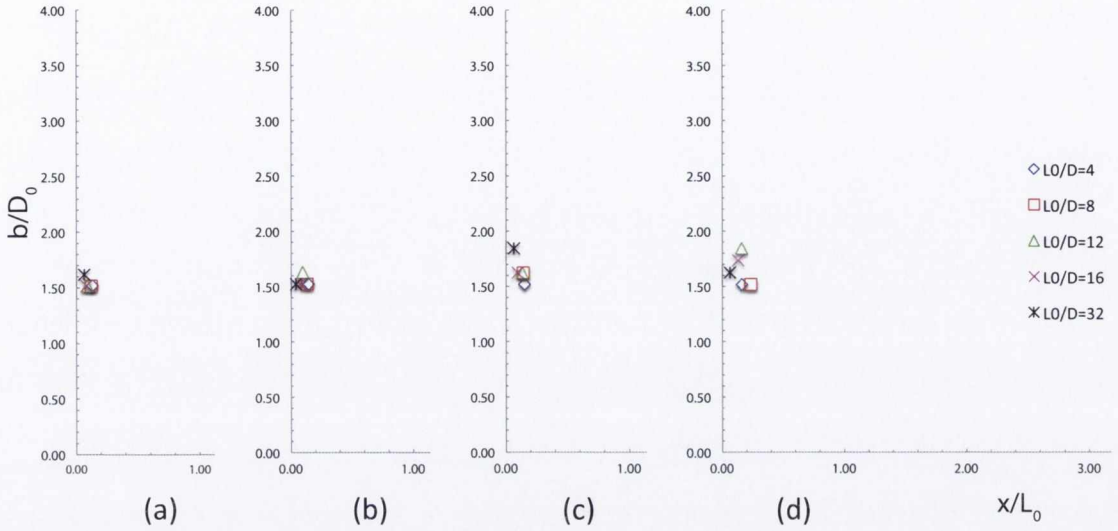

Figure 6.21 – Jet width against location of vortex formation for H/D=4. b/D_0 is plotted versus x/L_0. L_0/D=4, 8, 12, 16, 32. (a) Re=500 (b) Re=1000 (c) Re=1500 (d) Re=2000.

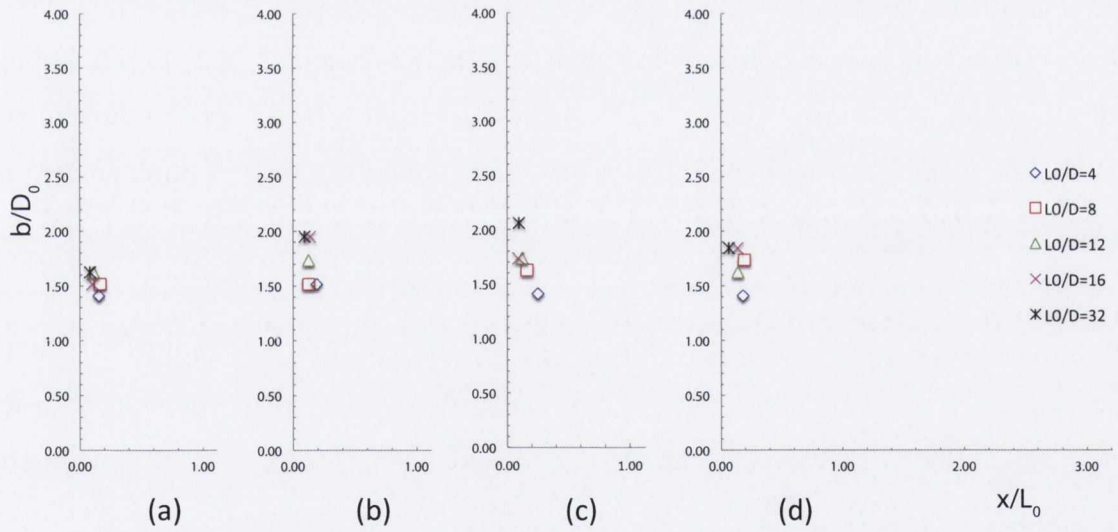

Figure 6.22 – Jet width against location of vortex formation for H/D=8, b/D_0 is plotted versus x/L_0. L_0/D=4, 8, 12, 16, 32. (a) Re=500 (b) Re=1000 (c) Re=1500 (d) Re=2000.

mation for high Reynolds numbers at H/D=4. Thus, increasing the Reynolds number from 1500 to 2000 results in a reduction in the dimensionless jet width. This suggest that as the Reynolds number is increased confinement and recirculation influence the width of the formed vortex.

6.2.1.1 Findings

The location of vortex formation data is seen to collapse quite well when scaled on the actuator stroke L_0. The location of vortex detachment is seen to be $x/L_0 \approx 0.12$ for both axial spacings, H/D=4 and H/D=8. The spread in jet width b/D_0 as the jet Reynolds number is increased indicates that the jet width at the vortex formation location is growing. However, the jet width for the highest stroke length value L_0/D=32 at both axial spacings is seen to decrease in jet width. The reason for this is not yet understood.

6.3 Vortex roll up

6.3.1 Characteristics of vortex subsequent to impingement

This section presents simultaneous surface heat transfer measurements and stereoscopic PIV measurements. These data present what is deemed to be the final stage of development of the synthetic jet as it has evolved from formation to impingement. This section attempts to understand the vortex roll up subsequent to impingement of a synthetic jet and the effect it has on heat transfer at an axial spacing of H/D=12, a jet Reynolds number of Re=1500 and dimensionless stroke lengths of L_0/D=12, and 28. Work completed by Persoons et al. [134] identified four heat transfer regimes for a synthetic air jet. Comparing the test parameters selected to the heat transfer regimes identified by Persoons et al. [134], the stroke length of L_0/D=12 falls in the heat transfer regime B and for the stroke length L_0/D=28, regime C.

It has been documented that vortex roll up occurs subsequent to jet impingement [64]. Stereoscopic PIV data with the light sheet parallel to the impingement surface was implemented in order to show the three dimensional nature of the vortices subsequent to impingement as they expand radially outwards. A numerical paper by Hadžiabdić [135] presents the results of near wall turbulence and local heat transfer coefficients for an impinging steady jet; their work focussed on the vortical structures within the shear layer from the jet exit up to impingement. It was suggested by Hadžiabdić [135]

that the periodic and asymmetric impingement of strong large-scale eddy structures enhanced the surface heat transfer through surface renewal. Subsequent to impingement Hadžiabdić [135] noted that in the wall jet that there was a development and organisation of the flow structures as the jet deflects from the impingement plate. This consisted of a scrambling of the ring-like structures in the impingement zone, along with a tendency towards vortical self-organisation in the form of a new roll up of ring-like vortical structures formed at the wall-jet edge. Some of these features are seen in data presented here for the vortex roll up.

The stereoscopic PIV data are presented here along with local heat transfer measurements for a radial location of $r/D = 3$. This radial location corresponds to the position of the hot film sensor on the impingement surface in jet diameters from the jet centre; the hot film sensor was used for the acquisition of the heat transfer measurement data.

For the heat transfer tests, the copper plate was heated to $60° C$ and provided a nominally uniform wall temperature boundary condition due to the thickness and conductivity of copper[7]. The time lag and phase lag between the local velocity and surface heat flux is calculated from these measurements to understand the effects of stroke length on the vortex ring as it approaches and rolls over the hot film sensor. The laser light sheet was parallel to and axially located at approximately $2.5\,mm$ (0.5D) above the impingement surface. Positioning the light sheet parallel to the impingement surface at a height of $2.5\,mm$ was based on observation of the size of the vortex subsequent to impingement from the 2D PIV data presented in section 5.2. Due to the orientation of the light sheet optics, the beam width at its thinnest point was approximately $1\,mm$; at the extremities of the measurement zone and as a result of a slight misalignment in the light guide arm the light sheet could be as thick as $2\,mm$. An image of the stereoscopic PIV test setup is presented in figure 6.23; from this figure the orientation of the light sheet and of the high speed cameras with respect to the position of the synthetic jet generator in the centre of the image can be clearly seen.

[7] The details of the copper plate have been previously covered in chapter 4

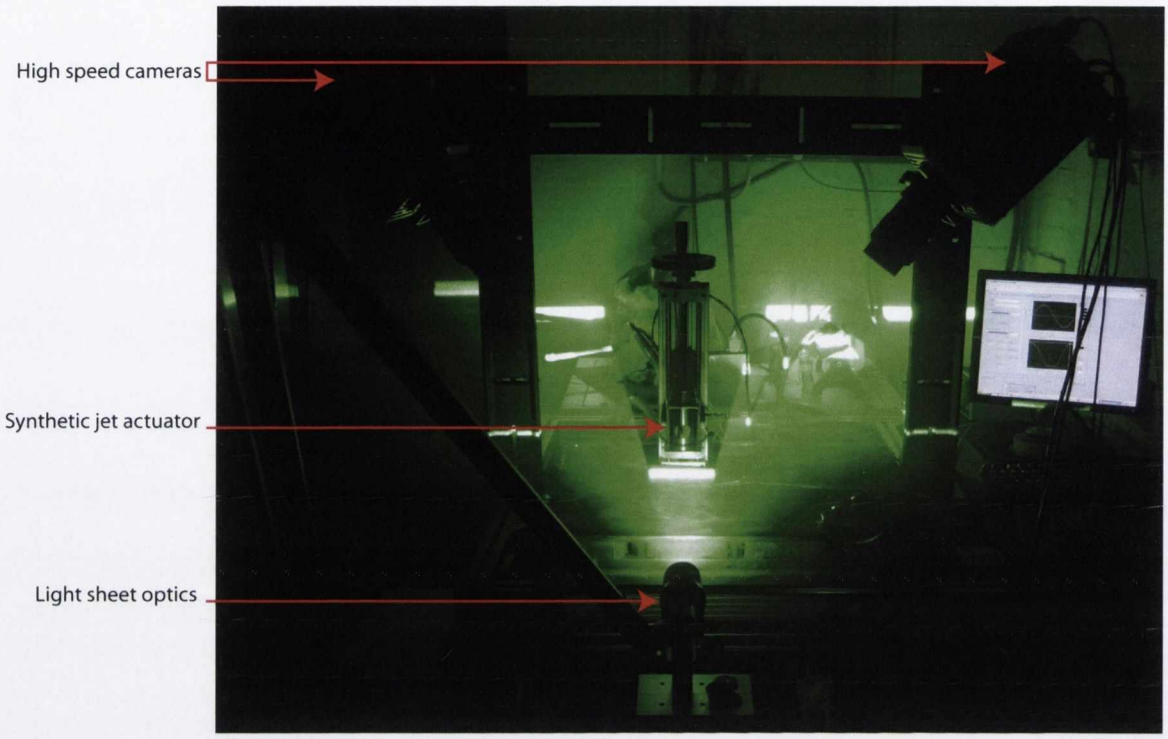

Figure 6.23 – Stereoscopic PIV test setup for H/D=12, Re=1500, L_0/D=12 and 28.

Two examples of the instantaneous 2D PIV data utilised for visual inspection, in order to gauge the vortex diameter subsequent to impingement, are presented in figures 6.24 and 6.25 for the axial spacings of H/D=4 and H/D=8 respectively. The vertical extent of the estimated vortex diameter once vortex roll up has commenced is indicated by the white line in these figures. The data presented in section 6.2 for the vortex time of flight are used to estimate the averaged vortex centre locations prior to impingement and are presented in table 6.4 for all stroke lengths. The data presented in table 6.4 provided a starting point for estimating the vortex diameter subsequent to impingement. The diameter of the vortex created after impingement is approximately $5.5\,mm$, while from table 6.4 the average vortex centre for all the test parameters is approximately $3\,mm$. Thus, locating the light sheet at $\approx 2.5\,mm$ means that the intersection point of the light sheet and the vortex subsequent to impingement is approximately in the centre of the vortex. This allows in and out of plane velocity to be calculated and vortex roll up to be observed. These stereoscopic PIV data are presented in figures 6.27, and 6.30. This data comprises of a compiled image of the vortex ring on the impingement surface

as it grows and dissipates subsequent to impingement of the synthetic jet. When the calibration was performed for the stereoscopic PIV setup, the velocity measured towards the surface was set as the positive, therefore according to the colour bar, red signifies the positive velocity and blue the negative velocity.

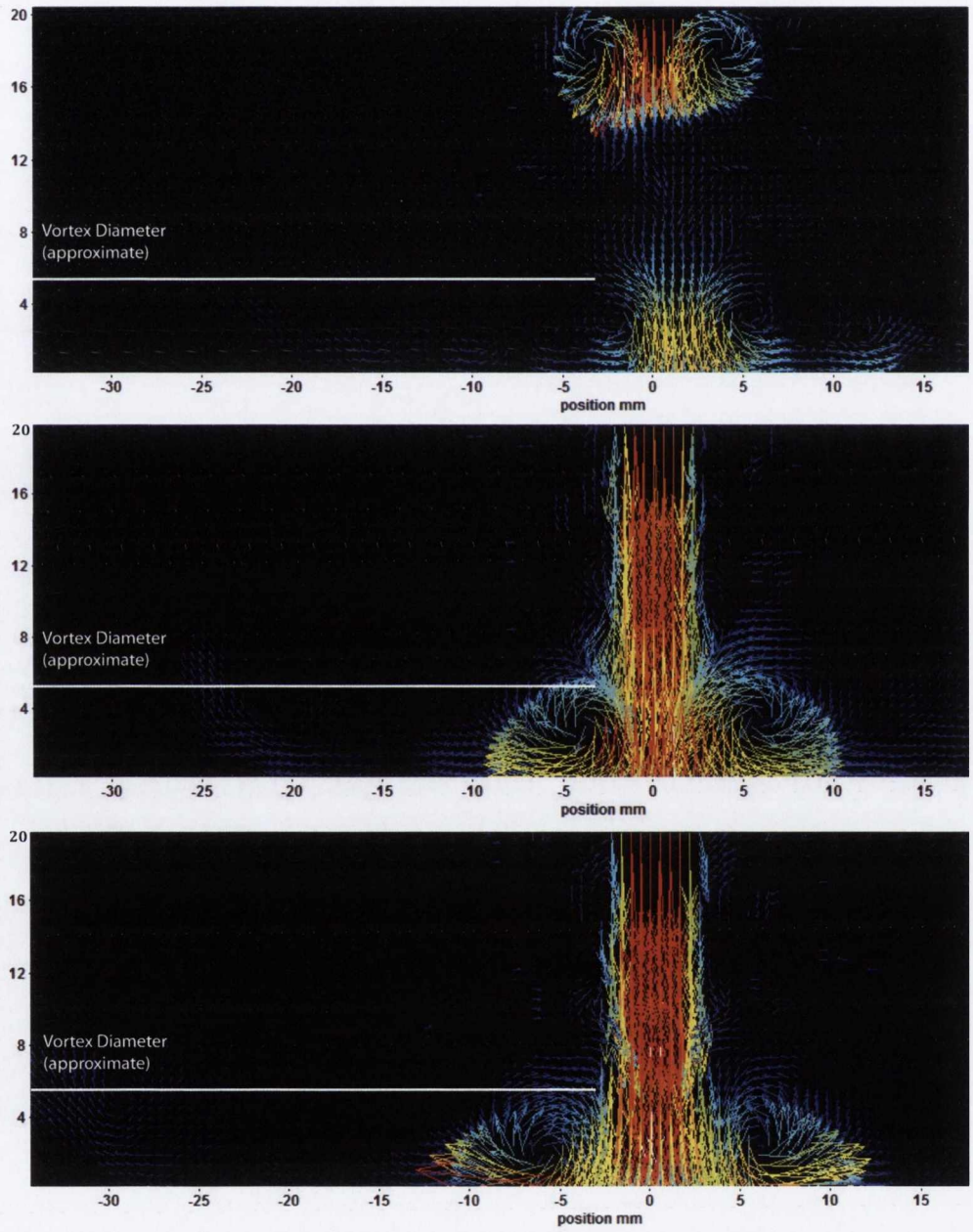

Figure 6.24 – Approximate vortex diameter subsequent to impingement, H/D=4, Re=1500 descending-L_0/D=4, $\phi = 90°$. L_0/D=12, $\phi = 150°$. L_0/D=32, $\phi = 75°$

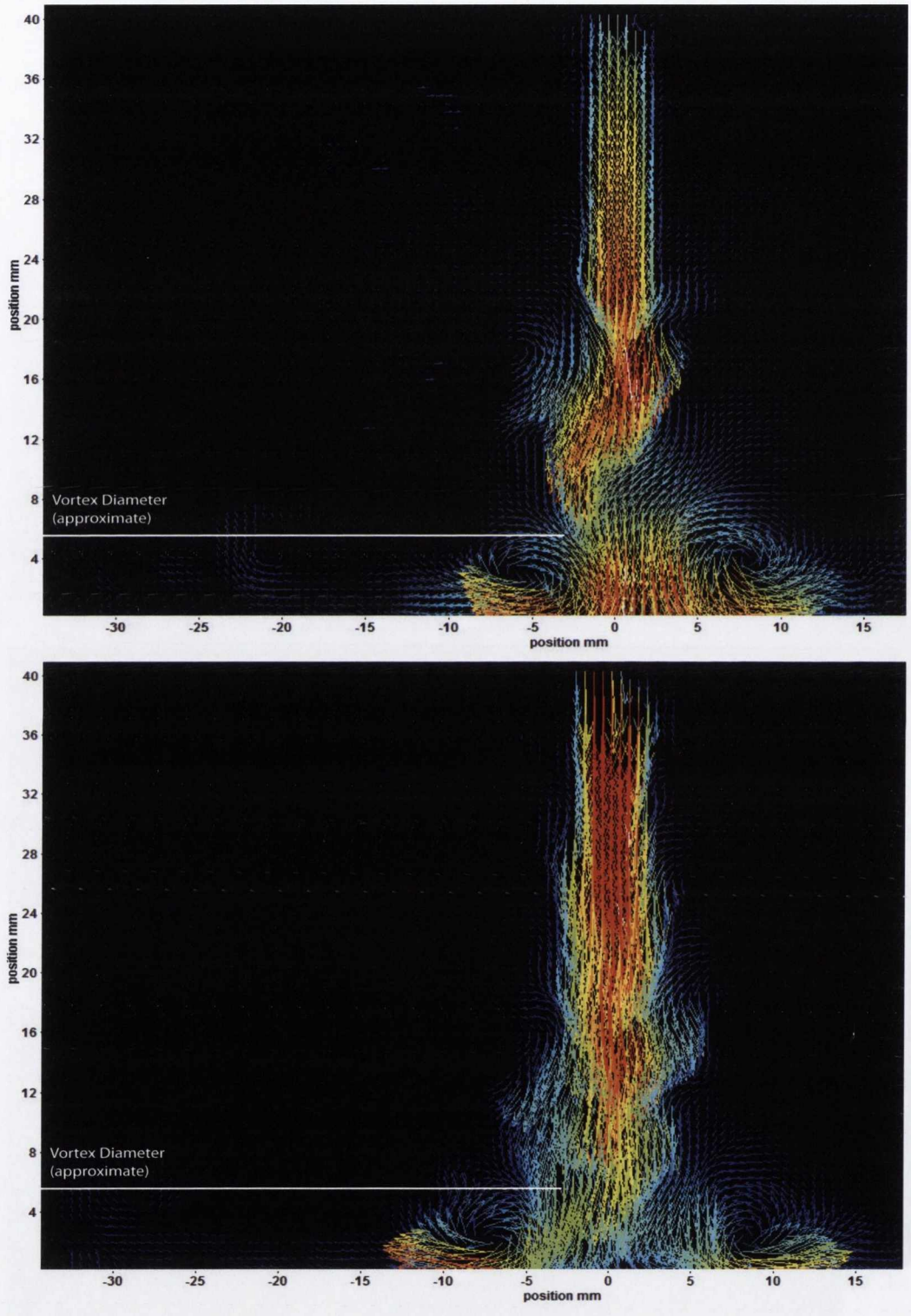

Figure 6.25 – Approximate vortex diameter subsequent to impingement, H/D=8, Re=1500 descending-L_0/D=16, $\phi = 225°$. L_0/D=32, $\phi = 115°$

Table 6.4 – Averaged vortex centre locations from estimated time of flight calculations (mm)

Re	$H/D = 4$	$H/D = 8$
500	3.549	3.359
1000	3.494	3.251
1500	3.413	3.427
2000	3.156	2.722

6.3.2 Estimation of vortex characteristics

In order to relate the characteristics of the vortex that passes over the hot film sensor to the heat transfer measurements, these characteristics need to be estimated from a visual inspection of the stereoscopic PIV data from DaVis [102]. It is suggested that the phase lag that is present in the phase averaged data presented in figures 6.28 and 6.31 is related to the velocity and size of the passing vortex. Once the vortex characteristics were estimated, the following formulae were used to calculate the Δtime and Δphase.

$$Vortex\ Diameter = x_2 - x_1 \tag{6.6}$$

$$\Delta Time = \frac{Vortex\ Diameter}{Vortex\ velocity\ (V_x)} \tag{6.7}$$

$$\Delta Phase = \frac{360 * (Delta\ time)}{1/F_j} \tag{6.8}$$

where,

1. Vortex diameter represents the estimated vortex diameter from PIV data according to x coordinates from DaVis, see figure 6.26 and associated explanation.

2. $\Delta Time$ is equal to a propagation time i.e. the time it takes the vortex to travel a distance of ≈ 1 vortex diameter.

3. Vortex velocity represents the vortex velocity from PIV data in the x direction (V_x), as that is the direction the vortex is travelling (m/s).

4. The synthetic jet velocity is based on a sine wave. Each wave has a frequency, which is a function of time. There are many sine waves that constitute a synthetic jet cycle (360°). $\Delta Phase$ is an angular measure of the time delay or difference between the waves.

5. F_j=corresponding jet frequency (Hz).

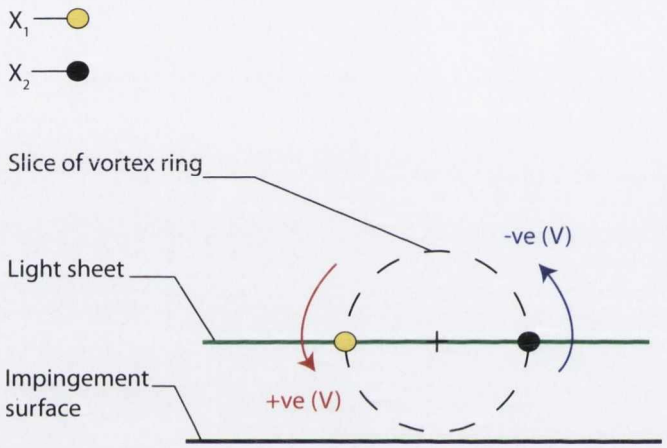

Figure 6.26 – Schematic explaining vortex diameter coordinates for ΔTime and ΔPhase calculations in equations 6.10 and 6.11

The x coordinates used in equation 6.6 are based on the coordinates seen in the velocity map of the z-plane (V_z) of the synthetic jet[8]. Figure 6.26 presents a section view of the vortex ring subsequent to impingement[9] with the light sheet intersecting its centre; the points indicated on this sketch are where the x coordinates are taken from the 3D PIV images presented in figures 6.30 and 6.27. The x coordinates correspond to the location in proximity to the hot film sensor where the vortex velocity at x_1 is a positive value and the velocity recorded at x_2 is a negative, thus indicating the anti-clockwise rotation of the vortex ring as it expands radially outwards on the impingement surface[10]. The V_x velocity used in equation 6.10 is taken from a velocity plot of V_x not presented here. The V_z velocities for both stroke lengths are extracted from figures 6.30 and 6.27,

[8] The z-plane was used as this was the direction used for the calibration of the PIV setup.

[9] It is worth noting that this is an ideal scenario

[10] This is in agreement with the calibration.

respectively. The hot film sensor is approximately at the location indicated by the rectangle. Table 6.5 presents the values that have been extracted from the PIV data. Referring to table 6.5, the x_1 and x_2 values for velocity are positive and negative, respectively, this means that the vortex is rotating in the counter clockwise direction as indicated in figure 6.26.

Table 6.5 – Estimation of vortex characteristics

L_0/D	$x_1(mm)$	$x_2(mm)$	$V_x(m/s)$	$V_z(m/s)$		$\Delta Phase$	$\Delta Time$
				x_1	x_2		(ms)
12	16.23	20.5	1.48	1.13	-0.19	9.2°	3.2
28	16.24	20.2	1.34	0.59	-0.17	33.6°	2.7

A sample calculation is shown for the test case of dimensionless stroke length L_0/D=28, followed by the results for L_0/D=12. These visual inspection data are taken from analysis of figure 6.30, which corresponds to the individual frame of the 3D-PIV data series where the vortex has just passed over the location of the hot film sensor as indicated in figure 6.30 by the rectangle. Figure 6.30 corresponds to the phase angle of 270° for the phase averaged heat transfer measurements where the maximum Nusselt number occurs, as indicated in figure 6.32. For the purpose of calculating the vortex propagation time from equation 6.10, and consequently equation 6.11, the vortex velocity used in equation 6.10 is $V_x = 1.49\,m/s$ as this is the direction the vortex ring is travelling in, measured at the axial distance of $2.5\,mm$ above the impingement surface.

Firstly, from figure 6.30, the coordinates of what is interpreted as a vortex are subtracted from one another to yield the vortex diameter as it travels over the hot film sensor.

$$Vortex\ Diameter = 20.2001\,mm - 16.2399\,mm \tag{6.9}$$

Vortex diameter=0.00396 m

$$\Delta Time = \frac{0.0039602}{1.485} \tag{6.10}$$

$\Delta Time$=2.667 ms

$$\Delta Phase = \frac{360 * (2.667)}{(1/35)} \tag{6.11}$$

$\Delta Phase$=33.6°

Table 6.6 – Estimated ΔTime and ΔPhase values for L_0/D=28 and L_0/D=12

Stroke length (L_0/D)	ΔTime (ms)	ΔPhase
12	3.176	9.2°
28	2.667	33.6°

Table 6.6 presents the estimated values for Δtime and Δphase for both dimensionless stroke lengths tested here. It is interesting to note that the Δphase increases as the dimensionless stroke length is increased, which should occur as the number of vortices that are generated decrease as stroke length is increased. Referring to figure 5.1 it can be seen that as the stroke length (L_0/D) is increased the vortex is formed, followed by the ejection of a trailing jet at large stroke lengths. The values for Δtime are seen to decrease, which should occur due to the fact that as stroke length is increased the velocity increases as well.

The vortex diameter prior to impingement is estimated to be $\approx 5.5mm$, the vortex thickness (diameter) subsequent to impingement is calculated from equation 6.6 and is approximately $4mm$. This decrease in vortex size is thought to be due to the breakdown of the vortex ring prior to impingement from the effects of the trailing jet[11], followed by 'vortex breakdown' on impingement, [7], [64], [136]. The interaction between the vortex ring and the impingement surface has to be taken into consideration as well; in the experimental environment the behaviour of this interaction is quite complicated.

[11] As outlined in section 6.2

Table 6.7 – Phase and time lag, Nu-velocity

Stroke length (L_0/D)	12	28
Jet frequency (Hz)	80	35
Radial location (r/D)	3	3
Max velocity, (V_{abs}=$\sqrt{{V_x}^2 + {V_y}^2}$) (m/s)	0.89	1.04
Max velocity, V_z (m/s)	0.89	0.65
Nu	7.4	5.9
Phase of max Nu	195°	270°
Phase of max (V_{abs})	60°	120°
Phase lag (V_{abs})	135°	150°
Time lag (V_{abs}) (ms)	4.7	11.9
Phase of max V_z	195°	180°
Phase lag V_z	0°	90°
Time lag V_z (ms)	0.0	7.1

It has been documented that when a vortex ring reaches a certain distance from an impingement surface a slight reversal in direction is experienced [29], [30], [31], [33]. As discussed in section 2.2.2, the proximity of the vortex ring to the wall leads to the generation of secondary vorticity along the boundary, seen in figure 2.11, [137]. Yamada et al. [32] suggested that the presence of an adverse pressure gradient beneath the vortex core leads to the 'rebound' effect experienced by the vortex ring; this vorticity layer eventually separates from the boundary and rolls up to form a "secondary vortex ring". This "secondary vortex ring" will cause the primary vortex ring to rebound from the impingement surface and cause a level of expansion to occur within the vortex ring due to the induced velocity of the "secondary vortex ring".

This all precedes vortex roll up, which occurs subsequent to impingement. In this case, the synthetic jet flow has broken down entirely at this stage, new vortices have formed on the impingement surface and the original diameter of the vortex, which was estimated to be $\approx 5.5mm$ has now been distorted and appears to have reduced in size to the calculated value of $\approx 4mm$ from equation 6.6. This decrease in size of the

vortex is attributed to the high velocity trailing jet interacting with the vortex ring, destabilising it prior to impingement, which leads to the vortex ring reducing in size[12] subsequent to impingement; these are some of the processes that occur in the transfer of vorticity from an axial to a radial direction.

6.3.3 Simultaneous PIV and heat transfer

Figures 6.27 through 6.32 present simultaneous stereoscopic PIV and surface heat transfer data; both the PIV velocity results and the heat transfer at the radial location $r/D = 3$ of the hot film sensor have been phase averaged. The jet Reynolds number was set to Re=1500. Visual access[13] restricted the minimum axial spacing at which stereoscopic PIV testing could be performed to H/D=12. The stroke lengths investigated were L_0/D=12 and 28. The phase averaged velocity profiles presented in figures 6.28, 6.31 and 6.29, 6.32 represent $V_{abs} = \sqrt{{V_x}^2 + {V_y}^2}$ and V_z respectively. The $V_{abs} = \sqrt{{V_x}^2 + {V_y}^2}$ profiles are included to show the phase lag between vortex velocity and heat transfer in the same plane as the light sheet. V_z illustrates the phase lag between velocity and heat transfer in the plane towards the impingement surface. The synthetic jet actuator used in the simultaneous stereoscopic PIV and surface heat transfer described in section 4.1.3 is different to the one used for the heat transfer studies from parallel research [7] and for the 2D-2C PIV presented here. The main difference of the synthetic jet actuator used for this set of tests, labelled actuator 2, is the surface area of its orifice plate i.e. the orifice plate of actuator 2 has a surface area approximately half of the orifice plate of the synthetic jet actuator seen in figure 4.4 for example. This reduces the confinement effects of the synthetic jet actuator.

Research completed by Persoons et al. [134] documented the stagnation point Nusselt number for a synthetic jet operating at an axial spacing of H/D=10, $L_0/D > 20$ and a jet Reynolds number of Re=1500 to be approximately 15. When compared to the

[12] Interaction of a vortex ring with an impingement surface enhances viscous diffusion, which leads to a reduction in vorticity [138].

[13] To overcome this problem a smaller synthetic jet actuator designed specifically for this experiment had to be designed, the design of this actuator is explained in section 4.1.3.

Nusselt number of 7.4 in this study, the differences in geometry of the synthetic jet actuator, testing environment and the radial location ($r/D = 3$) that the heat transfer was measured at, accounts for the differences seen in heat transfer performance.

6.3.3.1 $L_0/D = 12$, $r/D = 3$

The stereoscopic PIV data presented in figure 6.27 represents the flow field at a dimensionless stroke length of L_0/D=12 with the hot film sensor at the radial location $r/D = 3$, and figures 6.28 and 6.29 present the phase averaged velocity and heat transfer for V_{abs} and V_z respectively for this stroke length. It is interesting to note from table 6.7 that this set of parameters produced the highest Nusselt number of the two stroke lengths tested. According to table 6.6 for L_0/D=12 it is thought that the Δtime value suggests the vortex ring takes slightly longer to pass over the hot film sensor than for L_0/D=28, thus entraining more 'fresh' air from further afield and enhancing the heat transfer. The Δphase value suggests that the angular measure between vortices reaching the hot film sensor is significantly smaller than for L_0/D=28, thus leading to a higher Nusselt number being recorded. This is also interesting in the context of the results presented in section 6.2, and in particular the data presented for the test parameters of H/D=8, Re=1500 and L_0/D=12. The velocities measured for the synthetic jet seen in figure 6.15 show that the synthetic jet records the highest velocity at L_0/D=12 and that as the stroke length is increased beyond this the velocity decreases. Although the data presented in figure 6.27 are not at the same axial spacing as the data presented in figure 6.15, because of the experimental constraints there are similarities that can be noted. Thus, the velocity recorded for L_0/D=12 is greater than that of L_0/D=32 in figure 6.15, and the velocity V_z and Nusselt number recorded for L_0/D=12 in figure 6.27 are greater than the comparable values recorded for L_0/D=28 in figure 6.30. Although the explanation for why the stroke length of L_0/D=12 appears to have the optimal characteristics in terms of heat transfer and V_{max} is far from completely clear, it is encouraging to see this trend in all data presented here.

The rectangle seen in figure 6.27 marks the hot film sensor location and it is at this

point that the velocities (V_{abs} and V_z) have been extracted. This is where the vortex is passing over the hot film sensor and corresponds to the phase averaged heat transfer plots presented in figures 6.28 and 6.29. From figure 6.27 it can be seen that there is a large region in which air is directed toward the impingement surface (red). It could be that this apparent large area with entrained fresh air gives the synthetic jet at L_0/D=12 a higher Nusselt number than that of L_0/D=28, when compared to figure 6.30. This is also reflected in the higher V_z velocity displayed in the phase averaged velocity plot of figure 6.29, when compared against figure 6.32.

The dashed line circle in figure 6.27 corresponds to the 'ring-like' region of the vortex ring that is created subsequent to impingement as it travels along the plate. From table 6.7 it can be seen that the heat transfer lags the velocity $V_{abs} = \sqrt{{V_x}^2 + {V_y}^2}$ by a phase difference of 135° and time gap of 4.7 ms, and for V_z, heat transfer and the velocity are in phase. It is suggested that due to vortex interactions and the large x_1 value of 1.13 m/s seen in table 6.5 that this leads to the velocity for V_abs being lower and out of phase

6.3.3.2 $L_0/D = 28$, $r/D = 3$

The data presented in figure 6.30 is a stereoscopic PIV image of the flow, and figures 6.31 and 6.32 present the phase averaged velocity of $V_{abs} = \sqrt{{V_x}^2 + {V_y}^2}$, V_z and heat transfer respectively for a stroke length of L_0/D=28. This data produced phase averaged plots with a sine wave like profile, as seen in figures 6.31 and 6.32; the data for the calculated phase lag and time lag from this figure are seen in table 6.7. Figure 6.30 presents the stereoscopic PIV data for stroke length L_0/D=28, with the hot film sensor at $r/D = 3$; this image corresponds to the phase averaged heat transfer profiles at 270° of figures 6.31 and 6.32 where the maximum Nusselt number occurs, and indicated in figure 6.30 with the rectangle is the location of the hot film sensor.

It is at the location of the rectangle seen in figure 6.30 that the velocities (V_{abs} and V_z) have been extracted in order to correlate them to the heat transfer data. The dashed line circle in figure 6.30 corresponds to the 'ring-like' region of the vortex ring that

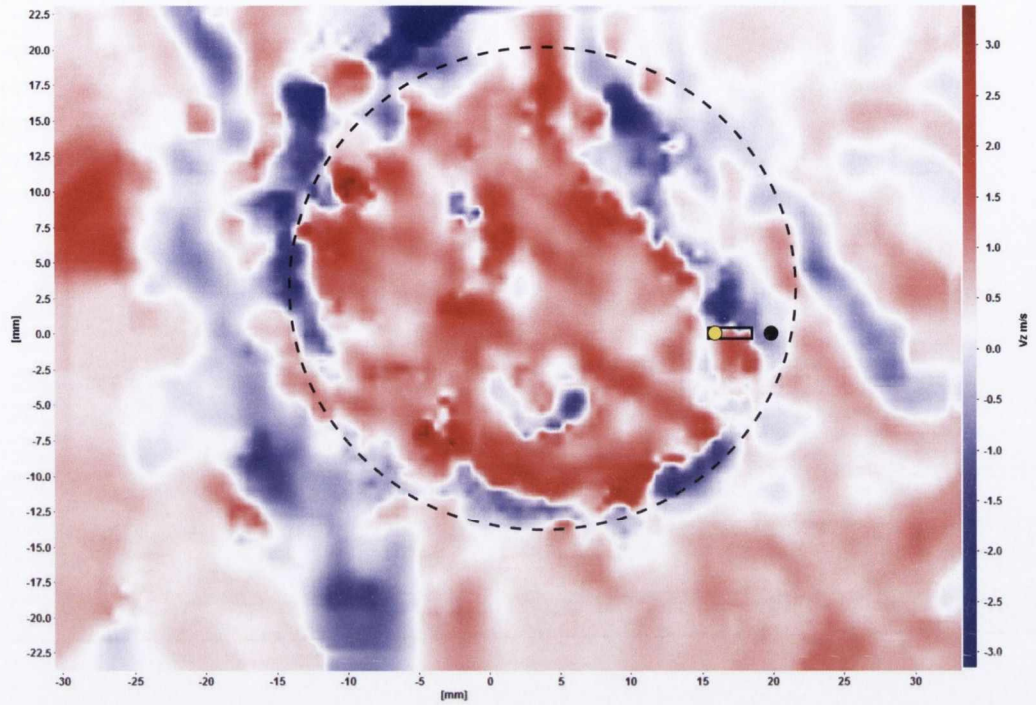

Figure 6.27 – Stereoscopic PIV image of vortex roll up, corresponding to phase (195°) when heat transfer is a max. H/D=12, Re=1500, L_0/D=12, r/D=3

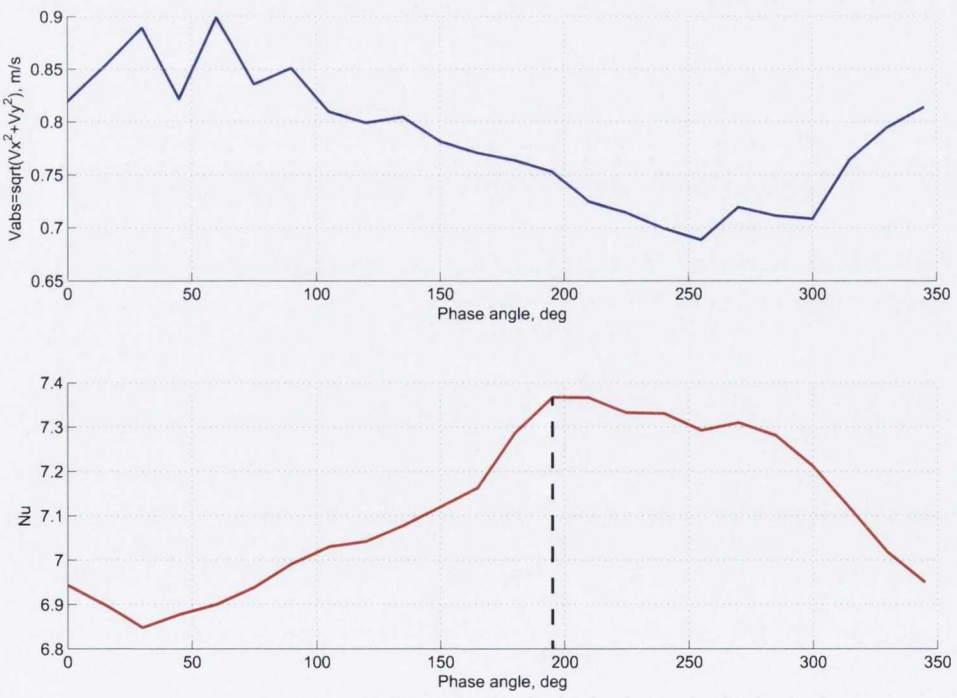

Figure 6.28 – Phase averaged velocity (V_{abs}, in plane velocity) and heat transfer variation with phase angle, H/D=12, Re=1500, L_0/D=12, r/D=3, (- - -) corresponds to max Nu, phase of 195°.

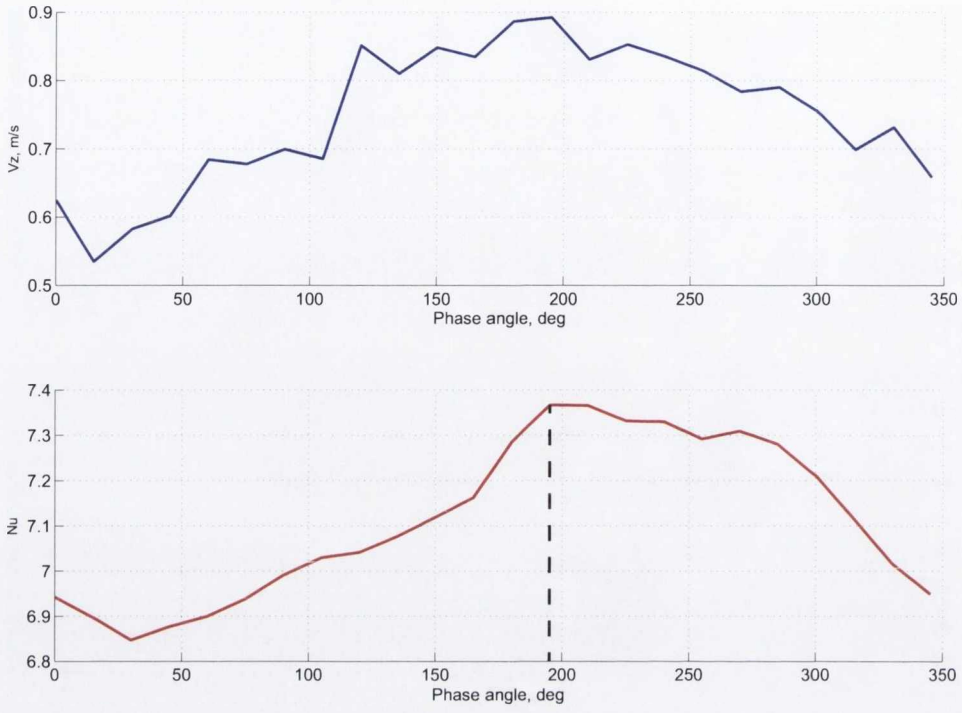

Figure 6.29 – Phase averaged velocity (V_z) and heat transfer variation with phase angle, H/D=12, Re=1500, L_0/D=12, r/D=3, (- - -) corresponds to max Nu, phase of 195°.

is created subsequent to impingement as it travels along the plate. From table 6.7 it can be seen that the heat transfer lags the velocity $V_{abs} = \sqrt{{V_x}^2 + {V_y}^2}$ by a phase difference of 150° and time gap of 11.9 ms, and for V_z, heat transfer lags the velocity by 90° and a time gap of 7.1 ms.

6.3.3.3 Findings

Section 6.3.3 presented results for simultaneous stereoscopic PIV and surface heat transfer data for an impinging synthetic jet. Overall, the data presented in this section for L_0/D=12 and 28 show that as the dimensionless stroke length is increased the phase lag and time lag increases, these are two values that are linked so this is expected to occur. The values for phase lag and time lag are also related to the velocity of the passing vortex over the location where the data was extracted from i.e. over the hot film sensor. A relationship between the increase in stroke length leading to an increase in the size of the trailing jet behind the formed vortex ring is identified,

it is interesting to note the difference between the Δphase values of L_0/D=12 and L_0/D=28, which aids in understanding the effect of the trailing jet and how large stroke length values perform, this can be seen in the Δphase and Δtime values presented. The trailing jet has an effect on heat transfer, as seen when comparing Nusselt number values of L_0/D=12 and L_0/D=28. The data from section 6.2 showed that for the dimensionless stroke length of L_0/D=12 the highest velocity was consistently recorded for all test setups. This is interesting when compared to the Nusselt number data for the dimensionless stroke length L_0/D=12 presented in this section 6.3.3 as the highest Nusselt number recorded was for this dimensionless stroke length, further investigation is required to elucidate the reasons behind this as test data is limited for the heat transfer tests, as such a conclusion can not be drawn from this link.

The heat transfer regimes identified in figure 6.33 are one of the key findings from the work published my McGuinn in 2011 [7], in these regions in terms of the heat transfer there are mechanisms at work that enhance the heat transfer, but it has not been documented clearly in terms of the fluid dynamics as to what occurs in these regions. The overall aim of this thesis was to understand the mechanisms at play in the identified heat transfer regimes seen in figure 6.33 with regard to the fluid mechanics of the synthetic air jet at the established test parameters.

The range of parameters investigated in chapters 5 and 6 address the regions indicated in figure 6.33 and fully investigate the structures found in this flow through the use of high speed PIV. The flow field data presented in section 5.2 identified structures present in the flow that are responsible for a continual mixing of the boundary layer on the impingement surface. This suggests that a similar 'mixing' effect would occur on a heated surface, thus enhancing the heat transfer. The findings presented in section 5.2.2.8 detail the occurrences of specific flow structures at the defined test parameters. It is suggested that the structures listed in this section all influence the heat transfer capabilities of an impinging synthetic air jet.

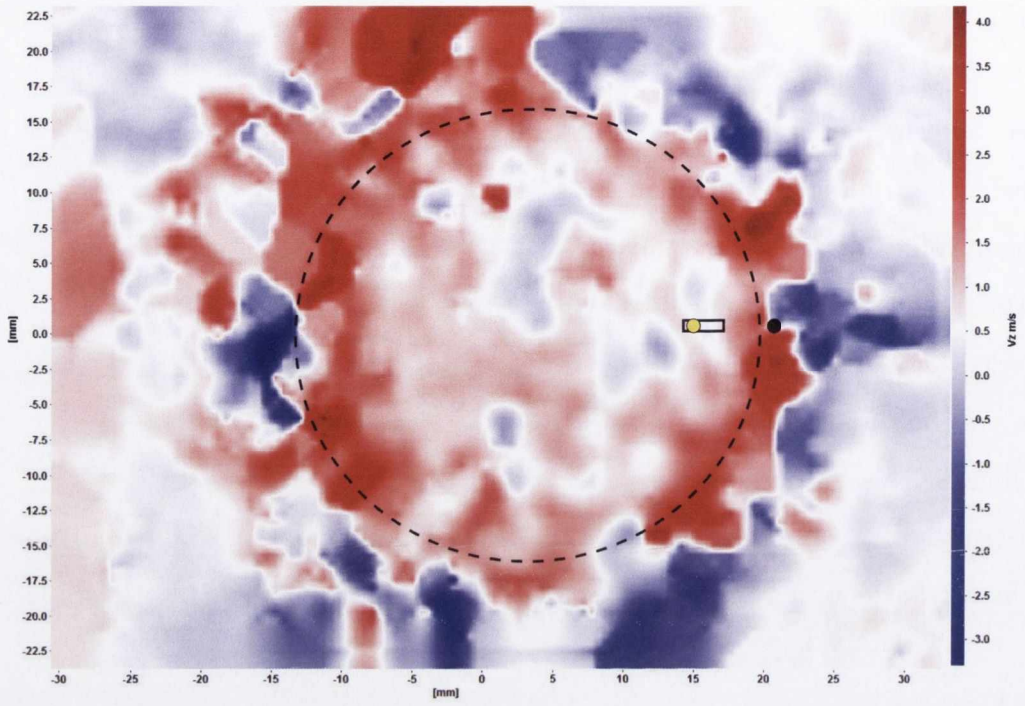

Figure 6.30 – Stereoscopic PIV image of vortex roll up, corresponding to phase (270°) when heat transfer is a max. H/D=12, Re=1500, L_0/D=28, r/D=3

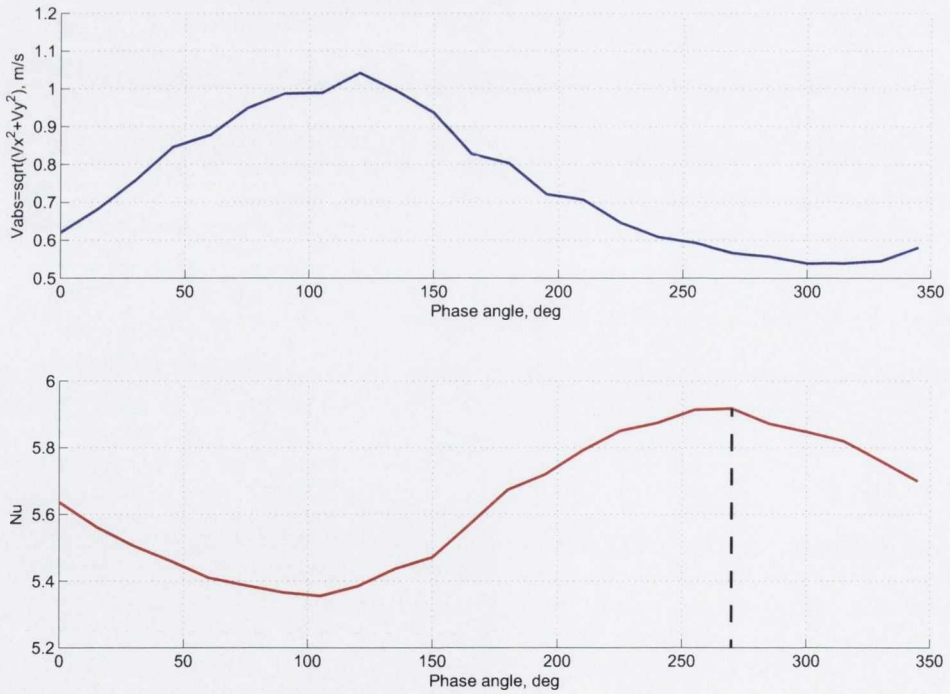

Figure 6.31 – Phase averaged velocity (V_{abs}, in plane velocity) and heat transfer variation with phase angle, H/D=12, Re=1500, L_0/D=28, r/D=3, (- - -) corresponds to max Nu, phase of 270°.

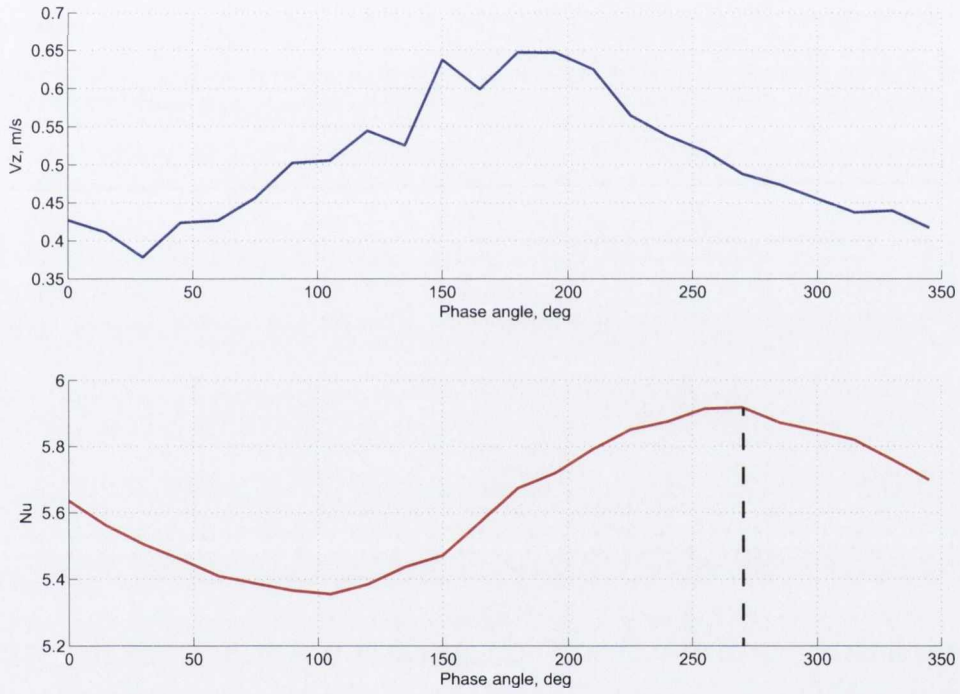

Figure 6.32 – Phase averaged velocity (V_z) and heat transfer variation with phase angle, H/D=12, Re=1500, L_0/D=28, r/D=3, (- - -) corresponds to max Nu, phase of 270°.

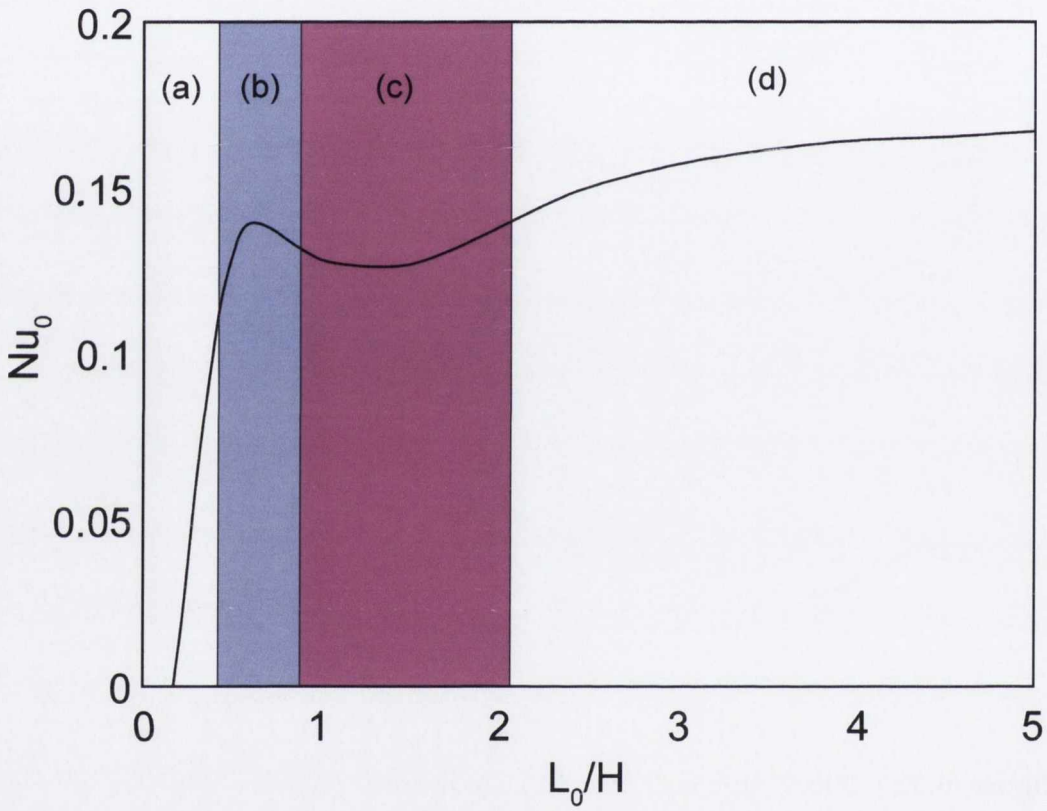

Figure 6.33 – Heat transfer regimes identifying the regions of interest relating to the dimensionless stroke lengths of a synthetic air jet, [7].

Chapter 7

Conclusions

The evolution of an impinging synthetic air jet at three axial spacings has been investigated experimentally. This study involves the variation of operational parameters and configuration along with the completion of simultaneous fluid flow and surface heat transfer measurements.

A comprehensive literature review identified that the majority of studies reported in the literature relate to the flow structures of a free synthetic jet. An impinging synthetic jet involves flow structures that are more complex. The evolution of an impinging synthetic jet from vortex formation to impingement and the characteristics of the flow subsequent to impingement were poorly documented and understood. An experimental rig was refined to allow for the implementation of high speed, high resolution 2D-2C and 3D-3C particle image velocimetry testing.

Results have been presented detailing the evolution of the synthetic air jet from formation to impingement, for jet Reynolds numbers Re=500, 1000, 1500 and 2000 and for dimensionless stroke lengths L_0/D=4, 8, 12, 16, 28 and 32. A range of dimensionless jet to surface spacings of H/D=4, 8 and 12 was investigated. Instantaneous and time averaged particle image velocimetry has identified flow structures that, to the author's knowledge, have not been documented. The results obtained indicate that above the dimensionless stroke length L_0/D=4 the trailing jet begins to dominate the overall flow

field, but it is only seen to affect the synthetic jet flow at stroke lengths $L_0/D \geq 16$. The results obtained suggest that the dimensionless stroke length, L_0/D=12, is optimal in terms of the flow structure, and associated heat transfer, at impingement. This was found to hold for the full range of jet to plate spacings investigated. The key features for this stroke length of L_0/D=12 are:

- A vortex time of flight, from formation to impingement, that is shorter than the higher stroke length of L_0/D=16
- The highest vortex formation velocity of all the stroke lengths considered.
- Volume flux values close to, and in some cases higher than, the largest stroke length of L_0/D=32
- A small phase difference between the vortices subsequent to impingement, i.e. a synthetic jet is made up of vortices; a small phase difference between vortices equates to a low time delay between the passage of each vortical structure.
- A Nusselt number that is higher than that for the larger stroke length of L_0/D=28, although it is very small.

From the limited test results it is suggested that the dimensionless stroke length L_0/D=12 has the optimal flow structure at impingement for effective cooling, as confirmed by the heat transfer measurement, however, due to the lack of extensive testing, further investigation is required.

Although further work is needed to extend these findings to a broader range of test parameters, this research goes some way towards improving our understanding of impinging synthetic jet flow and towards identifying optimal configurations for synthetic jet cooling systems.

7.1 Future work

It would be interesting to perform a simultaneous surface heat transfer and fluid flow study, focussing on the dimensionless stroke length L_0/D=12, for a broader range of

jet to surface spacings, with a view to establishing the range of validity of the current findings.

A study utilising simultaneous stereoscopic PIV and surface heat transfer measurements based on high speed infrared thermography with a heated foil as the heated impingement surface could be completed. This would provide a three dimensional flow map of the vortex roll up with an infrared map of the vortex ring as it expands radially and would aid in understanding the mechanisms involved in vortex roll up with respect to heat transfer, particularly in the stagnation region of the synthetic jet.

A study focussing on the effect of different orifice shapes on the evolution of an impinging synthetic jet would be interesting to quantify the influence of different orifice geometries.

A higher frame rate PIV study of the recirculation regions of the impinging synthetic jet could shed light on the effects of confinement, recirculation and entrainment.

Publications

Previous work by the author has yielded publications in conference proceedings in the following fields: Steady and synthetic jet heat transfer. Synthetic jet flow field analysis. The following is a list of these publications.

- R. Farrelly, T. A. McGuinn, T. Persoons and D. B. Murray. A heat transfer comparison between a synthetic jet and a steady jet at low Reynolds numbers. In *Proceedings of the ASME International Mechanical Engineering Congress and Exposition*, Boston, MA, U.S.A., 2008.

- R. Farrelly, T. A. McGuinn, T. Persoons and D. B. Murray. Fluctuating and time averaged heat transfer characteristics of a steady jet at low Reynolds numbers. In 7^{th} *World Conference on Experimental Heat Transfer, Fluid Mechanics and Thermodynamics*, Krakow, Poland, 2009.

- R. Farrelly, T. A. McGuinn, T. Persoons and D. B. Murray. Heat transfer behaviour and flow field characterisation of impinging synthetic jets for a wide range of parameters. In *Proceedings of the International Heat Transfer Conference*, Washington D.C., U.S.A., 2010.

- T. Persoons, R. Farrelly, T. A. McGuinn and D. B. Murray. High dynamic range whole-field turbulence measurements in impinging synthetic jets for heat transfer applications. In 15^{th} *International Symposium on Applications of Laser Techniques to Fluid Mechanics*, Lisbon, Portugal, 2010.

Bibliography

[1] M. Amitay, D. R. Smith, V. Kibens, D. E. Parekh, and A. Glezer. Aerodynamic flow control over an unconventional airfoil using synthetic jet actuators. *American Institute of Aeronautics and Astronautics Journal*, 39(3):361–370, 2001.

[2] B. L. Smith and A. Glezer. Vectoring and small-scale motions effected in free shear flows using synthetic jet actuators. *American Institute of Aeronautics and Astronautics*, 0213, 1997.

[3] R. G. Nevins and H. D. Ball. Heat transfer between a flat plate and a pulsating impinging jet. In *Proceedings of the National Heat Transfer Conference*, volume 60, pages 510–516, Boulder, CO, 1961.

[4] K. Kataoka, M. Suguro, H. Degawa, K. Maruo, and I. Mihata. The effect of surface renewal due to large-scale eddies on jet impingement heat transfer. *International Journal of Heat and Mass Transfer*, 30:559–567, 1987.

[5] J. Vukasinovic and A. Glezer. An active radial countercurrent heat sink driven by a synthetic jet actuator. In *Proceedings of International Mechanical Engineering Congress and Exposition*, volume EEP-6AI-2, 2001.

[6] W. Z. Black, A. Glezer, and J. G. Hartley. Heat transfer modules for cooling electronics packages. In *4th International Symposium on Advanced Packaging Materials*, pages 209–214, Braselton, GA, 1998.

[7] T. A. McGuinn. *A study of the heat transfer processes and related flows of a synthetic jet impinging perpendicular to a heated surface.* PhD thesis, University of Dublin, Trinity College, Mechanical Engineering, 2011.

[8] R. Farrelly, T. A. McGuinn, T. Persoons, and D. B. Murray. A heat transfer comparison between a synthetic jet and a steady jet at low Reynolds numbers. In *Proceedings of the ASME International Mechanical Engineering Congress and Exposition*, Boston, MA, 2009.

[9] N. Didden. On the formation of vortex rings: rolling up and production of circulation. *Journal of Applied Mathematics and Physics*, 30(1):101–116, 1979.

[10] A. Glezer. The formation of vortex rings. *Physics of Fluids*, 31(12):3532–3542, 1988.

[11] J. M. Shuster and D. R. Smith. Experimental study of the formation and scaling of a round synthetic jet. *Physics of Fluids*, 19(4), 2007.

[12] J. A. Fitzgerald and S. V. Garimella. A study of the flow field of a confined and submerged impinging jet. *Heat and Mass Transfer*, 41(8-9):1025–1034, 1998.

[13] R. Viskanta. Heat transfer to impinging isothermal gas and flame jets. *Experimental Thermal and Fluid Science*, 6:111–134, 1993.

[14] A. J. Yule. Large-scale structure in the mixing layer of a round jet. *Journal of Fluid Mechanics*, 89:469–495, 1978.

[15] C. O. Popiel and O. Trass. Visualization of a free and impinging round jet. *Experimental Thermal and Fluid Science*, 4:253–264, 1991.

[16] D. C. Donaldson and R. S. Snedeker. Study of free jet impingement: Part 1: Mean properties of free and impinging jets. *Journal of Fluid Mechanics*, 45:281–319, 1971.

[17] M. B. Glauert. The wall jet. *Journal of Fluid Mechanics*, 1(625-643), 1956.

[18] J. Serrin. Handbuch der physik. *Springer-Verlag*, 8(1):248, 1959.

[19] M. J. Lighthill. *Laminar Boundary Layers*. Oxford University Press, New York, 1963.

[20] A. J. Majda and A. L. Bertozzi. *Vorticity and Incompressible Flow.* Cambridge University Press, 2002.

[21] L. Prandtl. Über flüssigkeitsbewegung bei sehr kleiner reibung. *Verh. III. Intern. Math. Kongress*, 1904.

[22] D. Auerbach. Some open questions on the flow of circular vortex rings. *Fluid Dynamics Research*, 3, 1988.

[23] N. Didden. Untersuchung laminarer, instabilier ringwirble mittels laser doppler anemometrie. *Technical report Max Planck Institut für Strömungsformschung und der Aerodyn. Versuchsant.*, 64, 1977.

[24] M. Gharib, E. Rambod, and K. Shariff. A universal time scale for vortex ring formation. *Journal of Fluid Mechanics*, 360:121–140, 1998.

[25] P. G. Saffman. On the formation of vortex rings. *Stud. Appl. Math.*, 51:261–268, 1976.

[26] T. Maxworthy. Some experimental studies of vortex rings. *Journal of Fluid Mechanics*, 81:465–495, 1977.

[27] C. Krutzsch. Über eine experimentell beobachtete erscheinung an wirbelringen bei inrer translatorischen bewegung in wirklichen flüssigkeiten. *Annual Physics*, 35:497, 1939.

[28] T. Maxworthy. The structure and stability of vortex rings. *Journal of Fluid Mechanics*, 51(1):15–32, 1972.

[29] R. H. Magarvey and C. S. Maclatchy. The disintegration of vortex rings. *Canadian Journal of Physics*, 42:684–689, 1964.

[30] H. Yamada, T. Kohsaka, H. Yambe, and T. Matsui. Flowfield produced by a vortex ring near a plane wall. *Journal of Physics Society of Japan*, 51:1663–1670, 1982.

[31] J. D. Walker, C. R. Smith, A. W. Cerra, and T. L. Doligalski. The impact of a vortex ring on a wall. *Journal of Fluid Mechanics*, 181:99–140, 1987.

[32] H. Yamada, O. Mochizuki, H. Yamabe, and T. Matsui. Pressure variation on a flat wall induced by an approaching vortex ring. *Journal of Physics Society of Japan*, 54:4151–4160, 1985.

[33] U. Boldes and J. C. Ferreri. Behaviour of vortex rings in the vicinity of a wall. *Physics of Fluids*, 16(11):2005–2006, 1973.

[34] J. K. Harvey and F. J. Perry. Flowfield produced by trailing vortices in the vicinity of the ground. *American Institute of Aeronautics and Astronautics Journal*, 9:1659–1660, 1971.

[35] Lord Rayleigh. On the instability of jets. *Proceedings of the London Maths Society*, 10(4), 1879.

[36] Lord Kelvin. On a disturbance in Lord Rayleigh's solution for waves in a plane vortex stratum. *Math and Physics Papers*, 4:186, 1880.

[37] H. Von. Helmholtz. Über discontinuierliche flüssigkeitsbewegungen. *Monatsberichte der königl*, page 215, 1868.

[38] O. Reynolds. An experimental investigation of the circumstances which determine whether the motion of water shall be direct or sinuous, and of the law of resistance in parallel channels. *Philosophical Transactions of the Royal Society*, 174(0):935–982, 1883.

[39] V. Strouhal. Über eine besondere art der tonerregung. *Annual Physics of Chemistry*, 5:216, 1878.

[40] H. Bénard. Formation de centres de giration à l'arrière d'un obstacle en mouvement. *Comptes rendus*, 147(970), 1908.

[41] L. Prandtl. *Gesammelte Abhandlungen.* Springer Berlin, 1961.

[42] H. Tennekes and J. L. Lumley. *A First Course in Turbulence.* The MIT Press, 1972.

[43] U. Ingard and S. Labate. Acoustic generation of circulation currents and jet effects. *The Journal of the Acoustical Society of America*, 22(1):87, 1950.

[44] E. P. Mednikov and B. G. Novitskii. Experimental study of intense acoustic streaming. *Soviet Physics Acoustics-USSR*, 21(2):152–154, 1975.

[45] B. L. Smith and A. Glezer. The formation and evolution of synthetic jets. *Physics of Fluids*, 10(9):2281–2297, 1998.

[46] A. Glezer and M. Amitay. Synthetic jets. *Annual Review of Fluid Mechanics*, 34:503–529, 2002.

[47] S. Zhong, M. Jabbal, H. Tang, L. Garcillan, F. Guo, N. Wood, and C. Warsop. Towards the design of synthetic-jet actuators for full-scale flight conditions : Part 1: The fluid mechanics of synthetic-jet actuators. *Flow, Turbulence and Combustion*, 78(3-4):283–307, 2007.

[48] H. Tang, S. Zhong, M. Jabbal, L. Garcillan, F. Guo, N. Wood, and C. Warsop. Towards the design of synthetic-jet actuators for full-scale flight conditions : Part 2: Low-dimensional performance prediction models and actuator design method. *Flow, Turbulence and Combustion*, 78(3-4):309–329, 2007.

[49] A. Seifert, S. Eliahu, D. Greenblatt, and I. Wygnanski. Use of piezoelectric actuators for airfoil separation control. *American Institute of Aeronautics and Astronautics Journal*, 36(8):1535–1537, 1998.

[50] A. Crook. *The control of turbulent flows using synthetic jet actuators.* PhD thesis, School of Engineering, Manchester, UK, 2002.

[51] M. Amitay, A. M. Honohan, M. Trautman, and A. Glezer. Modification of the aerodynamic characteristics of bluff bodies using fluidic actuators. In *AIAA Fluid Dynamics Conference and Exhibit*, volume 28, 1997.

[52] Y. Chen, K. Liang, A. Aung, A. Glezer, and J. Jagoda. Enhanced mixing in a simulated combustor using synthetic jet actuators. In *AIAA Paper*, volume 0449, 1999.

[53] B. D. Ritchie and J. M. Seitzman. Controlled fuel-air mixing using a synthetic jet array. In *AIAA Paper*, number 3465, 2000.

[54] S. A. Davis and A. Glezer. Mixing control of fuel jets using synthetic jet technology. In *AIAA Paper*, volume 0447, 1999.

[55] D. S. Kercher, J. B. Lee, O. Brand, M. G. Allen, and A. Glezer. Microjet cooling devices for thermal management of electronics. *IEEE Transactions on Components and Pachaging Technologies*, 26(2):359–366, 2003.

[56] R. Mahalingam, N. Rumigny, and A. Glezer. Thermal management using synthetic jet ejectors. *IEEE Transactions on Components and Packaging Technologies*, 27(3):439–444, Sept 2004.

[57] R. Holman, Y. Utturkar, R. Mittal, B. L. Smith, and L. Cattafesta. Formation criterion for synthetic jets. *AIAA Journal*, 43(10):2110–2116, 2005.

[58] T. S. O'Donovan and D. B. Murray. Jet impingement heat transfer - part 1: Mean and root-mean-square heat transfer and velocity distributions. *International Journal of Heat and Mass Transfer*, 50(17-18):3291–3301, 2007.

[59] B. E. Launder and W. Rodi. The turbulent wall jet-measurements and modeling. *Annual Review of Fluid Mechanics*, 15:429–459, 1983.

[60] W. K. George, H. Abrahamsson, J. Eriksson, R. I. Karlsson, L. Löfdahl, and M. Wosnik. A similarity theory for the turbulent plane wall jet without external stream. *Journal of Fluid Mechanics*, 425:367–411, 2000.

[61] D. L. Quintana. Heat transfer in the forced laminar wall jet. *Journal of Heat Transfer*, 119(3):451–459, 1997.

[62] Y. Katz, E. Horev, and I. Wygnanski. The forced turbulent wall jet. *Journal of Fluid Mechanics*, (242):577–609, 1992.

[63] T. A. McGuinn, T. Persoons, T. S. O'Donovan, and D. B. Murray. Heat transfer and air temperature measurements of an impinging synthetic air jet. In *Turbulence, Heat and Mass Transfer 6*. Begell House, Inc., 2009.

[64] A. A. Pavlova and M. Amitay. Electronic cooling using synthetic jet impingement. *Journal of Heat Transfer*, 128(9):897 – 907, 2006.

[65] T. A. McGuinn, T. S. O'Donovan, and D. B. Murray. Heat transfer measurements of impinging synthetic air jet. In *ASME-JSME Thermal Engineering Summer Heat Transfer Conference*, Vancouver, British Columbia, Canada, 2007.

[66] L. D. Gomes, W. J. Crowther, and N. J. Wood. Towards a practical piezoceramic diaphragm based synthetic jet actuator for high subsonic applications - effect of chamber and orifice depth on actuator peak velocity. In *3rd AIAA Flow Control Conference*, pages 1–17. American Institute of Aeronautics and Astronautics, Inc., 2006.

[67] Q. Gallas, R. Holman, T. Nishida, B. Carroll, M. Sheplak, and L. Cattafesta. Lumped element modeling of piezoelectric-driven synthetic jet actuators. *AIAA Journal*, 41(2):240–247, 2003.

[68] T. J. Cox and P. D'Antonio. *Acoustic absorbers and diffusers: theory, design and application*. Spon Press, London, 2004.

[69] U. Ingard and H. Ising. Acoustic nonlinearity of an orifice. *The Journal of the Accoustical Society of America*, 42(1), 1967.

[70] Y. Utturkar, R. Holman, R. Mittal, B. Carroll, M. Sheplak, and L. Cattafesta. A jet formation criterion for synthetic jet actuators. In *41st Aerospace Sciences Meeting and Exhibit*, volume 0636, Reno, NV, 2003. AIAA.

[71] B. L. Smith and G. W. Swift. Synthetic jets at large Reynolds number and comparison to continuous jets. In *AIAA*, volume 3030, 2001.

[72] K. Mohseni and M. Gharib. A model for universal time scale of vortex ring formation. *Physics of Fluids*, 10(10):2436–2438, 1998.

[73] Z. Trávníček, Z. Broučková, and J. Kordík. Formation criterion for axisymmetric synthetic jets at high stokes numbers. *AIAA Journal*, 50(9):2012–2017, 2012.

[74] H. Tang and S. Zhong. Incompressible flow model for synthetic jet actuators. *AIAA Journal*, 44(4):908–912, 2006.

[75] R. Rathnasingham and K. S. Breuer. Coupled fluid-structural characteristics of actuators for flow control. *AIAA Journal*, 35(5):832–837, 1997.

[76] F. Guo and S. Zhong. A comparison of the characteristics of micro-scale and macro-scale synthetic jets. In *AIAA Paper*, volume 3183, 2006.

[77] Z. Trávníček, P. Dančová, J. Kordík, T. Vít, and M. Pavelka. Heat and mass transfer caused by a laminar channel flow equipped with a synthetic jet array. *Journal of Thermal Science and Engineering Applications*, 2(4), 2010.

[78] G. M. Di Cicca and G. Iuso. On the near field of an axisymmetric synthetic jet. *Fluid Dynamics Research*, 39(9-10):673–693, 2007.

[79] C. Nae. Numerical simulation of a synthetic jet actuator. In *International Congress of the Aeronautical Sciences*, volume 22, 2002.

[80] T. Persoons and T. S. O'Donovan. A pressure-based estimate of synthetic jet velocity. *Physics of Fluids*, 19(12), 2007.

[81] B. L. Smith and A. Glezer. Jet vectoring using synthetic jets. *Journal of Fluid Mechanics*, 458:1–34, 2002.

[82] J. L. Gilarranz and O. K. Rediniotis. Compact, high-power synthetic jet actuators for flow separation control. In *AIAA Aerospace Sciences Meeting and Exhibit*, volume 39, 2001.

[83] S. R. Fugal, B. L. Smith, and R. E. Spall. Displacement amplitude scaling of a two dimensional synthetic jet. *Physics of Fluids*, 17(4), 2005.

[84] T. A. McGuinn, T. Persoons, P. Valiorgue, T. S. O'Donovan, and D. B. Murray. Heat transfer measurements of an impinging synthetic air jet with constant

stroke length. In *5th European Thermal-Sciences Conference*, Eindhoven, the Netherlands, 2008.

[85] J. E. Cater and J. Soria. The evolution of round zero-net-mass-flux jets. *Journal of Fluid Mechanics*, (472):167–200, 2002.

[86] S. G. Mallinson, J. A. Reizes, G. Hong, and P. S. Westbury. Analysis of hot-wire anemometry data obtained in a synthetic jet flow. *Experimental Thermal and Fluid Science*, 28(4):265–272, 2004.

[87] B. L. Smith and G. W. Swift. A comparison between synthetic jets and continuous jets. *Experiments in Fluids*, 34(4):467–472, 2003.

[88] N. E. Kotsovinos. A note on the spreading rate and virtual origin of a plane turbulent jet. *Journal of Fluid Mechanics*, 77(2):305–311, 1976.

[89] D. O. Rockwell. External excitation of planar jets. *Journal of Applied Mechanics*, 39:883–890, 1972.

[90] T. Persoons and T. S. O'Donovan. High dynamic velocity range particle image velocimetry using multiple pulse separation imaging. *Sensors*, 11(1):1–18, 2011.

[91] M. B. Gillespie, W. Z. Black, C. Rinehart, and A. Glezer. Local convective heat transfer from a constant heat flux flat plate cooled by synthetic air jets. *Journal of Heat Transfer*, 128(10):990–1000, 2006.

[92] T. A. McGuinn, T. Persoons, T. S. O'Donovan, and D. B. Murray. Surface heat transfer from an impinging synthetic air jet. In *Proceedings of The 10th UK National Heat Transfer Conference*, Edinburgh, Scotland, 2007.

[93] D. Lytle and B. W. Webb. Air jet impingement heat transfer at low nozzle-plate spacings. *International Journal of Heat and Mass Transfer*, 37(12):1687–1697, 1994.

[94] T. S. O'Donovan. *Fluid flow and heat transfer of an impinging air jet.* PhD thesis, Trinity College, Dublin, 2005.

[95] R. Mahalingam and A. Glezer. Design and thermal characteristics of a synthetic jet ejector heat sink. *Journal of Electronic Packaging, Transactions of the ASME*, 127(2):172–177, 2005.

[96] M. Chaudhari, B. Puranik, and A. Agrawal. Heat transfer characteristics of synthetic jet impingement cooling. *International Journal of Heat and Mass Transfer*, 53(5-6):1057–1069, 2010.

[97] L. Hesselink. Digital image processing in flow visualisation. *Annual Review of Fluid Mechanics*, 20:421–485, 1988.

[98] K. D. Hinsch. Three-dimensional particle image velocimetry. *Measurement Science and Technology*, 6:742–753, 1995.

[99] LaVision. LaVision-intelligent imaging, 2012.

[100] M. Raffel, C. Willert, S. Wereley, and J. Kompenhans. *Particle Image Velocimetry: A Practical Guide, 2nd Edition.* Springer, 2007.

[101] C. D. Meinhart, S. T. Wereley, and J. G. Santiago. A PIV algorithm for estimating time averaged velocity fields. *Journals of Fluids Engineering-Transactions of the ASME*, 122(2):285–289, 2000.

[102] LaVision. *DaVis 7.2 software product manual.* Anna-Vandenhoeck-Ring 19, D-37081, Goettingen, Germany, 2008.

[103] M. Stanislas, K. Okamoto, C. Kähler, and J. Westerweel. Main results of the second international PIV challenge. *Experiments in Fluids*, 39:170–191, 2005.

[104] J. Westerweel and F. Scarano. *Particle image velocimetry from the Springer handbook of experimental fluid mechanics.* Springer, 2007.

[105] A. K. Prasad and K. Jensen. Scheimpflug stereocamera for particle image velocimetry to liquid flows. *Appl. Optics*, 34:7092–7099, 1995.

[106] M. Gaydon, M. Raffel, C. Willert, M. Rosengarten, and J. Kompenhans. Hybrid stereoscopic particle image velocimetry. *Experiments in Fluids*, 23:331–334, 1997.

[107] C. Willert. Stereoscopic particle image velocimetry. *Measurement Science and Technology*, 8:1465–1479, 1997.

[108] R. E. Fischer and W. J. Smith. *Practical optical system layout and use of stock lenses*. McGraw-Hill, 1998.

[109] A. K. Prasad, R. J. Adrian, C. C. Landreth, and P.W. Offutt. Effect of resolution on the speed and accuracy of particle image velocimetry interrogation. *Experiments in Fluids*, 13:105–116, 1992.

[110] R. D. Keane and R. J. Adrian. Optimization of particle image velocimeters. Part 1. double pulsed systems. *Measurement Science and Technology*, 1(11):1202–1215, 1990.

[111] K. J. Brown, D. B. Murray, T. Persoons, and T. S. O'Donovan. Heat transfer characteristics of swirling impinging jets. In *Proceedings of International Mechanical Engineering Congress and Exposition*, 2009.

[112] D. L. Donoho and P. B. Stark. Unceratinty principlpes and signal recovery. *Journal of Applied Mathematics*, 49(3):906–931, 1989.

[113] Quantronix. Quantronix laser systems.

[114] Pea Soup. Pea soup smoke machines, 2012.

[115] Photron. Photron high speed video cameras, 2012.

[116] Holroyd components. Surface heating specialists, 2012.

[117] MKS Instruments. MKS mass flow controller, 2012.

[118] G.R.A.S. sound and vibration. Sound and vibration microphones, 2012.

[119] Dantec dynamics. Dantec Dynamics-laser optical measurement systems sensors, 2012.

[120] J. W. Scholten and D. B. Murray. Measurement of convective heat transfer using hot film sensors correction for sensor overheat. *Journal of Heat Transfer*, 118(4):982–984, 1996.

[121] T. S. O'Donovan and D. B. Murray. Jet impingement heat transfer - part II: A temporal investigation of heat transfer and local fluid velocities. *International Journal of Heat and Mass Transfer*, 50(17-18):3302–3314, 2007.

[122] T. Persoons. *Experimental flow dynamics in automotive exhaust systems with close-coupled catalysts.* PhD thesis, Katholieke Universiteit Leuven, 2006.

[123] P. S. Shadlesky. Stagnation point heat transfer for jet impingement to a plane surface. *AIAA Journal*, 21, 1983.

[124] J. W. Scholten. *Fluctuating heat trasnfer of cylinders in cross flow.* PhD thesis, Department of Mechanical and Manufacturing Engineering, University of Dublin, Trinity College, 1996.

[125] National Instruments. National Instruments data acquisition, 2012.

[126] P. F. Linden and J. S. Turner. The formation of 'optimal' vortex rings, and the efficiency of propulsion devices. *Journal of Fluid Mechanics*, 427:61–72, 2001.

[127] P. S. Krueger, J. O. Dabiri, and M. Gharib. The formation number of vortex rings formed in uniform background co-flow. *Journal of Fluid Mechanics*, 556:147–166, 2006.

[128] E. Aydemir, N. A. Worth, and J. R. Dawson. An investigation of vortex ring formation in strongly forced jet flows by high speed particle image velocimetry. In *15th International Symposium on Applications of Laser Techniques to Fluid Mechanics*, July 2012.

[129] T. Crittenden and A. Glezer. A high-speed, compressible synthetic jet. *Physics of Fluids*, 18(1):017107(1–18), 2006.

[130] S. G. Mallinson, G. Hong, and J. A. Reizes. Some characteristics of synthetic jets. In *AIAA Paper*, volume 3651, pages 1–10, 1999.

[131] J. O. Dabiri and M. Gharib. Fluid entrainment by isolated vortex rings. *Journal of Fluid Mechanics*, 511:311–331, 2004.

[132] A. Glezer and D. Coles. An experimental study of a turbulent vortex ring. *Journal of Fluid Mechanics*, 211:243–283, 1990.

[133] Y. Nago, T. Ogawa, K. Obara, H. Yano, O. Ishikawa, and T. Hata. Time-of-flight experiments of vortex rings propagating from turbulent region of superfluid 4 He at high temperature. *Journal of Low Temperature Physics*, 162:322–328, 2011.

[134] T. Persoons, T. A. Mcguinn, and D.B. Murray. A general correlation for the stagnation point nusselt number of an axisymmetric impinging synthetic jet. *International Journal of Heat and Mass Transfer*, 54(17-18):3900–3908, 2011.

[135] M. Hadžiabdić and K. Hanjalić. Vortical structures and heat transfer in a round impinging jet. *Journal of Fluid Mechanics*, 596:221–260, 2008.

[136] J. P. J. Van Jaarsveld, A. P. C. Holten, A. Elsenaar, R. R. Trieling, and G. J. F. van Heijst. An experimental study of the effect of external turbulence on the decay of a single vortex and a vortex pair. *Journal of Fluid Mechanics*, 670:214–239, 2011.

[137] T. T. Lim, T. B. Nickels, and M. S. Chong. A note on the cause of rebound in the head-on collision of a vortex with a wall. *Experiments in Fluids*, 12:41–48, 1991.

[138] P. G. Saffman. A model of vortex reconnection. *Journal of Fluid Mechanics*, 212:395–402, 1990.

Appendix A

OMEGA ENGINEERING LIMITED
ONE OMEGA DRIVE
RIVER BEND TECHNOLOGY CENTRE
NORTHBANK
IRLAM
MANCHESTER
M44 5BD
UNITED KINGDOM

Tel: +44 (0)161 777 6611
Fax: +44 (0)161 777 6622

FREEPHONE SALES 0800 488 488 (UK ONLY)

Website:

ISO 9002 REGISTERED COMPANY

NEWPORT® OMEGA® omega.co.uk

V.A.T. REG No. GB 620 0439 89

COMPANY REG No. 2564017

Certificate of Calibration

Certificate Number:	M04481	**Issue Date:**	14-04-2003
Customer.:	University of Dublin		
Description.:	RTD Probe	**S. O. No.:**	09971
Type No.:	PR-11-2-100-M30-200-1/10DIN	**Serial No.:**	4

The above instrument has been calibrated. All measurements made were referenced to standards of the laboratory whose values are traceable to UK National Standards. Copies of tests performed are on file at Omega Engineering Limited, Irlam, Manchester and are available upon request.

STD Temperature °C	Recorded Probe Temperature °C	Uncertainty of Measurement °C
0.00	0.05	0.15
49.95	50.10	0.18
99.90	100.05	0.20
200.20	200.20	0.27
300.20	300.1	0.37

Test Conditions	Humidity	35 %
	Temperature	22 °C

Instruments Used:	OE01, OE204, OE52
Calibrated By:	S. C. Roach

Signed:

Quality Manager

Ref: RTD.doc

The expanded uncertainties are based on the standard combined uncertainty multiplied by a coverage factor of K=2 providing a confidence probability of 95%

OMEGA ENGINEERING LIMITED
ONE OMEGA DRIVE
RIVER BEND TECHNOLOGY CENTRE
NORTHBANK
IRLAM
MANCHESTER
M44 5BD
UNITED KINGDOM

Tel: +44 (0)161 777 6611
Fax: +44 (0)161 777 6622

FREEPHONE SALES 0800 488 488 (UK ONLY)

Website:

ISO 9002 REGISTERED COMPANY

NEWPORT® OMEGA® omega.co.uk

V.A.T. REG No. GB 620 0439 89 COMPANY REG No. 2564017

Certificate of Calibration

OMEGA ENGINEERING, INC.

One Omega Drive, Box 4047, Stamford, CT 06907
(203) 359-1660 – http://www.omega.com – e-mail: info@omega.com

CERTIFICATE OF CALIBRATION

Model CL 26 **Serial Number** T-218386

Omega Engineering, Inc., certifies that the above listed instrument has been calibrated using standards whose accuracy is traceable to the U.S. National Institute of Standards and Technology, and meets or exceeds its published specifications. Calibration traceability of the above listed instrument is in full compliance with ANSI/Z540-1-1994 standards and requirements.

DATE 6-22-00

TESTED BY RE

AUTHORIZED SIGNATURE mck

mks
Technology for Productivity
MKS Instruments UK Limited - Telvac Engineering

Certificate of Calibration

Certificate Number:	090265827		
Date:	12-Jan-2009		
Calibration Data:	Final		
Mfg:	MKS		
Instrument Model:	1179A24CS1BVAB		
Serial number:	090265827		
Identifier:			
Test Gas:	N2	**GCF**	1.00
Nameplate Gas:	Air	**GCF**	1.00
Range (sccm):	20000		
Accuracy (%fsd):	1.00%		

Setpoint %	STD sccm	DUT sccm	Error sccm	Error mV	Error %
0%	0.00	0.00	0.00	0.00	0.00%
25%	5000.00	4964.00	-36.00	-9.00	-0.18%
50%	10000.00	10020.00	20.00	5.00	0.10%
75%	15000.00	15004.00	4.00	1.00	0.02%
100%	20000.00	19980.00	-20.00	-5.00	-0.10%
110%	22000.00	21844.00	-156.00	-39.00	-0.78%

The above calibration data was measured on the MKS Mass Flow Standard identified below:

UK Ref.:	FS111
Range (sccm):	20000
Nameplate Gas:	N2
Serial Number:	477879
Part number:	1179A24CS1BV
Commissioned:	03-Apr-2001
Last cal date :	16-Jun-2008
Cal by:	MKS-UK
Technique:	ROR
Cal Gas:	N2

Leak Check: **Valve** <0.5% FS **Ext:** <1.0E-9 mb/L/s

Data By: GD **Comment:** MANUFACTURE

Checked By: **Next Cal. due date:** 12-Jan-2010

MKS Instruments UK Limited - Telvac Engineering., Pegasus Court, Stafford Park 7, Telford TF3 3BQ
Tel: +44 (0) 1952 200664 Fax: +44 (0) 1952 200341 www.mksinst.com

Registered in England No: 6391618

CERTIFICATE No: 0964508

VISATON FR-8 8 OHM

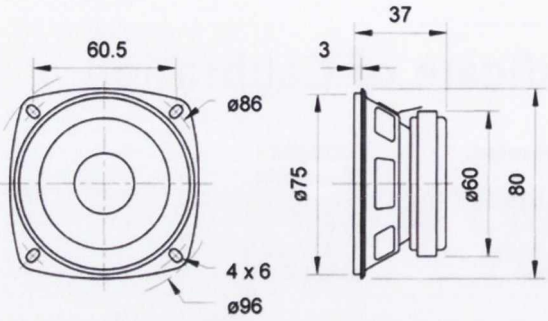

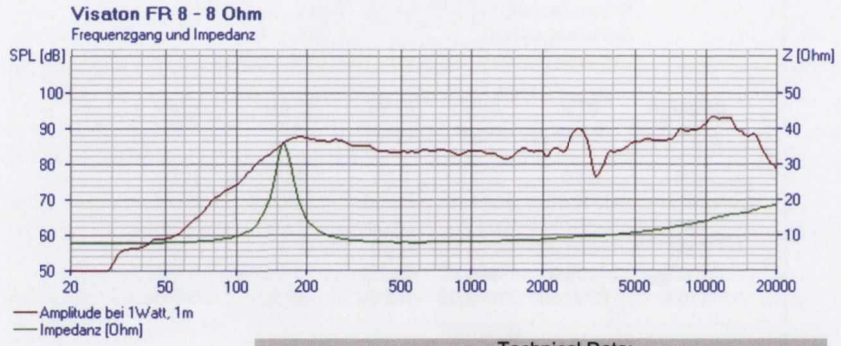

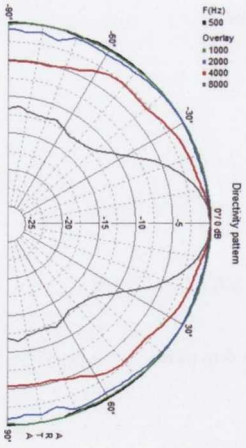

Technical Data:	
Rated power	10 W
Maximum power	15 W
Nominal impedance Z	8 Ohm
Frequency response	130–20000 Hz
Mean sound pressure level	86 dB (1 W/1 m)
Opening angle (-6 dB)	180°/4000 Hz
Excursion limit	+/−2 mm
Resonance frequency fs	150 Hz
Magnetic induction	1,4 T
Magnetic flux	200 µ Wb
Height of front pole-plate	3 mm
Voice coil diameter	15 mm
Height of winding	5 mm
Cutout diameter	75 mm
Net weight	0,24 kg
D.C. resistance Rdc	7,4 Ohm
Mechanical Q factor Qms	5,3
Electrical Q factor Qes	1,38
Total Q factor Qts	1,09
Equivalent volume Vas	0,7 l
Effective piston area Sd	30 cm²
Dynamically moved mass Mms	1,7 g
Force factor Bxl	2,5 Tm
Inductance of the voice coil L	0,6 mH
Temperature range	−25 ... 70 °C

¼-inch Pressure Microphone Type 40BP

Product Data and Specifications

Typical applications

- ***Sound pressure measurements***
- ***High frequency measurements***
- ***High level pressure measurements***

The G.R.A.S. Microphone Type 40BP is a ¼-inch precision condenser microphone for general purpose acoustic measurements, e.g. in couplers and at boundaries. It is an externally polarized pressure microphone with a large dynamic range and a wide frequency response.

As a pressure microphone, the Type 40BP measures the sound pressure at the location of its diaphragm. It has a flat pressure-frequency response over its entire working frequency range (see Fig. 2).

In an open sound field, a pressure microphone will also include the disturbing effects of its presence in the sound field. These are minimal for most of its frequency range because of its small dimensions (see Fig. 1 inset). At higher frequencies, the effects of reflections and diffractions must be accounted for. Generally, they lead to an increase in the measured sound pressure and corrections have to be made. Fig. 3 shows what these corrections are in a free field for various angles of incidence.

G.R.A.S. ¼-inch preamplifiers (see data sheet for Types 26AA, 26AB, 26AC and 26AL) are also available for use with the Type 40BP. The mounting thread (5.7 mm - 60 UNS-2) is compatible with other available makes of similar microphone preamplifiers.

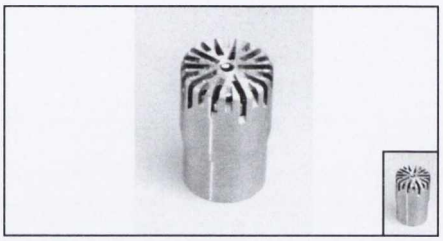

Fig. 1 ¼-inch Pressure Microphone Type 40BP (inset shows true size)

All G.R.A.S. microphones comply with the specifications of IEC 1094: *Measurement Microphones, Part 4: Specifications for working standard microphones*.

Non-corrosive, stainless materials are used in manufacturing these microphones to enable them to withstand rough handling and corrosive environments.

All G.R.A.S. microphones are guaranteed for 5 years and are individually checked and calibrated before leaving the factory. An individual calibration chart is supplied with each microphone.

Specifications

Frequency response:	
4 Hz - 70 kHz	±2.0 dB
10 Hz - 25 kHz	±1.0 dB
Nominal sensitivity:	
	1.6 mV/Pa
Polarization voltage:	
	200 V
Upper limit (3 % distortion):	
	174 dB re. 20 µ Pa
Microphone thermal noise:	
	31 dBA re. 20 µ Pa
Capacitance:	
	7 pF

...continued overleaf

Ver 06 Aug 2010

G.R.A.S.
Sound & Vibration

Skovlytoften 33
2840 Holte, Denmark
Tel +45 45 66 40 46 Fax +45 45 66 40 47
e-mail: gras@gras.dk www.gras.dk

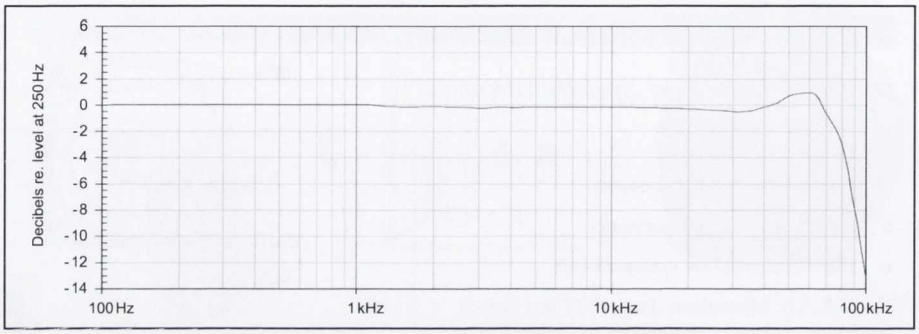

Fig. 2 Typical frequency response for Type 40BP (without protection grid)

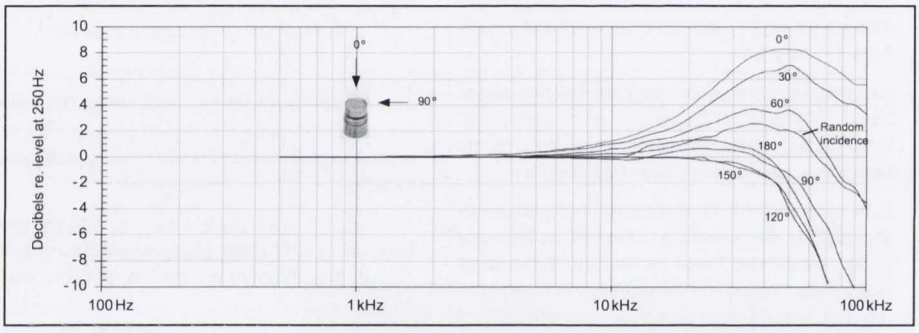

Fig. 3 Free-field corrections for various angles of incidence (without protection grid)

Specifications (continued)

Temperature:
Range: . . . . . −40 °C to +150 °C
Coeff. (250 Hz): . . . . . −0.01 dB/°C
Static-pressure coefficient:
−0.003 dB/k Pa
Humidity range:
0 - 100 % (non-condensing)
Influence of humidity (250 Hz):
<0.1 dB (0 - 100 % RH)
Influence of axial vibration, 1 m/s²:
69 dB re. 20 µ Pa
Venting:
Rear vented
Note: for most applications, rear venting is more advantageous particularly where phase response is critical. If front venting is preferred, please add "front venting" to the Type number of the microphone when ordering.
Dimensions (with protection grid):
Length/Diameter: . . . . . 10.5 mm/6.9 mm
(without protection grid):
Length/Diameter: . . . . . 9.1 mm/6.3 mm
Diameter (diaphragm ring):
5.9 mm
Threads:
Protection Grid: . . . . . 6.35 mm - 60 UNS
Preamplifier Mounting: . . . . . 5.7 mm - 60 UNS
Weight:
2 g

G.R.A.S. Sound & Vibration reserves the right to change specifications and accessories without notice

G.R.A.S.
Sound & Vibration

Skovlytoften 33
2840 Holte, Denmark
Tel +45 45 66 40 46 Fax +45 45 66 40 47
e-mail: gras@gras.dk www.gras.dk

¼" Preamplifier Type 26AC, General-purpose

Product Data

Typical Applications

- General-purpose preamplifier
- High-frequency measurements
- High-pressure measurements

Special Properties

- Wide Frequency Range
- Low Noise Level
- Very Small

Description

The G.R.A.S. ¼" Preamplifier Type 26AC is a small robust unit optimised for acoustic measurements using condenser microphones. It has a very low inherent noise level, a wide dynamic range and a frequency response from below 2 Hz to above 200 kHz.

Design

All G.R.A.S. microphone preamplifiers are based on a small ceramic thick-film substrate with a very high input impedance. The ceramic substrate is shielded by a guard ring to minimise the influence of stray capacitance and microphonic interference. The casing is made of stainless steel for maximum strength and durability. The small dimensions of this preamplifier ensure reliable operation under humid conditions owing to the heat generated by internal power dissipation.

Dynamic Range

Type 26AC can handle both single and dual-sided power supplies. The supply can vary between 28 V_{DC} and 120 V_{DC} single-sided or ±14V_{DC} and ±60 V_{DC} dual-sided. When using the high supply voltage (120V_{DC} or ±60V_{DC}), the dynamic range exceeds 140 dB.

Noise

The electrical circuit in Type 26AC is built on a ceramic substrate using selected low-noise components to gain very low self-noise. The electrical self-noise is so low that system noise is mainly determined by the microphone capsule's thermal noise.

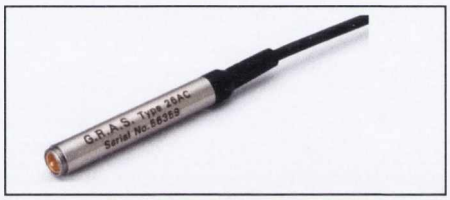

Fig. 1 ¼" Preamplifier Type 26AC

Frequency response

The low-frequency cut-off of the Type 26AC preamplifier is mainly determined by the input impedance of the preamplifier and the capacitance of the microphone capsule (see Fig. 3). The capacities 20 pF, 6.5 pF and 3 pF equal the typical capacitances of ½", ¼" and ⅛" microphone capsules respectively.

The high-frequency cut-off is determined by the preamplifier's ability to drive capacitive loads (slew rate), caused by the cable. For large-signals, the effects of these parameters must be accounted for when measurements are performed. Fig. 4 shows the large-signal response for Type 26AC for various capacitive loads corresponding to different cable lengths. The output level is in decibels relative to 1 Volt. Typical capacitance for the cable is 100pF/m (30pF/foot).

Connector

Preamplifier Type 26AC (Fig. 1) is provided with a 3-m lightweight cable terminating in a 7-pin LEMO series 1B plug (Fig. 2). The cable is only 2.5 mm in diameter and will withstand temperatures from -40 °C to +150 °C. An adaptor (GR0010) for G.R.A.S. ½" microphones is included.

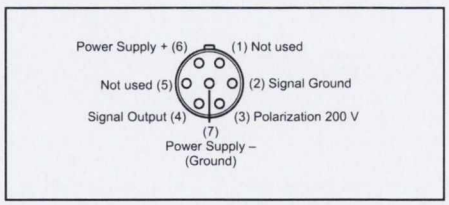

Fig. 2 7-pin LEMO plug 1B male (ext. view)

Type 26AC, Vers. 12.05.2009

G.R.A.S.
SOUND & VIBRATION

Skovlytoften 33,
2840 Holte, Denmark
www.gras.dk gras@gras.dk

¼" Preamplifier Type 26AC, General-purpose

Specifications

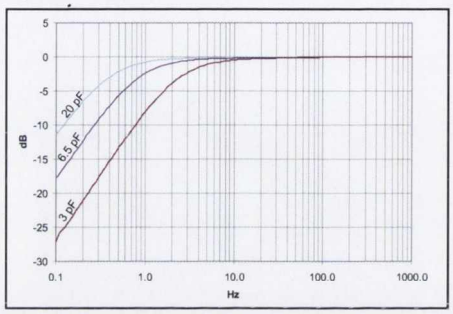

Fig. 3 Typical low-frequency response of Type 26AC for ½" (20 pF), ¼" (6.5 pF) and ⅛" (3 pF) microphones

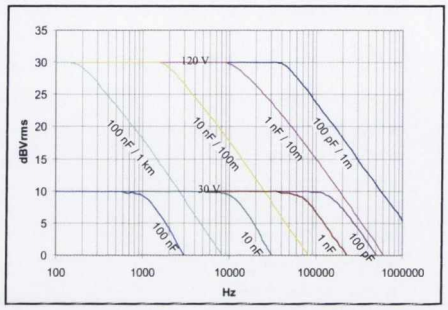

Fig. 4 Typical max. rms output signal with 120 V and 30 V supply

Technical Data

Frequency response (18pF/small signal):
2 Hz - 200 kHz . . . . . ±0.2 dB
Slew rate:
20 V/µs
Input impedance:
20 GΩ, 0.4 pF
Output impedance (Cs = 20 pF, f = 1000Hz):
Typical . . . . . 55 Ω
Noise (measured with 20 pF ½" dummy mic.):
A-weighted: . . . . . ≤2.5 µV rms
(typically 1.8 µV rms)
Linear (20 Hz - 20 kHz): . . . . . ≤6 µV rms
(typically 3.5 µV rms)
Gain:
Typical: . . . . . -0.25 dB
Power supply:
Single: . . . . . 28 V (0.7 mA) to 120 V (2.5 mA)
Dual: . . . . . ±14 V (0.7 mA) to ±60 V (2.5 mA)
Maximum signal-output voltage (peak):
from ±10 V to ±50 V
Temperature:
Operation: . . . . . -30 °C to +70 °C
Storage: . . . . . -40 °C to +85 °C
Relative humidity:
Operation: . . . . . 0 to 95 %
Storage: . . . . . 0 to 95 %
Dimensions and Weight:
Diameter: . . . . . 6.35 mm (¼")
Length: . . . . . 43 mm (1.7")
Weight (without cable): . . . . . 6 g (0.2 oz)
Weight (with cable + LEMO conn.): 50 g (1.8 oz)

Accessories

Included

GR0010:	¼" to ½" adapter for use with G.R.A.S. ½" microphones

Optional

RA0001:	Right-angled (90°) Adapter for ½" microphone and ¼" preamplifier
RA0003:	Adapter for ½" microphone and ¼" preamplifier
RA0006:	Angled (90°) Adapter ¼" to ¼".
AA0008:	Extension cable, 3 metres
AA0009:	Extension cable, 10 metres
AA0012:	Extension cable, 30 metres
AA0014:	Extension cable, 100 metres
AA0020_XX:	Extension cable, XX metres (customer-specified length)
AA0013:	Tripod adapter for ¼" preamplifier
RA0096:	Tripod adapter for ¼" preamplifier with angular adjustment

G.R.A.S. Sound & Vibration reserves the right to change specifications and accessories without notice.

G.R.A.S.
SOUND & VIBRATION

Skovlytoften 33,
2840 Holte, Denmark
www.gras.dk gras@gras.dk

Power Module Type 12AN

Product Data and Specifications

Typical applications and features

- ***General-purpose measurements***
- ***Precision measurements***
- ***Acoustic monitoring***
- ***Microphone calibration***
- ***Four channels***
- ***0 V or 200 V polarization***

The G.R.A.S. Power Module Type 12AN (Fig. 1) is a four-channel power supply for preamplifiers used with condenser microphones. It is for general use in acoustic measurements; both in the laboratory and in the field.

The Type 12AN can be powered either by internal standard batteries or an external DC supply (6 V - 20 V), e.g. the supplied mains/line adapter. It is built into a sturdy anodized aluminium cabinet.

The polarization voltage for the microphones fitted to the preamplifiers can be set to:

- 0 V — for prepolarized microphones, or
- 200 V — for externally polarized microphones

The Type 12AN also supplies ±15 V to power the preamplifiers. With four G.R.A.S. preamplifiers, it will run for approximately 25 hours on fresh standard alkaline batteries. A **Low Batt** LED indicates the condition of the batteries.

Fig. 1 Power Module Type 12AN

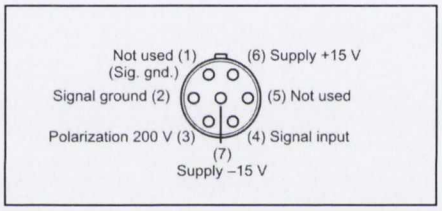

Fig. 2 7-pin LEMO female socket 1B (external view)

The inputs are 7-pin LEMO sockets on the front panel, which are wired up (see Fig. 2) for G.R.A.S. microphone preamplifiers, e.g. Types 26AB, 26AC, 26AJ and 26AK, but are also compatible with other available makes of similar microphone preamplifiers.

The signals from the preamplifiers are AC coupled to their respective outputs which are standard BNC sockets also on the front panel.

Vers.07-01-03

G.R.A.S.
Sound & Vibration

Skovlytoften 33
2840 Holte, Denmark
Tel +45 45 66 40 46 Fax +45 45 66 40 47
e-mail: gras@gras.dk www.gras.dk

Specifications

Input/Output sockets:
4 x Inputs: ..... 7-pin LEMO 1B female
4 x Outputs: ..... BNC coaxial

Output voltages:
Preamplifier supply: ..... ±15 V
Polarization voltage: ..... 0 V or 200 V

Frequency response:
0.05 Hz - 200 kHz: ..... ±0.2 dB

Output impedance:
30 Ω

Power supply:
4 x LR6 (AA) standard alkaline cells, or
Mains/line adapter: ..... 6 V - 20 V DC

Power consumption using an ext. power supply:
With 4 G.R.A.S. preamps.: ..... 135 mA

Fuse:
200 mA (Slow), 250V

Battery life (valid for 23 °C and alkaline cells):
With 4 G.R.A.S. preamps.: .....≈25 hours

Operating temperature range:
–10 °C to +50 °C

Dimensions:
Height: .....44 mm (1.73 in)
Width: ..... 210 mm (8.27 in)
Depth: ..... 194 mm (7.64 in)

Weight:
Without batteries ..... 1.2 kg (2.65 lbs)

Accessories included:
EL0001: ..... 4 x LR6 (AA) batteries
Mains/line adapter supply regulated to 15 V DC
AB0002: ..... for 230 V AC
or
AB0003: ..... for 120 V AC

G.R.A.S. Sound & Vibration reserves the right to change specifications and accessories without notice

G.R.A.S.
Sound & Vibration

Skovlytoften 33
2840 Holte, Denmark
Tel +45 45 66 40 46 Fax +45 45 66 40 47
e-mail: gras@gras.dk www.gras.dk